NASA Reference Publication 1401

The Magnetosphere Imager Mission Concept Definition Study Final Report

L. Johnson, M. Hermann, and the MSFC MI Study Team

April 1997

NASA Reference Publication 1401

The Magnetosphere Imager Mission Concept Definition Study Final Report

---

L. Johnson, M. Hermann, and the MSFC MI Study Team
Marshall Space Flight Center • MSFC, Alabama

National Aeronautics and Space Administration
Marshall Space Flight Center • MSFC, Alabama 35812

April 1997

TABLE OF CONTENTS

Page

INTRODUCTION 1

MAGNETOSPHERE IMAGER SCIENCE 2

MAGNETOSPHERE IMAGER MISSION EVOLUTION 2

INTERMEDIATE CLASS MISSION 4

- Science Instrument Complement 4
- Single Spacecraft Option 4
- Dual Spacecraft Option 10

SOLAR TERRESTRIAL PROBE MISSION 13

- Science Instrument Complement 13
- Launch Vehicle Options 14
- STP Baseline Vehicle 15
- Configuration 16
- Structures 17
- Electrical Power Subsystem (EPS) 17
- Thermal Control Subsystem (TCS) 18
- Attitude Control and Determination (ACAD) 20
- Propulsion Subsystem 23
- Communications and Data Management Subsystem (CDMS) 24
- Mass Properties 24

SOLAR CONNECTIONS MISSION 26

- Science Instrument Complement. 26
- Mission Analysis and Orbit Mechanics 26
- Launch Vehicle Options 32
- Structures 39
- TCS 46
- EPS 56
- C&DH 64

ACAD Requirements 71
Mass Properties 84
Natural Space Environments 86
Operations 87
System Requirements 94

APPENDIX A: ACKNOWLEDGMENTS A–1

APPENDIX B: NASA RESEARCH ANNOUNCEMENT (NRA) B–1

Techniques and Technologies for Magnetospheric Imaging B–1
NRA Solicitation B–1
Funded Research B–3

APPENDIX C: SOLAR ARRAY RADIATION ANALYSIS FOR THE MAGNETOSPHERE IMAGER C–1

APPENDIX D: PRELIMINARY SPACECRAFT CHARGING ANALYSIS FOR THE MAGNETOSPHERE IMAGER D–1

LIST OF ILLUSTRATIONS

Page

1. IMI POLAR single spacecraft option 4
2. IMI Hughes HS–376 single spacecraft option 5
3. Candidate orbits from initial Delta II insertion 6
4. Solar radiation on the spacecraft 8
5. Orientation of spacecraft with respect to the Sun vector 9
6. Dual spacecraft option 11
7. STP option launch vehicle candidates 14
8. Perigee trade study 15
9. Conestoga 3632 launch vehicle 15
10. IMI STP baseline configuration 16
11. STP spacecraft structure 17
12. Effective area versus ß angle 18
13. STP with radiators on spacecraft ends 19
14. MI with radiator on cylindrical portion of spacecraft body 19
15. Radiator band size versus radiator temperature 20
16. STP ACS components 21
17. Solar radiation torque 21
18. Gravity gradient torque 22
19. Aerodynamic torque 22
20. Environmental torques 22
21. STP schematic for propulsion system 23
22. Evolution of MI science instruments 26
23. Solar Connections mission orbit 27
24. Spacecraft time in umbra 28
25. Mission ß angle varies during a year 28
26. Mission orbit apsidal precession 29
27. Ground station contact 30
28. Mission perigee altitude history for 2 years 31
29. Composition of the LLV3(6) 32
30. Composition of the Conestoga 3632 33
31. Composition of the Taurus S 34
32. MI spacecraft within the Taurus S fairing 34
33. Nominal flight profile (provided by OSC) 35
34. Isometric spacecraft configuration 36
35. Spacecraft panel assembly 37
36. Science instrument FOV requirements 38
37. Spacecraft configuration top view 38
38. Spacecraft frame structure 39

39. Taurus XL/S and Taurus XL spectral density curves 40
40. Panel-to-longeron mounting options 44
41. Deckplate and panel mounting concepts 44
42. Preliminary assembly flow 45
43. MI thermal design 48
44. MI finite element model 49
45. MI orbits modeled showing spacecraft orientation 50
46. Typical spacecraft radiator panel 53
47. MI thermal control heater system design 53
48. Thermal verification process 54
49. Summary of the EPS 56
50. EPS block design 57
51. Total effective spacecraft surface area 60
52. Solar array power versus ß angle 61
53. MI C&DH subsystem 64
54. Antenna system 67
55. Antenna pattern 68
56. Link margins 69
57. C&DH block diagram 70
58. Location of science instruments 71
59. ACAD system -derived requirements 72
60. ACAD system hardware block diagram 73
61. A functional mounting arrangement for the ACAD components 75
62. Principal axis precesses around the angular momentum vector, which is perturbed by the environmental disturbances 76
63. Options for damper orientation 77
64. Nutation angle after worst case launch vehicle tip-off conditions 78
65. Position and velocity for damper mass 1 79
66. Position and velocity for damper mass 2 79
67. Angle between the spacecraft spin axis and the orbit normal after worst case launch vehicle tip-off conditions 80
68. Angle between the spacecraft spin axis and the orbit normal due to environmental disturbances 80
69. Angular velocity component along the spacecraft X-axis 81
70. Angular velocity component along the spacecraft Z-axis 81
71. X-axis angle of the 2–1–3 Euler angles from an inertial frame aligned with the orbit to the spacecraft-fixed frame 82
72. Z-axis angle of the 2–1–3 Euler angles from an inertial frame aligned with the orbit to the spacecraft-fixed frame 82
73. Spacecraft spin rate over two orbits 83
74. Change in spin rate over two orbits 83
75. Subsystem masses as a percentage of the total mass 85
76. Mass properties summary 85
77. Taurus S/MI flight operations profile 90
78. Mission operations flow 91

79. MI system external interfaces 94
80. Overall MI system diagram 95
81. C&DH connectivity diagram 95

LIST OF TABLES

Page

1. Strawman instrument payload list. 2
2. Options for the Magnetosphere Imager mission. 3
3. Weight (in kg) estimates for the spacecraft concept options. 5
4. Spacecraft attitude control requirements. 10
5. MI STP strawman instrument list. 13
6. Mass summary for the STP baseline. 24
7. Quasi-static load factors for Taurus XL/S. 40
8. Comparison of thermal conductivity of some carbon fibers. 41
9. Structures mass statement. 46
10. Thermal requirements. 47
11. 0˚ ß thermal analysis results. 50
12. 66.5˚ ß analysis results. 51
13. Heater power requirements. 51
14. EPS design. 56
15. PSE features 58
16. Solar array performance analysis factors 60
17. Electrical power loads summary 62
18. EPS mass statement. 63
19. Science instrument data rate requirements. 64
20. *Clementine* recorder characteristics. 66
21. DSN compatible transponder and amplifier characteristics 66
22. Antenna gain predicted and typical coverage 68
23. C&DH equipment list 70
24. Science instrument ACAD requirements 72
25. ACAD system equipment list. 74
26. Environmental torques on MI 78
27. Detailed mass summary. 84
28. 90th percentile worst case geomagnetic substorm plasma environment 87

ABBREVIATIONS AND ACRONYMS

ACAD	attitude control and determination
ACS	attitude control subsystem
AKM	apogee kick motor
BOL	beginning of life
C&DH	command and data handling subsystem
CDMS	command and data management subsystem
DMS	data management system
DSN	Deep Space Network
EOL	end of life
EPS	electrical power subsystem
FEA	finite element analysis
FOV	field of view
GN&C	guidance, navigation, and control
HPI	Hot Plasma Imager
IMI	Inner Magnetosphere Imager
IMU	inertial measurement unit
MI	Magnetosphere Imager
MLI	multilayer insulation
NASCOM	NASA Communications Network
OV	orbital verification
PCDU	power control and distribution unit
PI	Plasma Imager
PKM	perigee kick motor
PSE	power supply electronics
RCS	reaction control system
RPI	Radio Plasma Imager
S/C	spacecraft
SDT	Science Definition Team
STP	Solar Terrestrial Probe
TCS	thermal control subsystem
TPS	thermal protection subsystem

REFERENCE PUBLICATION

THE MAGNETOSPHERE IMAGER MISSION CONCEPT DEFINITION STUDY FINAL REPORT

INTRODUCTION

One of the most important discoveries of the space age was that of the Van Allen radiation belts around the Earth. These belts are vast clouds of intense radiation that are caused by the Earth and its rotating magnetic field being impacted by the supersonically expanding atmosphere of the Sun. After 30 years of spacecraft flights through this region, it is known that these radiation clouds contain electrical storms and disturbances that play an important role in the Earth's atmospheric processes.

Through technology advances, pictures of this magnetospheric cloud can be made similar to the satellite photos of ordinary clouds commonly used for weather reports. Thus, NASA is poised to explore and expose this violent and variable region that surrounds the planet with entirely new types of satellite images.

The George C. Marshall Space Flight Center (MSFC) is responsible for defining potential future space science programs, one of which is the proposed Magnetosphere Imager (MI) mission. For three decades, magnetospheric field and plasma measurements have been made in situ by diverse instruments flown on spacecraft in many different orbits, widely separated in both space and time, and under various solar and magnetospheric conditions. Scientists have used this information to piece together an intricate, yet incomplete view of the magnetosphere. A simultaneous global view, using various light wavelengths and energetic neutral atoms (ENA), could reveal exciting new data and help explain complex magnetospheric processes, thus providing a clearer picture of this region of space.

To provide these measurements, NASA assembled a Science Definition Team (SDT) to develop the scientific objectives of a magnetospheric imaging mission. Concurrent with the formation of this team, MSFC was given responsibility for defining the mission and subsequently formed an engineering team to begin concept studies. (Appendix A lists MI study and science definition participants.) The result of these efforts is the MI mission.

In order to better understand this environment, the MI mission will pose the following questions:

- What does the global magnetosphere look like in quiet and disturbed conditions?
- How do the principal magnetospheric regions globally change in response to internal and external influences?
- How are the principal magnetospheric regions interconnected?
- What are the remote global signatures of the important astrophysical processes occurring in the magnetosphere?

MAGNETOSPHERE IMAGER SCIENCE

For a detailed discussion of the scientific objectives of the MI mission, refer to NASA Reference Publication 1378. Appendix B presents a copy of the NASA Research Announcement (NRA) that solicited related instrument technology development, along with synopses of funded research in this area.

MAGNETOSPHERE IMAGER MISSION EVOLUTION

The MI, originally the Inner Magnetosphere Imager (IMI), was conceived to be a part of the Space Physics Division’s intermediate class of missions with a cost ceiling of $300M. The engineering studies performed at MSFC indicated that a spinning spacecraft with a despun platform, similar to General Electric’s (now Lockheed Martin’s) POLAR and Hughes’ HS–376 spacecraft, launched aboard a Delta, could easily accommodate the strawman science instruments (SI) defined by the NASA Headquarters-appointed SDT in table 1.

TABLE 1.—*Strawman instrument payload list.*

No.	**Instrument Name (Energy Spectrum)**	**Mass (kg)**	**Power (W)**	**Data Rate (kbps)**	**Field of View (FOV)**
1	Hot Plasma Imager (20–1,000 KeV Neutral Atoms)	14.0	4.0	12	4 π steradians (str)
	Hot Plasma Imager (1–50 KeV Neutral Atoms)	7.0	7.0	6	4 π str
	Electronics	8.0	12.0		
2	Plasmasphere Imager (He^+304 Å)	7.2	4.5	7	135° × 180°
	Electronics	11.8	16.5		
3	Plasmasphere Imager (O^+834)	7.2	4.5	7	135° × 180°
	Electronics	11.8	16.5		
4	Geocoronal Imager (1216 Å)	15.0	15.0	2	4 π str
	Electronics	12.0	15.0		
5	Auroral Imager (1304, 1356 Å)	18.0	20.0	15	30° × 30°
	Electronics	12.0	15.0		
6	Proton Auroral Imager (1216 Å)	20.0	25.0	8	30° × 30°
	Electronics	10.0	15.0		
7	Electron Precipitation Imager (0.3–10 KeV)	24.5	11.0	2	3° × 3°
	Electronics	3.0	9.0		

In the summer of 1993, the Space Physics Division directed the SDT and MSFC engineering team to redefine the mission to fit within a new class of missions—the Solar Terrestrial Probe (STP). STP missions are to cost no more than $150M (excluding launch cost) and be accommodated on launch vehicles smaller than a Delta. The SDT met in November 1993 and developed a new strawman instrument complement suitable for a smaller spacecraft but still capable of meeting the core science objectives necessary for magnetospheric imaging.

In the spring of 1994, the SDT and MSFC engineering team were again directed by the Space Physics Division to redefine the mission. Subsequently, it was renamed MI—Magnetosphere Imager—and programmatically it was redefined to fit within the proposed Solar Connections Program. The cost ceiling for a Solar Connections mission is to be $80M and all such missions are to utilize a medium-to-light (med-lite) class launch vehicle. The SDT responded with a descoped strawman payload for the MI mission. A summary of all three missions is found in table 2.

TABLE 2.—*Options for the Magnetosphere Imager mission.*

	Intermediate Class Mission	**STP and Solar Connections Missions**
Cost Ceiling ($)	300M	150M/80M
Launch Vehicle	Delta II	Med-Lite Class
Orbital Parameters	4,800-km by 44,600-km (7 R_E) 90° Inclination	4,800-km by 44,600-km (7 R_E) 90° Inclination
Instruments	7 (4 on spinning spacecraft; 3 on despun platform)	3 “core” (1 is a consolidation of 3 from the original list) plus up to three “mission enhancing”/3 “core”
Total Spacecraft Mass (kg) (wet; including 30% contingency)	1,000 (HS–376) 1,300 (POLAR)	413/330

This report briefly summarizes the Intermediate and STP mission concepts, and focuses on the proposed Solar Connections version.

INTERMEDIATE CLASS MISSION

Science Instrument Complement

The SDT defined a strawman instrument payload to meet mission objectives. The instruments and their accommodation requirements are summarized in table 1.

Single Spacecraft Option

Early in the mission feasibility study, it was determined that no new or stressing technology would be required for the spacecraft. In fact, it was determined that several spacecraft have been flown that can meet the mission objectives, with some minor modifications. In order to facilitate cost savings, it would be advantageous to use this existing capability for the spacecraft—thus the assessment made by way of potential spacecraft determines their compatibility for the mission. As the study progressed and NASA’s emphasis on advanced technology development began to manifest, an examination was made of selected new technologies with high probability of decreasing spacecraft weight and potentially increasing performance. These new technologies will be most advantageous to the STP or Solar Connections mission.

Keeping in mind the use of existing spacecraft, it was determined that both Lockheed Martin and Hughes have spacecraft that could be easily modified for the mission. Both are spin stabilized with despun platforms that allow for precision pointing of specific instruments. The size of each spacecraft is comparable, as are general performance capabilities. The POLAR spacecraft was built as a part of the International Solar Terrestrial Physics program and was launched in 1996. The Hughes HS–376 has a long and successful history as a communications satellite—more than 30 have been flown in the last 13 years. Figures 1 and 2 show the location of the IMI instruments on such spacecraft.

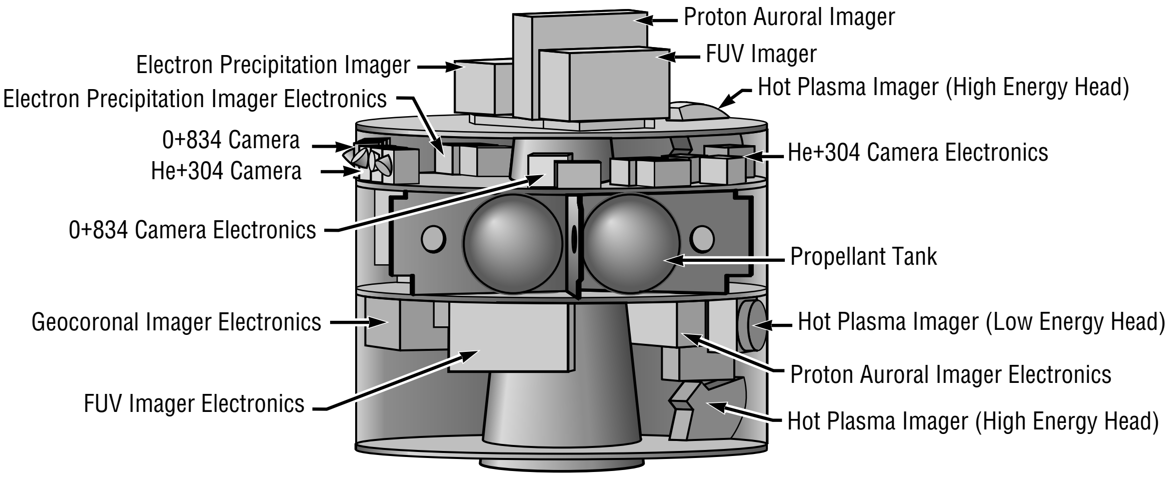
Proton Auroral Imager
FUV Imager
Electron Precipitation Imager
Hot Plasma Imager (High Energy Head)
Electron Precipitation Imager Electronics
0+834 Camera
He+304 Camera Electronics
He+304 Camera
0+834 Camera Electronics
Propellant Tank
Geocoronal Imager Electronics
Hot Plasma Imager (Low Energy Head)
Proton Auroral Imager Electronics
FUV Imager Electronics
Hot Plasma Imager (High Energy Head)

FIGURE 1.— IMI POLAR single spacecraft option.

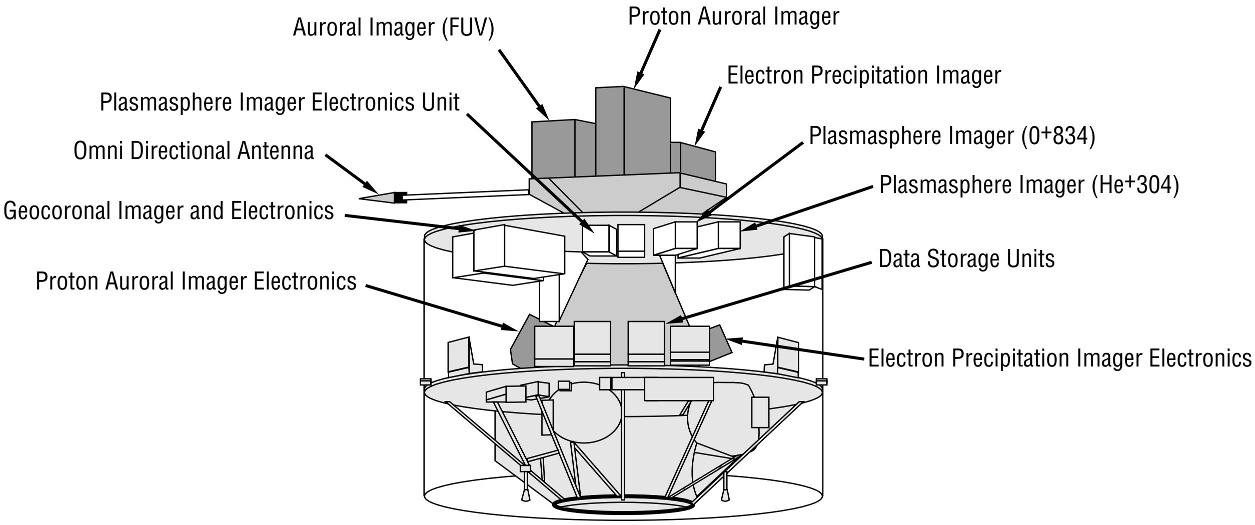
Auroral Imager (FUV)
Proton Auroral Imager
Electron Precipitation Imager
Plasmasphere Imager Electronics Unit
Plasmasphere Imager (0+834)
Omni Directional Antenna
Plasmasphere Imager (He+304)
Geocoronal Imager and Electronics
Data Storage Units
Proton Auroral Imager Electronics
Electron Precipitation Imager Electronics

FIGURE 2.—IMI Hughes HS–376 single spacecraft option.

The placement of the instruments is optimized to meet viewing and thermal requirements, and to achieve spacecraft balance. There are three instruments on the despun platform with a total weight (including electronics) of 88 kg. The remaining four instruments are placed on the spinning portion of the spacecraft and have a total weight of 93 kg. The weight breakdown for this spacecraft concept, as well as the dual spacecraft option, is listed in table 3.

TABLE 3.—*Weight (in kg) estimates for the spacecraft concept options.*

Subsystem	Single Spacecraft Approach	Spin-Stabilized Small Spacecraft	Three-Axis Stabilized Small Spacecraft
Structures	252	35	67
Thermal Control	18	4	6
Attitude Control	16	13	30
Electrical Power	161	51	45
Harness	80	12	18
Communications	100	20	19
Propulsion (Dry)	33	16	21
Science Instruments	181	93	88
Subtotals	**841**	**244**	**294**
Science Contingency	54	29	26
Spacecraft Contingency	198	45	62
Orbit Adjust Propellant	See RCS	70	69
RCS Propellant	226	10	10
Totals	**1,319**	**398**	**461**

The mission orbit is to have a perigee altitude of 4,800 km, and an apogee altitude of 44,500 km (7 Earth R_E). The apogee of 7 R_E is a requirement specified by the SDT, and the perigee altitude of 4,800 km was driven by the performance capability of the POLAR spacecraft propulsion system, the Intermediate Class mission spacecraft mass, and the Delta II launch vehicle performance capability. Other concerns driving the orbit selection include avoiding monatomic oxygen in the upper atmosphere at the 1,000- to 1,500-km altitudes and high plasma densities at altitudes less than 4,800 km. Because of these environmental constraints and to maintain instrument viewing perspective, this orbit is considered nominal for the STP mission.

Mission Analysis and Orbit Mechanics

The proposed orbit was established by analysis and by SDT cooperation and compromises. Initially, the spacecraft was to be placed in a polar orbit with a 400-km perigee and 5-Earth-R_E apogee. Early in the study, a change in the orbit after the first year was proposed to allow the gathering of additional scientific information. This maneuver would require a separate onboard propulsion system, but it would not affect the performance capabilities of the chosen launch vehicle. However, the requirement for this orbit change was later removed.

Due to many concerns raised by the SDT, higher perigee and apogee values were desired for the spacecraft's orbit. (All perigee and apogee values are altitudes measured from the surface of the Earth.) They requested the apogee altitude to be 7 R_E for three possible perigee altitudes: 1,000 km, 2,000 km, and 1 R_E, as shown in figure 3. Because a polar-orbiting spacecraft is required, the most likely launch site would be the Western Test Range (WTR) at Vandenberg Air Force Base (VAFB), CA.

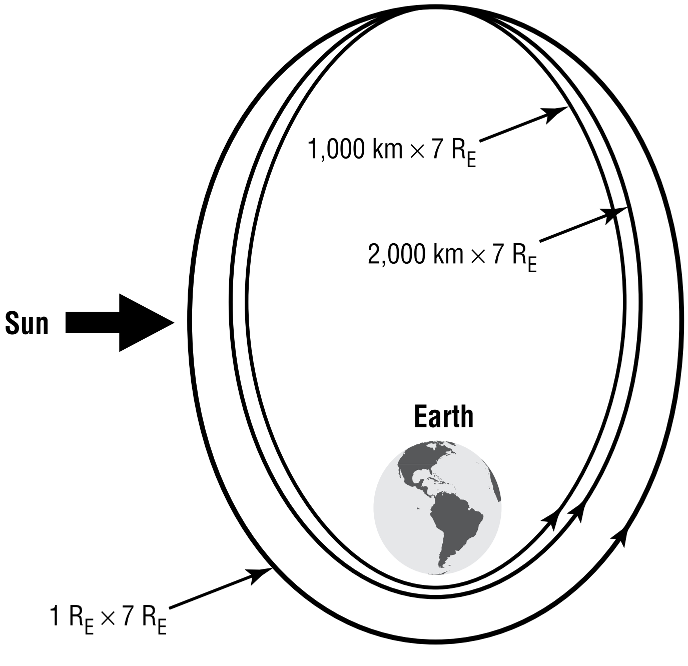

FIGURE 3.—Candidate orbits from initial Delta II insertion.

With these constraints, the Delta II, the largest vehicle initially under consideration, cannot accomplish the mission. The spacecraft mass exceeded the capability of the launch vehicle. To reduce the demands placed upon the launch vehicle, an onboard propulsion system was proposed so that the satellite could reach the required perigee altitudes. The vehicle would only be required to place the spacecraft into a 185-km by 7-R_E orbit; the perigee raise would be accomplished by the spacecraft's onboard propulsion system. The analysis discussed in the Mission Analysis and Orbit Mechanics section that follows places the optimal perigee at 4,800 km. This allows for the higher spacecraft mass to be placed into orbit.

Continued analysis and programmatic changes altered the spacecraft launch requirements. The perigee and apogee have remained at 4,800 km and 7 R_E, respectively, for the polar orbit. However, the spacecraft has been reduced in size and complexity to meet the new constraints.

Thermal Control Subsystem (TCS)

The TCS uses multilayer (MLI) insulation, thermal coatings, thermal radiators, and heaters to keep the spacecraft and instruments within the specified temperature requirements. Heat rejection is achieved through thermal radiation of heat generated by the instruments and their electronics. The electronics boxes have higher temperature requirements and wider temperature ranges than the science instruments. Because of this wide temperature range, the electronics can be easily accommodated on the spacecraft. The boxes can be located on the lower level of the bus where they can radiate the generated heat to the walls. Placement of the electronics on the lower level isolates them from of the instruments that need to operate at a lower temperature.

Some of the instruments require low temperatures and should, therefore, be located at or near the top of the spacecraft to give their radiative coolers a better view to space. Cutouts in the top of the spacecraft allow the spacecraft components and instruments in the spinning portion to radiate directly to space. For example, the Far Ultraviolet (FUV) Imager, the Geocoronal Imager (GI), and the Proton Auroral Imager (PAI) require cooling to temperatures of –100 °C or lower and have to be located at the top of the vehicle to provide an adequate view to space for the thermal radiators. Because the FUV imager and the PAI are on the despun platform, their radiators will intrinsically have an adequate view to space. The radiators for the despun platform instruments will have to be shielded to help minimize the amount of incident solar radiation. MLI and other low conductivity materials will be used to isolate them from the spacecraft thermal loads in order to achieve the low temperatures needed.

Critical to maintaining the heat rejection capabilities of the spacecraft and the instruments on the despun platform is the limitation of solar incident radiation on the spacecraft radiators. The orbit plane of the spacecraft requires that after 6 months the spacecraft radiators will begin to receive direct solar radiation as shown in figure 4. This "precession" would severely degrade the performance of the radiators. To avoid the direct illumination of their surfaces, a 180° reorientation maneuver of the spacecraft is needed every 6 months.

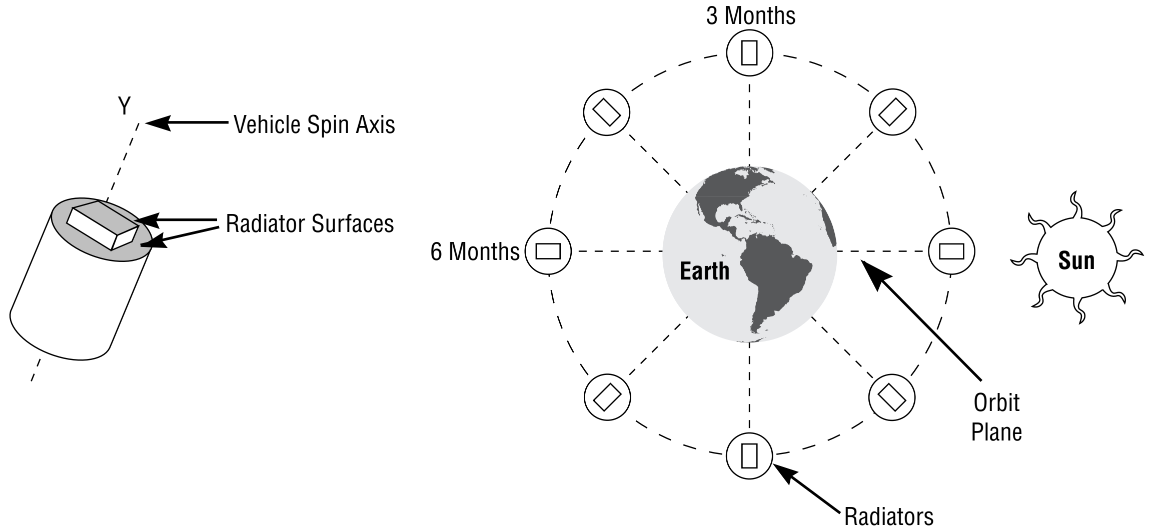

FIGURE 4.—Solar radiation on the spacecraft.

Battery-operated heaters are required to enhance spacecraft component and instrument survivability during the coldest portions of the mission, particularly during umbra. The spacecraft is capable of surviving approximately 90 minutes in umbra with an increase in heater power needed for longer time periods.

Electrical Power Subsystem (EPS)

The spacecraft is estimated to require 325 W electrical power from the solar arrays. This total power represents 190 W for the instrumentation suite, with the remaining power designated for other subsystems, housekeeping, and contingency requirements. Active solar array surface area is estimated to be approximately 14.9 m^2. This includes body-mounted silicon solar cells on both the cylindrical and end panel surfaces.

Figure 5 shows the orientation of the spacecraft spin axis with respect to the Sun vector. The Sun angle is the angle between the spin axis and the Sun vector, and the beta (ß) angle is the angle between the Sun vector and the orbit plane. With the spacecraft spin axis perpendicular to the orbit plane, the worst case ß angle is 66.5°. At these angles, the beginning-of-life (BOL) power output of the solar array is 415 W.

This array output provides a worst case BOL system power margin of 20 W (between the array output and load demand). End-of-life (EOL) performance of the system with a 25 percent radiation-induced degradation will result in no power margin at the worst case ß angles. Power degradation greater than 25 percent will require system power management of instrument resources.

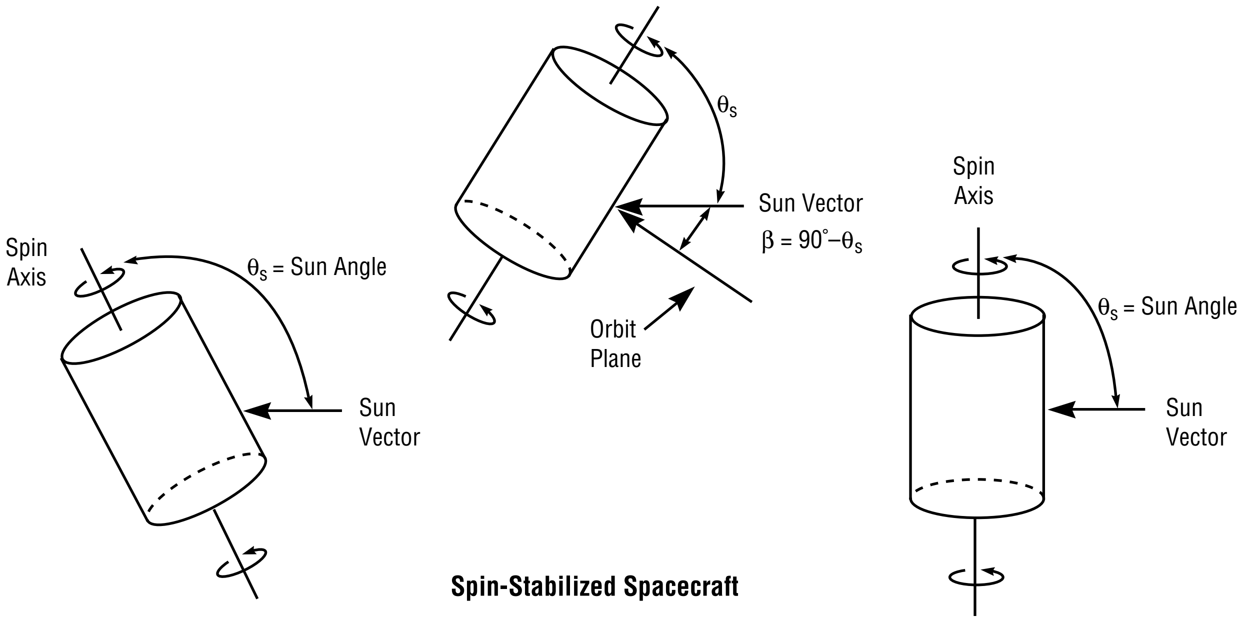

FIGURE 5.—Orientation of spacecraft with respect to the Sun vector.

Communications and Data Management Subsystem

The communications system for the spacecraft utilizes the Deep Space Network (DSN) 26-m ground antenna network on S-band. The spacecraft could have four hemispheric beam antennas (two on each end of the spacecraft) and one belt antenna around its midsection, or an omnidirectional antenna. One spacecraft system has a transmitter power of 16 W and a solid state power amplifier output of 46 W. The spacecraft's data management subsystem (DMS) will need to operate at a 59-kbps rate.

The POLAR spacecraft data storage system consists of two dual transport digital tape recorders, each with a capacity of 1.29 GB. The data produced in one orbit (15 hours) would be 1.98 GB. This would require alternating use of the data recorders. At a 512 kbps playback rate, a full recorder would downlink its data in 42 minutes and return to standby status until the other recorder reaches its capacity. At this point, the process would reverse and the full recorder would downlink. There is also a backup capability for a real-time data downlink in case of recorder malfunction. The 59 kbps downlink time would be limited by ground station availability and spacecraft to ground station line-of-sight viewing times.

Attitude Control and Determination

To simulate the spacecraft performance with the science instruments, a model of the environmental disturbance torques (such as the solar radiation torques and the gravity gradient torques) was completed for a 1,000-km by 7-R_E (altitude) orbit. These data were used to calculate the reaction control system (RCS) propellant usage from the estimates for attitude maneuvers and environmental torques. The spacecraft attitude control requirements are listed in table 4.

TABLE 4.—*Spacecraft attitude control requirements.*

	Accuracy	Stability	Knowledge
Spinning Platform			
Mission Requirements	0.5°	0.5°/min	
Spacecraft Performance	0.193°	0.06°/min	0.025 (0.149 Phase)
Despun Platform			
Mission Requirements	0.4°	0.06°/sec	0.05
Spacecraft Performance	0.345°	0.59°/min	0.074 (Roll/Yaw) 0.043 (Pitch)

A preliminary assessment of the inertia properties was performed. The onboard use of the science instrument data to improve pointing knowledge would enhance the control system performance.

Propulsion Subsystem

The spacecraft propulsion subsystem uses a monopropellant hydrazine in a blowdown pressurization operation. The propellant tanks, every other one belonging to a set, are located on the spinning portion of the spacecraft about the center of mass in order to minimize the influence of propellant depletion during operation. The two groups of three tanks feed three sets of thrusters: spin control, precession control, and orbit adjust. The amount of redundancy for the system is held to a minimum.

Dual Spacecraft Option

The dual spacecraft approach also focused on existing spacecraft with flight heritage in hopes of minimizing project costs. A survey was taken of major aerospace contractors using small satellites and it was found that not many had a proven flight heritage in this class of spacecraft. The scope of the assessment was then broadened to encompass those contractors *developing* small satellite capability. It was determined early that the pointing instruments can be accommodated by several potential vendors' three-axis stabilized spacecraft. Given the unique viewing constraints and envelopes of the remaining instruments, a suitable commercial spin-stabilized spacecraft could not be found. The MSFC engineering team designed a new spin-stabilized spacecraft using as many commercially available subsystems as possible. Both concepts are described below.

Launch Vehicle Options

Two options for launching the spacecraft are considered: (1) a launch of two Taurus 120 XLS vehicles or (2) a single Delta II or Titan II vehicle. To obtain simultaneous viewing of magnetospheric regions, the spacecraft should be coorbital with no more than 1,000 km separation. The Taurus would place each spacecraft into a 185-km by 7-R_E elliptical orbit. A spinning Star 37 upper stage would then boost the spacecraft into the mission orbit of 4,800 km by 7 R_E. Both small spacecraft could be stacked and launched on a single Delta II or Titan II vehicle.

Three-Axis Stabilized Spacecraft

The MSFC engineering team concentrated its efforts on the TRW Eagle spacecraft being built for the Total Ozone Mapping Spectrometer (TOMS) mission. Figure 6 shows the locations of the IMI instruments on the Eagle-based spacecraft.

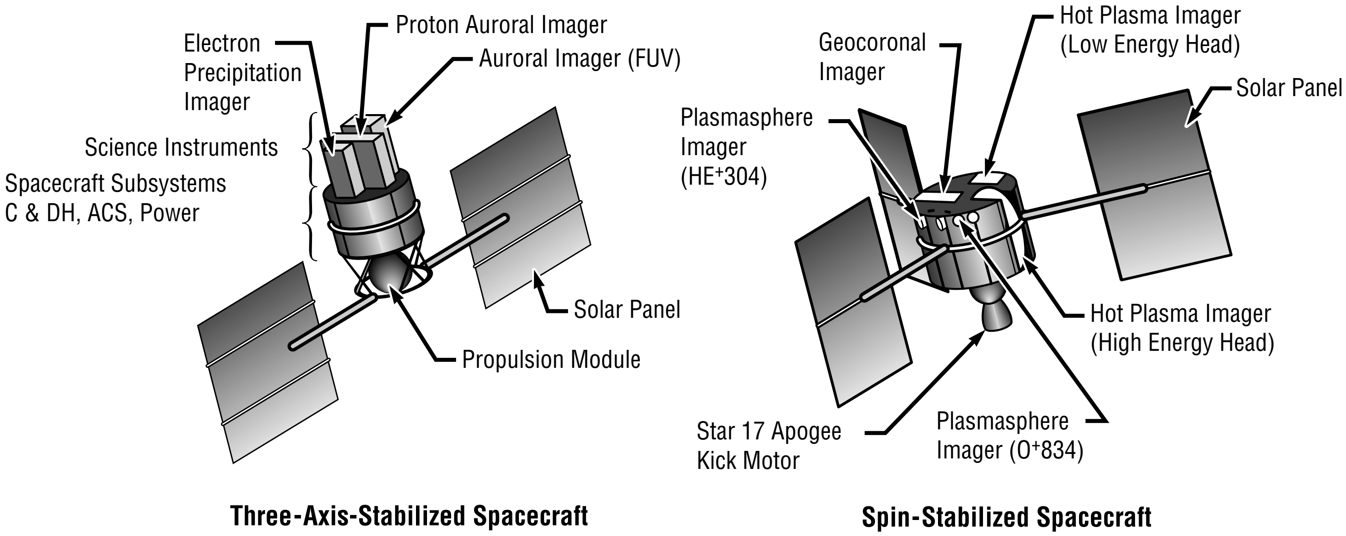
Electron Precipitation Imager
Proton Auroral Imager
Auroral Imager (FUV)
Science Instruments
Spacecraft Subsystems C & DH, ACS, Power
Solar Panel
Propulsion Module
Three-Axis-Stabilized Spacecraft
Geocoronal Imager
Hot Plasma Imager (Low Energy Head)
Solar Panel
Plasmasphere Imager (HE$^+$304)
Hot Plasma Imager (High Energy Head)
Star 17 Apogee Kick Motor
Plasmasphere Imager (O$^+$834)
Spin-Stabilized Spacecraft

FIGURE 6.—Dual spacecraft option.

The placement of the instruments on the three-axis stabilized spacecraft is optimized to meet viewing and thermal requirements, and to achieve spacecraft balance. There are three instruments on the spacecraft, with a total weight of 88 kg and a power requirement of 95 W.

The power system for the three-axis stabilized spacecraft would use articulated solar arrays to maximize solar array efficiency. Each wing would measure 2.4 m^2 and provide 144 W EOL power to the spacecraft (288 W total). The arrays would have 1 degree of freedom with a second supplied by a spacecraft yaw maneuver about nadir. The pointing of the solar arrays greatly complicates the function of the attitude control subsystem (ACS) in that continuous array pointing and yaw are required to maintain optimum spacecraft power. The Eagle ACS cannot meet these requirements and a new system would need to be designed for the spacecraft. In addition, the Eagle TCS might not be adequate to meet the instruments' thermal requirements without some minor modifications.

The three instruments on the spacecraft will have a combined data rate of 25 kbps. Up to one full orbit of data would be stored in solid state memory. It would then be downlinked through an S-band omnidirectional antenna to the 26-m DSN.

Spin-Stabilized Small Spacecraft

The most technically challenging aspect of the dual spacecraft approach is in the placement of the instruments on the spinning bus. Not only are there the engineering difficulties in meeting the instrument power, thermal, and pointing requirements with the relatively constrained capabilities of a small satellite, but there is the problem of accommodating the stated instrument FOV, particularly the high energy portion of the Hot Plasma Imager (HPI).

The power system would also use articulated solar arrays to maximize solar array efficiency. Each wing would measure 1.7 m^2, have silicon cells on both sides, and provide a total of 250 W EOL to the spacecraft. Using the ACS subsystem from the Small Explorer (SMEX) program, the spacecraft should be able to maintain attitude and solar array pointing with only minor hardware modification (primarily through the elimination the magnetic torquers and addition of a pitch wheel and four thrusters for orbit adjust and nutation control). The SMEX TCS appears adequate to meet instrument requirements. (Instrument placement on the spin-stabilized spacecraft is shown in figure 11.)

The four instruments on the spacecraft will have a combined data rate of 34 kbps, or approximately 1.8 GB per orbit. Up to one full orbit of data would be stored in solid state memory. It would then be downlinked through an S-band omnidirectional antenna to the 26-m DSN.

SOLAR TERRESTRIAL PROBE MISSION

Science Instrument Complement

An MI mission meeting STP mission guidelines necessitated the development of a new strawman instrument list by the SDT. This list includes three core instruments and three enhancing instruments as described in table 5. The concept discussed in this section only accommodates the three core instruments. The instruments' technical parameters were also provided by the SDT. Other sources have indicated that a reduction in electronics by 30 percent in volume, mass, and power is possible. This potential reduction was presented to the SDT and was considered reasonable, but not preferred.

TABLE 5.—*MI STP strawman instrument list.*

Instrument Name	FOV	Dimensions (W×D×H) m	Mass (kg)	Power (W)	Data (kbps)	Pointing Accuracy
CORE						
HPI (HEH)	4 π str	0.51 × 0.35 × 0.51	14.0	4.0	12	5.0°
HPI (LEH)	4 π str	0.30 × 0.30 × 0.25	7.0	7.0	6	
Electronics	4 π str	0.30 × 0.30 × 0.30	8.0	12.0		
PI (He^+304)	135° × 180°	0.48 × 0.16 × 0.20	7.2	4.5	7	1.0°
Electronics		0.23 × 0.18 × 0.20	11.8	16.5		
FUV Imager and Electronics	40° × 360°	0.70 × 0.80 × 0.30	30.0	25.0	15	1.0°
Total			**78.0**	**69.0**	**40**	
ENHANCING						
PI (O^+834)	135° × 180°	0.48 × 0.16 × 0.20	7.2	4.5	7	1.0°
Electronics		0.23 × 0.18 × 0.20	11.8	16.5		
Electron Precipitation Imager (EPI)	3° × 3°	0.20 × 0.20 × 0.60	24.5	11.0	2	0.3°
Electronics		0.25 × 0.18 × 0.18	3.0	9.0		
Radio Sounder (4 units)		0.22 × 0.12 × 0.12	35.2	10.8	6	N/A
Spin Axis Antenna (2 units)		0.50 × 0.20 × 0.18				
Electronics		0.20 × 0.18 × 0.15				

Two of the core instruments are from the original IMI instrument list but the third, the FUV Imager, is a combination of three of the original instruments: two staring and one scanning. All three core instruments operate in the scanning mode, eliminating the requirement for a despun platform. The total core instrument mass is 78 kg and the power requirement is 69 W. The EPI must operate in a staring mode and would require the addition of a despun platform, driving up the cost and complexity of the mission. The other two enhancing instruments operate in a scanning mode, thus making their potential inclusion on the STP mission somewhat less difficult.

Launch Vehicle Options

Three launch vehicles—the Taurus 120 XL/S, Conestoga 3632, and Lockheed Launch Vehicle (LLV3)—were considered for the STP mission. Performance estimates were generated by the respective vehicle manufacturers, and the capability of each vehicle is graphically represented in figure 7. The values for the 185-km-perigee insertion assume that the spacecraft's propulsion system will be used to achieve the final 4,800-km by 7-R_E orbit. The 4,800 km direct perigee insertion places the entire burden on the launch vehicle to put the spacecraft into the desired orbit.

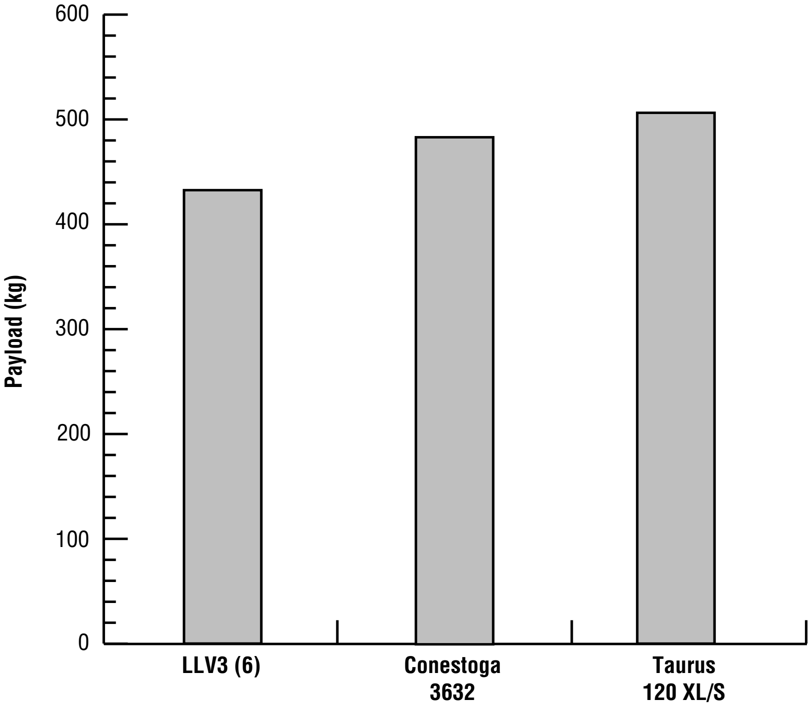

FIGURE 7.—STP option launch vehicle candidates.

The achievable IMI perigee is dependent upon the amount of propellant that can be loaded onto the spacecraft, the spacecraft mass, and the launch vehicle capability. A trade study to determine the available payload mass as a function of perigee altitude was performed for this concept.

The results of this trade study, presented in figure 8, can be summarized by stating that for every 100 km that perigee is reduced, 1 kg of additional mass (science instrument or spacecraft) can be placed into the desired orbit. Any spacecraft subsystem mass changes directly affect the science instrument mass that can be accommodated.

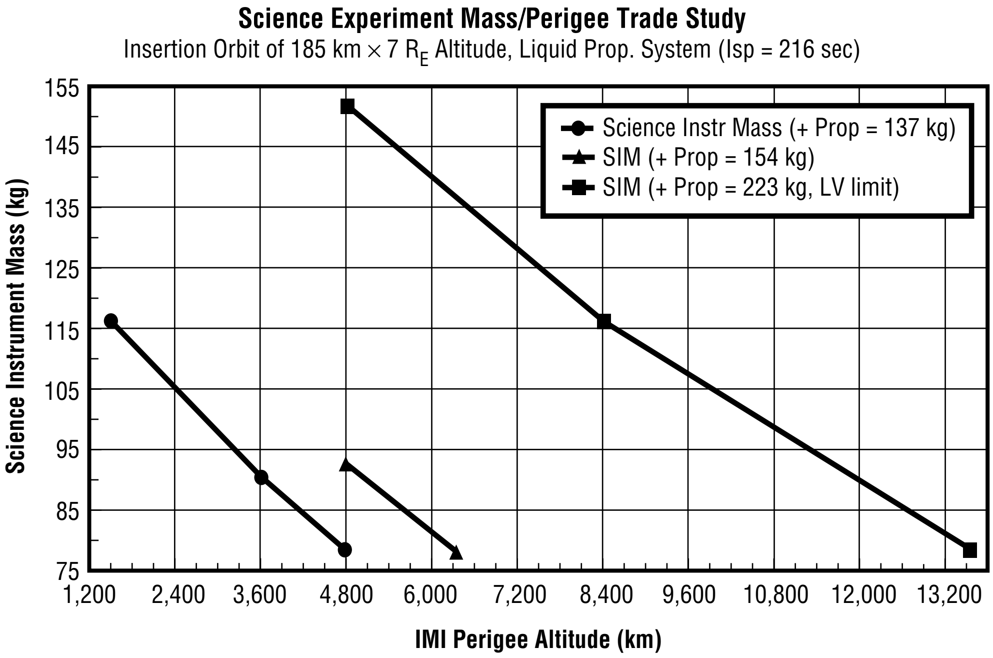

FIGURE 8.—Perigee trade study.

STP Baseline Vehicle

The baseline launch vehicle chosen for the mission is the Conestoga 3632, presented in figure 9. The decision is based on the performance estimate and the vehicle's large fairing size.

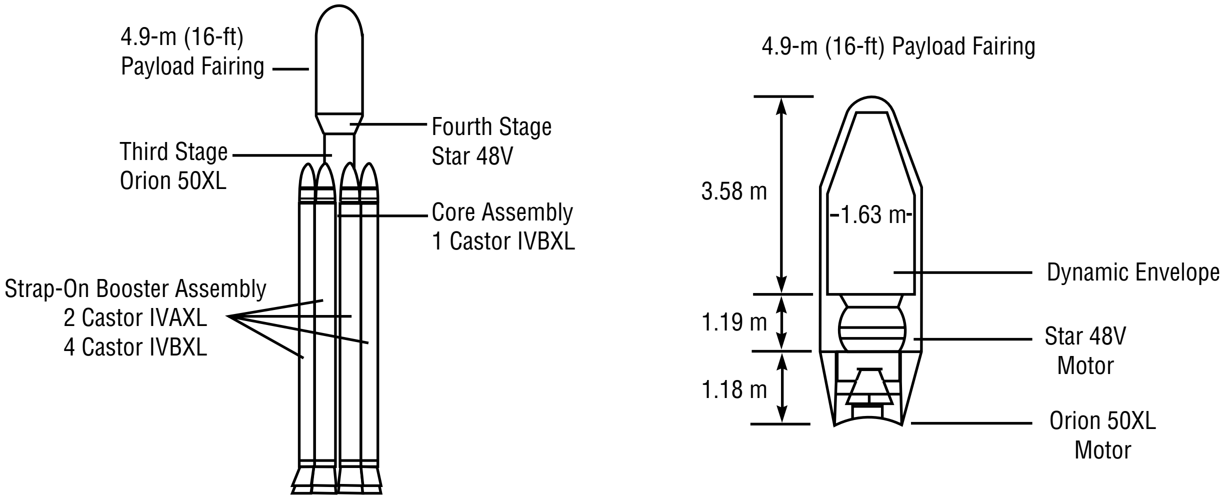
4.9-m (16-ft)
Payload Fairing
Third Stage
Orion 50XL
Fourth Stage
Star 48V
Core Assembly
1 Castor IVBXL
Strap-On Booster Assembly
2 Castor IVAXL
4 Castor IVBXL
4.9-m (16-ft) Payload Fairing
3.58 m
1.63 m
1.19 m
1.18 m
Dynamic Envelope
Star 48V
Motor
Orion 50XL
Motor

FIGURE 9.—Conestoga 3632 launch vehicle.

Configuration

The baseline configuration seen in figure 10 is sized to fit a medium launcher such as the Conestoga 3632 or LLV3. The instrument complement includes the three core instruments: the HPI, the PI (He^+304), and the FUV Imager.

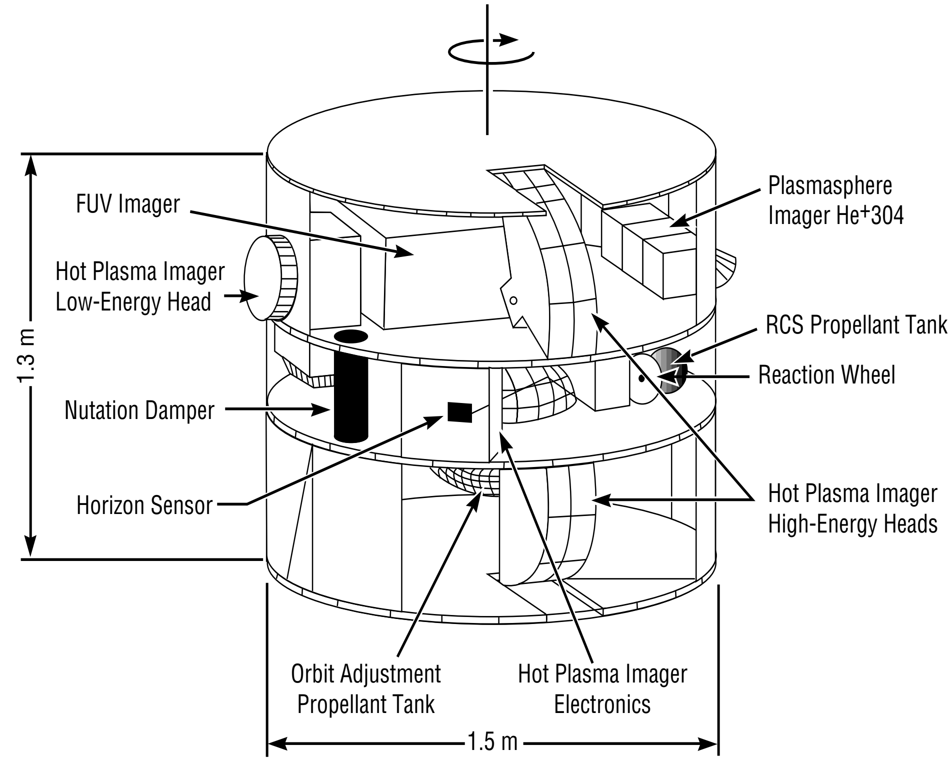
FUV Imager
Hot Plasma Imager Low-Energy Head
1.3 m
Nutation Damper
Horizon Sensor
Plasmasphere Imager He+304
RCS Propellant Tank
Reaction Wheel
Hot Plasma Imager High-Energy Heads
Orbit Adjustment Propellant Tank
Hot Plasma Imager Electronics
1.5 m

FIGURE 10.—IMI STP baseline configuration.

The spacecraft diameter of 1.5 m was chosen as a compromise between launch vehicle payload capacity, power system surface area requirements, and spacecraft stability requirements. Minimizing the spacecraft size reduces the mass. Maximizing diameter and minimizing spin axis length improves spin stability. The spacecraft length of 1.3 m provides sufficient side wall surface area for solar cells, radiators, antennas, and science instrument view ports. The length is also dictated by the spacecraft subsystems and scientific instrument volumes.

The spacecraft subsystems and science instruments are arranged within the spacecraft to optimize the mass moments of inertia. Placement of the science instruments is restricted by their FOV requirements. The spacecraft subsystems are positioned to account for balancing and compatibility with adjacent components. The addition of any mission enhancing instruments would necessitate rearrangement of the internal components.

Structures

The baseline structural design of the spacecraft calls for three aluminum honeycomb plates supported by a side wall and longerons constructed from either aluminum or graphite composite (fig. 11). Modifications to the spacecraft to accommodate the radiator band would result in changes to the plates, which are no longer required to reject heat. These panels may now be fabricated from a graphite composite, although the material selection will be a trade of cost and mass. Construction methods and materials selection may result in a shifting of the structural masses, but no significant mass change is expected.

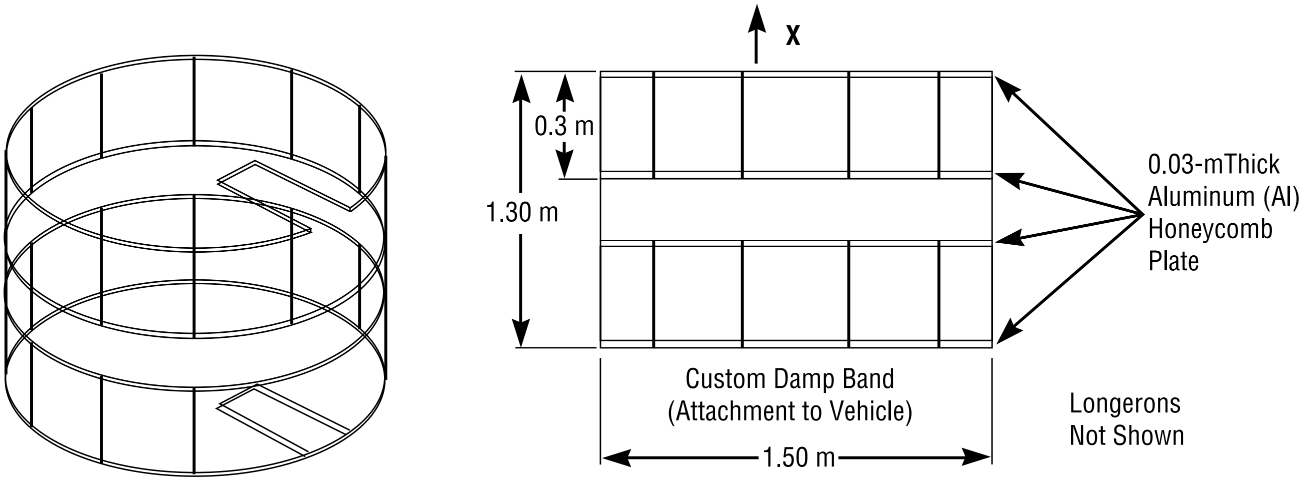

FIGURE 11.—STP spacecraft structure.

Electrical Power Subsystem (EPS)

Electrical power load requirements for the spacecraft are estimated to be 182 W. The total power requirements represent 69 W for the three-instrument payload suite, with the remaining power designated for other subsystems, housekeeping, and contingency.

The polar orbiting spacecraft is spin stabilized with body mounted solar cells on the cylindrical section and both ends. Total active solar array surface area is estimated to be 7.58 m^2 with a maximum effective illumination area of 2.1 m^2 as shown in figure 12.

Platform orbit orientation of the spin axis is normal to the orbit plane. The results of this orbital profile is a worst case angle of a ±66.5° between the Sun vector and the orbital plane (ß angle). At these angles, the solar array power output is 363 W. The worst case ß angle of 0° will give a power output of 252 W. This will result in a power margin of 70 W between the solar array output and the total load demand at EOL shown in figure 12.

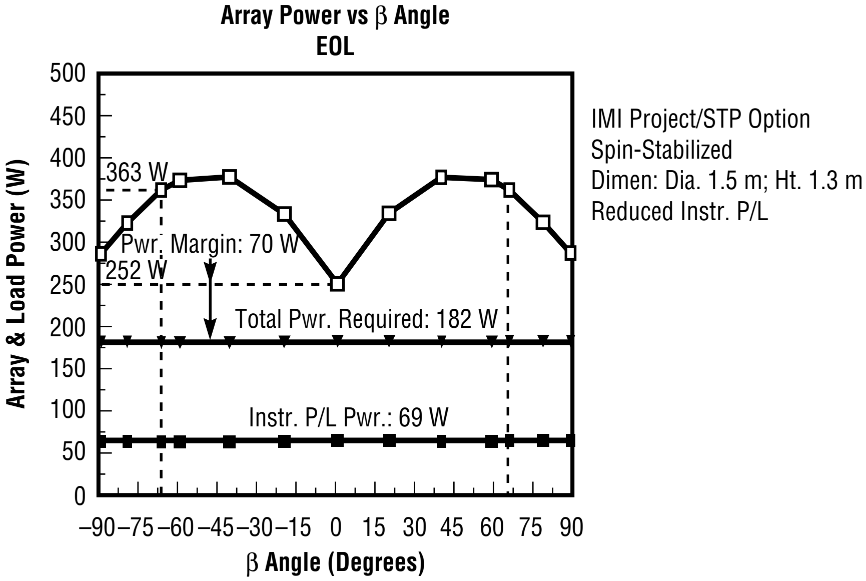

FIGURE 12.—Effective area versus ß angle.

Power calculations are based upon an 18.5-percent efficient gallium arsenide (GaAs) cell. A trade study was performed on several types of GaAs cells:

- 2 by 4 cm, 3.5 mils thick, 18.5 percent efficient (baseline)
- 4 by 4 cm, 5.5 mils thick, 18.6 percent efficient
- 5.5 by 6.5 cm, 5.5 mils thick, 18.1 percent efficient.

The 2- by 4-cm cell was chosen as the baseline solar cell for the IMI STP mission. Two batteries were considered: a new small satellite nickel hydrogen (NiH_2) cell design and a nickel metal hydride (NiMH) battery. The NiH_2 cell design was chosen for the baseline.

Thermal Control Subsystem (TCS)

The possible addition of the Radio Sounder, with the attendant requirement to not perform the 180° spacecraft maneuver every 6 months, presents some solar incident radiation problems for the TCS. Without flipping the spacecraft, the surfaces used for thermal radiators will be exposed to solar heating for extended periods, thereby degrading the performance of the radiators. Furthermore, there is no position on the spacecraft that radiator panels could be located that would not at some time during the mission be exposed to the Sun. The 180° flip provides an ideal heat sink to deep space for the spacecraft systems’ thermal loads and the FUV detector, which needs to be maintained at about –100 °C.

Two options, shown in figures 13 and 14, were considered for thermal control of the spacecraft in the absence of an orbital “flip” maneuver: (1) locating the radiator surfaces on the ends of the spacecraft, and (2) locating the radiator on the cylindrical body of the spacecraft. The TCS design was forced to consider impacts on the EPS design because both require part of the scarce surface area of the spacecraft body. Option 1 would require that the radiator and solar arrays share the ends of the spacecraft.

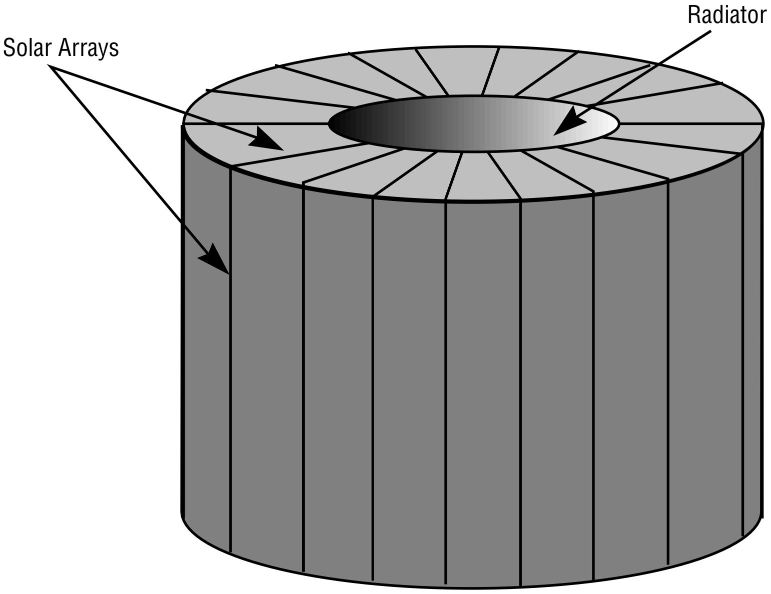

FIGURE 13.—STP with radiators on spacecraft ends

A requirement of the EPS only allows the thermal radiators 30 percent of the spacecraft ends, which is about 0.5 m^2 for each. Option 2 requires that the solar arrays and the thermal radiators share the cylindrical portion of the spacecraft, leaving the ends free for solar arrays. The radiating surfaces would need to have optical properties similar to those of the space shuttle orbiter radiators, which have a low absorptivity (α=0.09) and a high emissivity (ε=0.81). This optical surface reflector (OSR) would limit the solar radiation absorbed by the radiator while still allowing the surface to radiate effectively.

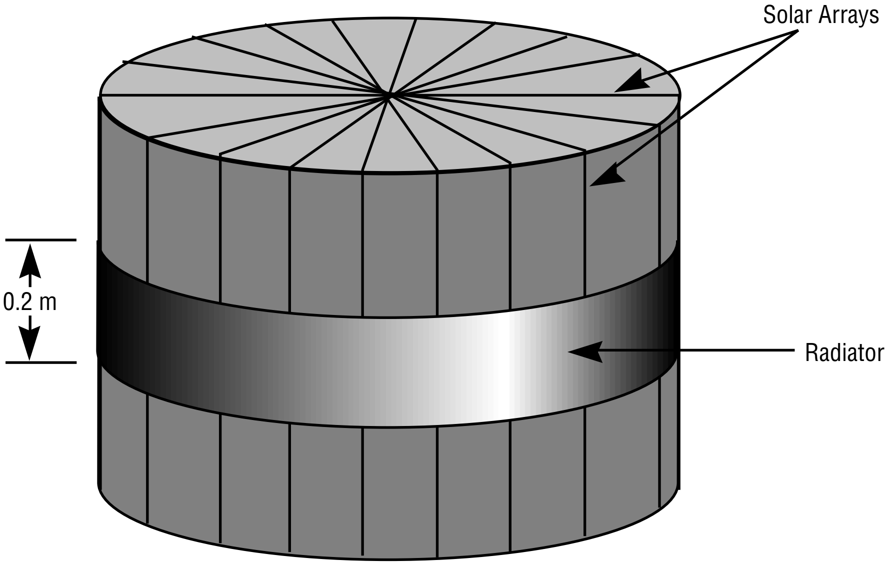

FIGURE 14.—MI with radiator on cylindrical portion of spacecraft body.

Steady-state thermal analyses were performed to evaluate the performance of the two concepts. The end mounted radiators were modeled in their worst case condition, where one end of the spacecraft is facing the Sun and the other end is anti-sunward. The analysis of this concept showed that only about 168 W of heat could be rejected at 273 K. Using 0.6 m^2 (or 34 percent) of the end surface area, 193 W could be rejected, which is about 10 W more than the 182 W required. Results of the analysis of the radiator mounted on the cylindrical portion of the spacecraft, shown in figure 15, indicate that a band approximately 0.2-m wide about the circumference of the body would reject the 193 W in the worst case condition when the spacecraft cylinder is normal to the solar vector. Therefore, the baseline design is to locate the thermal radiator on the cylindrical portion of the spacecraft.

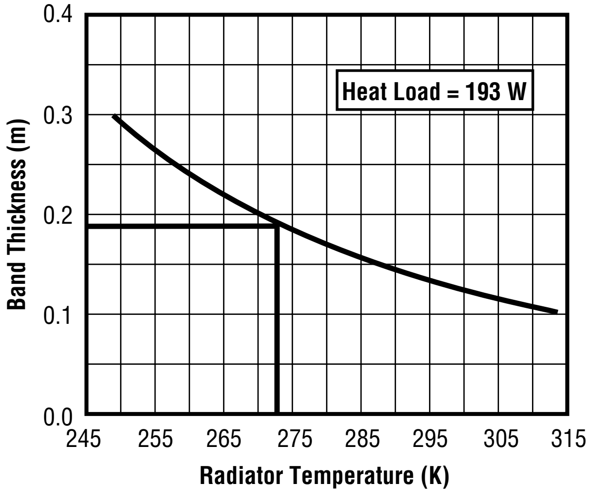

FIGURE 15.—Radiator band size versus radiator temperature.

Attitude Control and Determination (ACAD)

The spacecraft ACS should provide a stable spinning platform that meets the science instrument pointing requirements of 0.5° for knowledge, accuracy, and stability over a 1-minute period. The spacecraft system should also provide guidance, navigation, and control (GN&C) during orbit transfer from separation of the launch vehicle upper stage to the orbit perigee. Requirements during orbit transfer include a full inertial reference system with sensors and algorithms for orbit and attitude determinations, and a complement of RCS thrusters to maintain vehicle attitude during orbit transfer. After the spacecraft attains orbit perigee, the RCS thrusters will align the spacecraft spin axis along the orbit normal, remove attitude errors, and then spin the spacecraft to the required 10 rpm. Attitude sensors include rate gyros, fine and coarse Sun sensors, and horizon sensors. A spin-axis damper located at the spacecraft perimeter will provide passive nutation damping; the RCS could augment this nutation damping and provide spin axis control if needed.

To avoid orbit perturbations due to RCS forces, six pairs of thrusters apply pure couples on the spacecraft and employ simpler control algorithms than those needed for single thrusters. A representation of the spacecraft ACS is shown in figure 16; the four pairs of pitch-thrusters will be replaced by two pairs.

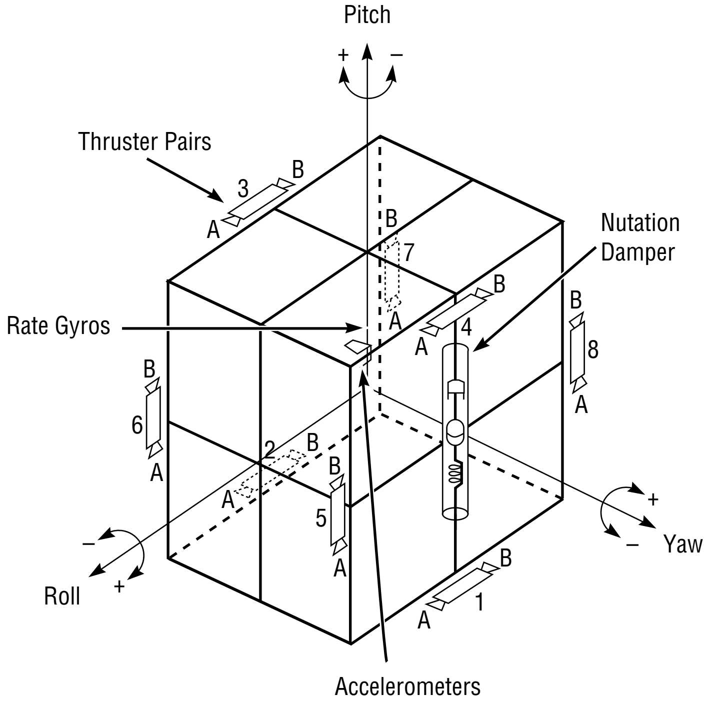

Attitude Sensors:
2 Coarse Sun Sensors
2 Fine Sun Sensors
2 High–Resolution Horizon Sensors

FIGURE 16.—STP ACS components.

An estimate of disturbance torques for the spacecraft concept is shown in figures 17–20. The orbit is 4,800-km altitude by 7 R_E, on March 21, 2001, using a 2σ Jacchia density model. Magnitudes of the solar radiation torque, gravity gradient torque, and aerodynamic torque are plotted in figures 17, 18, and 19, respectively. Figure 20 shows the sum of these torques about the spacecraft x, y, and z axes. RCS propellant usage to manage these torques is estimated at 1 kg over the 2-year lifetime. An additional 1 kg of propellant is needed for initial reorientation and spin-up after orbit acquisition, and 5 kg of propellant is estimated for RCS control during the orbit insertion.

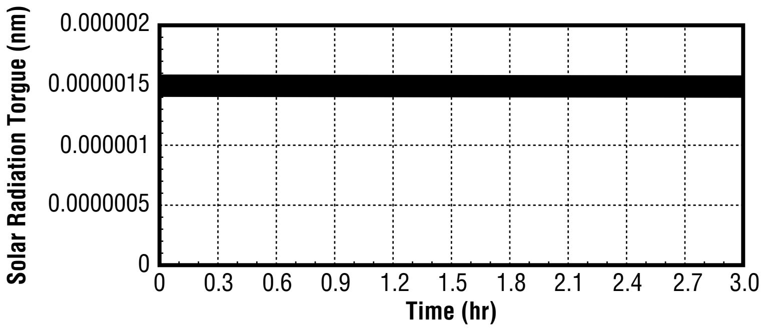

FIGURE 17.—Solar radiation torque.

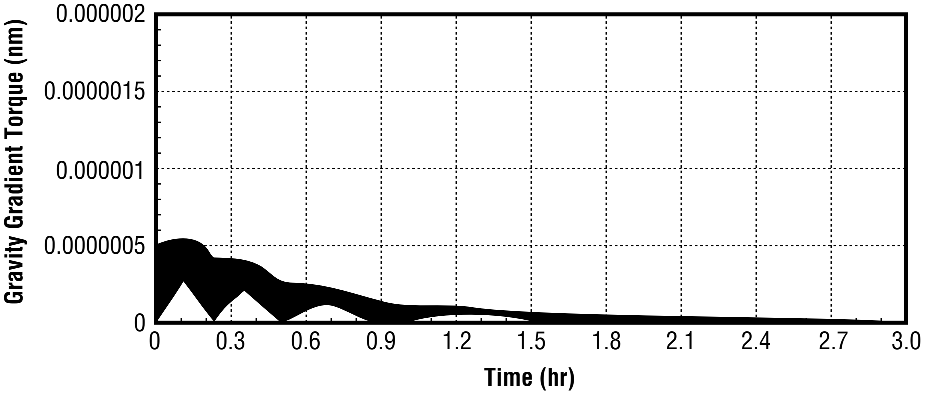

FIGURE 18.—Gravity gradient torque.

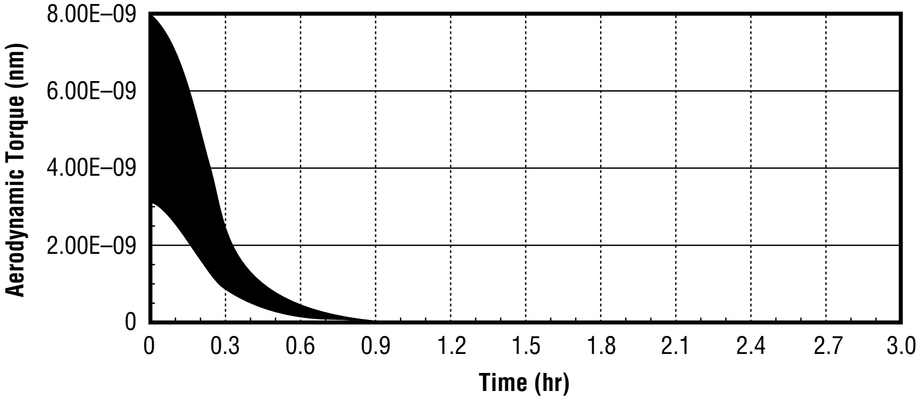

FIGURE 19.—Aerodynamic torque.

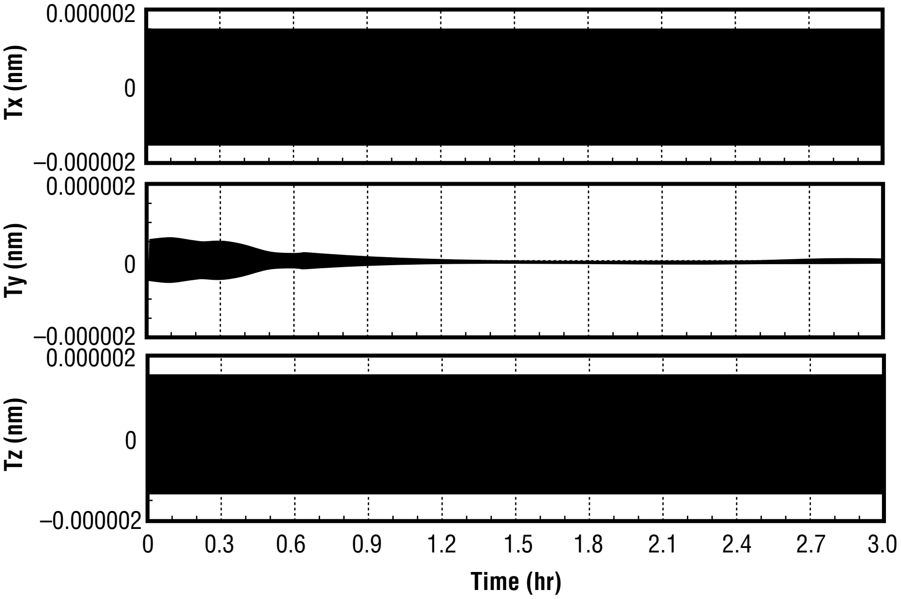

FIGURE 20.—Environmental torques

The ACS equipment list includes one nutation damper, two coarse and two fine Sun sensors, two high-resolution horizon sensors, three rate gyros, two single-axis accelerometers, control electronics, and cabling. The total system mass estimate is 22 kg, with a total power estimate of 42 W.

Propulsion Subsystem

Two options were considered for the spacecraft propulsion subsystem. The first uses an off-loaded Star 17 solid propellant motor for the orbital reboost, with a blowdown monopropellant hydrazine RCS. The mass summary for this option indicates that the total payload mass exceeds the launch vehicle capability: structural accommodation would require a thrust structure, a mission-specific payload attachment fixture, and a minimum of two separation systems. An all-liquid blowdown monopropellant hydrazine propulsion subsystem was, therefore, selected following a trade which indicated that this reduced the overall payload weight due to elimination of the motor structural accommodations.

The number of tanks required, placement of the tanks, and the systems operation were all taken into account in the design of the propulsion system. The design consists of two systems: RCS and orbit adjust. The orbit adjust is accommodated by using a single 55.73-cm (21.94-inch) diameter tank located along the vehicle centerline, with two nominal 66.75 N (15 lbf) thrusters on the spacecraft aft end. A single string isolation system is assumed, with all hardware being available “off the shelf.”

The RCS is a similar design based on the same philosophy. Two 23.29-cm (9.17-inch) diameter tanks are required in order to keep the spinning spacecraft balanced as the propellant is depleted. The tanks are located in the plane of the vehicle center of mass. Bladders are also required as the RCS provides attitude control during orbit transfer. The tanks are purposely oversized in order to maintain the high thrust during the mission. Total propulsion system weight is estimated to be on the order of 100 kg. A summary of the all-liquid propulsion system is shown in figure 21.

IMI Solar Terrestrial Probe
All Liquid Spinner Spacecraft

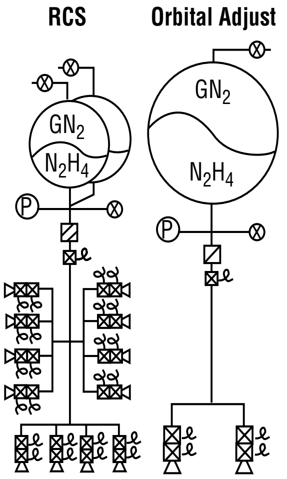

Number	Equipment	Weight (lb)	Weight (kg)
5	Fill and Drain Valves	2.50	1.14
1	O/A Propellant Tank (22.14")	12.50	5.68
2	RCS Propellant Tank (9.41")	6.50	2.95
2	Pressure Transducer	2.20	1.00
2	Filter	2.00	0.91
2	Isolation Valve	4.20	1.91
12	Thrusters (1 lbf)	9.60	4.36
2	Thrusters (15 lbf)	5.00	2.27
	Miscellaneous (15%)	6.68	3.03
	Total Dry Weight	51.18	23.26
	Propellant — Usable	165.20	75.09
	Residual	3.37	1.53
	Pressurant	2.11	0.96
	Total Subsystem Weight	221.86	100.85

FIGURE 21.—STP schematic for propulsion system.

Communications and Data Management Subsystem (CDMS)

The performance of the communications and data handling (C&DH) subsystem depends primarily on the data rate and the transmitter power output. The data rate is fixed at 40 kbps for the three core instruments, which would yield about 2 GB of data for each 15-hour orbit. The data could be stored on a solid state recorder and downlinked once per orbit. Sizing of the recorder is limited by mass and power restrictions. A minimum size would be about 2.5 GB, with additional capacity being used as safety margin.

The downlink time and rate are dependent on antenna gain and transmitter power. With a spinning spacecraft, the use of an omnidirectional antenna is indicated. These antennas usually have little or no gain. Transmitter output is limited by the direct current (dc) power availability on the spacecraft. For the IMI STP, 10 W of radio frequency (RF) power was chosen as an acceptable compromise. A downlink rate of 1.5 Mbps was chosen as a value that will give acceptable transmission times at positive link margins. The 1.5 Mbps rate and 10 W of RF power will give positive link margins out to about 4 Earth R_E with either the DSN 26- or 34-m antennas, and a downlink time of about 24 minutes for one orbit of data. A minimum of 24 minutes of contact time with one of the DSN stations will be available on most of the orbits.

Commands to the spacecraft will be at a much lower data rate and should be possible at any point in the orbit. Refinements of the C&DH system may be possible by varying data rate, transmitter power, or antenna type.

Mass Properties

The launch mass summary for the STP baseline configuration is presented in table 6.

TABLE 6.—*Mass summary for the STP baseline.*

	Baseline Core Instruments
Structures	60.4
TCS	4.8
ACS	22.0
EPS	24.5
Cabling/Harness Assembly	20.1
Communications and Data Handling	25.0
Propulsion System (dry)	23.3
Spacecraft Contingency (30 percent)	54.0
Spacecraft Dry Mass	234.1
Total Propellant	77.6
Science Instruments	78.0
Science Instrument Contingency (30 percent)	23.4
Total Launch Mass	**413.1**
Launch Margin (Conestoga)	67.7

The configuration includes the three core instruments identified in table 5. The results of subsystems trades resulted in a new baseline design that is approximately 0.3 m longer and does not require a 180° flip every 6 months. The mass margin estimated assumes the use of a Conestoga launch vehicle. The launch margin for this option is the last entry in the table. As in the previous studies, a 30 percent engineering contingency was applied to both the spacecraft and instrument dry masses.

SOLAR CONNECTIONS MISSION

Science Instrument Complement

The instrument payload for this option is basically unchanged from that of the STP. Figure 22 illustrates the evolution of the science instruments from the first IMI mission concept to Solar Connections. The most significant impact on spacecraft design from the STP to Solar Connections is the omission from the spacecraft of capabilities to support "enhancing" science. The STP option was intentionally over designed to allow for one or more of the mission "enhancing" instruments to be included, which was not done for the Solar Connections concept. The payload accommodation requirements are identified in table 5.

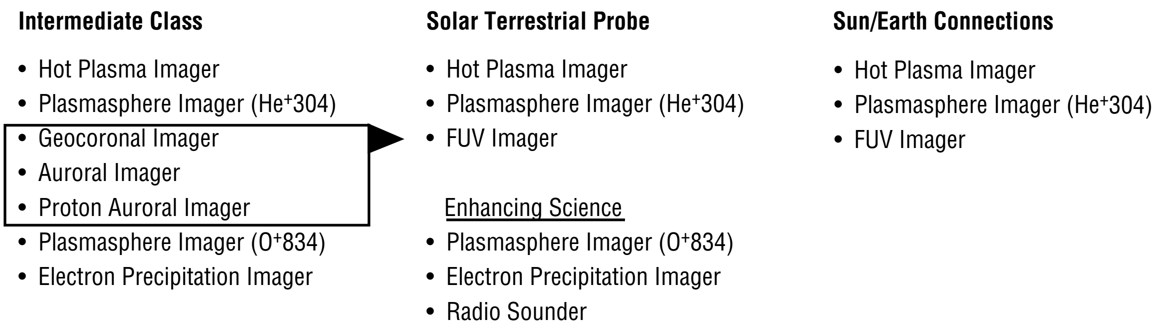
Intermediate Class
• Hot Plasma Imager
• Plasmasphere Imager (He+304)
• Geocoronal Imager
• Auroral Imager
• Proton Auroral Imager
• Plasmasphere Imager (O+834)
• Electron Precipitation Imager
Solar Terrestrial Probe
• Hot Plasma Imager
• Plasmasphere Imager (He+304)
• FUV Imager
Enhancing Science
• Plasmasphere Imager (O+834)
• Electron Precipitation Imager
• Radio Sounder
Sun/Earth Connections
• Hot Plasma Imager
• Plasmasphere Imager (He+304)
• FUV Imager

FIGURE 22.—Evolution of MI science instruments.

Mission Analysis and Orbit Mechanics

Initial Orbit

The mission orbit of 4,800 km by 7 R_E (shown in fig. 23) is met from a typical optimum launch vehicle insertion orbit of 185 km by 7 R_E and the capability of an added fourth stage to raise perigee to the desired 4,800 km altitude. This added stage will be a solid rocket apogee kick motor (AKM), with the capability to provide the necessary spacecraft spin-up and orientation. The use of a modified Star 17 as the core of this upper stage is possible, or a Star 13B may be used if the eventual spacecraft is lighter and does not require the greater total specific impulse of the Star 17. The selected orbit for all three mission options has not changed, thus allowing for the same orbit precession rates, the same viewing/imaging of both the Earth and neighboring space, and the same amount of magnetosphere volume to be viewed during the mission life.

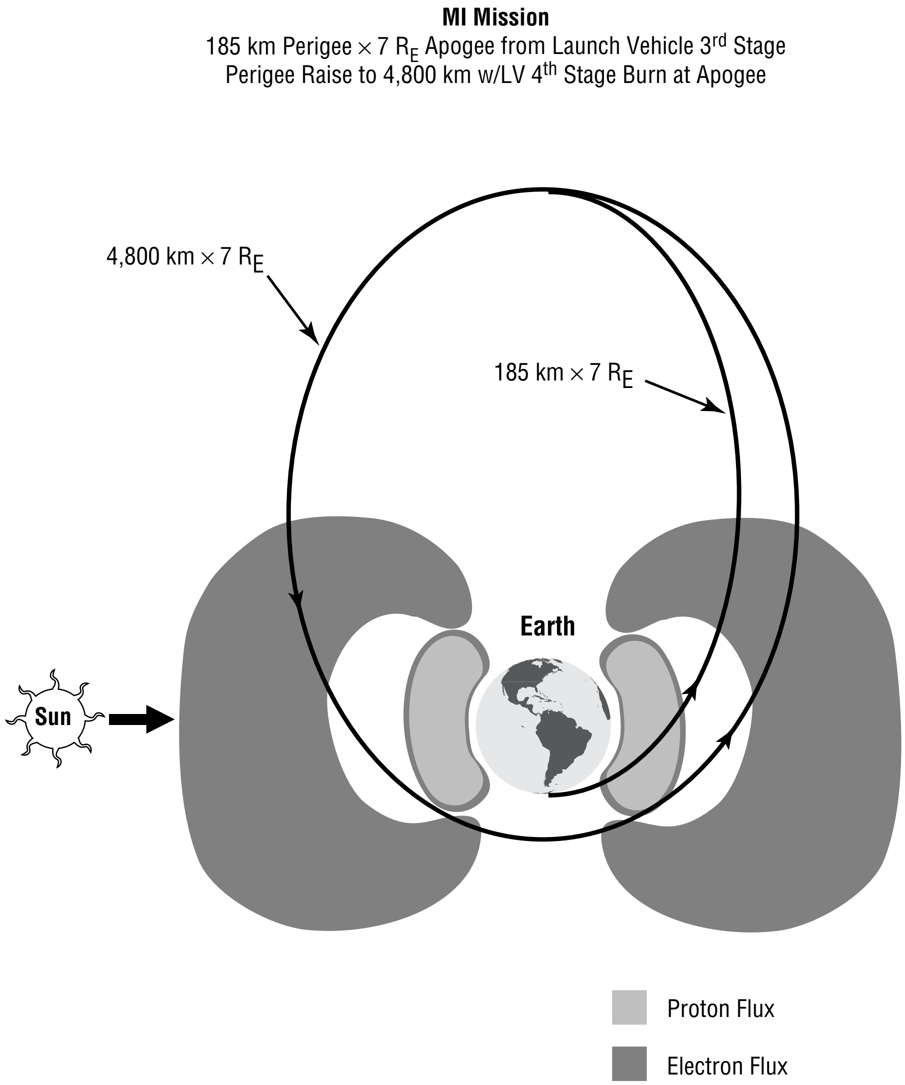
MI Mission
185 km Perigee × 7 R_E Apogee from Launch Vehicle 3rd Stage
Perigee Raise to 4,800 km w/LV 4th Stage Burn at Apogee
4,800 km × 7 R_E
185 km × 7 R_E
Earth
Sun
Proton Flux
Electron Flux

FIGURE 23.—Solar Connections mission orbit.

Mission Analysis Parameter Characterization

The mission analysis parameters of time in umbra, shown in figure 24, and ß angle, in figure 25, are of particular concern for the mission. Since the orbit is in a 90° inclination, spacecraft in the orbit plane can have all orientations from edge-on-to-the-Sun to perpendicular. The larger ß angle excursions should be avoided to minimize power losses. Selecting the appropriate daily launch time can satisfy this concern. However, the need for the spinner spacecraft to accommodate almost all orientations while generating enough power for instrument and spacecraft operations still exists to a great degree. Because of the Earth's natural tilt of 23.5° with respect to the ecliptic plane, the variation of ß can ideally be limited to ±66.5°. Any allowances for launch windows and solar and lunar perturbations will increase the ß angle excursions.

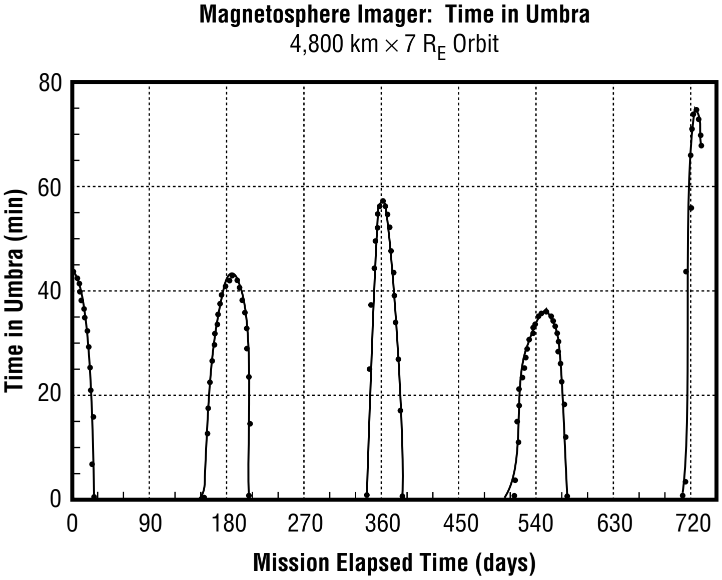

Figure 24.—Spacecraft time in umbra.

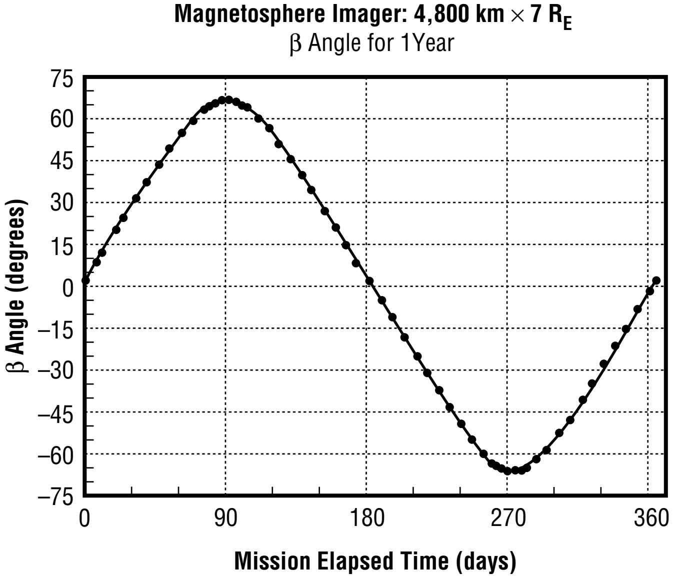

Figure 25.—Mission ß angle varies during a year.

The time in umbra affects the heater sizing and power requirements. The longest shadow time occurs during the last days of the 2-year mission and is approximately 80-minutes long. This particular peak can be avoided if another smaller peak is accommodated at the beginning of the mission. Again, this is determined by the time of the year the mission is launched and launch window duration. Including this smaller peak at the beginning of the mission will drop the longest shadow time to approximately 60 minutes. However, once lunar and solar perturbations are characterized, the maximum shadow duration may increase to a value approaching 80 minutes.

The apsidal precession in the 4,800-km by 7-R_E orbit will be 41° during the 2-year mission life (shown in fig. 26). The apogee will move from its initial position over the North pole down to a latitude of 49°N (90°–41°=49°) in a smooth manner. However, due to both lunar and solar perturbations, this precession may be greater and (in all likelihood) increase the total precession to more than 41°. This increase will cause the apogee to move to a lower latitude near the end of the 2-year mission and increase the shadow times.

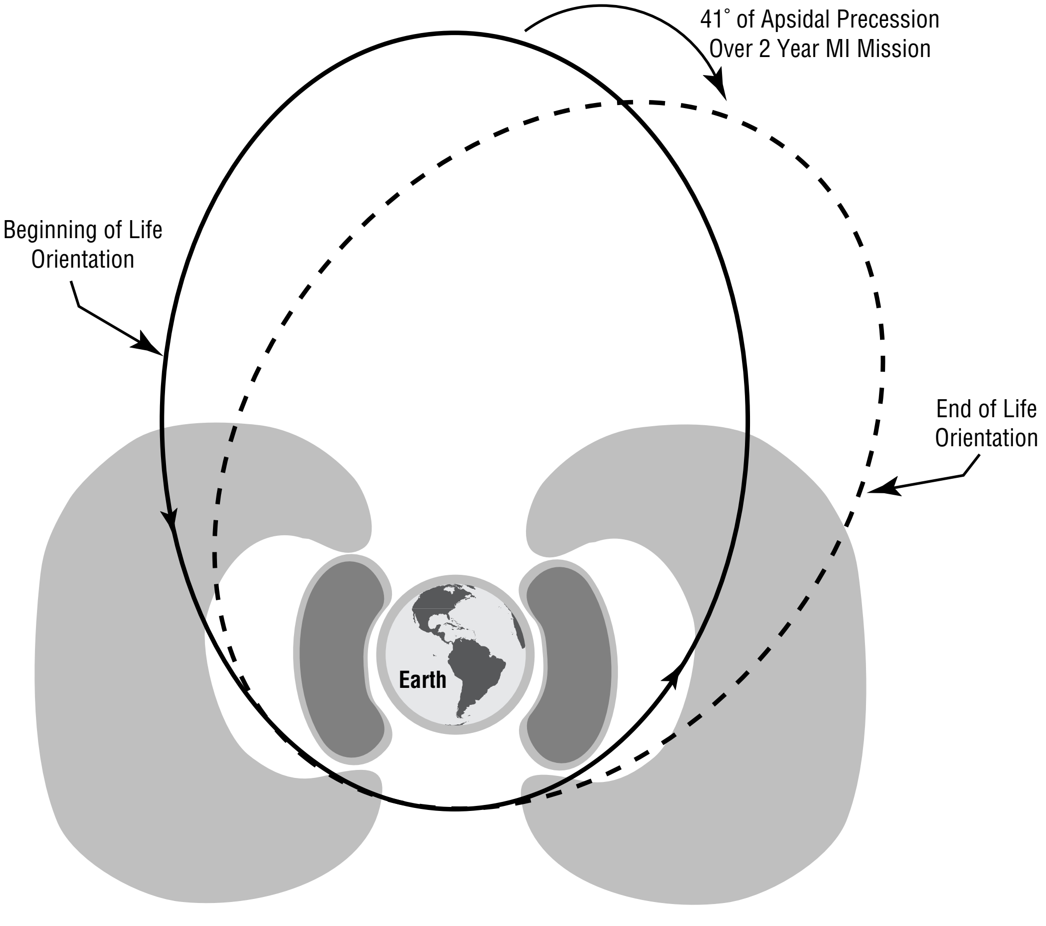

Figure 26.—Mission orbit apsidal precession.

Once a launch date has been recommended (a phase B activity) the actual ß angle and umbra duration time histories can be determined, along with the amount of apsidal precession that will occur over the 2-year mission.

Ground Station Contact Analysis

The previous maximum contact range of up to approximately 3 R_E limited the maximum ground station contact time to only 2 hours of the 15.16-hour orbit. Ground station viewing analyses further showed that, on the average, only 1.4 to 1.5 hours of this 2-hour window is available on any particular pass (through the ±94° of true anomaly around perigee as shown in fig. 27). With improvements made in the antennas performance and design, the range limitation has been increased to 6 R_E, thus allowing the contact times to be as long as 10 hours, with the minimum still at least 4 hours per orbit. The apparent diameter of the Earth is smaller at higher altitudes, thus allowing use of the higher gain parts of the antennas, which will offset some of the antennas' gain loss resulting from the larger distance over which the signal/data must be sent.

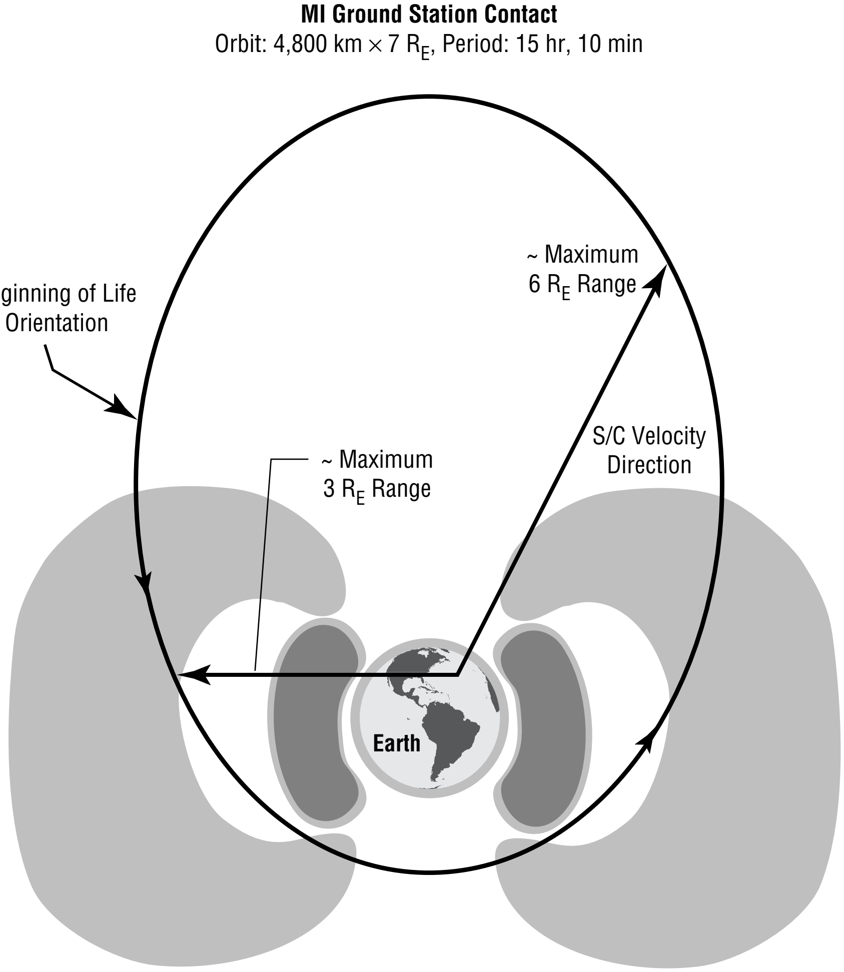
MI Ground Station Contact
Orbit: 4,800 km × 7 R_E, Period: 15 hr, 10 min
~ Maximum 6 R_E Range
Beginning of Life Orientation
S/C Velocity Direction
~ Maximum 3 R_E Range
Earth

FIGURE 27.—Ground station contact.

Launch Window Constraints

The launch window duration will be dependent on a number of factors. The limit on the ß angle excursions (from ±66.5° up to ±74°), the effects of solar and lunar perturbations on the limit of the amount perigee and apogee can shift (perhaps ±1,000 km), and the desired limitation on shadow durations (up to 80 minutes) will all affect the length of the launch window. The phase B study will determine the length of the launch window, as well as determine daily launch opportunities (and if there are any days during the year when a launch cannot occur). If these launch “blackouts” do exist, they should still be minimal since all three mission analysis parameters (ß, time in umbra, and apsidal precession) are somewhat flexible in the ranges that are currently being considered.

Effects of Lunar Perturbations on the Orbit

Another phase B activity will be to determine the extent that lunar and solar perturbations affect the orbit (fig. 28). The analysis will provide the actual time histories of the mission analysis parameters of concern to be determined with appropriate accuracy. Such perturbations could shift the perigee and apogee of the orbit from a few hundred kilometers up to 1,000 km or more (over the mission life) depending upon the initial condition. The affected conditions are the launch time and the two orbit orientation angles (right ascension of the ascending node and augment of perigee) with respect to the Sun and Moon. The Earth-trapped particle-radiation environment seen by the spacecraft is dependent upon the changes these perturbations cause in the orbit perigee.

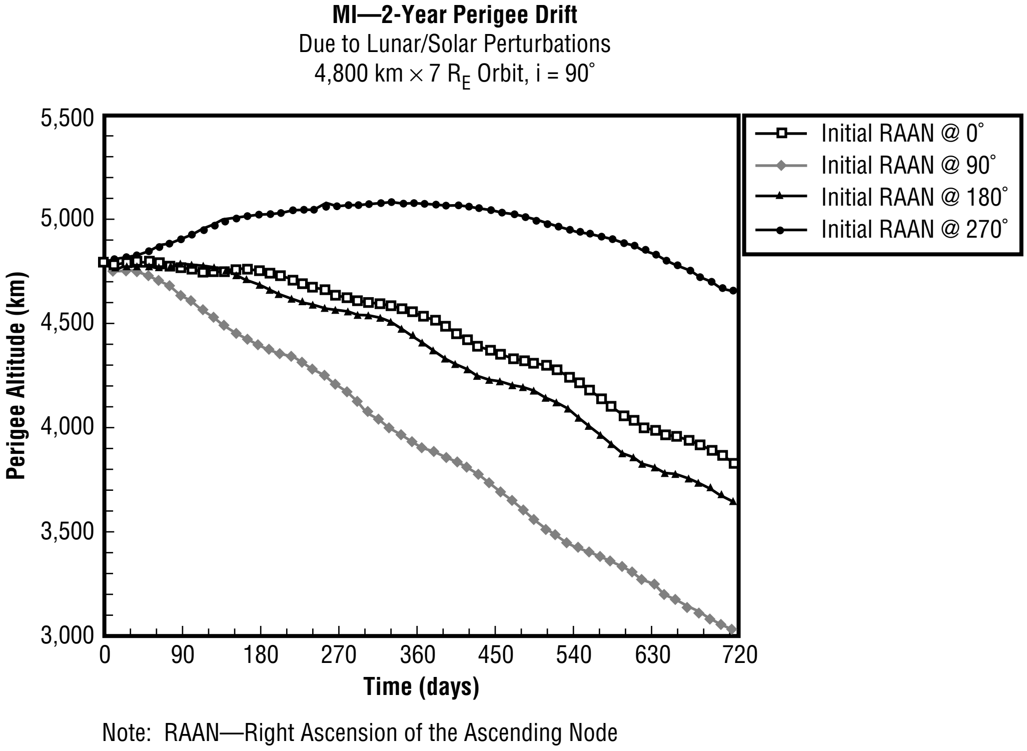

FIGURE 28.—Mission perigee altitude history for 2 years.

Launch Vehicle Options

Candidate Vehicle Descriptions and Performance Estimates

Many launch vehicles were considered for the mission. Changes in mission requirements and funding limited the launch vehicle selection to three primary candidates. The spacecraft was originally designated a Delta II-class mission, but due to various requirement changes, the mission must fly on a smaller and cheaper launch vehicle such as the Med-Lite. New launch vehicles, such as the Taurus, Conestoga, and the LLV, have approximately one-half the payload capability as the Delta II, but with a much smaller price tag.

The manufacturers of these vehicles analyzed the trajectory needed for the MI orbit and estimated the performance of their respective vehicles (refer to fig. 7). The Taurus S was chosen as the baseline for the MI mission in the Solar Connections program because of its performance capability and availability.

LLV 3(6). The LLV is a new series of small launch vehicles. The LLV3(6) is the smallest member of this family to meet the requirements of the MI mission (fig. 29). This vehicle is an assemblage of solid motors. The first two stages require a Castor 120 and the third stage is an Orbus 21D. In addition to these motors, there are six first stage strap-on Castor IVA motors. An orbit adjust module (OAM), located above the Orbus 21D, is attached to the payload. The OAM provides various control functions during flight and can be used for additional maneuvers, such as transfer burns.

With this configuration, Lockheed estimates that 428 kg can be placed into the 185-km by 7-R_E orbit. With additional hydrazine propellant in the OAM, the LLV3(6) can place the spacecraft into the final orbit of 4,800 km by 7 R_E. The maximum payload attainable is 288 kg. However, when Lockheed evaluated the mission, the attitude and spin rate constraints were not added. It is possible that these constraints may further decrease the launch vehicle's performance.

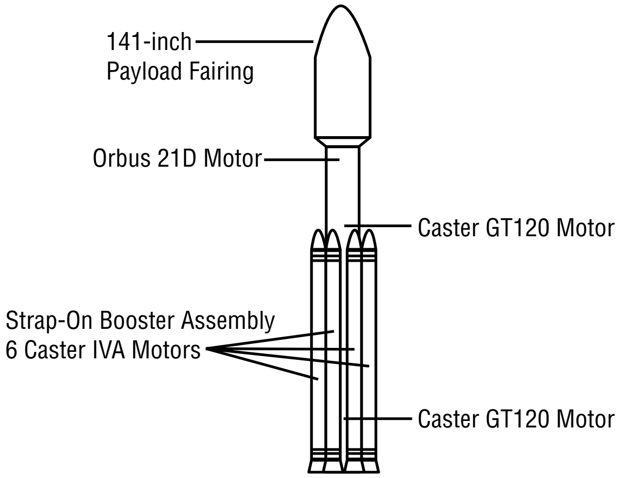

FIGURE 29.—Composition of the LLV3(6).

Conestoga 3632. Currently under development by EER Systems, Inc., the Conestoga series is a family of solid rocket launch vehicles. EER analysis determined that the Conestoga 3632 is the vehicle most capable of meeting the orbital requirements. The five-stage Conestoga 3632 is necessary to place a satellite into the 185-km by 7-R_E orbit. The first three stages are comprised of the core Castor IVB XL, and surrounding it are two Castor IVA XL and four Castor IVB XL strap-on motors. The fourth and fifth stages are an Orion 50XL and a Star 48V, respectively (fig. 30).

EER estimates the performance of the Conestoga 3632 to be 453 kg into the 185-km by 7-R_E orbit. This requires the satellite to have an onboard propulsion system for the perigee raise to 4,800 km. If special attachment structure is needed, the weight would be included in the quoted payload value along with the separated spacecraft weight. The recent requirements of spin rate and orientation at the final orbit pose some difficulties. The vehicle was designed to release a spacecraft into a three-axis stable orientation. The spin rate requirement may necessitate some additional design, fabrication, and testing of a new upper stage.

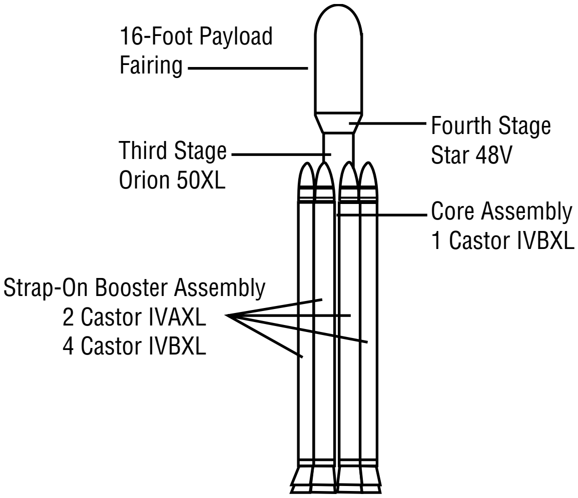

FIGURE 30.—Composition of the Conestoga 3632.

Taurus. Two versions of the Taurus launch vehicle have been considered for the mission, the Taurus S and the Taurus XL/S. A larger spacecraft can be inserted into the 185-km by 7-R_E orbit by the XL/S version. However, an onboard propulsion system is needed to deliver the spacecraft to the final orbit. Reduction in size, weight, and complexity eliminates the need for an onboard propulsion system. This in turn places additional burdens on the launch vehicle; it then becomes responsible for proper orientation and spin rate at the final orbit. Orbital Sciences Corporation (OSC) studied the mission and believes the Taurus S would be the best configuration. It is smaller and less expensive than the XL/S version, yet is fully capable of meeting mission requirements.

The Taurus became an operational launch vehicle with the first flight in March 1994. The Taurus S is a modification of the baseline vehicle, as shown in figure 31. It is composed of the Pegasus stages lifted by a Thiokol Castor 120 solid motor. In addition, it utilizes two Castor IVA's as strap-on boosters. For this mission, a spinning Star 37 solid motor is needed as the perigee kick motor (PKM). For the apogee raise, OSC would provide an appropriate AKM capable of placing the spacecraft into orbit with the proper attitude and spin rate.

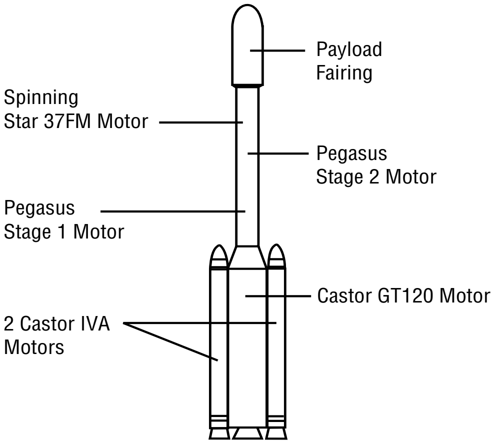
Payload
Fairing
Spinning
Star 37FM Motor
Pegasus
Stage 2 Motor
Pegasus
Stage 1 Motor
Castor GT120 Motor
2 Castor IVA
Motors

FIGURE 31.—Composition of the Taurus S.

The Taurus stands approximately 27.5 m and has a core diameter of 2.4 m. The standard payload fairing will be needed for this mission. With the 1.37-m diameter, the dynamic envelope is large enough to house the MI spacecraft. However, some of the cylindrical length of the dynamic envelope must be used to accommodate the spinning Star 37FM motor. As seen in figure 32, the payload easily fits within the fairing and allows some extra space for the AKM. This motor would be provided by OSC and should not impact the quoted payload capability of 330 kg.

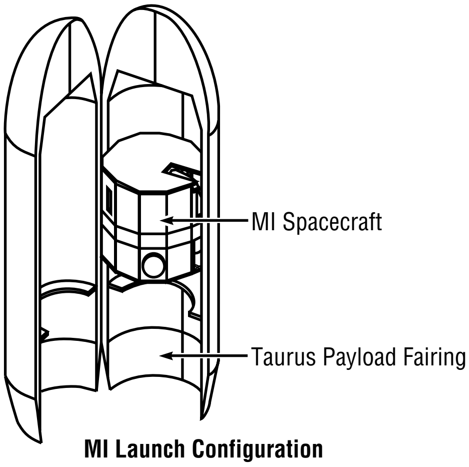
MI Spacecraft
Taurus Payload Fairing
MI Launch Configuration

FIGURE 32.—MI spacecraft within the Taurus S fairing.

As with any mission, attachment structure will be required to hold the spacecraft in the fairing. At the time of this study, this issue had not been investigated completely, and it is assumed that the standard clamp bands will be used.

Taurus Launch Sequence to Orbit Insertion. The flight of the Taurus S is expected to have some similarities to the maiden flight of the Defense Advanced Research Projects Agency (DARPA) version of the Taurus in March 1994. These vehicles are similar in the core motors, with the exception of stage 0. The DARPA vehicle used a Peacekeeper motor as stage 0 rather than the baseline Castor 120. The Peacekeeper motor produces more thrust and is heavier than the Castor 120. The Taurus S will use the Castor 120 with the addition of two Castor IVA motors. The added strap-on motors increases the total thrust and weight of the vehicle, giving the Taurus S similar liftoff characteristics to the DARPA vehicle.

OSC has analyzed the nominal trajectory for the MI mission. Naturally, further analysis is necessary as the vehicle and the payload are further defined. Information gathered from the first flight and from the trajectory analysis gives the following approximations for some of the flight parameters:

• Thrust-to-weight ratio at liftoff (T/W)	~ 3 g’s
• Maximum dynamic pressure (q_{max})	~ 3,000 lb/ft^2
• Maximum axial acceleration (g_{max})	~ 6.5 g’s.

The spacecraft design must be able to withstand the loads associated with these conditions.

The profile of the nominal flight is shown in figure 33. The flight duration for the launch vehicle from liftoff to payload deployment is 23,576 seconds. Since the AKM is responsible for orientation and spin-up of the spacecraft, long coast periods are necessary for the proper orbit.

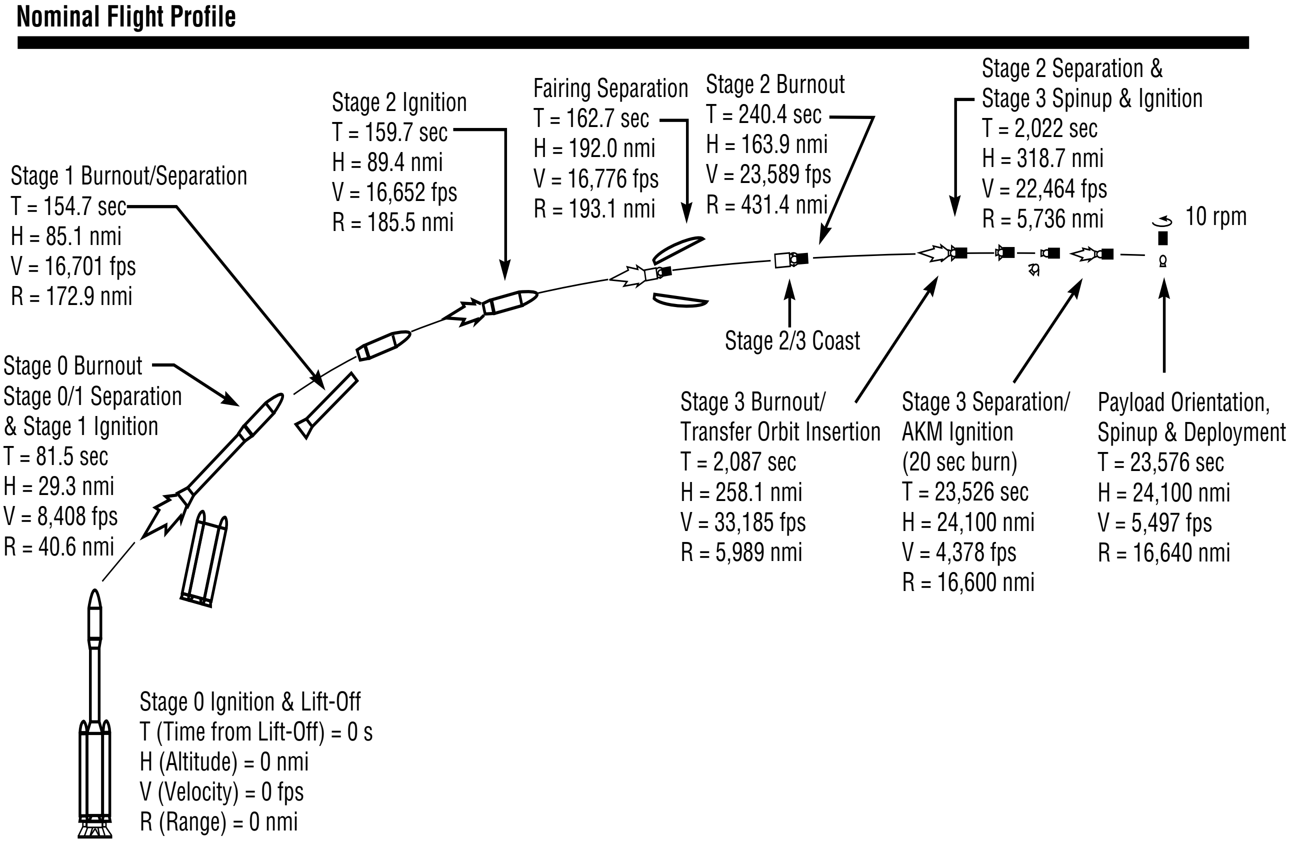

Nominal Flight Profile

Stage 0 Ignition & Lift-Off
T (Time from Lift-Off) = 0 s
H (Altitude) = 0 nmi
V (Velocity) = 0 fps
R (Range) = 0 nmi
Stage 0 Burnout
Stage 0/1 Separation
& Stage 1 Ignition
T = 81.5 sec
H = 29.3 nmi
V = 8,408 fps
R = 40.6 nmi
Stage 1 Burnout/Separation
T = 154.7 sec
H = 85.1 nmi
V = 16,701 fps
R = 172.9 nmi
Stage 2 Ignition
T = 159.7 sec
H = 89.4 nmi
V = 16,652 fps
R = 185.5 nmi
Fairing Separation
T = 162.7 sec
H = 192.0 nmi
V = 16,776 fps
R = 193.1 nmi
Stage 2 Burnout
T = 240.4 sec
H = 163.9 nmi
V = 23,589 fps
R = 431.4 nmi
Stage 2/3 Coast
Stage 2 Separation &
Stage 3 Spinup & Ignition
T = 2,022 sec
H = 318.7 nmi
V = 22,464 fps
R = 5,736 nmi
10 rpm
Stage 3 Burnout/
Transfer Orbit Insertion
T = 2,087 sec
H = 258.1 nmi
V = 33,185 fps
R = 5,989 nmi
Stage 3 Separation/
AKM Ignition
(20 sec burn)
T = 23,526 sec
H = 24,100 nmi
V = 4,378 fps
R = 16,600 nmi
Payload Orientation,
Spinup & Deployment
T = 23,576 sec
H = 24,100 nmi
V = 5,497 fps
R = 16,640 nmi

FIGURE 33.—Nominal flight profile (provided by OSC).

Vehicle Constraints on Ground Operations. The Taurus family was designed to be launched rapidly and is capable of lifting off from austere sites. DARPA placed the requirement that the vehicle must be assembled and launched within 8 days from arrival at the site. The Taurus system is capable of self-contained operation, but is typically launched from established sites. The Taurus system is compatible with the Air Force's Eastern and Western sites and with NASA's Wallops Flight Facility. For the MI mission, the probable launch site will be the WTR at VAFB. All the performance estimates for this study are based upon the WTR site.

The Taurus S poses no special requirements on the ground operations. The vehicle will use the standard ground support equipment already available for the Taurus family.

Spacecraft Configuration

The factors affecting the spacecraft configuration are the science instrument requirements, launch vehicle volumetric limits, launch vehicle performance to the desired orbit, spacecraft stability, structural loads, power requirements, thermal requirements, manufacturability, and costs.

The spacecraft diameter of 1.3 m was chosen to fit within the smallest of the available Med-Lite class launch vehicles—the Taurus (fig. 32). The length, 1.3 m, provides sufficient surface area for solar array mounting to meet the system power requirements. Figure 34 shows an isometric view of the spacecraft configuration.

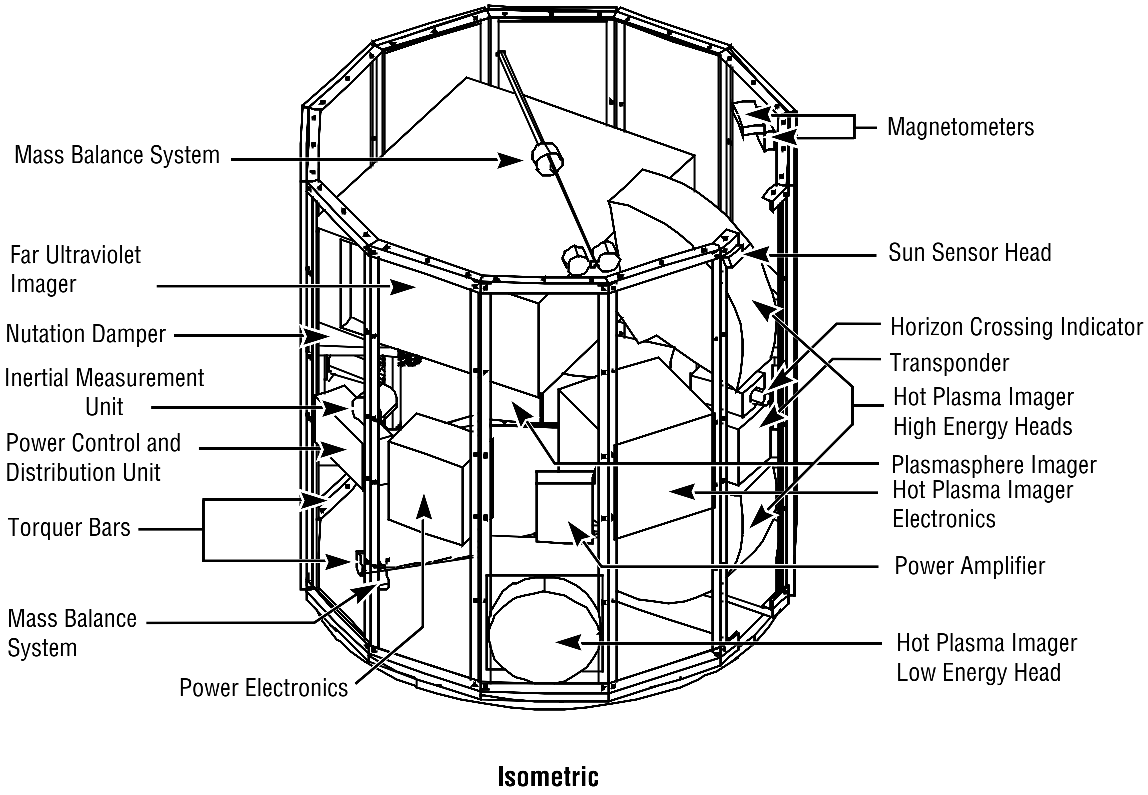
Mass Balance System
Far Ultraviolet Imager
Nutation Damper
Inertial Measurement Unit
Power Control and Distribution Unit
Torquer Bars
Mass Balance System
Power Electronics
Magnetometers
Sun Sensor Head
Horizon Crossing Indicator
Transponder
Hot Plasma Imager High Energy Heads
Plasmasphere Imager
Hot Plasma Imager Electronics
Power Amplifier
Hot Plasma Imager Low Energy Head
Isometric

FIGURE 34.—Isometric spacecraft configuration.

The structure is multifaceted to ease assembly. The individual panels are populated with subsystem components prior to assembly to the space frame. An example of the panel layout for the spacecraft is found in figure 35.

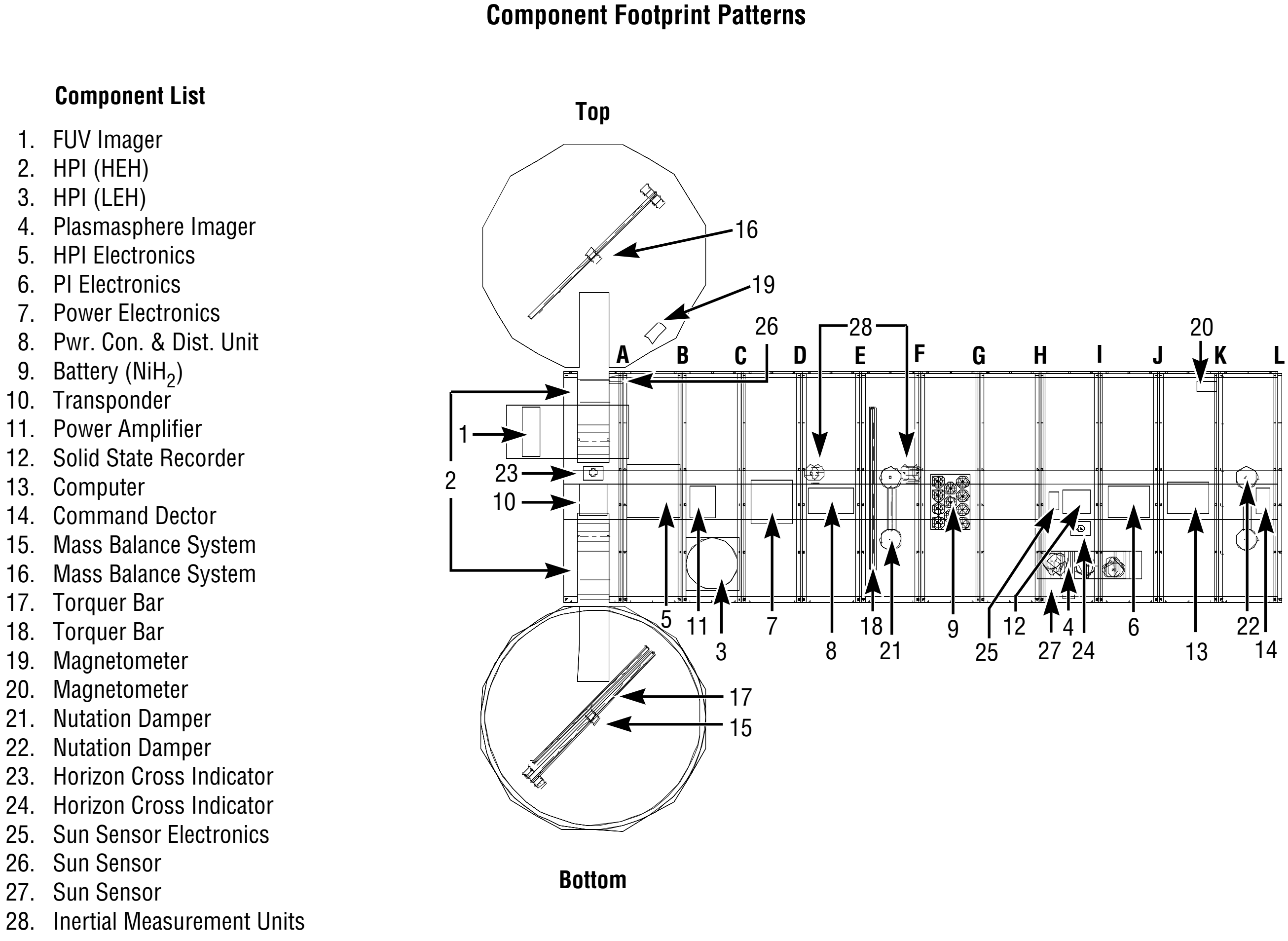
Component Footprint Patterns
Component List
1. FUV Imager
2. HPI (HEH)
3. HPI (LEH)
4. Plasmasphere Imager
5. HPI Electronics
6. PI Electronics
7. Power Electronics
8. Pwr. Con. & Dist. Unit
9. Battery (NiH$_2$)
10. Transponder
11. Power Amplifier
12. Solid State Recorder
13. Computer
14. Command Dector
15. Mass Balance System
16. Mass Balance System
17. Torquer Bar
18. Torquer Bar
19. Magnetometer
20. Magnetometer
21. Nutation Damper
22. Nutation Damper
23. Horizon Cross Indicator
24. Horizon Cross Indicator
25. Sun Sensor Electronics
26. Sun Sensor
27. Sun Sensor
28. Inertial Measurement Units
Top
16
19
26
28
20
A
B
C
D
E
F
G
H
I
J
K
L
1
2
23
10
5
11
3
7
8
18
21
9
25
12
27
4
24
6
13
22
14
17
15
Bottom

FIGURE 35.—Spacecraft panel assembly.

The science instruments are scanning-type instruments requiring a spinning spacecraft. To maintain spin stability with a simple control system, it is necessary to position the components so that the spacecraft's greatest moment of inertia is about the spin axis. The subsystem components are mounted near the center of the side panels to optimize the moment ratio. Mounting the components to the side panels also shortens the heat paths for thermal energy rejection.

The belt antenna position midway up the spacecraft is a result of providing for the 180° FOV requirement for the HPI HEH. The remaining instruments are positioned such that the apertures are above or below the belt antenna. Figure 36 shows a top view of the spacecraft, with the individual instrument FOV requirements pictorially represented.

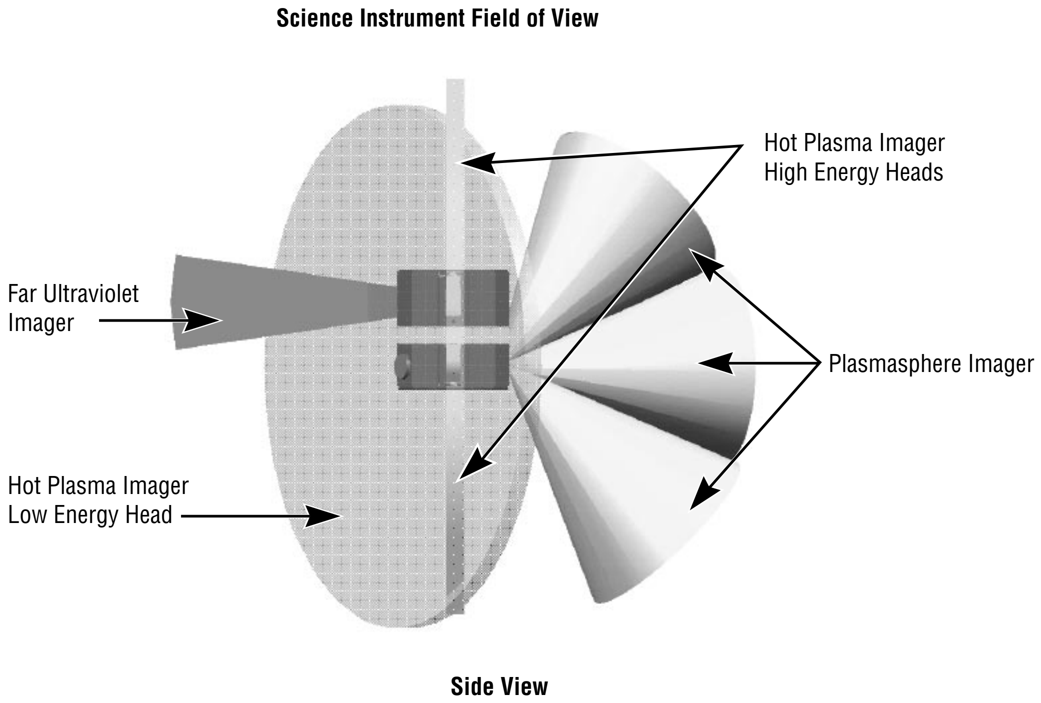
Science Instrument Field of View
Hot Plasma Imager High Energy Heads
Far Ultraviolet Imager
Plasmasphere Imager
Hot Plasma Imager Low Energy Head
Side View

FIGURE 36.—Science instrument FOV requirements.

The subsystem components are arranged to minimize electrical and data cable lengths while maintaining the overall spacecraft balance about the spin axis. A ball-screw mass balance system is included to fine-tune the mass distribution on orbit and is shown in a top view of the spacecraft layout in figure 37. Magnetic torquer bars are used to fine-tune the spacecraft attitude and spin rate. Passive nutation dampers diminish nutation effects and wobble.

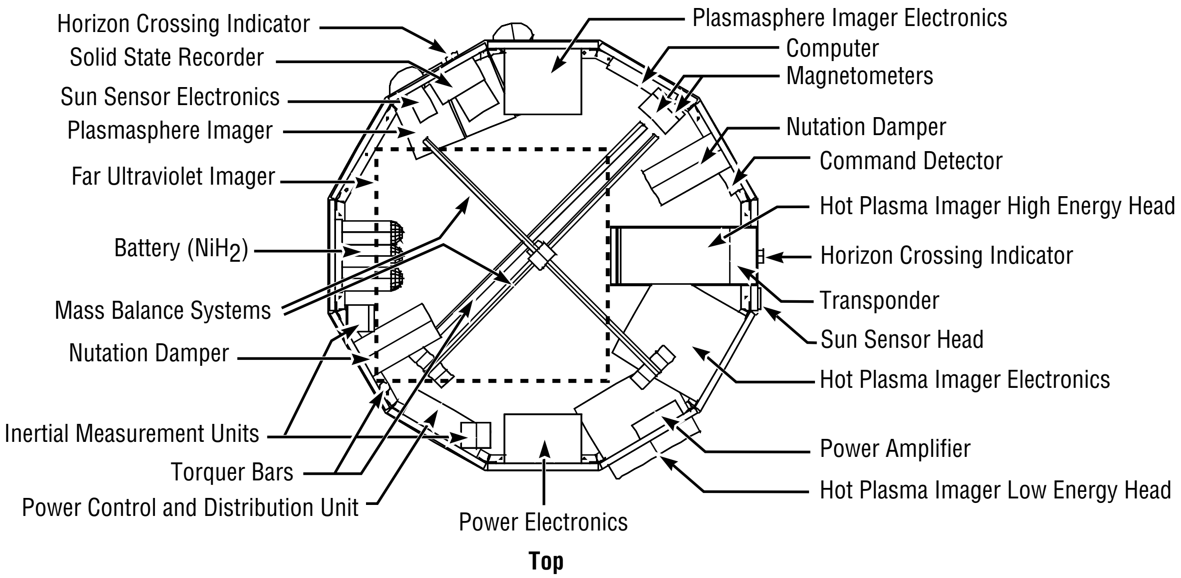
Horizon Crossing Indicator
Solid State Recorder
Sun Sensor Electronics
Plasmasphere Imager
Far Ultraviolet Imager
Battery (NiH$_2$)
Mass Balance Systems
Nutation Damper
Inertial Measurement Units
Torquer Bars
Power Control and Distribution Unit
Power Electronics
Plasmasphere Imager Electronics
Computer
Magnetometers
Nutation Damper
Command Detector
Hot Plasma Imager High Energy Head
Horizon Crossing Indicator
Transponder
Sun Sensor Head
Hot Plasma Imager Electronics
Power Amplifier
Hot Plasma Imager Low Energy Head
Top

FIGURE 37.—Spacecraft configuration top view.

Structures

The MI spacecraft is a 12-sided structure composed of an internal frame and covered with flat aluminum honeycomb plates. The frame is composed of 12 aluminum longerons and 2 aluminum rings (fig. 38). The rings are designed with open sections to accommodate the apertures of the HPI. The science instruments, due to their size, will be mounted to the frame by specially designed brackets and structural members. The side panels and upper and lower deckplates provide the required mounting surfaces for the solar cells. Aluminum honeycomb with aluminum face sheets allows the heat to be conducted away from the solar cells, while at the same time accommodating the requirements for a thermal radiator. The central portion of each panel is designated as the radiator. The spacecraft components that require heat rejection will be mounted directly to the radiator. The belt antenna will also be attached to the spacecraft in the radiator region. The only mechanisms on the spacecraft, other than those contained within the science instruments, are the mass balance systems, which are a part of the ACS.

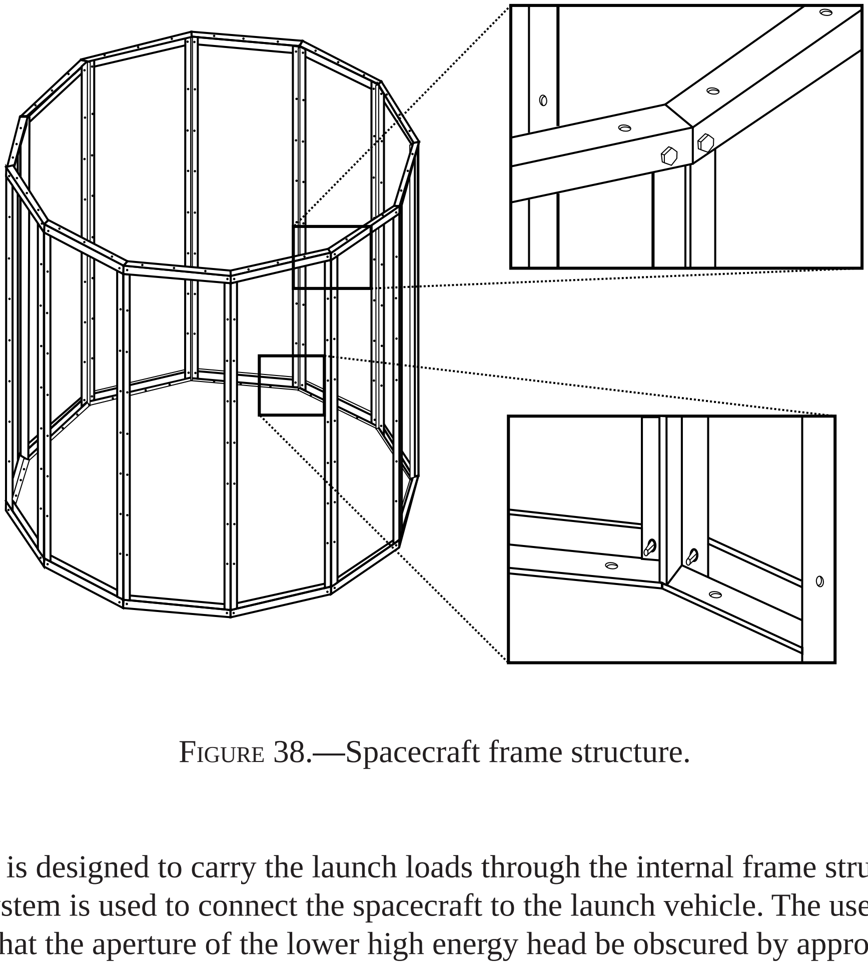

FIGURE 38.—Spacecraft frame structure.

The spacecraft is designed to carry the launch loads through the internal frame structure. A clamp band separation system is used to connect the spacecraft to the launch vehicle. The use of the clamp band will require that the aperture of the lower high energy head be obscured by approximately 2°. The weight of the clamp band separation system, about 18.3 kg, was estimated by scaling an OSC designed system. There will be approximately 7.4 kg remaining with the spacecraft after separation. A lower mass system has been proposed and will be investigated. The proposed system has the added potential of eliminating the blockage of the science instrument.

Structural Requirements

The spacecraft is designed to be flown on a Taurus S launch vehicle. The *Commercial Taurus™ Launch System Payload User's Guide*, release 1.00 (August 1992), does not include the Taurus S vehicle structural requirements. For this study, the requirements for the Taurus XL/S were used as a reference. Also included will be data concerning the latest variants of the launch vehicle.

For the Taurus XL/S the quasi-static load factors are defined as follows in table 7.

TABLE 7.—*Quasi-static load factors for Taurus XL/S.*

X	Y	Z
~9 g*	± 0.5 g	± 0.5 g

*For a 1,100 lbm payload weight

Random vibration loads are dependent on the payload mass and stiffness characteristics. The power spectral density curve for the Taurus XL/S and the Taurus XL is shown in figure 39. The random vibration portion of the load will be calculated based on the natural frequencies.

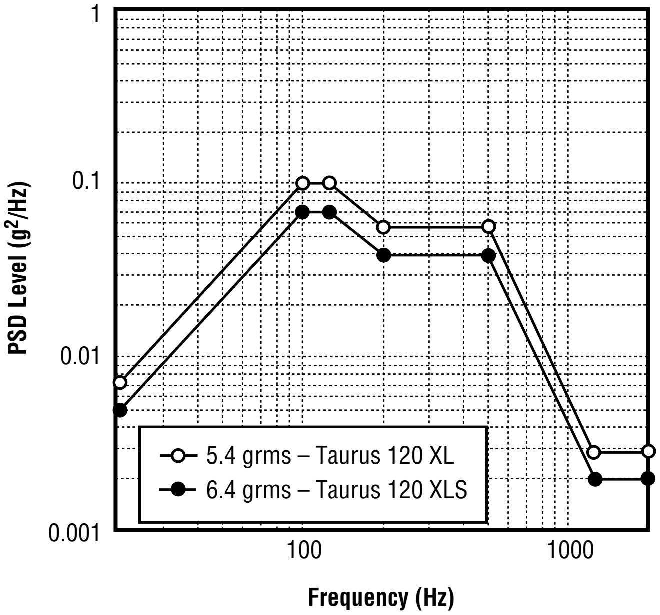

FIGURE 39.—Taurus XL/S and Taurus XL spectral density curves.

Safety factors for the structure will be 1.1 for the yield condition and 1.25 for ultimate loads, per MSFC–HDBK–505, *Structural Strength Program Requirements.*

Spacecraft Fabrication

Aluminum and aluminum honeycomb were chosen as the baseline materials for several reasons. Aluminum is lightweight, inexpensive, and available from a variety of sources. The mechanical and thermal properties are well understood and are consistent from lot to lot. For this application, aluminum honeycomb panels provide the desired thermal properties for heat rejection and good structural stiffness without excessive weight, though at a high cost.

Composite Material Options. Replacing the aluminum face sheets of the honeycomb sandwich panels with graphite/cyanate composites, as well as using composite longerons and brackets, may be considered as an option for the spacecraft. Another option utilizes the lightweight and high stiffness composite isogrid panels for the two decks. Since the dissipation of excess heat is a major concern for MI, high modulus fiber such as Amoco's P120 should be considered as reinforcement due to its high thermal conductivity. The matrix material under consideration for the composites is the polycyanate resin. This matrix material has been developed especially for spacecraft application due to its low water absorption and desorption, low dielectric properties, improved resistance to microcracking, and resistance to ultraviolet (UV) radiation. One major advantage of composites is that the strength and stiffness can be tailored in the desired direction to satisfy certain spacecraft design requirements. The innovative manufacturing process of composites also plays a very important role in reducing the part count and costs. These include the unibody design, co-curing two to three sandwich panels, and co-curing longerons and brackets to panels.

Carbon/Graphite Fibers. The demand of high strength and high modulus reinforcements for composites has led to the development of carbon or graphite fibers. Although the graphite fiber has higher carbon content and is stronger than carbon fiber, the terms have been used interchangeably. Carbon fibers can be manufactured by using polyacrylonitrile (PAN), rayon, and petroleum pitch. Rayon based carbon fibers are mainly used for making nozzles. Pitch-based fibers have a higher degree of graphite structure than do PAN-based fibers. Pitch fibers have high elastic moduli (480–830 GPa) but reduced tensile strength (up to 2.4 GPa). However, for small spacecraft, such as MI, the stiffness (elastic modulus) is more important than the strength of the material. Additionally, high modulus fibers are also high thermal conductors. The excess heat generated by electronic equipment and batteries can be dissipated to heat sink or radiator through these fibers in the composites. Amoco has developed some high modulus graphite fibers—such as P75, P100, and P120—which have thermal conductivities comparable to those of metals. Table 8 shows some of the thermal conductivities of these materials.

TABLE 8. —*Comparison of thermal conductivity of some carbon fibers.*

Fiber or Metal	Supplier	Thermal Conductivity (W_{mK})
P75	Amoco	185
P100	Amoco	520
P120	Amoco	640
T300	Amoco	10
Copper		450
Aluminum		200

Material Selection. Some of these fibers have thermal conductivity values comparable or even higher than that of pure coppers (450 W_{mK}). Since the thermal conductivity of polymeric resin is very low, the overall thermal conductivity of a composite laminate is linearly proportional to the fiber volume content. Nysten and Issi have conducted some measurements on the thermal conductivity of carbon fiber reinforced composites. The best composite measured (45 percent P120 fibers) showed a thermal conductivity value of 245 W_{mK}, which is higher than that of pure aluminum (200 W_{mK}).

Space environmental effects, such as radiation, outgassing, and atomic oxygen exposure, should also be carefully considered in choosing the proper type of matrix materials. ICI Fiberite, Hexcel, YLA, Dow Chemical, Ciba Geigy, and Bryte Technologies are the major sources of the polycyanate resins.

Composite Design Configuration. Composite materials, in general, are more expensive than aluminum alloy. However, the high stiffness and high strength-to-weight ratio of composites, along with innovative manufacturing methods, can dramatically reduce the overall cost of using composite structures for spacecraft design. The composite design configuration includes replacing the aluminum face sheets of the honeycomb sandwich panels with graphite/cyanate composites, as well as using composite longerons and brackets. Another option utilizes the lightweight and high stiffness composite isogrid panels for the two decks.

Replacing the aluminum face sheets (skins) in the baseline design with composites can reduce the skin weight by approximately 30 to 40 percent. The aluminum honeycomb core should be used for heat conduction through the thickness of the sandwich panel. Various options and design guidelines can be considered for MI spacecraft design using composite sandwich panels and composite isogrid panels:

- All panels should be co-cured to form the body of the spacecraft. Upper and lower decks can be attached to the body with potted insert fasteners. They can also be fastened to the co-bonded brackets at the ends of the panels. This design eliminates all longerons and the fasteners required to attach the panels, thus reducing the weight and the assembly cost. The only disadvantage is that difficulties may arise when installing and uninstalling the instruments and cables.

- Two to three panels should be co-cured to form sections. Longerons can be co-bonded and co-cured to the edges of each section of two to three panels. Deck attachment is the same as the above mentioned design. This option can eliminate one-half to two-thirds of the longerons and fasteners. However, since the body is formed in four to six sections, installing and uninstalling the instruments will no longer be a problem.

- Rib stiffened composite panels (isogrid) should be used for upper and lower decks. The composite ribs are arranged in an isogrid configuration and are bonded to the composite skin to replace the honeycomb core in a panel. This composite isogrid panel can further reduce the weight of the panels.

- Brackets for installing instruments and batteries can be co-cured and co-bonded to the skin of the panels.

- Local doublers can be incorporated in high shear and high stress concentration areas to maintain overall panel stiffness and local skin strength. These doublers can be embedded within the panel skins or bonded to the exterior of the panel skins.

- The exterior of the spacecraft will be mostly covered by solar cells. Since the graphite fibers are good electrical conductors along the fiber direction, the skin of the panels should be insulated from the solar cells by nonconductive films. These films can be co-cured with, or secondary bonded to, the composite panel skin.

These options can dramatically reduce the number of parts to be assembled, the number of fasteners, and the weight. With less human interaction and an automated manufacturing process, the cost can also be reduced.

Analysis of Composite Structures. The above mentioned composite sandwich panels are plates with stiff, thin face sheets supported by thick honeycomb cores. The Kirchoff assumptions for analyzing solid plates are made across the thickness of the sandwich plate. However, the honeycomb cores are flexible in shear. Thus the transverse shear effects should be included in the sandwich plate theory. For symmetrical face sheets, the laminate theory for composites can be greatly simplified. The lightweight core has negligible in-plane stiffness. The total stiffness is simply the sum of the face sheet stiffness. The forces acting on the sandwich plates are controlled by the in-plane stress resultants acting on the face sheets. The total in-plane and flexural loads can be defined from these resultants. The simplified theory is very useful in design. The error introduced by this approach is small provided that the face sheets are thin.

There are many micromechanics theories for composite analysis, none of which is entirely correct. However, the micromechanics formulas are still useful in predicting the material property variations in conjunction with the empirical data. Composite analysis using the elasticity theory often results in boundary value problems or optimization of functions. For practical spacecraft design, numerical approximations are necessary for finding the solutions. Numerical tools such as finite difference method and finite element analysis (FEA) are some of the useful tools. Commercial packages for FEA, such as NASTRAN, ANSYS, and CDA/SPRINT, are available for composites structures.

Assembly

The structural design was heavily influenced by the assembly process and the need for access to components during the test phase until just prior to launch. It is very desirable to address manufacturing, assembly, and access early in a program. A thoughtful design will result in fewer changes later during the product’s design and assembly.

As described earlier, the core of the structure is a space frame of longerons and rings. The large science instruments will be installed into the structure first, using brackets and specialized structural members for mounting. Other spacecraft and science instrument components will be mounted directly to the panels and deckplates which had previously been populated with solar cells. The panels assemblies will be mounted onto the space frame in a prescribed pattern, with the deckplates installed last. Two panel- to-longeron mounting options were defined—a surface mount and a flush mount. Detailed sketches of these two options are shown in figure 40. Cables must be routed and connected as each panel and deckplate is installed sequentially. During design, cable routing must be carefully planned to accompany the assembly process.

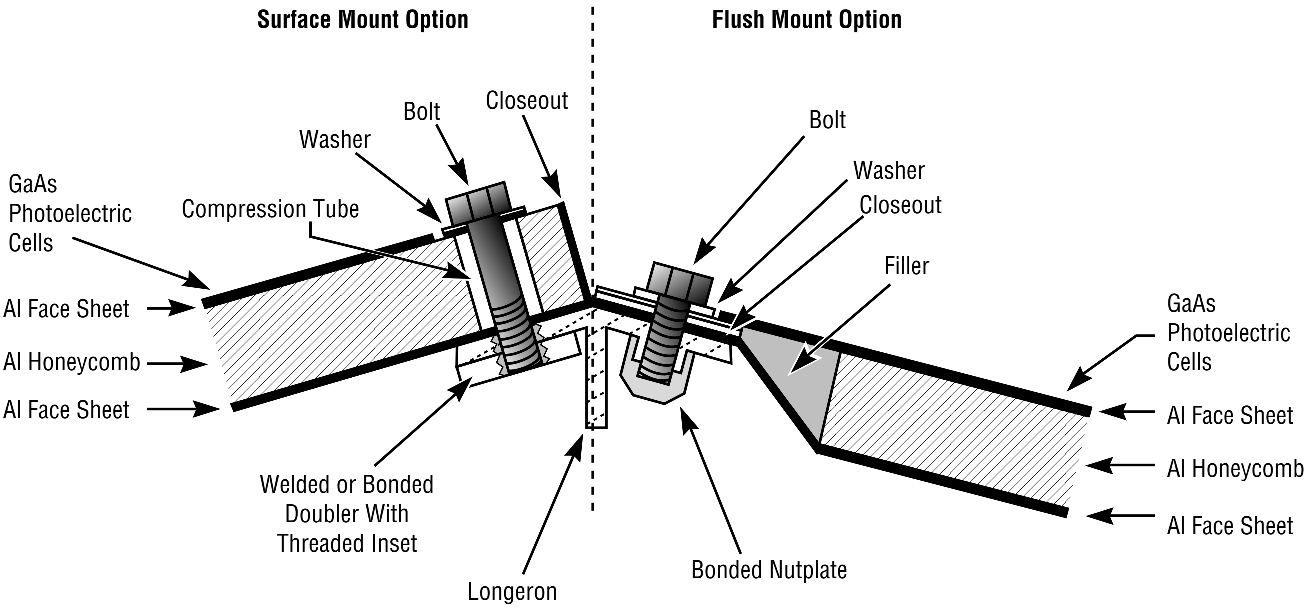
Surface Mount Option
Flush Mount Option
Bolt
Closeout
Washer
GaAs
Photoelectric
Cells
Compression Tube
Al Face Sheet
Al Honeycomb
Al Face Sheet
Welded or Bonded
Doubler With
Threaded Inset
Longeron
Bolt
Washer
Closeout
Filler
Bonded Nutplate
GaAs
Photoelectric
Cells
Al Face Sheet
Al Honeycomb
Al Face Sheet

FIGURE 40.—Panel-to-longeron mounting options.

After assembly is complete, components will be accessible by removing a particular panel (or panels) and a longeron, if necessary. Science instruments can be reached by removing either the top or bottom deckplates. The deckplate and panel mounting concepts are detailed in figure 41.

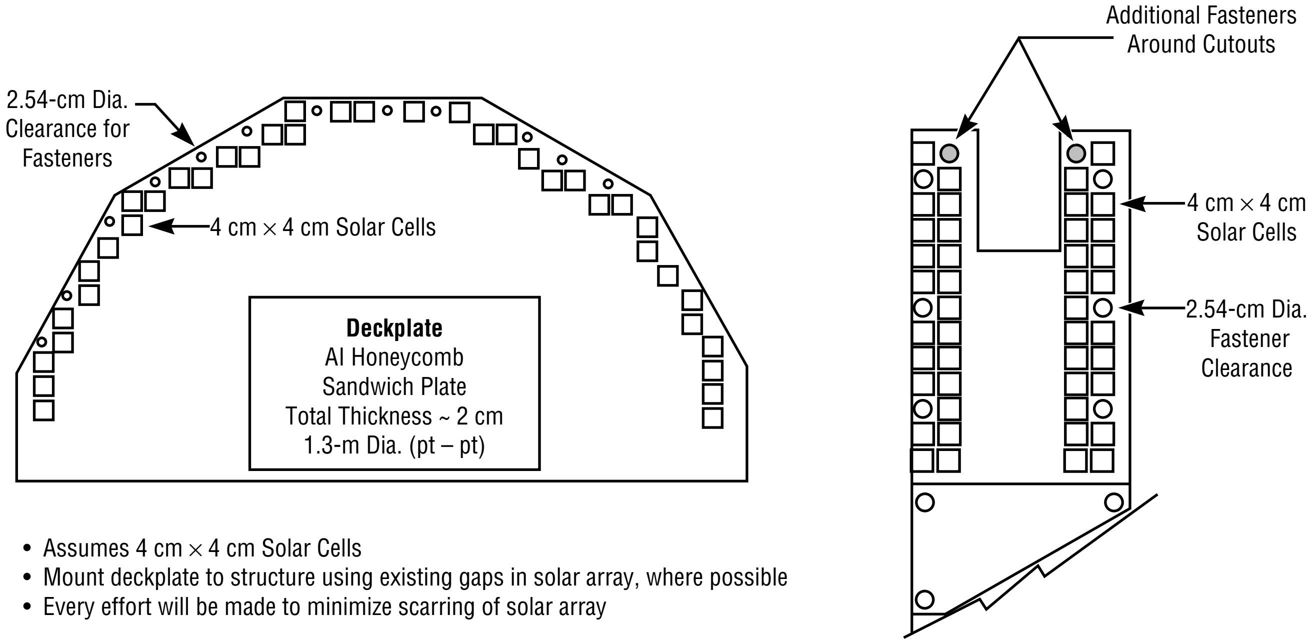
2.54-cm Dia.
Clearance for
Fasteners
4 cm × 4 cm Solar Cells
Deckplate
Al Honeycomb
Sandwich Plate
Total Thickness ~ 2 cm
1.3-m Dia. (pt – pt)
• Assumes 4 cm × 4 cm Solar Cells
• Mount deckplate to structure using existing gaps in solar array, where possible
• Every effort will be made to minimize scarring of solar array
Additional Fasteners
Around Cutouts
4 cm × 4 cm
Solar Cells
2.54-cm Dia.
Fastener
Clearance

FIGURE 41.—Deckplate and panel mounting concepts.

One area of concern is the installation of the belt antenna around the circumference of the spacecraft. Access to the components could be very limited after the antenna is installed and soldered. The design and installation of the antenna may influence the design and should be examined in detail as early as possible.

There are several options available to enhance the design for assembly and access. If composite face sheets are used, a maximum of two panels could be co-cured into one unit, thus reducing the number of longerons by a factor of 2. It is desirable to have each panel manufactured as a single unit to reduce the number of individual parts and touch labor. There may be some cases, especially in the case of the installation of the battery, where two or more sections in a panel may be required for late access.

In addition to the design of the spacecraft structure, the design of the handling fixtures for assembly and transportation must be carefully planned to take into consideration the assembly process and the need for accessibility. The preliminary assembly flow is illustrated in figure 42.

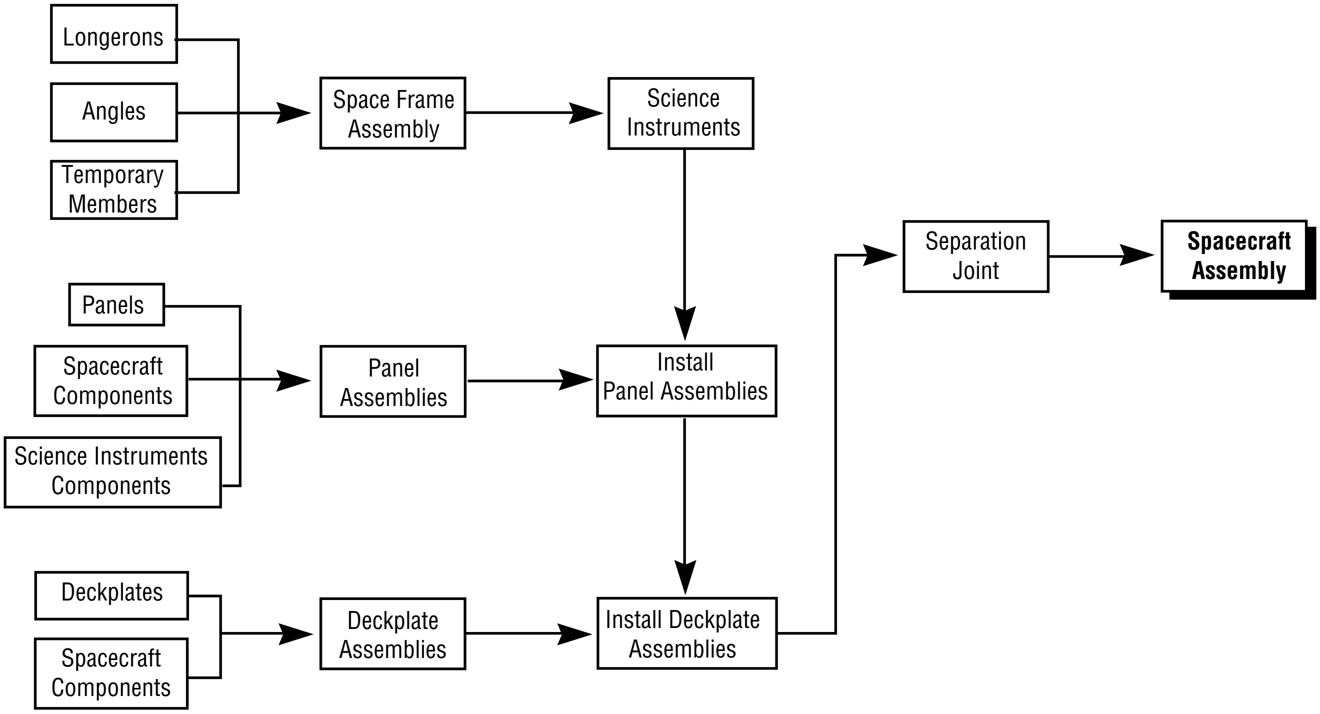
Longerons
Angles
Temporary Members
Space Frame Assembly
Science Instruments
Separation Joint
Spacecraft Assembly
Panels
Spacecraft Components
Science Instruments Components
Panel Assemblies
Install Panel Assemblies
Deckplates
Spacecraft Components
Deckplate Assemblies
Install Deckplate Assemblies

FIGURE 42.—Preliminary assembly flow.

By considering method of assembly, accessibility, number of parts, and handling in the early design phase, the needs of the individual subsystem components, as well as those of science instrument developers, can be better met. It is very desirable to identify any areas of concern and work toward the resolution as early as possible in the spacecraft design. The structures mass statement is found in table 9.

Table 9.—*Structures mass statement*.

	Mass Each	Quantity	Subtotal	Totals
Space Frame Assy				14.0 kg
Longerons	0.8 kg	12	9.1 kg	
Angles	0.2 kg	22	4.8 kg	
Panels	0.9 kg	12		10.3 kg
Deckplates	2.5 kg	2		5.0 kg
Fasteners	TBD	TBD		5.5 kg
Separation system				18.3 kg
Spacecraft side	7.3 kg	1	7.3 kg	
Launch vehicle side	11.0 kg	1	11.0 kg	
Mounting brackets	TBD	TBD		6.0 kg
Cabling brackets	TBD	TBD		1.2 kg
Total			**60.3 kg**	

TCS

Introduction

The function of the TCS is to maintain all components within acceptable temperature limits. To minimize the power and weight, the TCS should be as passive as possible, with heaters to augment heat input into the system whenever the temperatures of components drop below specified minimums. Passive thermal control uses coatings, MLI, louvers, and radiating surfaces to control the temperature of the equipment.

Launch Vehicle Thermal Environment

After the spacecraft has been integrated and the fairing is installed, the standard service ground support environmental control system is attached to the fairing to control inlet air temperatures to 21 ˚C ±11 ˚C until launch. A minimum of three air changes are provided per hour and a positive air pressure inside the fairing is maintained. After the vehicle is launched, the Taurus fairing wall temperature will reach approximately 80 ˚C before it is jettisoned. The acoustic blanket emissivity is 0.1.

Components Thermal Requirements

The MI spacecraft is made of several components, structure, electronic equipment, and solar arrays. Most of these components have power and temperature requirements. The function of the TCS is to maintain these components within specified temperature limits. Table 10 contains a partial list of components that have specified thermal requirements.

Table 10.—*Thermal requirements.*

Component	Power		Temperature (°C)
HPI HEH	4		–23 to 30
HPI LEH	7		–30 to 40
HPI Electronics	12		–30 to 40
FUV Imager Electronics	25		–20 to 40
FUV Imager	1.5 to 3.5		50 to 75 below ambient
PI	16.5		–30 to 40
PI Electronics	4.5		–30 to 40
Battery	21		0 to 25
Computer	10		–30 to 40
Solid State Recorder	15		–30 to 40
Transponder	21	(1.4 orbit avg.)	–30 to 40
Amplifier	41	(2.7 orbit avg.)	–30 to 40
Command Detector	5		–30 to 40
Power System Electronics	14.5		–30 to 40
Initial Measurement Unit (IMU)	10		–30 to 40
Horizon Sensors	1.5		–30 to 40
Sun Sensor Electronics	0.4		–30 to 40
Nutation Dampers	–		Lower temp. limit of –45

Design Approach

The MI thermal design evolved with the mission. The earlier IMI designs used the end surface of the spacecraft as a thermal radiator. This required a 180˚ flip maneuver to be performed every 6 months to prevent the radiating surfaces from receiving any solar incident radiation. As the design requirements changed, the flip maneuver was removed from the mission scenario. This requires a system that will reject the spacecraft heat while receiving solar radiation incident on all sides of the spacecraft during the mission.

The thermal design approach for the spacecraft was to develop a system that passively cooled the spacecraft components and used heaters to provide make-up heat where necessary (fig. 43). Initial concepts had the electronic components and science instruments mounted on two deckplates within the spacecraft. Later these deckplates were removed and, to maximize heat transfer, the components should now be mounted to the spacecraft cylinder walls. Where feasible, the components are to be mounted onto a radiator band 0.2-m wide to reject the heat. The components will be covered with MLI to thermally isolate each of them.

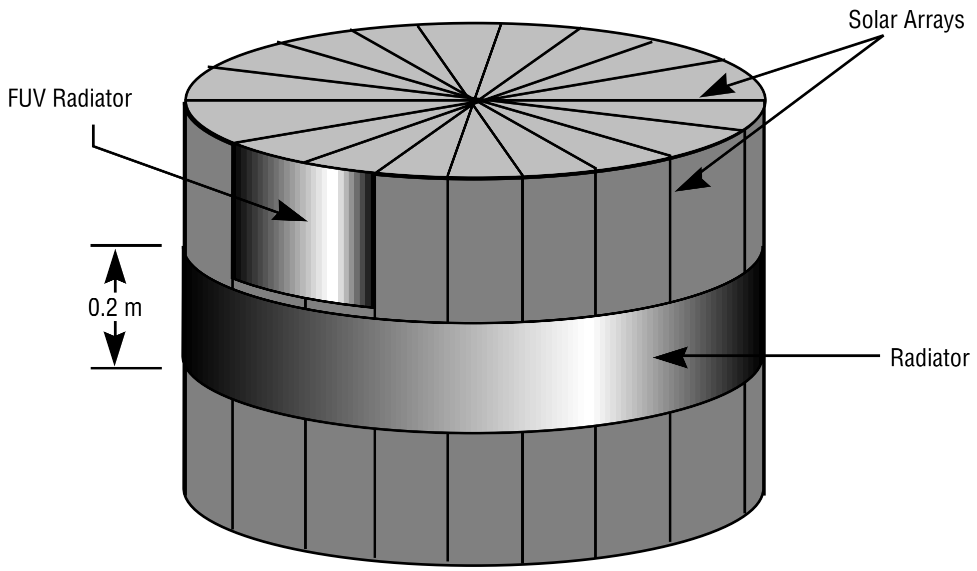

FIGURE 43.—MI thermal design.

Detailed thermal design of the individual science instruments was not considered. The thermal design of the spacecraft takes into account the temperatures that may be required at the spacecraft/science instrument interface. For instance, the FUV Imager has a temperature requirement of approximately –70 °C, but the other spacecraft components need to be much warmer. To accommodate the conflicting requirements, two thermal radiators will be needed: one to reject heat from the electronics and another to remove the Imager heat load. This radiator would be smaller but would be dedicated to FUV Imager cooling.

Analysis

The spacecraft thermal design was analyzed to determine the component temperatures and amount of heater power needed to maintain cold components above operational and survival temperature limits. For the analysis, the spacecraft walls are assumed to be aluminum honeycomb with a 3 pounds/foot^3 core. These walls are covered externally with 0.019-inch-thick GaAs/Ge solar cells. The solar cells are assumed to cover all surfaces except the radiator band. The effective α of the solar arrays is determined to be 0.652 based on a solar cell efficiency of 18.5 percent, and the ε is assumed to be 0.8. The radiator band is assumed to be coated with Z–93 which has an α of 0.15 and an ε of 0.9. The optical properties of the Z–93 would be stable throughout the 2-year mission.

A finite element model was built using I–DEAS/TMG (fig. 44). Thin-shell elements were used to model the spacecraft. The heat dissipated by the spacecraft components is assumed to be a constant load on the interior elements of the radiator band. The spacecraft is 12-sided, and each side of the radiator band has an individual heat load.

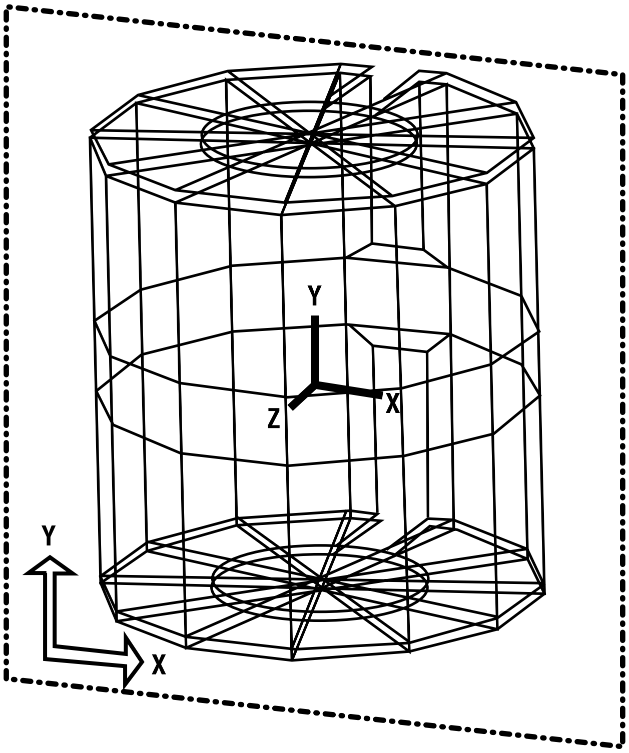

FIGURE 44.—MI finite element model.

The spacecraft will be placed into a 4,800-km by 7-R_E orbit that has a period of 15.16 hours. Because the orbit precesses, two different cases were modeled, one case where the angle between the orbit plane and the solar vector (ß) is 0˚ and the other case where ß is 66.5˚ (fig. 45). The case in which ß is 0˚ is the worst case cold condition for the solar arrays because the spacecraft is oriented such that the cylinder is perpendicular to the solar vector. The spacecraft will be in the Earth's shadow for 1.3 hours, which is the longest time that the vehicle will be in umbra during the mission. The 66.5˚ ß case will produce the warmest solar array temperatures because one end of the spacecraft is in the Sun with a high angle of solar incidence. This introduces some thermal difficulties because at 0˚ ß the solar vector is perpendicular to the thermal radiator surfaces, but at 66.5˚ ß the radiator will receive a small amount of solar incident radiation. The spacecraft was modeled to be spinning at 10 rpm in both cases. A transient analysis of the spinning spacecraft was run to calculate the temperatures during the two orbits. Heater power was calculated based on a survival temperature of –40 ˚C of the components and the minimum operational temperature requirements shown in table 10.

Another analysis was performed to determine the size of the thermal radiator to cool the FUV detector. The radiator properties were assumed to be those of Z–93. The detector heat load was assumed to be 3.5 W and the maximum temperature was assumed to be –70 ˚C. A steady-state calculation was performed to size the radiator.

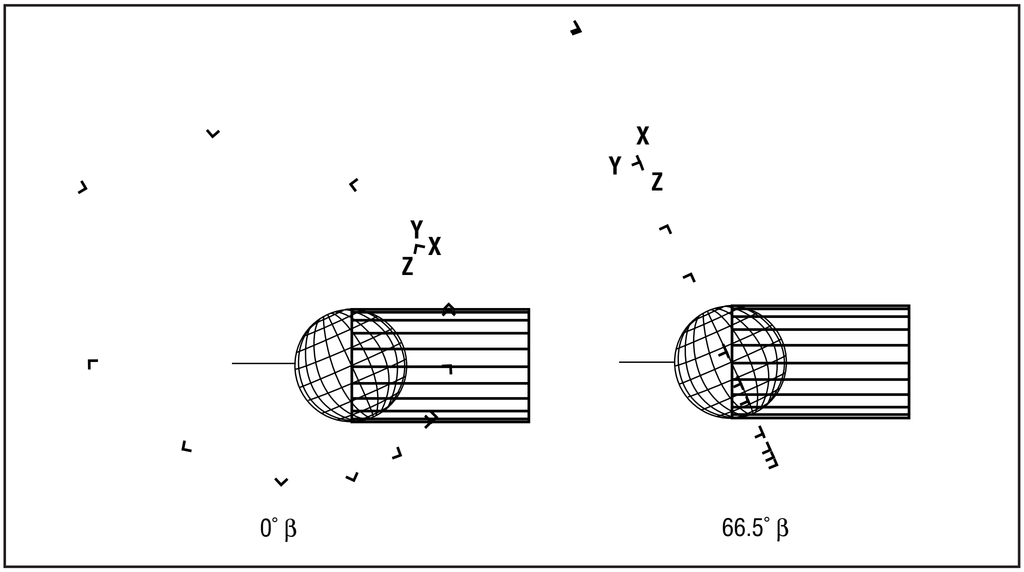

FIGURE 45.—MI orbits modeled showing spacecraft orientation.

Results

Analysis results show that the spacecraft will be able to effectively radiate the heat. With the assumptions given earlier, some components will require additional heater power to ensure their effective operation during the mission. Table 11 shows the spacecraft component maximum and minimum temperatures for the 0˚ ß case and table 12, the 66.5˚ ß case.

TABLE 11.—*0° ß thermal analysis results.*

Component	Power (W)	Temperatures (°C)	
		Max.	Min.
PI/Electronics	21	22.73	4.27
Computer	10	–11.66	–33.9
Solid State Recorder	15	5.1	–17.2
FUV Imager	25	32.9	16.4
Transponder/Amplifier	4	–39.6	–78.4
Command Detector	5	–34.2	–70.6
Battery	21	22.72	4.32
Power System Electronics	14.5	3.18	–19.17
HPI (LEH)	7	–24.7	–57.01
HPI (HEH)/Horizon Sensor/Sun Sensor	5.9	–27.6	–68.95
HPI Electronics	12	–4.67	–30.11
IMU	10	–13.68	–41.59
Solar Array		10.97	–105.9

Table 12.—*66.5˚ ß thermal analysis results.*

Component	Power (W)	Temperatures (°C) Max.	Min.
PI/Electronics	21	15.3	10.77
Computer	10	–13.14	–20.7
Solid State Recorder	15	–3.68	–9.11
FUV Imager	25	26.07	22.13
Transponder/Amplifier	4	–54.97	–65.26
Command Detector	5	–48.65	–58.39
Battery	21	15.17	10.75
Power System Electronics	14.5	–5.45	–10.99
HPI (LEH)	7	–37.42	–45.89
HPI (HEH)/Horizon Sensor/Sun Sensor	5.9	–25.91	–36.47
HPI Electronics	12	–14.99	–21.27
IMU	10	–13.78	–21.96
Solar Array	–	51.7	–51.73

The results of the analysis show that the spacecraft computer, the transponder/amplifier, command detector, and the HPI will have temperatures that fall below the low temperature requirements during the umbra period. The transponder and the command detector will be below the minimum requirement even at their maximum temperature. Methods to increase these temperatures will be discussed later.

In this case the transponder/amplifier, command detector and the HPI LEH will need heat constantly, while the HPI HEH will need power during the coldest part of the orbit. The survival and operational heater power required for the cases analyzed are shown in table 13.

Table 13.—*Heater power requirements*.

		0° ß Heater Power (W)		66.5° ß Heater Power (W)	
Component	**Power (W)**	**–30 °C**	**–40 °C**	**–30 °C**	**–40 °C**
Plasmasphere Imager/Electronics	21				
Computer	10	2.5	0.5		
Solid State Recorder	15				
FUV Imager	25				
Transponder/Amplifier	4	8.5	6.5	5.75	3.75
Command Detector	5	7.5	5.5	4.75	2.75
Battery	21				
Power System Electronics	14.5				
HPI (LEH)	7	5.5	3.5	2.75	0.75
HPI (HEH)/Horizon Sensor/Sun Sensor	5.9	8	4.6	5.25	1.85
HPI Electronics	12		0.5		
IMU	10		2.5	0.5	
Total Heater Power		**35**	**21.1**	**18.5**	**9.1**

The results of the FUV Imager cooler analysis show that to meet the thermal requirements of the FUV, the radiator surface area needs to be about 0.07 m^2. This area would be required in addition to the surface area needed for thermal control of the other components.

Heaters

Heaters are utilized in the design of the TCS to maintain electronic equipment within acceptable temperature limits. Two basic requirements govern the implementation of heaters into the MI TCS design. First of all, the TCS shall maintain all spacecraft systems at a minimum “turn-on” temperature of –40 ˚C during all spacecraft modes where EPS power is available and, secondly, the TCS shall provide make-up heat for spacecraft systems unable to maintain satisfactory operating temperatures (typically >30 ˚C) when powered on. The first requirement is intended to protect electronic equipment from permanent damage during nonoperational periods or during the transition from a nonoperational state. Heaters that are utilized to meet the first requirement are classified as “survival” heaters. The second requirement is intended to ensure proper functioning of all operating electronic equipment. Heaters that are utilized to meet the second requirement are classified as “operational” heaters.

Four additional requirements exist that deal with the redundancy and functionality of the MI TCS heater design. First, all survival heaters shall be single-failure tolerant. The justification for this requirement is that the failure of a survival heater implies permanent damage to a spacecraft system or component. A similar requirement was not levied upon operational heaters, as the consequence of an operational heater failure is most likely some type of compromise in the operation of the spacecraft system, but not a permanent failure. Secondly, the TCS shall provide the capability to disable survival heaters as required. Since the survival heaters operate autonomously from the spacecraft equipment items that they protect, a means must exist to disable the survival heaters if a spacecraft equipment item has permanently failed. This will prevent unnecessary power draw upon the MI EPS. Thirdly, the TCS design shall minimize the heater power required just after system startup or reset. If the MI spacecraft is transitioned from a dormant to an active state, the TCS design must provide means to selectively provide heater power to priority systems to prevent an overload of the MI EPS. Finally, the TCS survival heater function shall be autonomous for critical spacecraft systems. This requirement implies that, aside from EPS power, no intervention or input is required from any other spacecraft system or the ground for the survival heaters to function. The survival heaters may be disabled, however, per the second requirement.

A typical spacecraft bus radiator panel is shown in figure 46. Redundant survival heaters are attached to the spacecraft EPS essentials bus. Relays are contained in each string that allow the heaters to be enabled/disabled through the spacecraft control system. The relays may have a default (power on) setting of either normally open (NO) or normally closed (NC) depending upon the criticality of the spacecraft components mounted on the panel. Each survival heater string contains a current sensor that provides an indication of the heater’s operating state. Thermostats are used to control the heaters and simply open or close the circuit depending upon the temperature sensed in the radiator panel..

Operational heaters are available to the spacecraft equipment items that require them. The operational heater circuits do not contain the status sensors and enable/disable relays that the survival heater circuits do since the operational heaters are connected to each individual electronic box power supply. As such, the operational heaters are enabled or disabled automatically when an equipment item is powered up. Each electronic box also contains a set of three redundant temperature sensors. A composite layout of the entire MI spacecraft TCS heater system design is provided in figure 47.

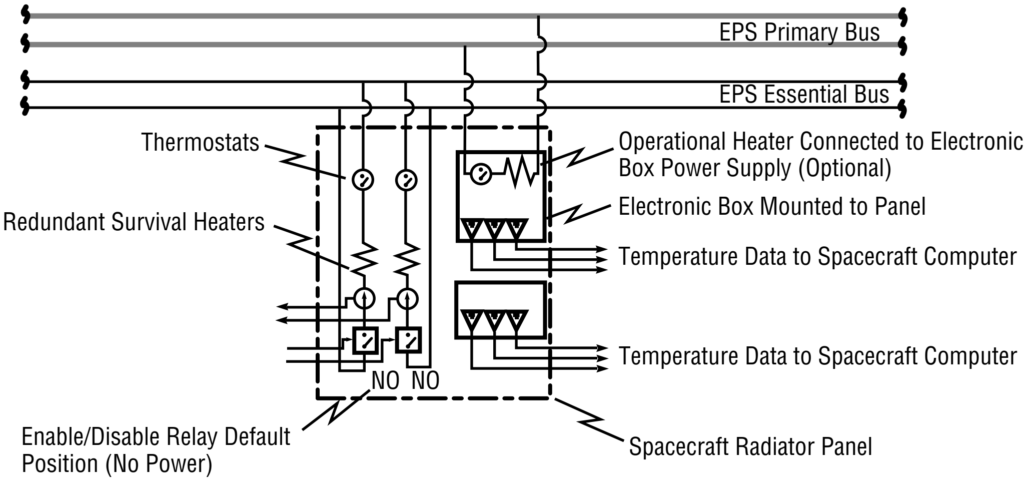
EPS Primary Bus
EPS Essential Bus
Thermostats
Redundant Survival Heaters
Operational Heater Connected to Electronic Box Power Supply (Optional)
Electronic Box Mounted to Panel
Temperature Data to Spacecraft Computer
Temperature Data to Spacecraft Computer
NO NO
Enable/Disable Relay Default Position (No Power)
Spacecraft Radiator Panel

FIGURE 46.—Typical spacecraft radiator panel.

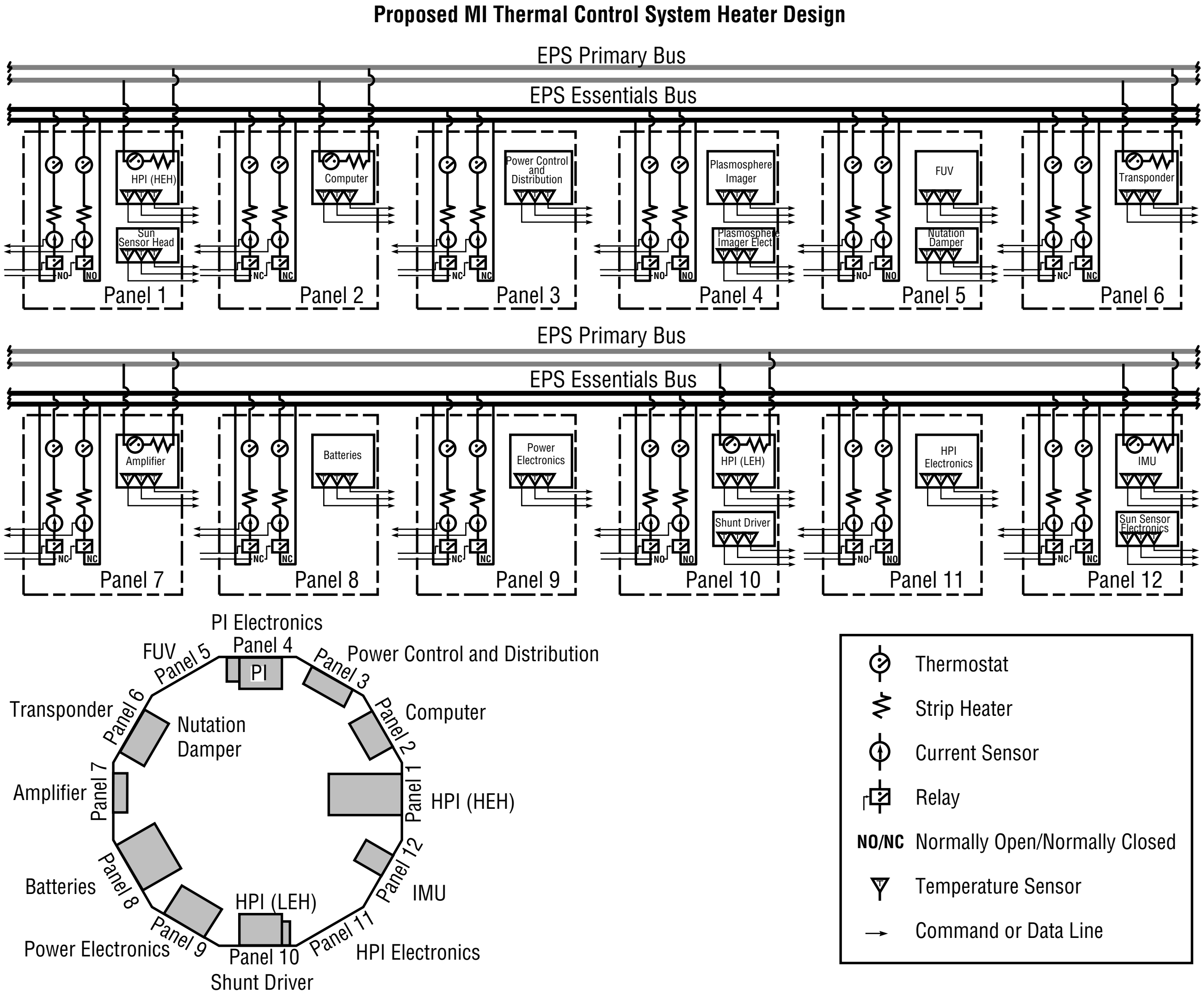
Proposed MI Thermal Control System Heater Design
EPS Primary Bus
EPS Essentials Bus
HPI (HEH)
Sun Sensor Head
Computer
Power Control and Distribution
Plasmosphere Imager
Plasmosphere Imager Elect
FUV
Nutation Damper
Transponder
NO NO NC NC NC NC NC NC NO NO NO NO NC NC
Panel 1
Panel 2
Panel 3
Panel 4
Panel 5
Panel 6
EPS Primary Bus
EPS Essentials Bus
Amplifier
Batteries
Power Electronics
HPI (LEH)
Shunt Driver
HPI Electronics
IMU
Sun Sensor Electronics
NC NC NC NC NC NC NO NO NO NO NC NC
Panel 7
Panel 8
Panel 9
Panel 10
Panel 11
Panel 12
PI Electronics
Panel 4
PI
FUV
Panel 5
Power Control and Distribution
Panel 3
Transponder
Panel 6
Nutation Damper
Computer
Panel 2
Amplifier
Panel 7
Panel 1
HPI (HEH)
Batteries
Panel 8
Panel 12
IMU
HPI (LEH)
Power Electronics
Panel 9
Panel 10
Panel 11
HPI Electronics
Shunt Driver
Thermostat
Strip Heater
Current Sensor
Relay
NO/NC Normally Open/Normally Closed
Temperature Sensor
Command or Data Line

FIGURE 47.—MI thermal control heater system design.

Testing and Verification

Two general approaches exist in the verification of spacecraft. In the first approach, a spacecraft and associated systems are typically verified through qualification and acceptance testing. Qualification proves that the design, manufacturing, and assembly process has resulted in a spacecraft that meets mission requirements. Qualification testing is performed on dedicated test articles separate from the flight unit and is intended to stress the articles beyond minimum and maximum predicted operating conditions. Acceptance testing ensures that the flight unit was manufactured as designed with no defects and performed at the minimum and maximum predicted operating conditions with no additional margin. In the second approach, a single protoflight hardware item is used in lieu of separate qualification and flight hardware items. This approach incorporates the use of reduced test levels and/or durations and posttest hardware refurbishment is performed as needed to allow tested hardware to be subsequently used for flight.

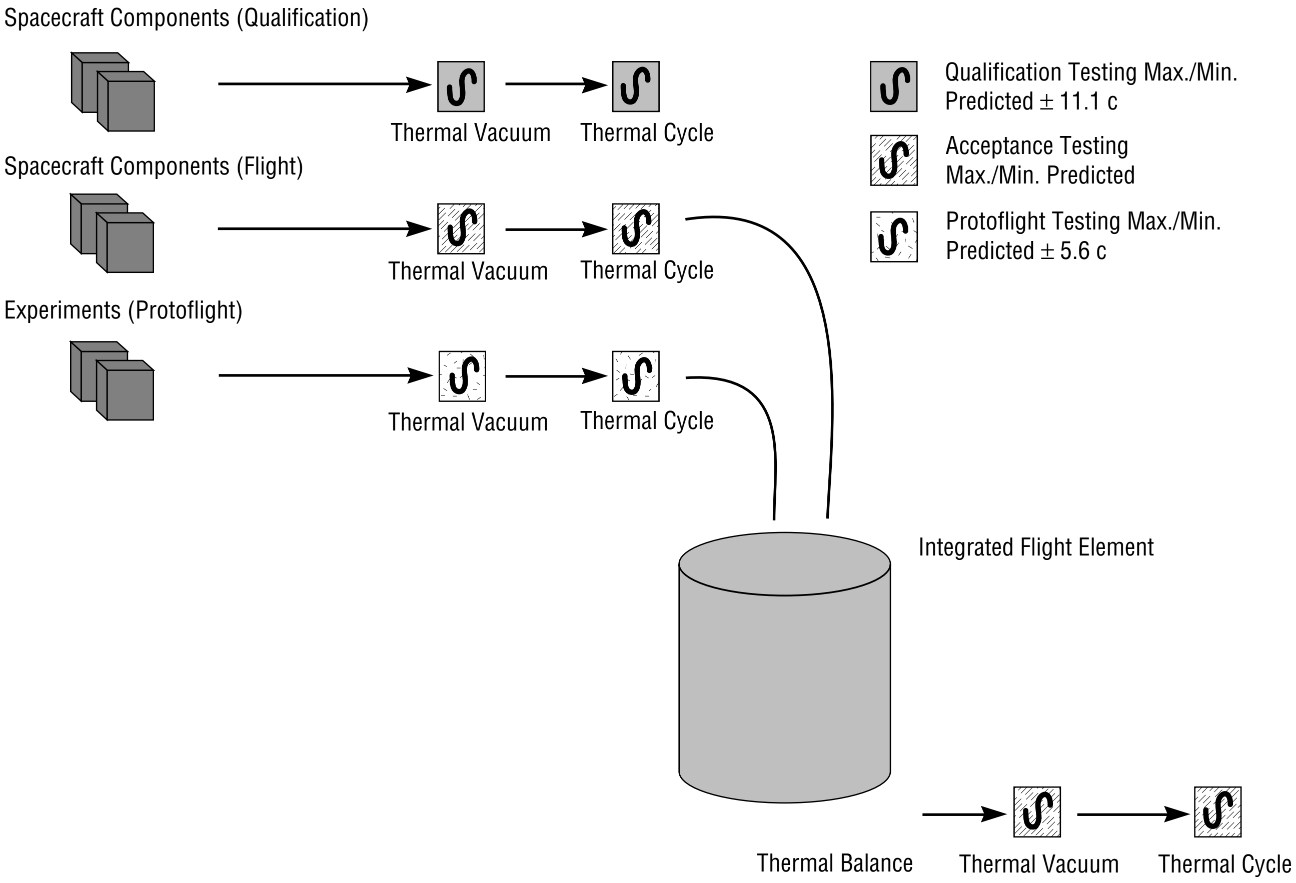
Spacecraft Components (Qualification)
Thermal Vacuum
Thermal Cycle
Spacecraft Components (Flight)
Thermal Vacuum
Thermal Cycle
Experiments (Protoflight)
Thermal Vacuum
Thermal Cycle
Qualification Testing Max./Min. Predicted ± 11.1 c
Acceptance Testing Max./Min. Predicted
Protoflight Testing Max./Min. Predicted ± 5.6 c
Integrated Flight Element
Thermal Balance
Thermal Vacuum
Thermal Cycle

FIGURE 48.—Thermal verification process.

Three different types of thermal vacuum tests are typically performed during the course of qualification/acceptance or protoflight testing. The basic thermal vacuum test is used to demonstrate the ability of a component, system, or integrated flight element to perform in its design environment. The test article is subjected to the predicted operating temperature extremes to identify design problems (qualification) or manufacturing defects (acceptance). The thermal cycling test is used to demonstrate the ability of a component, system, or integrated flight element to operate over the design temperature range. The test article is cycled between high and low temperature extremes to identify design problems (qualification) or manufacturing defects (acceptance). A third test, the thermal balance test, is used to verify analytical predictions for components, systems, or the integrated flight element.

The proposed thermal verification process for the MI is shown in figure 48. Non-experiment spacecraft components will undergo qualification and acceptance testing. Waivers may be granted for off-the-shelf components that have been qualified under equal or more stringent environments than predicted for the MI mission. The hybrid protoflight approach will be used for experiments to preclude constructing separate qualification and flight units. The qualified spacecraft components and the protoflight tested experiments will then be integrated into the spacecraft for thermal balance testing and final acceptance testing. Results from the thermal balance testing will be used to validate spacecraft-level thermal math models.

Recommendations

The temperatures of the some of the components are very low during parts of the MI mission. Heater power can be used to raise the temperature of these components. To avoid the overuse of heaters to meet the thermal requirements of the components, the radiator surface area can be reduced, which would raise the temperature of the components. Also the low power components could be moved off the radiator band and insulated such that their heat is retained. And, finally, the optical properties of the particular panels on the radiator band could be selected to specifically meet the requirement of the components mounted to that panel.

Other Issues

To minimize the amount of surface area taken from the EPS, the antenna needed to communicate with the MI spacecraft will be located on the surface designated for the radiator. Of concern with the use of this concept is the effect of the thermal properties of the antenna on the heat rejection capabilities of the radiator. The antenna would effectively become the thermal radiator and heat transfer through the band would therefore be important. The thermal properties and size of such an antenna were obtained from the manufacturer. The antenna is 0.062-inch thick and approximately 8-inches wide. It has a thermal conductivity of 0.25 Btu/hour-foot-˚F and is coated with Z–93. Preliminary calculations, assuming perfect contact between surfaces, show that the antenna would have only a minimal effect on the temperature of the radiating surface.

EPS

General Requirements

The EPS provides conditioned electrical power during all phases of operation. This is to include the launch and ascent phase, the separation and deployment phase, and the operational phase throughout the life of the spacecraft. A battery is provided to maintain the main load bus within specified tolerances during eclipse (occultation) periods and when peak loads exceed the instantaneous power capabilities of the solar array. An illustration depicting the primary components of the EPS is shown in figure 49.

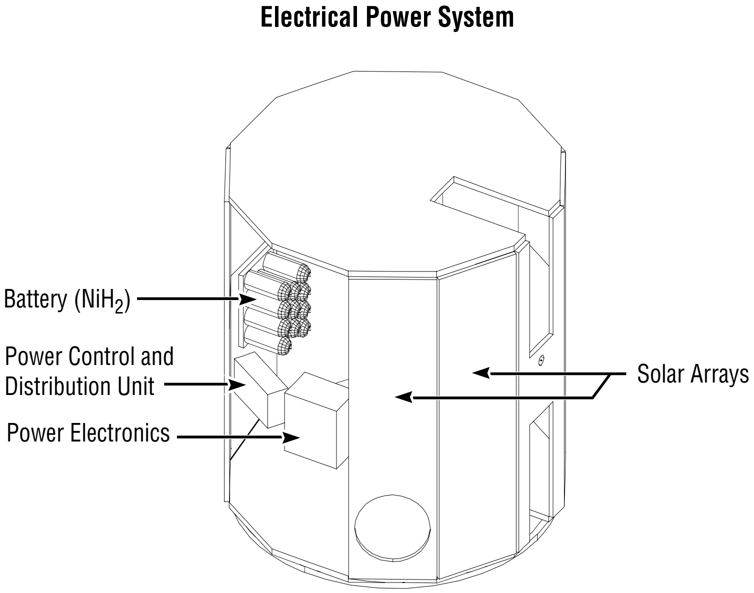

FIGURE 49.—Summary of the EPS.

Requirements

The EPS design satisfies the conditions listed in table 14.

TABLE 14.—*EPS design.*

- Operating voltage range from 22 to 34 Vdc
- Direct energy transfer system
- Provides 211 W orbital average power at EOL
- Single battery design
- Provides essential and nonessential busses
- Provides battery energy through the launch and ascent phases
- Provides shunt control of excessive power
- Mission life of 2 years
- Ground command response

EPS Overview

The EPS, as configured for the spacecraft and shown in figure 50, is a direct energy transfer system. The solar array system and battery are connected directly to the main bus. This bus is maintained at +28±6 Vdc at the input or interface to the power control and distribution unit. Further power distribution to the spacecraft subsystems and loads is provided by way of two additional busses: the essential bus and the nonessential bus.

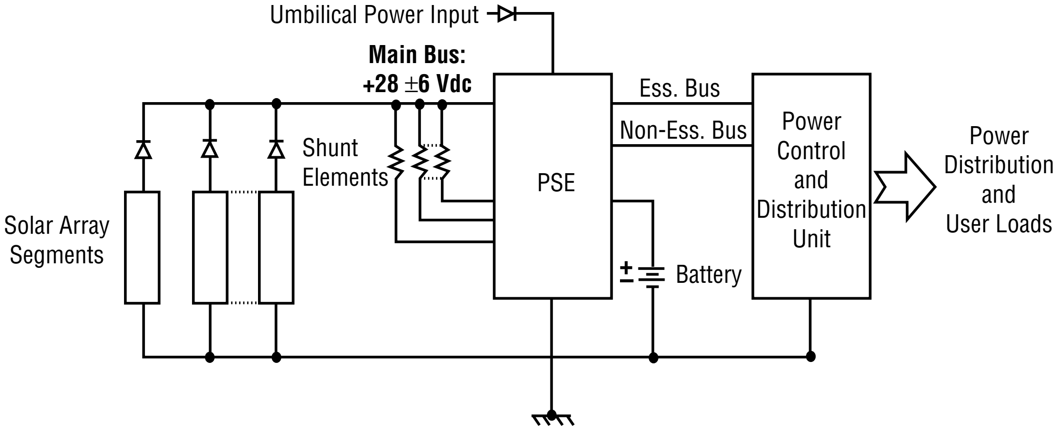

FIGURE 50.—EPS block design.

The spacecraft uses one advanced NiH_2 battery (12 amp-hours, 22 cells) to provide energy during eclipse periods or temporary overloads. The battery configuration consists of small diameter common pressure vessel (CPV) cells designed primarily for small spacecraft. Solar array panels are of a body-mounted configuration utilizing high efficiency, thin GaAs on germanium (Ge) substrate solar cells with 20 mil coverslides for radiation protection.

Solar Array

To maximize the power output, increase radiation resistance, and increase performance on a limited surface area spacecraft, the solar array uses GaAs/Ge solar cells. These body mounted cells populate the cylindrical body or sides, in addition to both ends. These single-junction cells have a BOL average efficient of 18.5 percent at 28 °C and air mass zero. The baseline cells measure 2- by 4-cm in area and have a thickness of 5.5 mils. A 20-mil-thick cerium oxide doped microsheet (CMX™) cover glass is used to provide protection against radiation, while maintaining the cover glass mass to a minimum.

The total surface area available for solar cells mounting is estimated to be 5.71 m^2. Of this area, 3.44 m^2 are available on the cylindrical (side) surface area and 1.13 m^2 on each of two ends.

This represents 35 percent and 15 percent surface loss respectively for apertures, openings, and other surface scarring. For simplicity, surface area scarring is assumed to be evenly distributed throughout the cylindrical and end areas.

Battery Module

The energy storage system is configured with one high performance NiH2 battery. This small diameter CPV battery assembly consist of 11 CPV’s. Each CPV contains dual or tandem battery cells per container and has a design capacity of 12 amp-hours. During the mission life (and battery life) of 2 years, the battery system encounters a maximum of five periods of occultation. A total of 345 charge/discharge cycles are experienced, with a worst case discharge time of 1.3 hours. Recharge time for this condition is 13.86 hours.

An alternative consideration for a battery module is the new 22-cell CPV battery of 15 amp-hour capacity that is very compact and has a specific energy density of 47.1 W-hours/kg. This CPV battery is 13 cm (5.1 inches) in diameter, 53.3 cm (21 inches) in length and was used on the recently launched *Clementine* spacecraft. Total mass of the battery assembly is 9.6 kg (21.2 pounds).

The battery provides power to the primary unregulated bus for distribution. This occurs during launch, eclipse periods, and during periods of peak power demands when needed to supplement the power generated by the solar array.

Power Supply Electronics (PSE)

The PSE are basically a single-string concept with design features that reduce catastrophic single-point failure. Some salient features are given in table 15.

TABLE 15—*PSE features.*

- Two battery charge modes
  - Amp-hour integration
  - Voltage/temperature limit control
- Provides selectable trickle charge levels
- Fuses and relays to isolate failure
- Function protection
  - Overvoltage
  - Undervoltage
  - Overcurrent
- Overcurrent load shedding
- Redundant sequential shunt controllers
- Ground command response
- Mil-Std-1773 optical bus interface for C&DH.

Internal to the PSE, the nonessential bus relay will disconnect nonessential loads as a result of overvoltage, undervoltage, and the safe-hold mode command.

Shunt Dissipator

To regulate the upper voltage excursions of the unregulated main bus, and also to remove excessive generated power, a full-shunt regulator is employed. This regulator consists of multiple resistive dissipative elements, externally mounted, that are sequentially controlled by shunt drivers located in the PSE. These are further controlled by either the bus overvoltage, battery voltage/temperature, or the battery current control loops. The dissipative resistive elements are connected in parallel across the bus and serve as a current sink for a source current greater than the load current demand of the regulated spacecraft system.

Power Control and Distribution Unit (PCDU)

The PCDU provides distribution of the main bus power to spacecraft systems and user loads via two separate busses. These are the essential bus and the non-essential bus. Electrical loads considered essential are the command receiver, survival heaters, C&DH system, and certain attitude control components. All other loads and systems are considered nonessential.

The PCDU also provides redundant fusing where appropriate, relay switching, current monitoring, autonomous command sequencing, and an interface to a Mil-Std-1773 bus. Regulated dc/dc converter power can also be provided.

Performance Analyses and Summary

Factors that limit the capability of a spin-stabilized spacecraft to generate electrical power are: physical size limitation, surface availability for cell mounting, surface scarring, and the radiation environment encountered during the mission. Inclusive in these factors are the requirements of the science payload and the mission scenario.

In determining the surface area of the spacecraft, a cylindrical shape was assumed. As defined, the spacecraft is a 1.3-m diameter cylinder. The maximum un-scarred surface area of the cylindrical section of the spacecraft is 5.30 m^2. Each end has a surface area of 1.32 m^2. Total surface area of the un-scarred spacecraft is 7.94 m^2.

To accommodate instrument payloads, antennas, handling fixtures, etc., the surface loss of the side or cylindrical section is estimated to be 35 percent. The end surface loss is estimated to be 15 percent. These surface losses are due to scarring and are assumed to be evenly distributed across the surfaces.

The total effective surface area of the MI spacecraft for all ß angles between the flight envelope of ±66.5° is shown in figure 51. As depicted, the total surface area is a summation of the effective cylindrical and end areas as a function of ß angle. The minimum total effective surface area, as seen by the Sun, occurs at 0 ß angle, that is, when the Sun vector is perpendicular to the spacecraft spin axis.

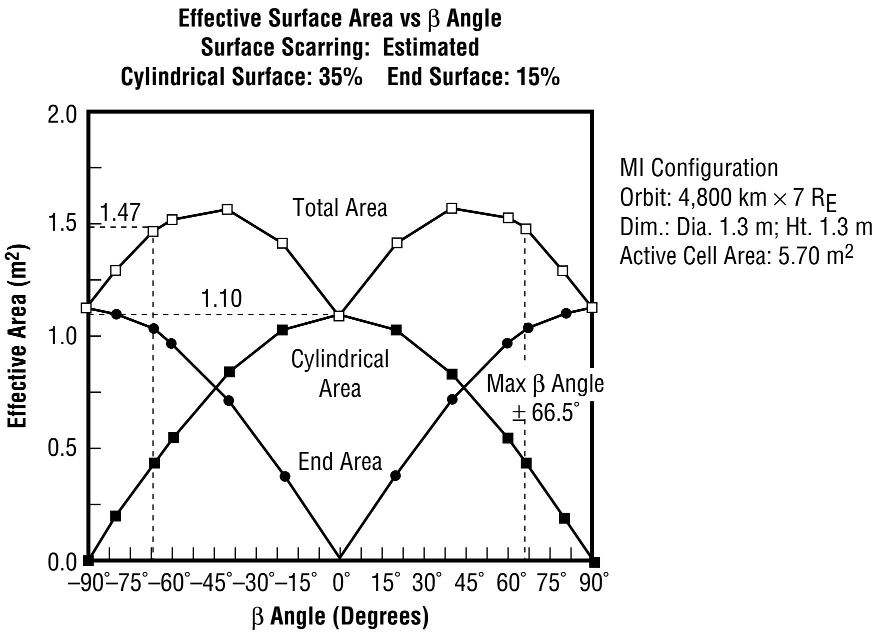

FIGURE 51.—Total effective spacecraft surface area.

Solar Array Performance Analysis

Since surface area availability is limited, and the radiation environment for the specified orbit is moderately severe, a high performance GaAs/Ge cell is recommended. The baseline technology is a thin, 18.5 percent efficient cell with an area of 2 by 4 cm. It is anticipated, however, that a cell of much larger area will be utilized.

Uncertainty factors, degradation, and array losses that were considered in the array sizing are given in table 16.

TABLE 16.—*Solar array performance analysis factors.*

• Installation and mismatch	0.985
• Measurement uncertainty	0.985
• Reliability	0.99
• Packing factor	0.82
• Cover darkening	0.992
• Adhesive darkening	0.98
• Thermal cycling	0.989
• Radiation	0.90 (20-mil CMX™)
• Temperature	1.00
• Micrometeoroid degradation	0.99
• Solar Intensity	0.967 (worst case)

The temperature profile of the solar array system is calculated from the average temperature of the side panels in conjunction with the temperature of the panels that are located at each end. Minimum average temperature of the rotational solar array system is at 0 ß. This is due to the lack of solar energy upon either of the end panels and also the rotational viewing of space to the sides. This orbital position is also the minimum power point of the orbit, and thus a point of interest.

Solar array degradation due to operating temperature was evaluated at the low power point or (at 0 ß angle). The projected average temperature of the panels that are producing power is approximately 0 °C. Using a temperature coefficient of –0.22percent/°C for the GaAs/Ge cells, a small power gain of 6 percent is realized. However, for this design phase, a factor of 1.00 was assured for operating temperature degradation.

From these factors, an EOL array power density of 160 W per m^2 is estimated. Figure 52 depicts the solar array power as a function of ß angle.

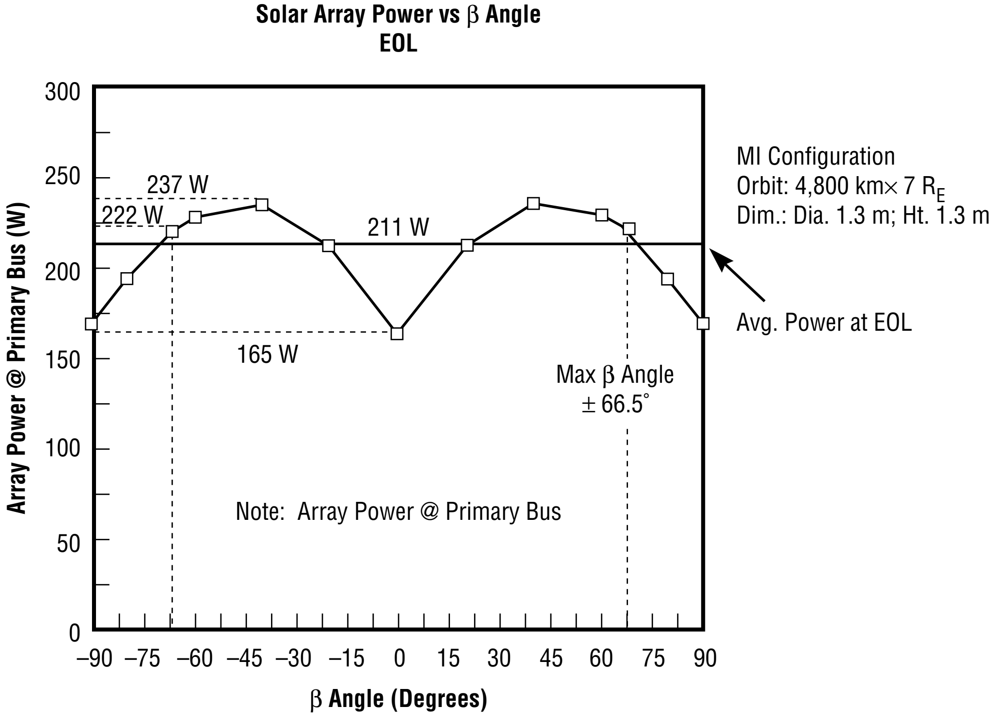

FIGURE 52.—Solar array power versus ß angle.

Radiation Degradation

The space environment contains electron and proton radiation that can damage and adversely affect the performance of the solar array. Irradiation of solar cells by protons and electrons can permanently reduce their energy conversion efficiency. This “damage” to the solar cells does not constitute mechanical damage, but rather a nearly permanent degradation of the cell’s energy conversion efficiency capability at the atomic level. The actual damage produced depends upon the type of radiation and its associated energy deposition. To determine the effect upon the solar cell, the number of particles of different types and their energy levels are multiplied by their associated damage coefficients. The sum of these values is then related to the actual irradiated solar cell data. The solar array damage equivalent totals are expressed in 1 MeV equivalents.

The radiation analysis was performed for coverslides with thicknesses of 6 mils, 12 mils, 20 mils, and 30 millionths of an inch. By increasing the thickness of the coverslides, increased protection of the solar cells can be provided from the detrimental effect of orbital radiation. The radiation degradation analysis indicates 43 percent degradation for a 6-mil coverslide, 20 percent for a 12-mil coverslide, 10 percent for a 20-mil coverslide, and 5 percent for a 30-mil coverslide. A need for a 20-mil coverslide thickness is recommended due to the moderately severe radiation environment of the orbit.

Load Characteristics

Table 17 gives the summation of the electrical power loads as defined for both the spacecraft subsystems and the payloads of the instrument suite. This power summation also includes a 25 percent power contingency.

Table 17.—*Electrical power loads summary.*

• **Subsystem Electrical Power Requirements**	
– C&DH (Transponder at 7 percent duty cycle)	32.0 W
– ACS	13.9 W
– TCS	14.0 W
– EPS	14.5 W
Subtotal	**74.4 W (orbital avg.)**
• **Total Electrical Power Loads**	
– Instrument suite (5 instruments) (Power conditioning included)	69.0 W
– Spacecraft subsystems	74.4 W
– Contingency (25 percent)	35.9 W
Total	**179.3 W (orbital avg.)**

Table 18 depicts the mass characteristics of the EPS. This 45-kg total represents approximately 15 percent of the total spacecraft dry mass, including cabling and harnesses.

Table 18.—*EPS mass statement.*

• **Surface area available (assumed)**		**5.70 m^2**
– Cylindrical surface: 65 percent	3.44 m^2	
– End surfaces (two): 85 percent	2.26 m^2	
• **EPS mass:**		
– Solar arrays: (103.2 gm/ft^2; 5-mil GaAs)		6.33 kg
– Electronics:		10.6 kg
• Power supply electronics:	7.5 kg	
• Power control and distribution unit	3.0 kg	
• Shunts (dissipators):	0.1 kg	
– Battery:		11.4 kg
– Cabling/harnesses:		16.7 kg
• Harness, electrical	16.2 kg	
• Umbilical	0.5 kg	
Total		**45.03 kg**

Battery Performance

In the elliptical orbit that has been defined for the 2-year mission, only four periods of occultation will occur. The worst case eclipse, or longest time in penumbra, is 1.3 hours in a 15.16-hour period. From this orbit profile, the total number of battery charge/discharge cycles is 345. As configured, the energy storage system provided during this time is a single NiH2 battery. The battery assembly is configured with CPV cells connected in series. This small 2.5-inch diameter CPV design has two electrode stacks connected in series and has a capacity of 12 amp-hours.

For an orbital average load (see table 14) of 179.3 W (payload=69 W) at the input of the PCDU interface, the battery “date of death” for the worst case eclipse condition is 71.4 percent. This increase in battery energy requirements defines a discharge “C” rate of 0.55C (C/1.8). The energy required at the solar array for battery recharge is approximately 315 W-hours. To meet the power requirements of 179.3 W for continuous spacecraft loads and battery recharge, 206 W at the solar array is required. From the EOL power profile as shown in figure 57, the spacecraft cannot meet the power demands of 206 W at low ß angles. This will dictate load shedding or power management between the ß angles of ±15°.

As a battery technology upgrade, a CPV battery similar to that used on *Clementine* could be adapted. This NiH2 battery assembly has high specific energy, contains 22 cells, and has a rated capacity of 15 amp-hours.

There are no design margins included in this analysis, and the EPS design is basically a single-string concept.

C&DH

Data Rate Considerations

The three science instruments will produce a data rate of 40 kbps, as shown in table 19. Typically, an overhead of 10 to 15 percent is added to accommodate diagnostic and engineering data; in this case 5 kbps is added for a total data rate of 45 kbps. This rate projected over the 15.16 hour orbit gives a total data per orbit figure of 2.456 GB (10E9). Since no real-time data other than emergency or diagnostic are anticipated for MI, the requirement for data storage for one orbit is approximately 2.5 GB. Ground contact studies show that sufficient time will be available in each orbit to downlink data to the ground station.

TABLE 19.—*Science instrument data rate requirements*.

Instrument	Mass (kg)	Power (W)	Data Rate (kbps)
HPI	29.0	23.0	18
PI	19.0	21.0	7
FUV Imager	30.0	25.0	15
Engineering Data			5
Total			**45**

An illustration depicting the primary components of the C&DH subsystem is shown in figure 53.

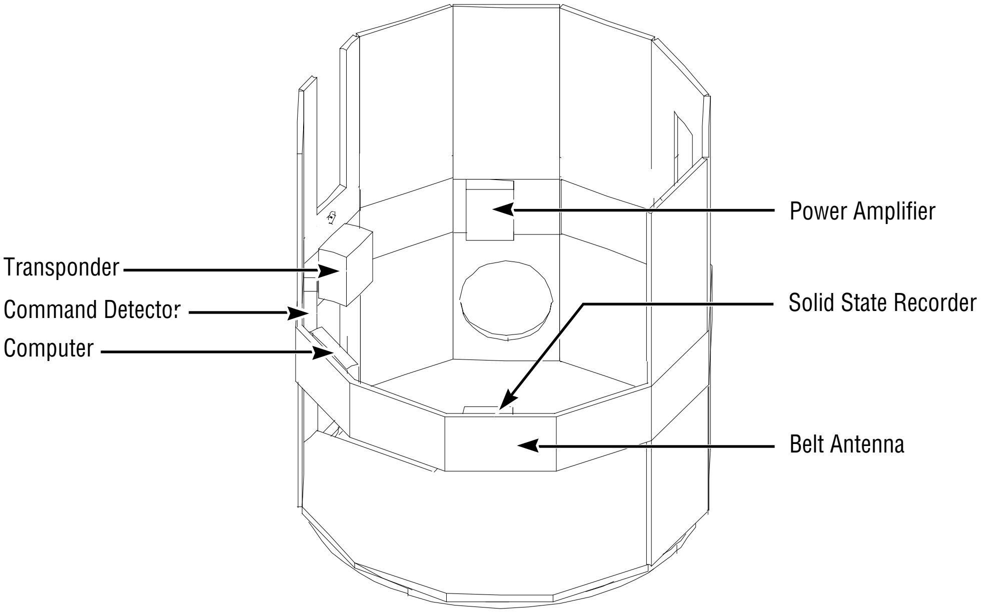

FIGURE 53.—MI C&DH subsystem.

DSN

The NASA DSN is recommended as the ground system to communicate with and receive the MI data. The DSN is a worldwide system for navigating, tracking, and communicating with spacecraft exploring the solar system. The Jet Propulsion Laboratory (JPL) manages the network of antennas that is the link to distant spacecraft, transmitting instructions to them and receiving the data they return to Earth from deep space. The DSN uses large antennas, low-noise receivers, and high-power transmitters at locations on three continents.

The DSN includes 12 deep-space antennas in a global network. The three DSN complexes are located at Goldstone in California's Mojave Desert; near Madrid, Spain; and near Canberra, Australia. The three locations are approximately 120° apart in longitude so that as the Earth turns on its axis, a distant spacecraft is almost always in view of one of the stations. JPL also operates a control center and a ground communications facility to control and monitor the complexes and link them together. Each complex is equipped with one 70-m, one 26-m, and two 34-m diameter antennas. The 26-m S-band network is anticipated for use with the MI spacecraft.

Commands

Commands needed to control the MI spacecraft and instruments will be generated in the MI Payload Operations Control Center (POCC) and forwarded to the DSN Ground Communications Facility via NASCOM. This traffic is sent via land lines, submarine cables, terrestrial microwave, and communications satellites. Data sent over these lines are automatically checked for transmission errors and outages by NASCOM error detecting and correcting techniques. Commands are then sent from the DSN control center to one of the DSN stations where they are loaded into a command processing computer, automatically verified for accuracy, and transmitted to the MI spacecraft. The command receiver and decoder on the spacecraft verifies the command and either sends it for execution immediately or stores it with a GMT time-tag for later execution. If immediate verification that the command has been executed is required, this can be done by a low-rate real-time transmission for the spacecraft back through DSN. If no immediate verification is required, the acknowledgment will be stored in the main memory and downlinked with the next scheduled transmission. The command data rate for MI is estimated to be 2 kbps.

Instrument and Spacecraft Computers

Various schemes for computer control of the spacecraft and instruments have been examined, with two major options emerging as viable. Option 1 is the distributed control option, with each instrument having its own independent controller/computer that acts as the interface between it and the main spacecraft computer. Option 2 would use a centralized instrument computer to which each of the instruments would interface. The latter would save weight, cost, and complexity, and if properly designed, the instrument computer could be used as a backup for the main spacecraft computer. The disadvantages are increased complexity in software and the necessity for significant coordination among instrument designers. For the purposes of this study, option 1 has been baselined, that is, using one main spacecraft computer and an internal computer for each instrument. This approach is recommended because it simplifies the software and gives the instrument developers, who may be widely separated geographically, independence in developing their instruments. No one central computer is specified due to the lack of definition of the instrument requirements, but several off-the-shelf spacecraft computers appear to be good candidates. In addition, the option of a card-cage type processor, with modular design and using only the needed card functions, is being considered. This option also offers the possibility of having the spacecraft main memory on cards as part of the main computer, requiring one less major component.

Solid State Recorder

As previously discussed, the mass memory required to store one orbit of data is 1.5 GB. This assumes that the recorder will be dumped to the ground station each orbit and provides no extra memory for overruns. Several companies were surveyed that have either flown solid state recorders (SSR) in space or have a funded contract to design and fabricate flight units. Due to the stringent constraints on weight, cost, and power, the recorder made by SEAKR of Torrance, CA, is baselined. This recorder was used on the *Clementine* spacecraft and has a 2.0 GB capacity. This capacity will be increased to a minimum of 2.5 GB for MI. The *Clementine* recorder has the characteristics presented in table 20.

TABLE 20.—*Clementine recorder characteristics*.

Weight:	3.77 kg
Size:	15 by 13 by 8 cm
Capacity:	2 GB
Power:	5 to 11 W (mode dependent)
Bit Error Rate:	1E–10
Maximum Data Rate:	25 Mbps
Reliability:	0.98 (1 year)
Recurring Cost:	$500–700k

Transponder

The MI RF communications transponder will consist of two separate physical units—the DSN compatible S-Band transponder and an RF power amplifier unit with the characteristics shown in table 21.

TABLE 21.—*DSN compatible transponder and amplifier characteristics*.

	RF Out	Mass (kg)	Size	Direct Current In
Transponder	100 MW	3.4	16.1×18.6×10.2	7 W
RF Amplifier	10 W	2.0	19.1×16.6×5.40	50 W

The power amplifier is capable of operating in two different RF output power modes. In the low-power mode, the output is a nominal 3.1 W with a 2.82 W minimum. The high-power mode furnishes 11.2 W nominal with a minimum of 10.0 W. The low-power mode will make it possible to send back a low-rate data stream for diagnostic or investigative purposes while reserving the high-power mode for a full recorder dump.

Antennas

The fact that MI is a spinning spacecraft dictates some sort of omnidirectional antenna. Several types of omni antennas were investigated before selecting a “belt” type, basically for its antenna pattern. Because belt antennas are characteristically narrow-band devices, two are required for MI: one for uplink and one for downlink. These antennas will be located around the center of the spacecraft (fig. 54). Physically, the antenna is a microstrip device: copper Durite™ traces (finished with a tin deposition technique) on a Teflon™-fiberglass substrate similar to a printed circuit board but only 4-mm thick. Each antenna assembly is approximately 10-cm (4-inches) wide and both antennas can be placed immediately adjacent to each other, for a total width of 20.4 cm (8 inches). The antennas will be assembled in 4 quarter-circle sections and soldered together, or will consist of 12 flat sections, one for each faceted side of the spacecraft, electrically phased to provide a circular wavefront so that access can be gained to the interior of the spacecraft through the side panels. The total weight of the antenna, combiners, and cables is approximately 3.7 kg.

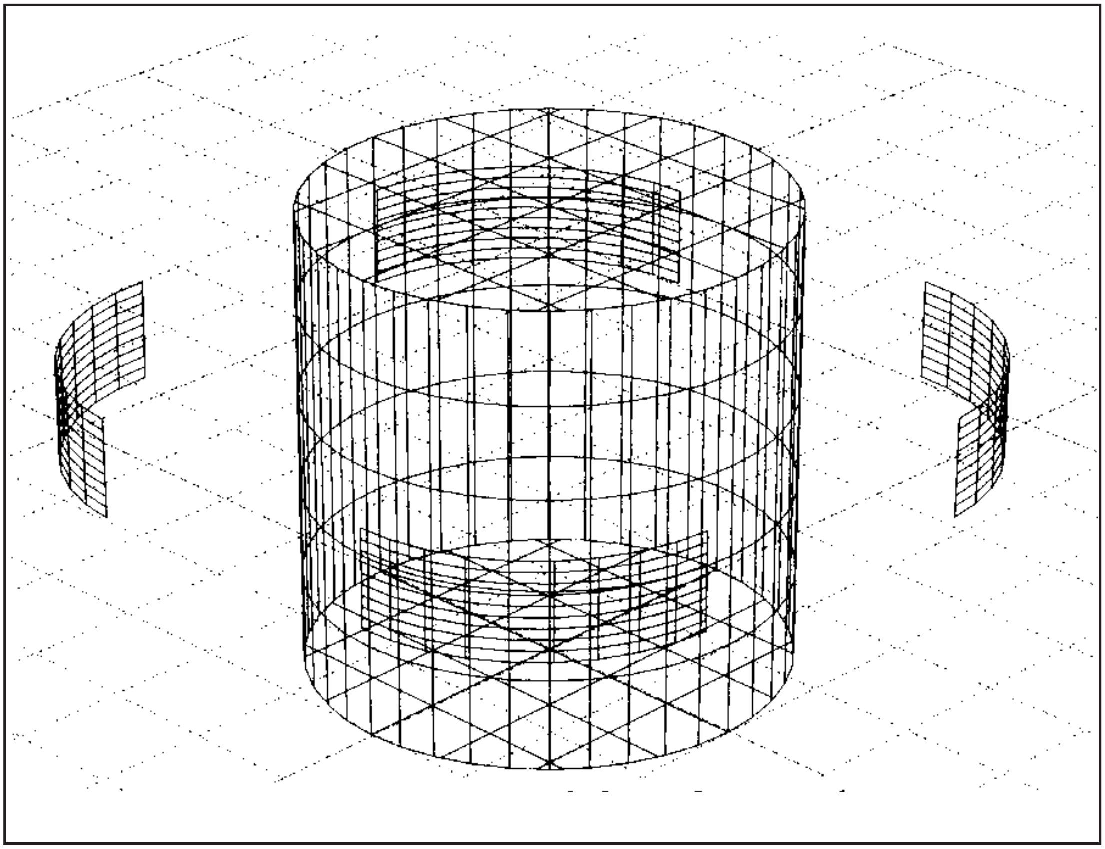

Figure 54.—Antenna system.

The belt antenna was chosen also because of the attitude profile of the spinning spacecraft. The antenna pattern is toroidal (fig. 55) with the on-axis gain being approximately 3 dB.

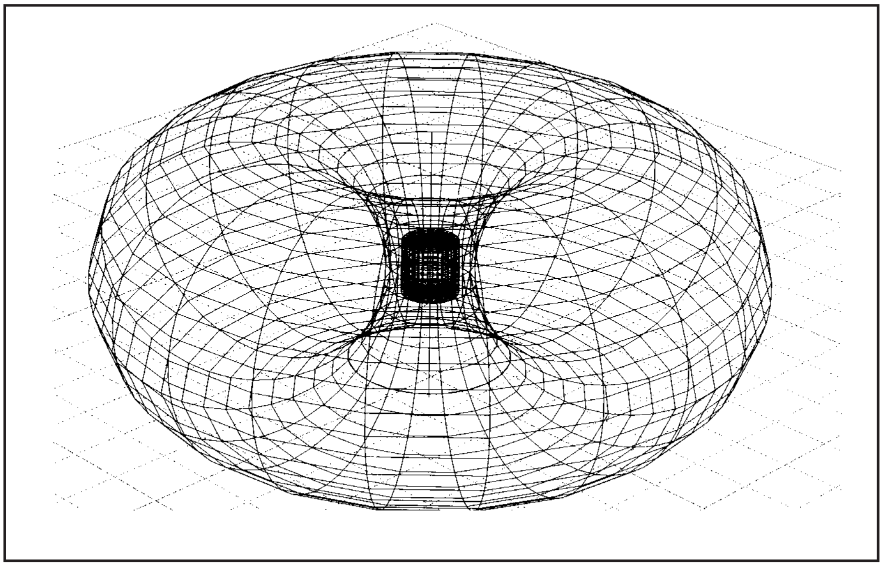

FIGURE 55.—Antenna pattern.

The gain decreases as it is measured away from the main axis, as shown in table 22.

TABLE 22.—*Antenna gain predicted and typical coverage.*

Antenna Gain	Predicted Coverage	Typical Coverage
–6 dB isotropic (dBi)	88 percent of sphere	90 percent of sphere
–8 dBi	93 percent of sphere	95 percent of sphere
–12 dBi	98 percent of sphere	99.8 percent of sphere

Link Analysis

In an effort to determine the capabilities of MI to transmit a full data stream to a ground station at any point in the orbit, several detailed link analyses were performed. Figure 56 shows the RF link from apogee with a downlink rate of 1.5 Mbps. The analyses indicate a required power of 17.14 W to transmit the data from this distance with a +3 dB link margin. Since the highest power output of the power amplifier is 10 W, it is obvious that a full data dump from apogee is not possible while maintaining a +3 dB margin. Extrapolation indicates that the maximum data rate from apogee while keeping the link margin is about 875 kbps. Conversely, the full 1.5 Mbps data rate can be achieved from distances 5 R_E and below. If a full data dump from apogee is a firm requirement, it can be accomplished in 48 minutes at the 875 kbps rate, in contrast to the 27 minutes required at a 1.5 Mbps rate. Since the DSN contact study shows contact times of up to 4 hours each orbit, this longer downlink time should not be a problem. However, obtaining use of the DSN on a longer period of time may not be possible.

As discussed earlier, the power amplifier has a low power mode that would permit a lower data rate stream to be transmitted as a diagnostic or exploratory type mode. This 3.0 W output would support a 250 kbps data rate from any point in the orbit and could provide real-time data for extended periods, if necessary.

MI S-Band Return Link

The MI spacecraft S-band return link margins are given in figure 56.

MI S-Band Return Link

DSN 25-Meter S-Band

		Comments
Vehicle Transmission Power (dBW)	10	
Frequency in MHz	2250	S–Band
Vehicle Antenna Dia. (m)	0	
Antenna Gain (dB)	–6.00	
Vehicle Circuit Loss (dB)	4	
Vehicle EIRP	0.00	
Distance in km	50072	
Space Loss (dB)	193.48	Calculated
Polarization Loss	0.2	
Antenna Pointing Loss	0	
Receiving Antenna Dia. (m)	26	
Receiving Antenna Gain	52.2	
Ps @ Receiving Antenna: Ps (dBW)	–141.48	
Boltzman's Construction (K)	–228.6	
System Temperature: Ts (deg. K)	80	
System Noise: KTs (dB/Hz)	–209.5691001	
Ps/KTs (dB/Hz)	68.09	
Transponder Loss	0	
RFI Degradation Loss	0	
Demod. Loss	0.3	
Antenna Beam Form Loss	0	For MA
PN Loss	0	For Pseudo Noise
Required (Eb/No)	9.9	
Encoding Gain	5.20	
Data Rate in kbps	1500	
Data Rate (dB)	61.76091259	
Additional Required PGP (dB)	–1.33	
Equivalent Additional Power (W)	–2.642400239	
Deltas for 10° Elevation & 90% Weather		
Path Loss (dB)	0.156	
Increase in Ts (deg. K)	10.1	
Antenna Gain Decrease (dB)	0	
Margin (dB)	3	
Required Delta PGP (dBW)	2.339709633	
Equivalent Additional Power (W)	7.138427172	
Total Required Power (W)	17.13842717	

FIGURE 56.—Link margins.

Equipment List and Block Diagram

A detailed equipment list for the C&DH subsystem was prepared for the purpose of providing estimates of power, weight, volume, and cost (see table 23). This list is not intended as a final determination of the exact items needed, but as an attempt to quantify power and weight numbers so that other subsystems can be designed. A preliminary block diagram is also included for reference in figure 57.

TABLE 23.—*C&DH equipment list.*

Component	Weight (kg)	Power (W)	Size (cm)
Transponder	3.41	3	16×18×10
Command Detector	1.20	5	15×8×4
Power Amplifier	2.00	41	19×15×5
Central Processor	3.00	10	23×18×4
Solid State Recorder	3.77	9	15×13×8
Belt Antenna	3.64	—	20×0.38
Structure and Cables	4.00	—	TBD
Totals	**21.00**	**68**	

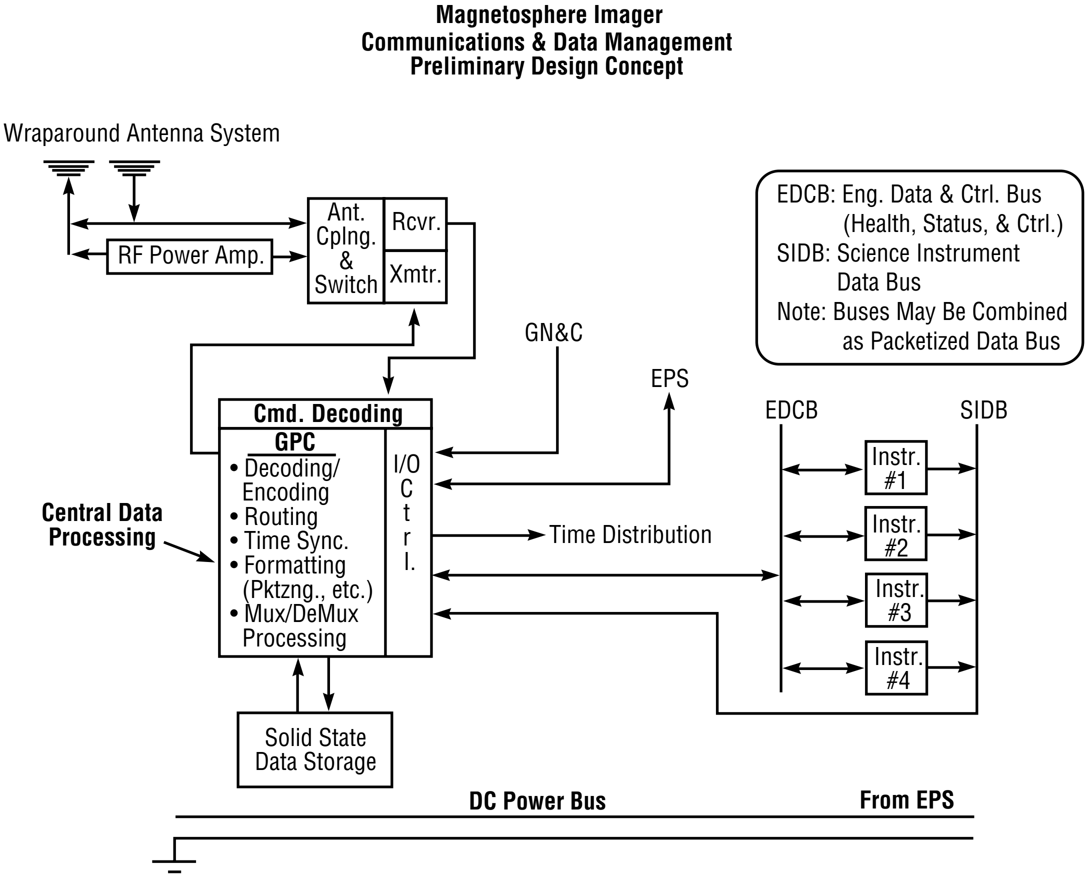
Magnetosphere Imager
Communications & Data Management
Preliminary Design Concept
Wraparound Antenna System
RF Power Amp.
Ant. Cplng. & Switch
Rcvr.
Xmtr.
GN&C
EPS
EDCB: Eng. Data & Ctrl. Bus (Health, Status, & Ctrl.)
SIDB: Science Instrument Data Bus
Note: Buses May Be Combined as Packetized Data Bus
EDCB
SIDB
Cmd. Decoding
GPC
• Decoding/ Encoding
• Routing
• Time Sync.
• Formatting (Pktzng., etc.)
• Mux/DeMux Processing
I/O Ctrl.
Central Data Processing
Time Distribution
Instr. #1
Instr. #2
Instr. #3
Instr. #4
Solid State Data Storage
DC Power Bus
From EPS

FIGURE 57.—C&DH block diagram.

Radiation Tolerance

Since the spacecraft will be periodically passing through various radiation belts, the radiation environment is of concern to all subsystems where electronic equipment is involved. A detailed analysis of the radiation environment for MI was prepared (see appendix C) and it indicates that varying degrees of radiation protection are required for the electronic equipment. Since the C&DH equipment is placed about the interior of the spacecraft structure, the solar arrays and the solar array covers, it has not been determined at this time exactly how much radiation each particular piece of equipment will have to withstand. Typical radiation tolerance numbers for avionics equipment run from 50 to 200 krd total dose. Manufacturers have indicated that these numbers can be increased by different packaging and selective shielding on critical components.

ACAD Requirements

The three science instruments are the HPI with its two high energy heads and one low energy head, the PI, and the FUV Imager. The location of these instruments in the spacecraft is shown in figure 58. Body-mounted solar panels for electrical power, not shown in the figure, are located all around the spacecraft. For these science instruments to obtain useful science data, the spacecraft must spin about a

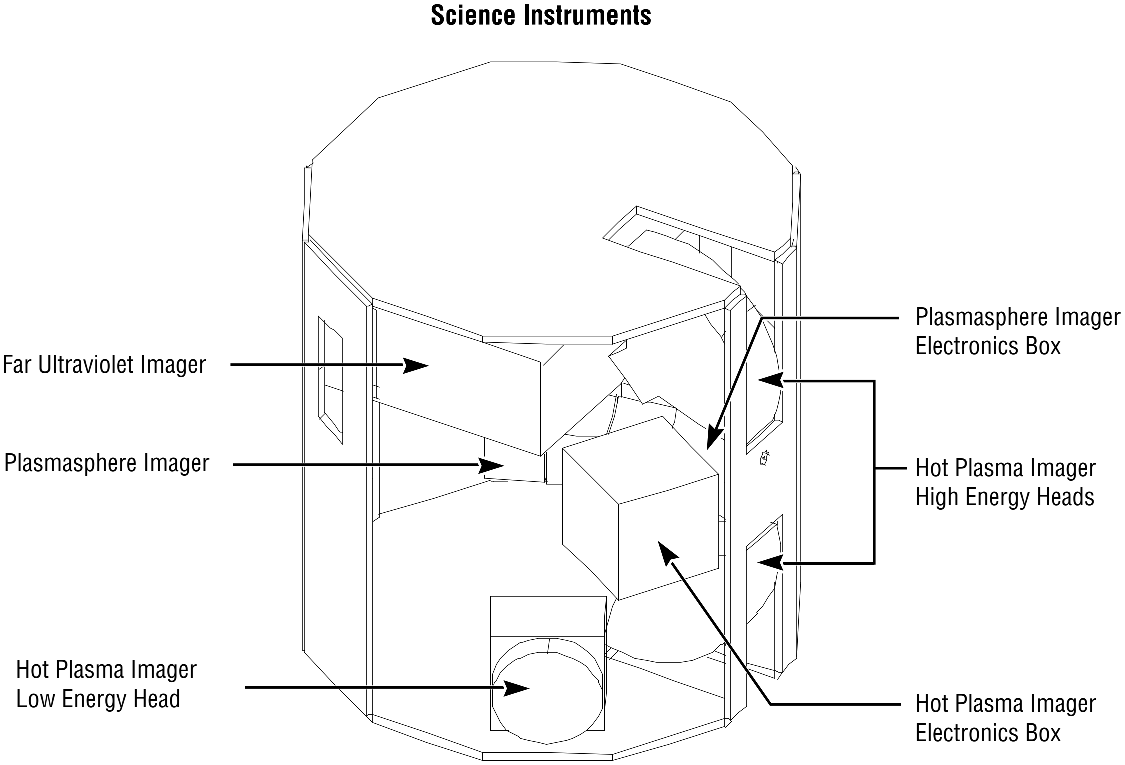
Science Instruments
Far Ultraviolet Imager
Plasmasphere Imager
Hot Plasma Imager Low Energy Head
Plasmasphere Imager Electronics Box
Hot Plasma Imager High Energy Heads
Hot Plasma Imager Electronics Box

FIGURE 58.—Location of science instruments.

body-fixed axis that is within 0.025° of the spacecraft's geometric centerline, at a spin rate in the range of 10 ±5 rpm, and the spin axis must be kept closely aligned with the orbit normal. How close depends on the science instrument, as shown in table 24. Other science instrument ACAD characteristics and requirements are shown in this table. From these and the other science instrument requirements identified, the MI ACAD system-derived requirements were established; these are shown in figure 59.

TABLE 24.—*Science instrument ACAD requirements*.

Science Instrument	**Field of View**	**Required Accuracy Orienting Spin Axis wrt Orbit Normal**	**Allowable Spin Axis Drift Over Any 60-Sec Period**	**Required Knowledge SI Attitude On Ground**
HPI	4 π str	5°	0.5°	0.5°
PI	135° ×180°	1°	0.5°	0.5°
FUV Imager	40° ×360°	1°	0.025°	0.025°

- Spin Spacecraft at 10 ± 5 rpm
- Keep Spin Axis:
  - Within 1˚ of Orbit Normal
  - Drift < 0.025˚ Over Any 60-Sec Period
- Keep Axis of Maximum Principal Moment of Inertia < 0.025˚ of Spacecraft Centerline
- Reconstruct Science Instrument Attitudes on Ground to:
  - < 0.5˚ for Hot Plasma Imager & Plasmasphere Imager
  - < 0.025˚ for FUV Imager

FIGURE 59.—ACAD system-derived requirements.

ACAD System Conceptual Design

The derived ACAD requirements in figure 59 and the requirement to make MI a “smaller-cheaper-faster” spacecraft drives the MI to be spin stabilized with an ACAD system that is simple and highly passive. A hardware block diagram for the proposed ACAD system is shown in figure 60. A component equipment list is given in table 25. A functional mounting arrangement for these components is shown in figure 61. Of course, variations to this are possible. A detailed description of this system, how it satisfies the requirements in figure 59, and its underlying design philosophy are given below. Refer to figures 60 and 61 and table 25 in this description. (For a more detailed discussion, refer to NASA Technical Paper 3560.)

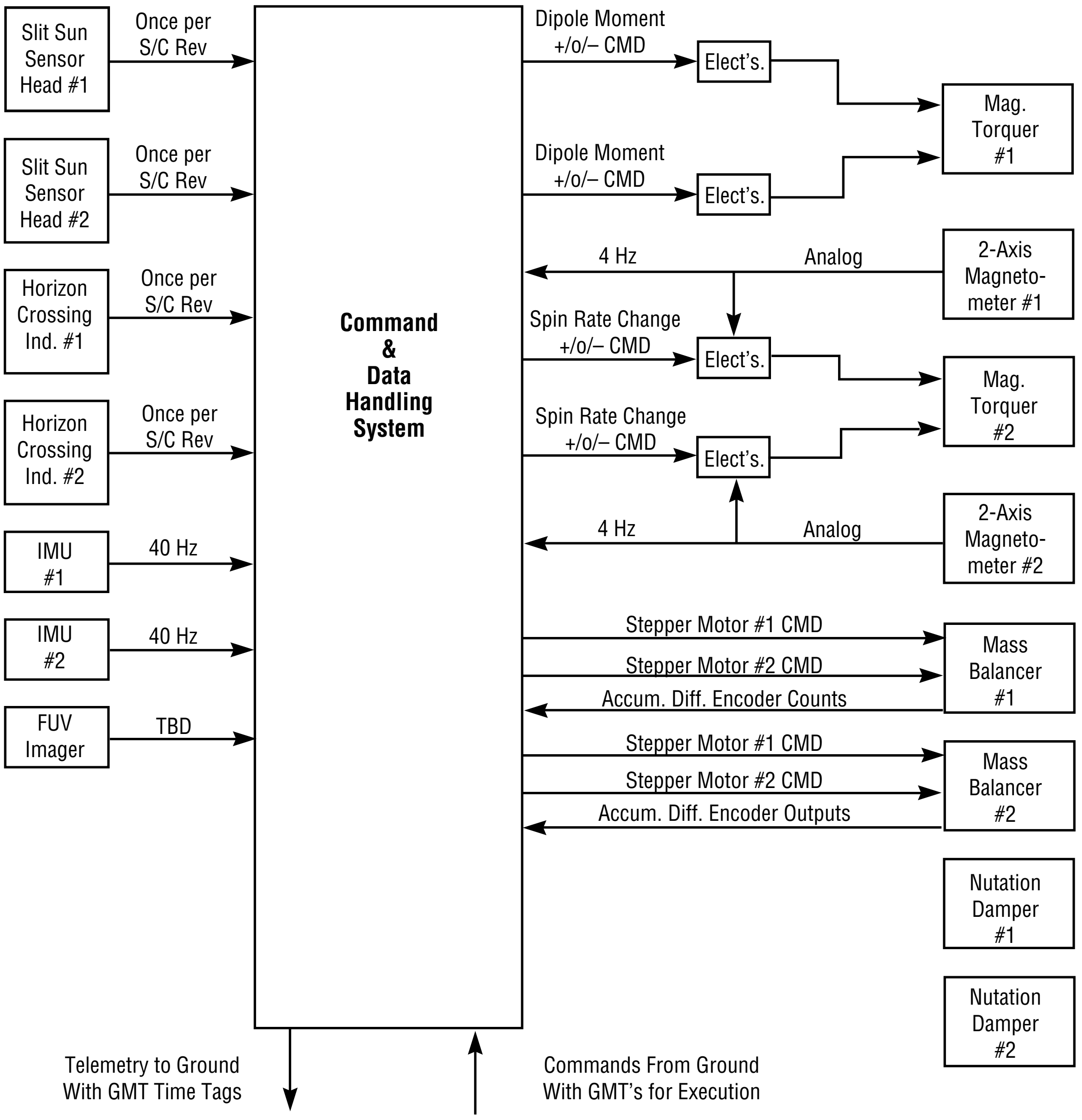
Slit Sun Sensor Head #1
Once per S/C Rev
Slit Sun Sensor Head #2
Once per S/C Rev
Horizon Crossing Ind. #1
Once per S/C Rev
Horizon Crossing Ind. #2
Once per S/C Rev
IMU #1
40 Hz
IMU #2
40 Hz
FUV Imager
TBD
Command & Data Handling System
Dipole Moment +/o/– CMD
Elect’s.
Mag. Torquer #1
Dipole Moment +/o/– CMD
Elect’s.
4 Hz
Analog
2-Axis Magneto-meter #1
Spin Rate Change +/o/– CMD
Elect’s.
Mag. Torquer #2
Spin Rate Change +/o/– CMD
Elect’s.
4 Hz
Analog
2-Axis Magneto-meter #2
Stepper Motor #1 CMD
Stepper Motor #2 CMD
Accum. Diff. Encoder Counts
Mass Balancer #1
Stepper Motor #1 CMD
Stepper Motor #2 CMD
Accum. Diff. Encoder Outputs
Mass Balancer #2
Nutation Damper #1
Nutation Damper #2
Telemetry to Ground With GMT Time Tags
Commands From Ground With GMT’s for Execution

FIGURE 60.—ACAD system hardware block diagram.

Table 25.—*ACAD system equipment list.*

Component	Vendor & Model #	# Units on S/C	Range	Accuracy	Size	Mass	Power	Design Status
Digital Sun sensor for spinning spacecraft	Adcole 18810	1 assembly with 2 heads	±64° linear FOV per head	LSC = 0.25°	6.6×3.3×2.5 cm per head & 10.4×5.8×9.4 cm for electronics	0.95 kg for complete assembly	0.4 W for complete assembly	Flight proven
Horizon crossing indicator	Barnes 3–210B	2	±5.7° lin. FOV per unit at apogee, ±24° at perigee	0.1° (3 sigma)	7.7×10.5×20.2 cm per	0.74 kg per unit	1.5 W for one unit	Flight proven
IMU	Litton LN–200	2	±1,000°/sec for rate & ±40 g for acc	Scale factor error = 50 PPM for rate & 300 PPM for accurracy	Each IMU is 8.9 cm dia. & 7.9 cm high	0.72 kg per IMU	10 W avg. for one IMU	Flown on *Clementine*
Two-axis magnetometer	Ithaco IM–102	2	±0.6 gauss	Noise=0.05 milligauss (rms)	11.4×5.8×2.5 cm per sensor	0.22 kg per sensor	0.04 W for one sensor	Off the shelf
Magnetic torquer	Ithaco TR230UPR	2 with redundant windings	Command ±200 a-m^2 or 0 a-m^2	±10% of command	Each torquer is 3.0 cm dia. & 91.4 cm long	4.4 kg per torquer	3.8 W per torquer when on & <1 W avg	Off the shelf
Nutation damper	URENCO	2	Reduces spin axis wobble from 1° to 0.025° in 1.2 hr		Each damper is 47×24×12 cm	0.54 kg per damper	None	Flown on ESA's COS–B S/C in 1975
Mass balancer	Build in house	2	Each unit has a 1 kg mass that can move ±0.5 m	Min change in mass position is ±2 mm	Each unit is 100×20×10 cm	3 kg per unit	2 W max & <1 W avg	Long flight heritage

ACAD Totals: Mass=20.2 kg; Power=12 W avg.

For the MI to be spin stabilized and spin about a body-fixed axis that is within 0.025° of the spacecraft's geometric centerline, several things are required. First, the axis of maximum principal moment of inertia needs to be accurately aligned with the geometric centerline prior to launch. Hence, all the spacecraft hardware needs to be mounted with this in mind. After all the hardware is mounted, a spin-balance machine is needed to determine where small trim masses can be strategically placed on the spacecraft to further reduce the principal axis offset angle. The process of spin balancing the spacecraft needs to be done during the hardware integration phase and at the launch site to ensure the offset angle is as small as possible at launch. A residual offset angle below 0.25° should be readily achievable with spin balancing. Secondly, the spacecraft needs an onboard mass balance system that can be certain to trim the offset angle to within 0.025° in orbit. The onboard system is described by figures 60 and 61 and table 18. Thirdly, the ratios of the maximum principal moment of inertia to the intermediate and the minimum should be 1.07 or more at launch; but, the design goal should be 1.2 or more.

Although not required, it is desirable to have the minimum and the intermediate principal moments-of-inertia numerically close to one another, to within about 1 kg-m^2, in order to minimize the gravity torque along the spacecraft spin axis. It is also desirable to have the center of mass close to the geometric center, to within about 2 cm, in order to minimize the solar radiation torque on the spacecraft. Preliminary mass properties for the MI, with no contingency mass added, reveal the following. When 3.1 kg and 1.3 kg trim masses are properly mounted on the spacecraft, the principal moments of inertia become 64.2 kg-m^2, 60.2 kg-m^2, and 60.0 kg-m^2; the axis of maximum principal moment of inertia becomes aligned with the spacecraft's geometric centerline; the total spacecraft mass becomes 224 kg; and the center of mass is within 1 cm of the spacecraft's geometric center. These mass properties satisfy the stated requirements and goals; however, as the spacecraft design matures, attempts should be made to increase the ratios between the maximum principal moment of inertia and the other two.

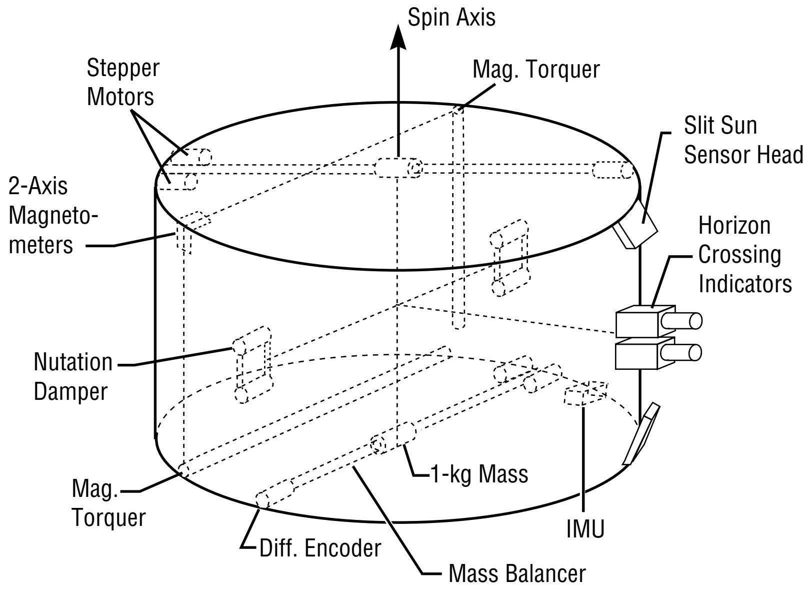

FIGURE 61.—A functional mounting arrangement for the ACAD components.

To achieve the desired spin rate, the last stage of the Taurus S is utilized. After orbit insertion and prior to separation, it can position the spacecraft's geometric centerline close to the orbit normal, to within 2°, according to estimates by OSC engineers. Then, it can spin the spacecraft down to the desired 10 rpm. OSC indicates that the last stage with the spacecraft will probably be spin stabilized at 30 rpm for the apogee burn that puts the spacecraft in the final desired orbit. At separation, the tip-off rates should be 3°/second or less, according to OSC.

Upon separation, redundant meridially-mounted passive nutation dampers can damp the spin axis wobble resulting from the tip-off rates to less than 0.025° in approximately 2 hours (see table 25). Then, the spacecraft should be spinning about its axis of maximum principal moment of inertia at a spin rate of approximately 10 rpm. After several days of spacecraft outgassing, one of the IMU's can be powered up. Then, the onboard CDMS can begin reading the IMU rate gyro and accelerometer outputs, time tagging them with Greenwich mean time (GMT), and storing this information on the onboard solid state tape recorder, every 0.025 seconds. Once per orbit, this stored data will be telemetered to ground.

With this data, ground control can determine the angle between the axis of maximum principal moment of inertia and the spacecraft geometric centerline. Stepper motor commands to the mass balance system that should reduce this angle to less than 0.025° can also be computed. These commands can be uplinked to spacecraft along with the desired GMT for execution. This process can be repeated until the angle is less than 0.025°.

ACAD System Analysis and Simulation Results

The MI spacecraft uses the mass balance system to align the axis of maximum principal moment of inertia with the spacecraft geometric centerline. Without a mechanism for energy dissipation, the principal axis would precess about the angular momentum vector, as shown in figure 62. The nutation damp-

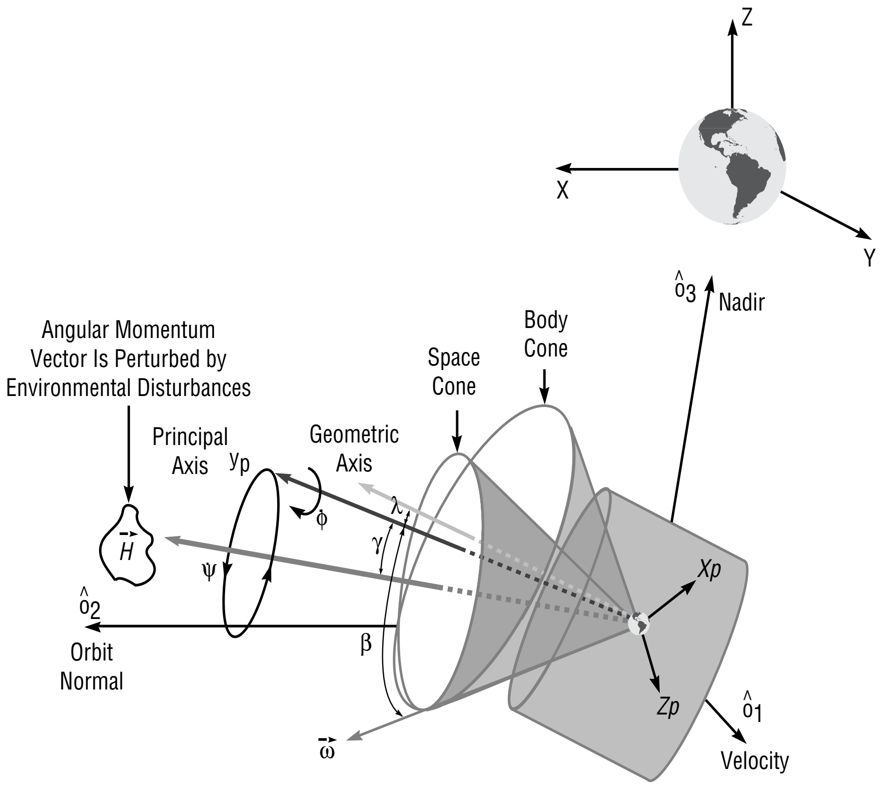
Z
X
Y
$\hat{o}_3$
Nadir
Body Cone
Space Cone
Angular Momentum Vector Is Perturbed by Environmental Disturbances
Principal Axis
y_p
Geometric Axis
λ
ϕ
γ
$\vec{H}$
ψ
$\hat{o}_2$
Orbit Normal
β
X_p
Z_p
$\hat{o}_1$
Velocity
$\vec{\omega}$

FIGURE 62.—Principal axis precesses around the angular momentum vector, which is perturbed by the environmental disturbances.

ers remove this spin axis wobble and align the principal axis with the angular momentum vector. The angular momentum vector nominally points along the orbit normal, but will be perturbed by the environmental disturbances. The magnetic torquer oriented along the spacecraft spin axis provides a control torque to realign the angular momentum vector with the orbit normal.

As shown in figure 63, two options were considered for nutation damper orientation: circumferentially-mounted dampers and meridially-oriented dampers. Equations of motion for both orientations were derived, and linearized systems of equations were determined. The circumferentially-mounted dampers provide damping through nonlinear terms in the equations of motion, and are in general more suitable for spacecraft that will encounter large nutational motion. Axially-mounted dampers are more effective for small nutation angles and affect the spacecraft motion directly through the linear terms. Since the largest nutation angle that the MI spacecraft will experience occurs at launch vehicle separation, and it will be less than 10° (using OSC's estimates), the meridially-mounted dampers were selected.

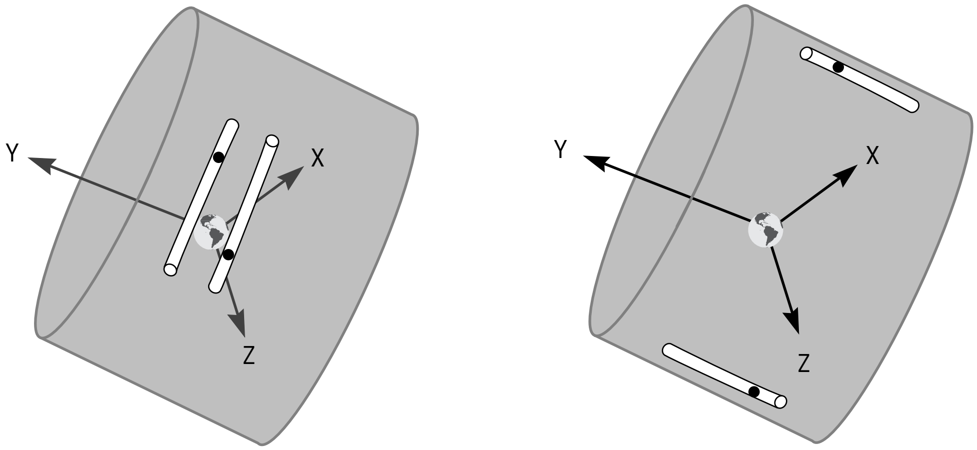

Circumferential Damper Option

Meridial Damper Option

FIGURE 63.—Options for damper orientation.

As indicated in table 26, the predominant environmental torque on MI is that due to solar radiation pressure. This disturbance is computed in the simulation assuming the spacecraft has 12 sides, covered with solar arrays, and two end plates. The force on each surface is determined using the geometric centroid of each surface as its center of pressure. The net torque about the spacecraft center of mass is computed assuming the center of mass is slightly offset from the spacecraft geometric center. To obtain a conservative estimate for this disturbance torque, the reflected solar radiation is assumed to be completely specular with a reflection fraction of 0.02 for the solar arrays. The end plates are assumed to be totally reflective. A similar conservative model is used to estimate the aerodynamic torques on MI, but these are still negligible because of the high orbit altitudes.

TABLE 26.—*Environmental torques on MI.*

Torque	Type	Maximum Value	Effect
Solar Radiation Pressure	Environmental Disturbance Torque	1.6×10^{-6} N-m	Causes Spin Axis to Drift 1° in 1 to 4 Wk
Drag Torque from Eddy Current Losses in Spacecraft Aluminum Structure	Environmental Disturbance Torque	0.9×10^{-6} N-m	Reduces Spin Rate 0.5 rpm in 2 Yr
Aerodynamic	Environmental Disturbance Torque	$<10^{-8}$ N-m	Negligible
Gravity Gradient	Passive Environmental Control Torque	3.4×10^{-6} N-m	Aligns Spin Axis With Orbit Normal
Magnetic Torque for Reorienting Spin Axis	Commanded Control Torque	$2{,}000\times10^{-6}$ N-m in 0.1 Gauss Field at Perigee	Reorients Spin Axis 1° in 13 Min
Magnetic Torque for Spin Rate Correction	Commanded Control Torque	$2{,}000\times10^{-6}$ N-m in 0.1 Gauss Field at Perigee	Changes Spin Rate 0.5 rpm per Orbit
Nutation Dampers' Viscous Friction Torque	Passive Control Torque		Reduces Spin Axis Wobble From 1° to 0.025° in 1.2 Hr

The system response to worst case tip-off conditions from the launch vehicle was simulated. The initial attitude errors were 2° in each axis, with an initial tip-off rate of 3°/second in each transverse axis. The ß angle was 0°. The nutation angle between the vehicle principal axis and the angular momentum vector is shown in figure 64, with the corresponding damper mass motion shown in figures 65 and 66. The dampers decrease the wobble to less than 0.025° in approximately 2 hours.

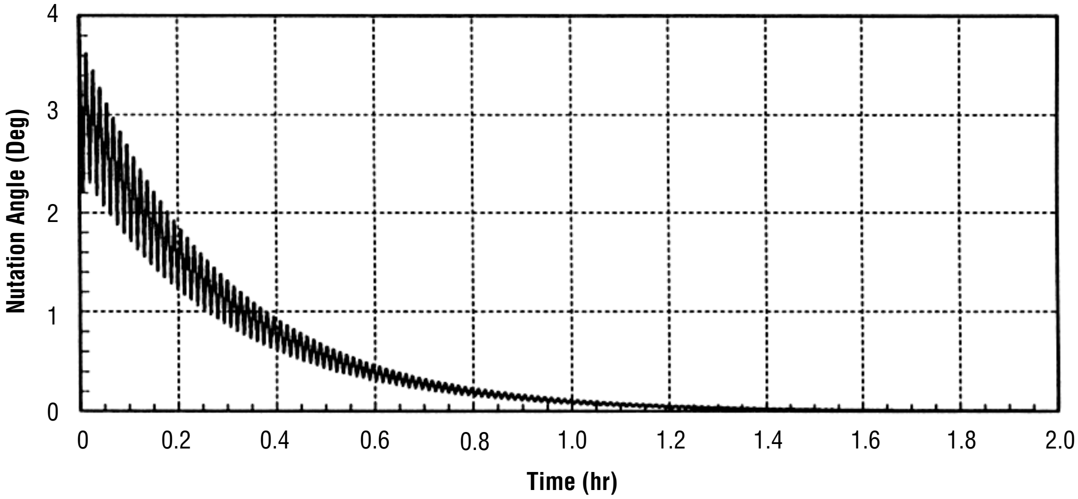

FIGURE 64.—Nutation angle after worst case launch vehicle tip-off conditions.

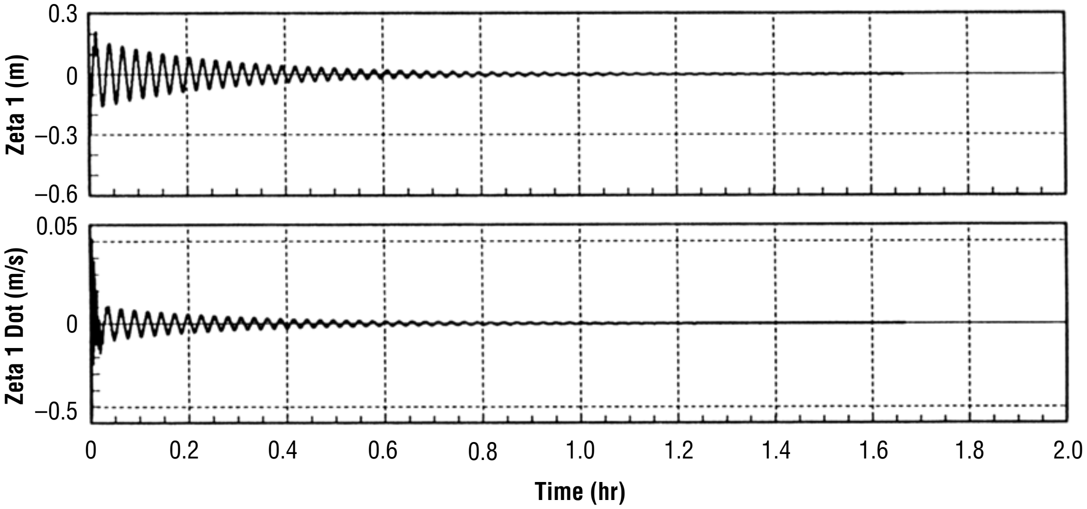

FIGURE 65.—Position and velocity for damper mass 1.

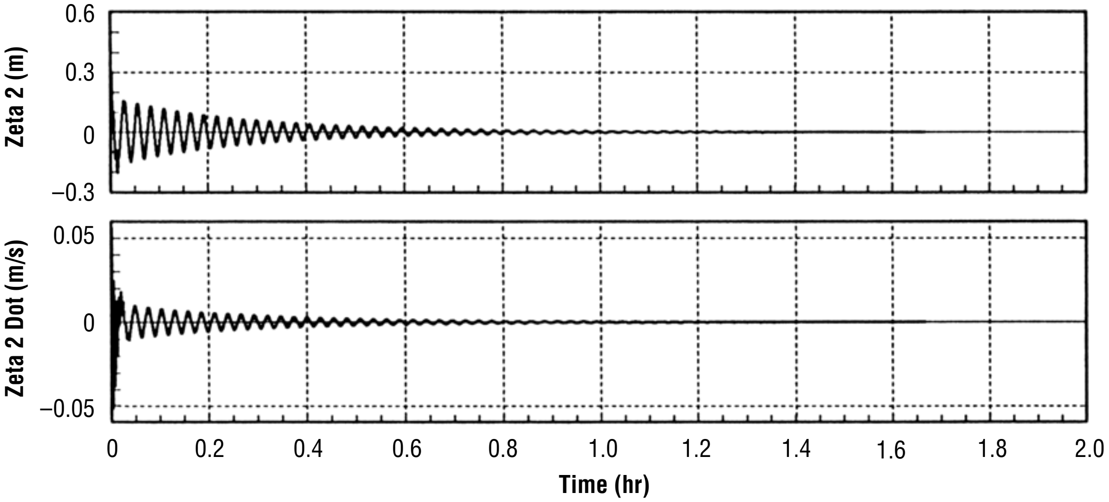

FIGURE 66.—Position and velocity for damper mass 2.

The launch vehicle tip-off rates not only produce alignment errors between the vehicle principal axis and the angular momentum vector, but also between the angular momentum vector and the orbit normal. Although the dampers remove the errors between the principal axis and the angular momentum vector, the magnetic torquer is needed to align the angular momentum vector with the orbit normal. The worst-case launch vehicle separation conditions produce an error between the spacecraft spin axis and the orbit normal that is equal to 3.5° after 2 hours, as shown in figures 67 and 68.

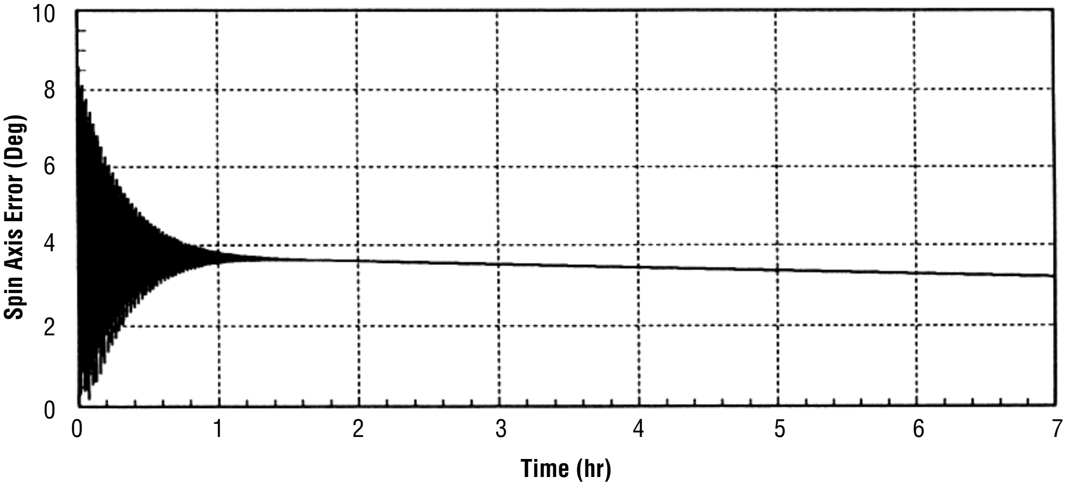

FIGURE 67.—Angle between the spacecraft spin axis and the orbit normal after worst case launch vehicle tip-off conditions.

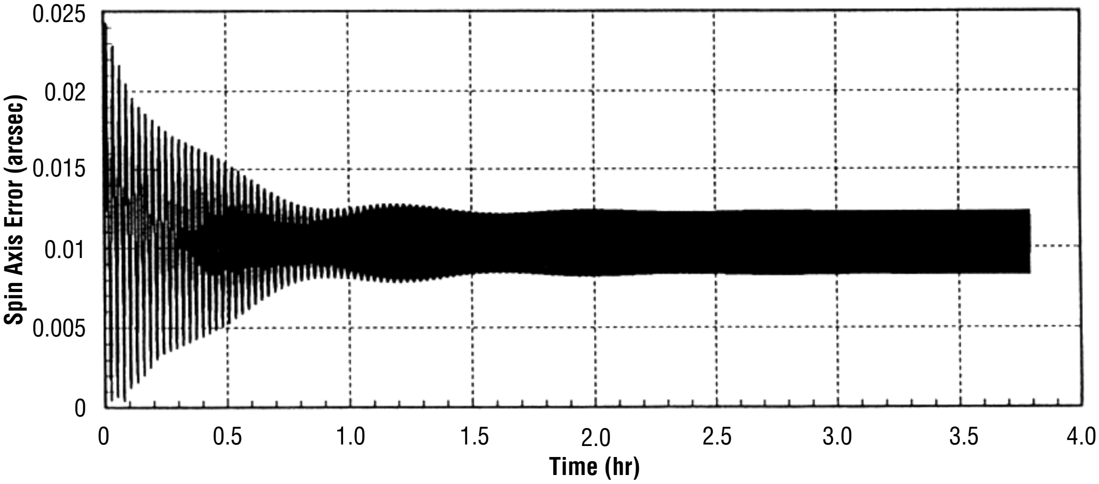

FIGURE 68.—Angle between the spacecraft spin axis and the orbit normal due to environmental disturbances.

As previously noted, the largest environmental disturbance torque is due to solar radiation pressure. It is a maximum when β is 45° and a minimum when β is 0°. The system response to these disturbance torques was simulated over a quarter of an orbit starting at perigee for $\beta = 45°$ and a 4,800-km by 7-R_E orbit. Initially, the spacecraft spin axis was aligned with the orbit normal, the spin rate was 10 rpm, and the angular rates in the other two axes were zero. Figure 74 shows the angle in arcseconds between the spacecraft spin axis and the orbit normal. It is well below 1° and the motion of the spin axis is well below 0.025° over any 60-second period. The corresponding angular velocity components along the two transverse axes are shown in figures 69 and 70, with the corresponding Euler angles in arcseconds plotted in figures 71 and 72. The spin rate over two full orbits is shown in figure 73, and its deviation from 10 rpm is plotted in figure 74. Perturbations to the spin rate are greatest at perigee, when the gravity gradient torques are maximum. Figure 80 shows that the spin rate decay due to gravity gradient, solar radiation pressure, and aerodynamic torques is expected to be 4 by 10^{-8} rpm per orbit. This corresponds to a negligible amount over the 2-year mission. Hence, the only significant loss in spin rate is that due to eddy current losses in the spacecraft aluminum structure, which could be about 0.5 rpm over 2 years, as shown in table 20. On the other hand, if it turns out the spin rate decay is much greater than anticipated, the magnetic torquing system for adjusting the spin rate can be employed as required to maintain it within the required range of 10 ±5 rpm.

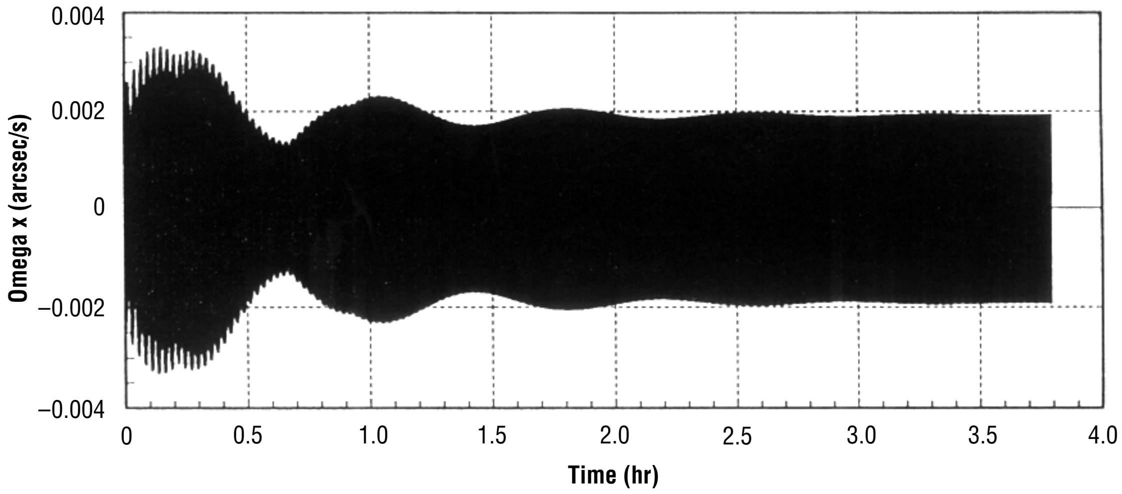

FIGURE 69.—Angular velocity component along the spacecraft X-axis.

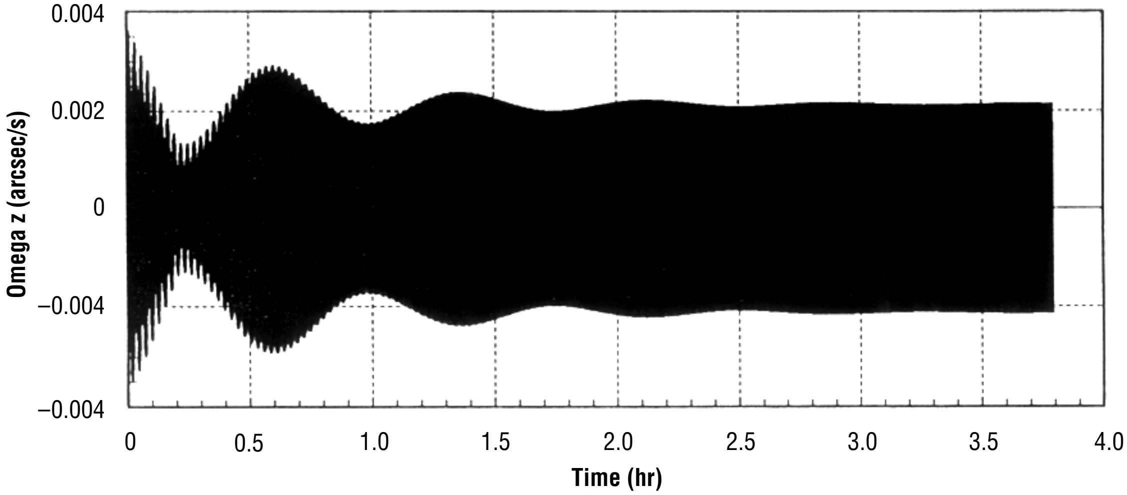

FIGURE 70.—Angular velocity component along the spacecraft Z-axis.

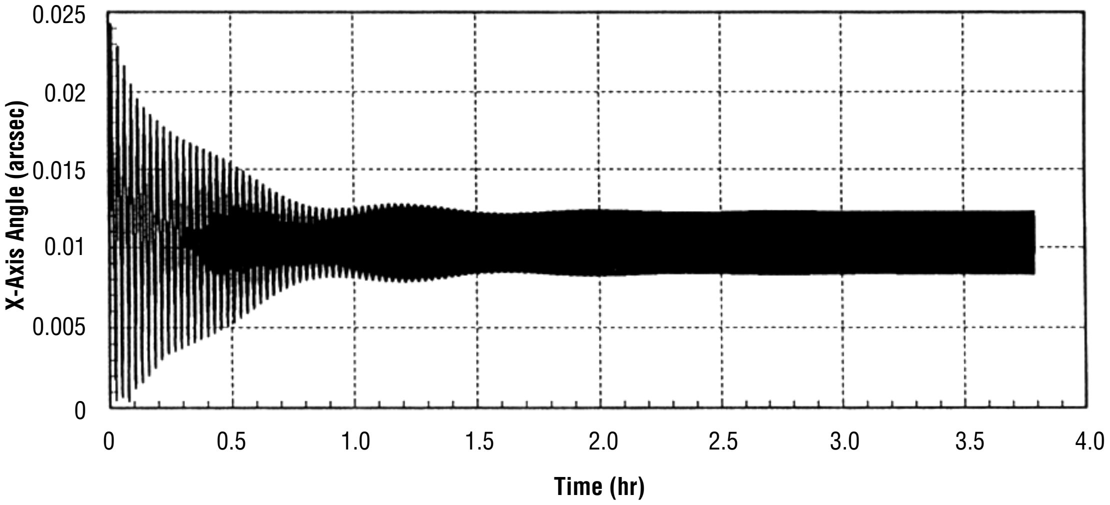

FIGURE 71.—X-axis angle of the 2–1–3 Euler angles from an inertial frame aligned with the orbit to the spacecraft-fixed frame.

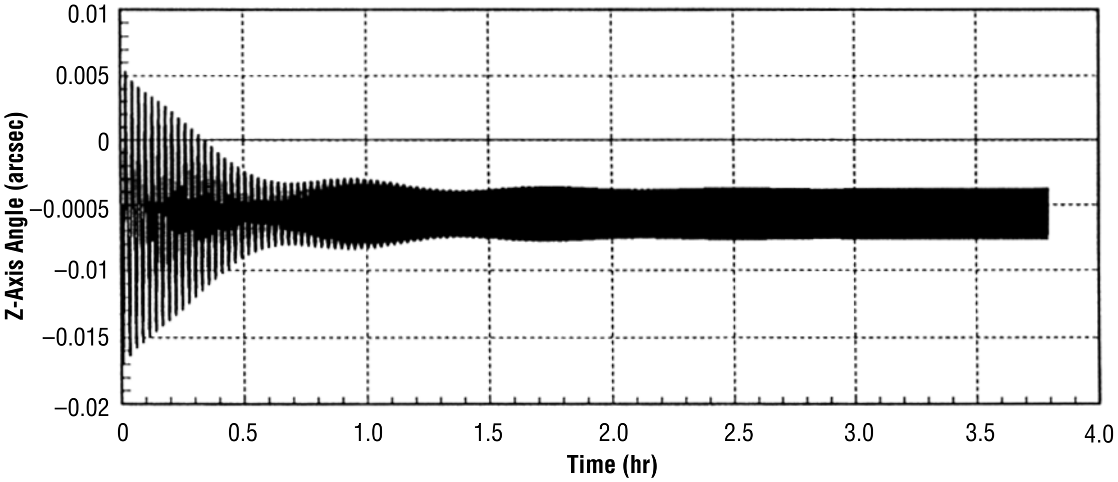

FIGURE 72.—Z-axis angle of the 2–1–3 Euler angles from an inertial frame aligned with the orbit to the spacecraft-fixed frame .

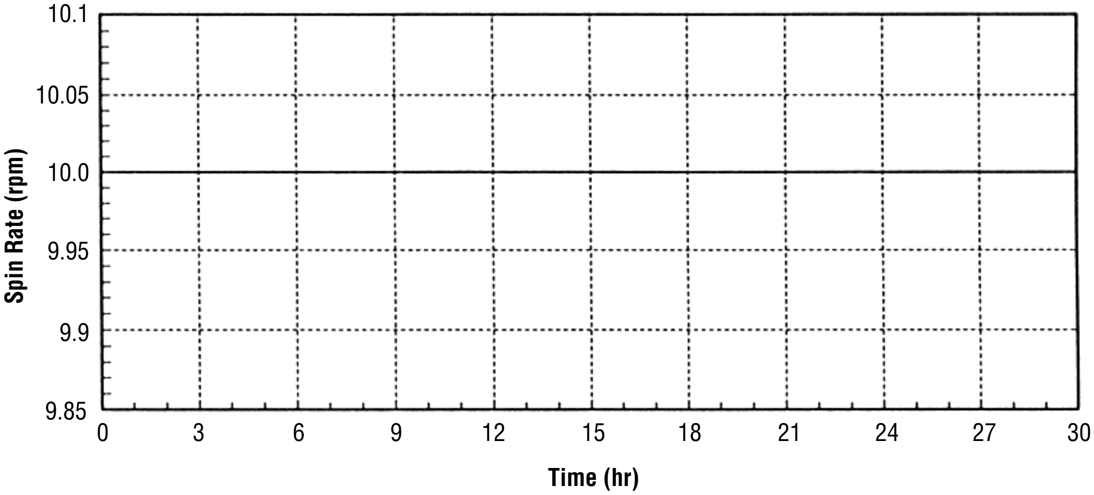

FIGURE 73.—Spacecraft spin rate over two orbits.

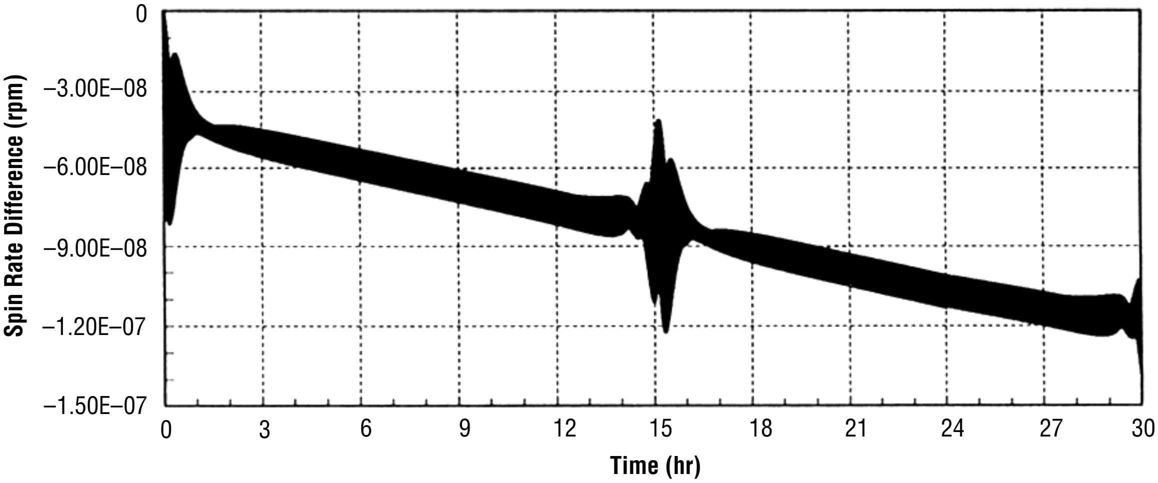

FIGURE 74.—Change in spin rate over two orbits.

Mass Properties

The detailed mass summary in table 27 for the MI follows the structure of the MI work breakdown structure (WBS). A 30 percent weight contingency has been added to the spacecraft and science instrument dry masses. A weight contingency is an allowance for: (1) deficiencies in calculated or estimated weights that result from the level of maturity of the design, and (2) growth due to changes in ground rules, manufacturing variations, test verification uncertainty, and the like. Allowance for items such as structural design margins, vehicle performance variations, and programmatic reserves are not included in this contingency but must be accounted for elsewhere in the program.

Table 27.—*Detailed mass summary*.

	Assy (kg)	Total (kg)		Assy (kg)	Total (kg)
Avionics		**TCS**	**7.3**		
C&DH		**21.0**	MLI Blankets	2.9	
Transponder	3.4		Heat Transfer Medium	0.3	
Command Detector	1.2		Thermostats	1.4	
Power Amplifier	2.0		Temperature Sensors	0.1	
Central Processor	3.0		Relays	1.1	
Solid State Recorder	3.8		Heater Current Sensors	0.1	
Belt Antenna	3.6		Heaters	0.6	
Structure/Cables	4.0		Mounting Material	0.6	
EPS		**45.0**	Paint	0.3	
Solar Arrays	6.3		**Structures**		**60.3**
Electronics	10.6		Space Frame Assy.	13.9	
Power Supply Electronics			Panels	10.3	
Power Control & Distribution			Deckplates	5.0	
Shunts (dissipators)			Fasteners	5.5	
Battery	11.4		Separation System	18.4	
Cabling/Harnesses	16.7		Mounting Brackets	6.0	
Elec. Harness			Cabling Brackets	1.2	
Umbilical			**Spacecraft Contingency (30%)**		**46.2**
ACS		**20.2**			
Nutation Dampers	1.1		**Science Instruments**		**78.0**
Two-Axis Magnetometer	0.4		Hot Plasma Imager and Electronics	29.0	
Magnetic Torquer	8.8		Plasmasphere Imager and Electronics	19.0	
Mass-Balancing System	6.0		FUV Imager and Electronics	30.0	
IMU	1.4		**SI Contingency (30%)**		**23.4**
Digital Sun Sensor Assembly	1.0				
Horizon Crossing Indicators	1.5		**Total**		**301.5**
			Margin (Taurus S)		**28.5**

The total system launch mass is 301.5 kg. Of this, the payload including the contingency (core science instrument complement) represents 34 percent of the total mass. This data for all the spacecraft subsystems masses as a percent of the total mass is presented graphically in figure 75. For the selected baseline launch vehicle, the Taurus S, the vehicle performance to our desired orbit is 330 kg. This provides MI with a launch margin of 28.5 kg. After the spacecraft has achieved its final orbit the total mass is 290.5 kg since a portion of the separation system remains with the launch vehicle.

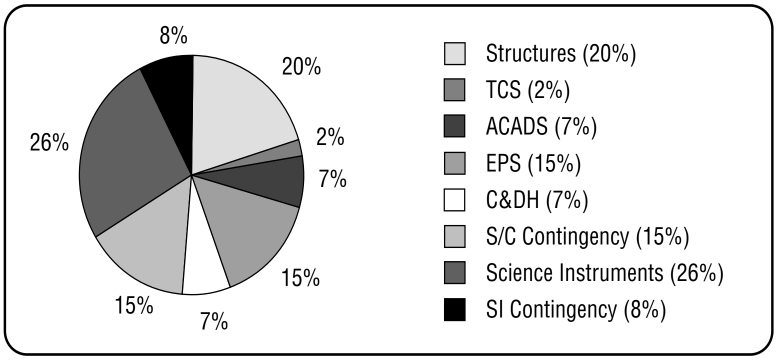

Figure 75.—Subsystem masses as a percentage of the total mass.

The mass properties for the spacecraft, shown in figure 76, are referenced from the geometric center of the spacecraft. The mass within the boxes was considered to be uniformly distributed. The launch vehicle portion of the separation system, the weight contingency, and some fastener weights are not included. The mass of the spacecraft and all the components were balanced with respect to the spin axis and the center of mass also was aligned closely with the geometric center of the spacecraft. The axis of maximum moment of inertia is the spin axis. These moments and products of inertia are adequate for a spin-stabilized spacecraft.

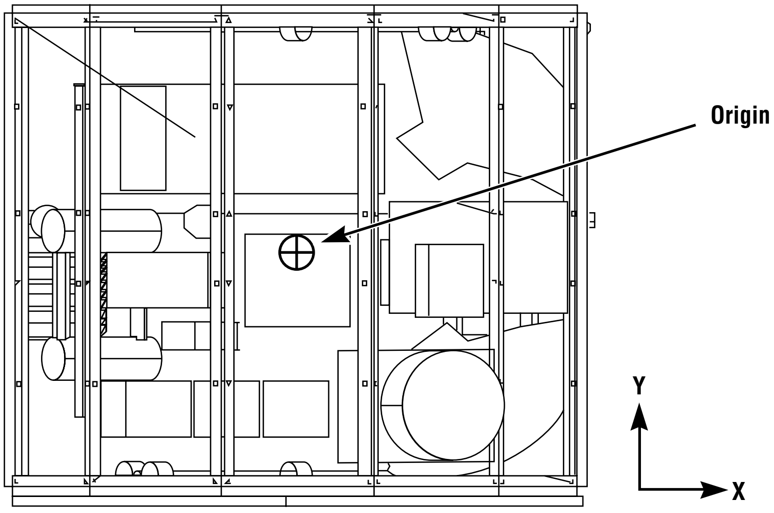

Mass Properties Summary

Mass = 219.4 kg

Xcg = –1.036 cm
Ycg = 0.330 cm
Zcg = –0.280 cm

Ixx = 57.78 kg m^2
Iyy = 62.34 kg m^2
Izz = 56.79 kg m^2

Ixy = –1.320 kg m^2
Ixz = 0.239 kg m^2
Iyz = 0.554 kg m^2

Figure 76.—Mass properties summary

Natural Space Environments

The natural space environment refers to the environment as it occurs independent of the presence of a spacecraft; thus, it includes both naturally occurring phenomena such as meteoroids, ionizing radiation, plasma, etc., and man-made factors such as orbital debris. Appendix D discusses the natural space environment and major areas of interaction with the spacecraft systems. For the phase A effort, each natural space environment was first given a cursory evaluation as to the applicability to the mission. It was determined that the ionizing radiation and plasma environments, and their effects on the spacecraft, require a more detailed analysis.

Ionizing Radiation Environment

The ionizing radiation environment is categorized into three main groups of energetic particles: trapped radiation belt particles, cosmic rays, and solar flare particles. As a result of these energetic particles, solar cells, electronics, and other spacecraft materials degrade over time. Also, the passage of an energetic particle through sensitive regions of electronics give rise to single event upsets (SEU's), which can be either hard or soft depending on whether the damage is permanent or temporary.

A description of the trapped and solar flare ionizing radiation environment that MI is expected to experience during its 2-year mission is given in appendix C. This description can be used to estimate solar array degradation, dose effects in electronics, and occurrences of SEU's.

In the case of MI, estimating the damage to the solar arrays is important since solar cells will occupy a considerable percentage of the exposed spacecraft surface, and the solar arrays must meet EOL power requirements. The amount of damage to solar cells depends on the type of cells being used, the type and thickness of the coverslide, and on the energy and fluence of the radiation particles. However, changing the design of the solar arrays to incorporate a thicker coverslide or using solar cells that are more radiation resistant can adversely impact weight and cost.

Appendix C also describes the solar array radiation analysis conducted for MI. The radiation environment given in the appendix was reduced to an equivalent 1 MeV unidirectional electron fluence to allow easy comparison of the damage caused by the different components of the radiation. The total fluence of 1 MeV electrons was then used to estimate the solar array power degradation due to radiation. The results showed that increasing the coverslide thickness and/or increasing the orbit perigee will decrease the solar array degradation. Increasing the coverslide thickness results in more of the particles being absorbed prior to reaching the solar cell while increasing the orbit perigee decreases the fluence of trapped protons.

The cosmic ray environment and predictions of SEU occurrences need to be addressed in phase B.

Plasma Environment

A collection of electrically charged particles consisting of positively charged ions and free electrons exists in all spacecraft orbits and is known as the natural space plasma. Definition of the natural space plasma depends on several factors. The most dramatic variations in its properties are due to changes in altitude and latitude.

The spacecraft will encounter several different plasma regimes due to its highly elliptical polar orbit. This highly elliptical polar orbit will place the spacecraft in a plasma environment conducive to spacecraft charging (i.e., the accumulation of charged plasma particles on the surfaces of a spacecraft). The effects attributed to spacecraft charging have proven to be a serious engineering concern. Therefore, to further quantify these effects, a preliminary spacecraft charging analysis was performed (appendix D).

Conducting a spacecraft charging analysis involves defining the properties of the natural space plasma to which the MI spacecraft will be exposed, developing design guidelines with the purpose of reducing or eliminating the effects attributed to spacecraft charging, and performing computer analysis to model the levels of spacecraft charging that occur. On the basis of the analysis, design recommendations are made to address any spacecraft charging issues that arise.

The orbit will transverse the plasma region occupied by geosynchronous satellites, a region that is exposed to geomagnetic substorms or “space weather” that is known to cause high levels of spacecraft charging. Therefore, the plasma environment properties associated with geomagnetic substorms were used as a preliminary worst case environment. Table 28 provides the plasma environment specifications used for this analysis.

TABLE 28.—*90th percentile worst case geomagnetic substorm plasma environment.*

Electron number density:	1.12 cm^{-3}
Electron temperature:	12,000 eV
Ion number density:	0.236 cm^{-3}
Ion temperature:	29,500 eV

Appendix D describes the results of the preliminary spacecraft charging analysis conducted on the MI. Preliminary results do not show a charging behavior that warrants critical design changes at this time. At this point in the development of the MI, the best approach is to design the spacecraft based on known techniques that will serve to limit the detrimental effects of spacecraft charging. In particular, shielding and electrical filtering should used to protect sensitive electronics from its effects.

Operations

The spacecraft will be launched on a Taurus S-class launch vehicle into a 4,800-km by 7-R_E elliptical polar orbit (90°). The spacecraft will be spin stabilized at a rate of approximately 10 rpm and will maintain an attitude that maintains the spin axis perpendicular to the orbit plane. All science instruments will operate independently of each other and may be operated in a standby mode for safe mode or on-orbit reconfiguration requirements. The operations required for the mission can be broken down into the development, verification, launch, flight, on-orbit, and mission phases. Operations in each of these phases have impacts on both the ground and space segments of the mission.

Ground segment operations consist of the development, test, integration, launch, and mission ground operations required to promote safe, reliable, and verifiable ground system design and operations processes.

Space segment operations consist of the test, flight, on-orbit, and mission support operations required to safely and successfully perform the mission.

Assumptions and Guidelines

A major goal of the MI program is to establish operational requirements that promote reduced costs and introduce innovative approaches to operations management, without jeopardizing mission success. Hence, use of existing facilities and resources in order to reduce ground system development cost is of prime interest to the MI ground system design and implementation process.

Ground Segment Support

Launch Operations. The spacecraft will undergo launch processing at VAFB located at the WTR, CA. The Taurus S launch vehicle is one of the launch vehicles being proposed for Earth-to-orbit transfer of the MI spacecraft. The following discusses implementation of the launch operations for a Taurus S/ MI.

The spacecraft will be processed offline from the Taurus launch vehicle over a period of approximately 40 days. The spacecraft will undergo a receiving inspection, alignment checks, battery installation, software loads, mission simulation, interface verification, and spacecraft encapsulation during this time period. MI will use the Space Launch Complex 6 Payload Preparation Room (PPR) airlock for processing and final launch integration of the payload. The PPR facility was originally designated for use with the WTR Space Transportation System (STS) payload processing before the WTR STS launch program was mothballed in the 1980’s. At approximately launch minus 5 days the encapsulated spacecraft will be transported vertically on a truck to the Taurus launch site where it will be integrated onto the launch vehicle.

Upon arrival at the PPR, the MI will undergo a visual inspection and checkout. Any last minute component installations will then occur, followed by a spin-balance test to determine spacecraft alignment and spacecraft dynamic properties. The spin-balance table is a portable hardware unit that arrives by truck from the final acceptance test location at the spacecraft vendor or spacecraft integrator’s facilities. Checkout ground support equipment will arrive at approximately the same time as the portable spin-balance table. Any required subsystem tests will then be performed, followed by electrical end-to-end test. Mission simulations will then be performed utilizing flight software loads via local or remote Space Operations Control Center (SOCC) data links. Other test software may be accessible via local or remote SOCC data links.

The spacecraft is encapsulated within the Taurus S shroud after testing has been completed at approximately 6 days before launch. A class 100k (no more than 100,000 particles per foot^3) clean environment, as well as a positive conditioned air purge, is maintained from this point on until launch. Temperature is also maintained and guaranteed to remain at some predetermined point ±10 °C beginning at encapsulation and continuing through launch. All ground commanding, monitoring, and telemetry is performed from the launch support van through the spacecraft's hardline launch support umbilical. This same umbilical will contain the necessary electrical path required to send a trickle charge current to the spacecraft onboard power management system. The charging current will be suspended and safed shortly before launch. As currently planned, no spacecraft-to-launch vehicle interfaces other than mechanical systems will exist. The following subsystems will be operating in some predetermined mode at the time of launch in order to super orbital startup of the MI spacecraft: EPS, TCS, the command receiver, and C&DH.

Taurus S Launch Operations. The candidate launch vehicle, the Taurus S, will be assembled at VAFB launch facilities and then transported to a refurbished missile launch site where the booster (zero) stage (S0) and the first three stages (S1, S2, and S3) are stacked/mated in preparation for final payload stacking. However, a consortium of private solid-based launch service provider's have a united effort funded privately and through Department of Defense grants to construct a new launch site located in the Cypress Ridge area of VAFB. The new site would be online at approximately the time that MI will be launched and could alleviate minor difficulties currently existing in transportation of an encapsulated Taurus payload from the PPR airlock to the current launch site. The first three stages of Taurus S are currently processed and checked out in the VAFB Missile Assembly Building (MAB).

Integration of the launch vehicle begins at approximately launch minus 8 weeks. The S1, S2, and S3 stages of the Taurus S are electrically mated and checked out in the MAB (formerly the Peacekeeper Integration Facility) located at VAFB. The integration is done in the horizontal orientation. Avionics and standoffs are installed and simulations are performed utilizing simulated IMU's. These stages are mechanically mated to each other and shipped to the launch site where they are stacked atop the booster or S0. Simulations are performed using simulated IMU's and electrical mates are verified. Pulse catchers are used to test all system pyrotechnic devices. The Taurus RCS is tested by firing and then is refurbished at approximately launch minus 5 days in preparation for launch. All simulations are performed with the spacecraft, S1, S2, S3, and S4 stages in a horizontal orientation. S1, S2, S3, S4, and the MI are then rotated to the vertical orientation at approximately launch minus 36 hours, immediately after completing the launch readiness review nominally scheduled at launch minus 5 days.

Flight Operations. Approximately 3 minutes after launch, the cylindrical solar arrays are exposed to the Sun immediately after completion of the fairing separation event shown in figure 77. At that time, power is available for use in power management tasks. Shortly after fairing separation and after S3 burnout, the Taurus S will achieve transfer orbit insertion. The third stage and AKM will remain in a spinning state for approximately 6 hours during this transfer orbit coasting maneuver. At approximately 7 hours mission elapsed time (MET) the AKM will separate from S3 (still spinning for stabilization) and initiate a 20-second burn and reorientation maneuver to bring the MI to deployment attitude. The AKM RCS will de-spin the AKM/MI assembly down from approximately 30 to 40 rpm to 10 rpm (nominal). After reaching a nominal spin rate, the AKM/MI will perform a separation maneuver and begin on-station activation and startup activities. This last startup event will mark the beginning of the orbital verification (OV) phase of the mission.

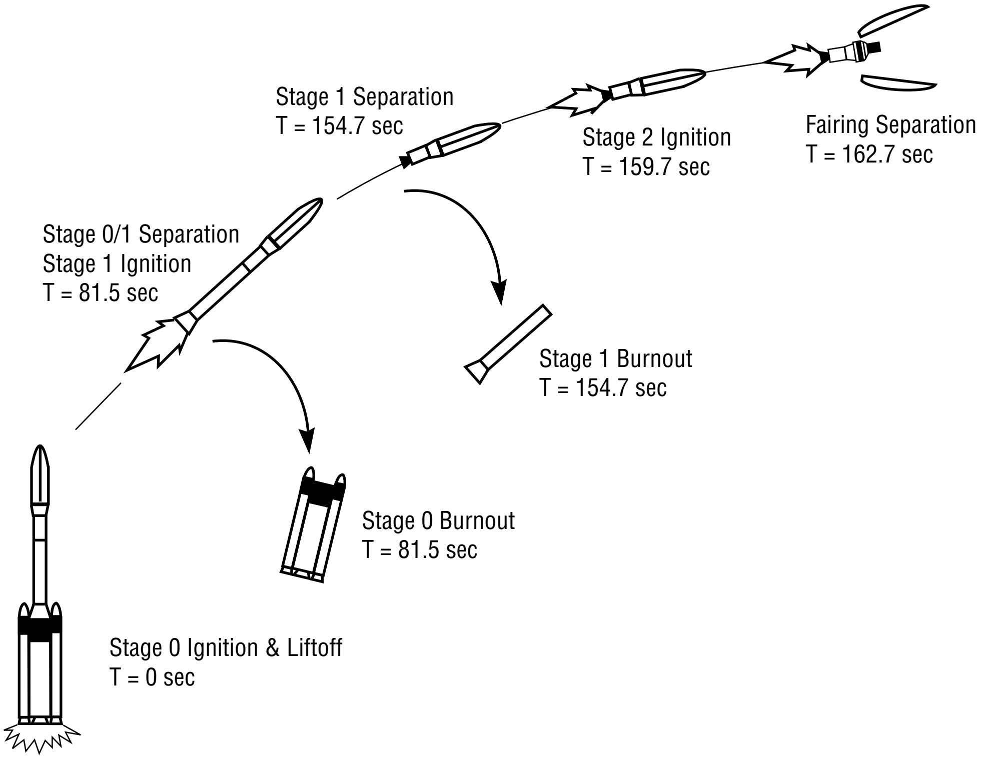

FIGURE 77.—Taurus S/MI flight operations profile.

Space Segment Support

SOCC. MI may utilize the capabilities of the Enhanced Huntsville Operations Support Center (EHOSC) and the Engineering Support Center located in the Mission Operations Laboratory at MSFC for mission operations support, as well as spacecraft engineering support. The Enhanced HOSC System (EHS) can support multiple projects and facilities. The system is currently supporting Spacelab, *International Space Station*, the Advanced X-Ray Astrophysics Facility (AXAF), and Space Shuttle, and is designed using a layered approach. Basic capabilities, common to multiple projects, make up the EHS generic system consisting of software modules and hardware components. This generic system may then have project-specific requirements in order to form a mission-specific MI EHS system. The EHS system architecture is based on a distributed processing concept, using workstations, server processors, and local area networks. The EHS distributed computing and communication resources are able to provide mission support to the prelaunch integration, simulation/training, launch operations, flight operations, data evaluation, and data routing functions of the MI mission operations requirements.

At present, it has been estimated that approximately six workstations will be required through the OV phase of the mission. One to two workstations may be then be required for the nominal, or routine, operations phase of the mission. One server/workstation will be required to support the ground based attitude adjustment computations necessary for attitude corrections. Some of the EHS hardware/resources required for these capabilities (especially OV) may become available as the AXAF mission terminates its OV phase at around the time MI goes into OV. This could further reduce the development requirements and investment needed to perform MI's OV.

POCC. One of the key features of the EHS is the fact that remote user and facility operations are supported and encouraged. Hence, remote POCC's may be accommodated with reduced development requirements. Utilization of such facilities, one for each science instrument or principal investigator, is envisioned as a likely candidate for conducting payload related support activities. These remote POCC facilities may be equipped with remote EHS workstation(s) for conducting the day to day mission operations management and engineering functions (see the Mission Operations section for specifics).

Mission Operations

Mission operations involve those activities related to the spacecraft control, spacecraft operational maintenance, data processing, and data dissemination functions of an overall spacecraft's operations infrastructure. Together, the MI ground system and the MI spacecraft provide these functions over the life of the mission. Figure 78 illustrates the overall data flow through the ground system mission support elements, along with a brief description of the major activities and responsibilities required from each of these elements. The MI ground system is composed of the MI remote POCC's, the SOCC, and NASCOM.

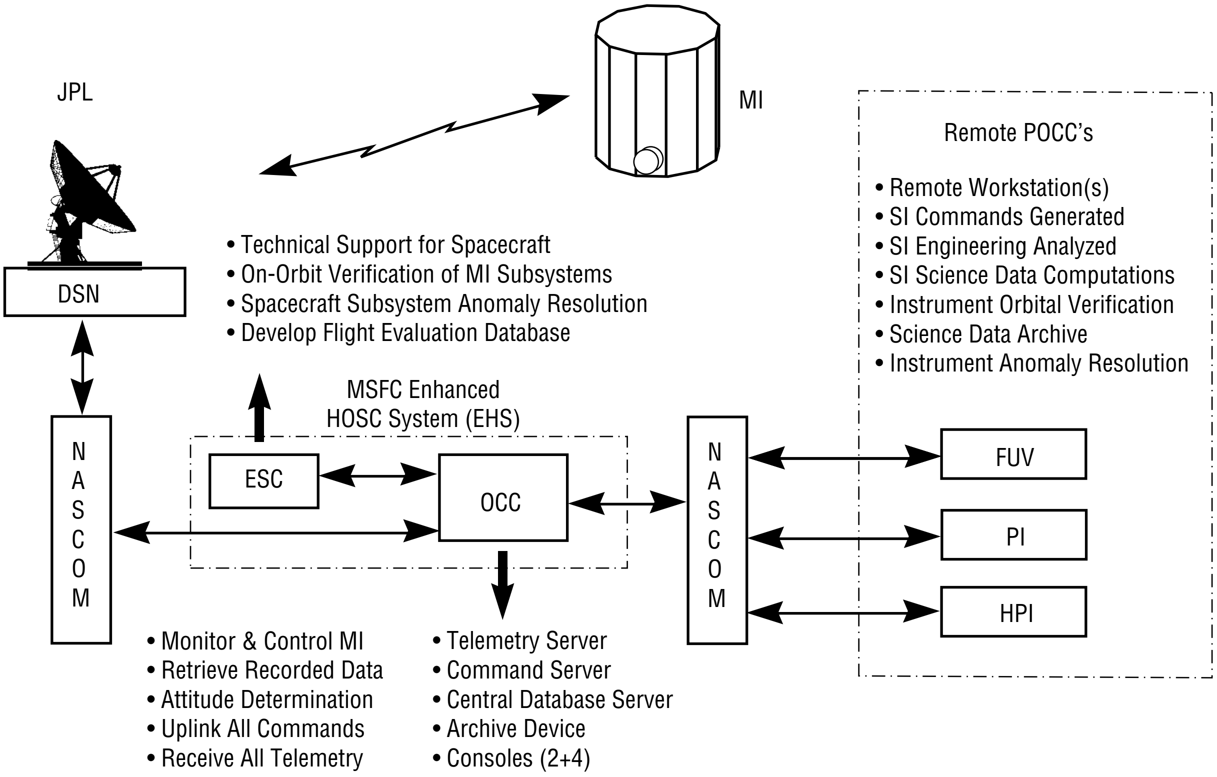

JPL
MI
DSN
Remote POCC's
• Remote Workstation(s)
• SI Commands Generated
• SI Engineering Analyzed
• SI Science Data Computations
• Instrument Orbital Verification
• Science Data Archive
• Instrument Anomaly Resolution
• Technical Support for Spacecraft
• On-Orbit Verification of MI Subsystems
• Spacecraft Subsystem Anomaly Resolution
• Develop Flight Evaluation Database
MSFC Enhanced
HOSC System (EHS)
NASCOM
ESC
OCC
NASCOM
FUV
PI
HPI
• Monitor & Control MI
• Retrieve Recorded Data
• Attitude Determination
• Uplink All Commands
• Receive All Telemetry
• Telemetry Server
• Command Server
• Central Database Server
• Archive Device
• Consoles (2+4)

FIGURE 78.—Mission operations flow.

A science instrument remote POCC may or may not be collocated in the same support facility as the other two science instrument POCC's. The POCC's can be divided into three different support functions. Each function supports a major science instrument—the FUV, PI, and HPI. Science instrument updated requirements, cost trades, and implementation studies must be performed prior to baselining any POCC facility development requirements. The proposed use of the MSFC EHS remote support capabilities could reduce the amount of development time and cost associated with bringing a project like MI to MSFC. Utilization of existing or planned EHS systems and software modules, and the distributed computing architecture of the EHS system, provide the means required to simplify, as well as accelerate, the development of the MI ground system. Use of OV workstations and other support elements derived from other EHS resident missions, which are concurrently into their normal operations phase, could also reduce development requirements to MI POCC's.

The POCC provides the necessary hardware, software, and personnel required to support the OV, normal, and EOL phases of the MI spacecraft science instruments. Workstations will be used to support the everyday interactions between the SOCC and POCC data systems, as well as provide science-specific computation capabilities needed for science instrument activities and data dissemination. The POCC is responsible for generating science instrument command sequences, analysis of science instrument engineering data, science instrument data computations, science instrument orbital verification, any science data archiving beyond SOCC's support, science instrument anomaly resolution, and science instrument trend analyses. All command sequences will be verified by the principal investigator, time-tagged, and shipped via the EHS remote interface (remote links) to the SOCC command servers for uplink. Science/engineering data will be received in such a store-and-forward way via the SOCC telemetry servers. Any science instrument schedules required by the principal investigator will be generated and maintained by the principal investigator (no SOCC support assumed).

The SOCC provides the necessary hardware, software, and personnel required to support the OV, normal, and EOL phases of the MI spacecraft. The SOCC will provide the capabilities needed for proper control and monitoring of the MI's day-to-day operations. This facility can be functionally divided into the Operations Control Center (OCC) and the Engineering Support Center (ESC).

The ESC is the primary provider of the technical and engineering support requirements requested by MI. The Technical Support Team (TST) members will consist of a combination of MSFC and contractor personal working primarily on an as-needed basis (part-time) to support the initial OV phase, the ongoing normal operations anomaly resolution, and flight evaluation requirements of the mission.

The OCC provides daily day-to-day support of the spacecraft safety, monitoring, and control operations. The personal associated with the SOCC is the Flight Operations Team (FOT). A goal of MI is to reduce the FOT requirements down to a minimum complement that can maintain safe and reliable management of the MI's day-to-day operations. Ideally, one to two full-time personnel working a standard 8-hour shift is a goal. Command servers located in the OCC will provide the mechanism required to support remote POCC SI command uploads to the science instruments and will also support spacecraft control workstation command uploads. Some level of command authentication and verification will be provided by this sort of arrangement. In a similar manner, telemetry servers will be provided to facilitate transfer of science instrument and spacecraft engineering data to properly equipped local and remote EHS components. A central database server will be provided to support computation and data analysis requirements. MI attitude determination requires the use of a workstation for computation of attitude update commands. Once calculated, the updates will be performed once per day (once per orbit).

As many as two data rates will be used to support MI uplink/downlink requirements. At least one low-data rate for engineering functions and at least one high-data rate for science data downloads. The high-data rate is used once per orbit (once per day) and the low-data rate may be used for real-time (anytime) corrective and health maintenance links with the spacecraft. The JPL DSN has been baselined to support the download/upload requirements for MI.

JPL's DSN consists of a set of 26- or 34-m ground antenna stations designed to support long duration mission spacecraft data downlink/uplink requirements. The NASCOM supports DSN by providing dedicated circuits from each Deep Space Control Complex to the JPL Ground Communications Facility (GCF). The GCF provides ground communication capabilities necessary for support of spaceflight operations. The GCF utilizes long-haul leased circuits, terminal equipment, switching facilities, and personnel to accomplish ground transmission, data reception, data recording, and data control requirements between the NASCOM's Network Operations Control Center at Goddard Space Flight Center and the various mission operations control centers across NASA.

Verification and Test

Assembly and Integration. Assembly/integration requirements are not fully developed at this phase of the design study process. However, structural assembly sequencing may be found in the Structures section. See the Launch Operations section for launch integration details.

Orbital Verification. The on-orbit verification period will last until approximately 1 month after reaching the on-station orbital position. MI spacecraft telemetry and tracking will continue from launch until the "on" command is given at the on-station position. Approximately one orbit will be utilized as a period for settling any final maneuvering perturbances. The FOT/TST will begin the OV phase of the mission shortly after the settling period ends. Approximately 2 calendar weeks have been assumed to verify the health and status of all major spacecraft subsystems. Verification will be accomplished through analysis of telemetry engineering data resulting from uploaded preplanned test procedures.

The ACS orbital calibration and checkout will last approximately 3 to 7 days after subsystems checkout begins. The following sequence of activities will be repeated periodically during the OV period to adjust ACS performance: orbit adjust data downlink (ACAD sensor measurements), ground software computation of spacecraft attitude (in GMT), and balance mass adjustments via uploaded commands. The ground software computation will compute spin axis wobble, compute moments of inertia, and then determine mass position changes required to reduce products of inertia to zero (further details are located in the ACAD Section).

CD&H, ECS, and TPS subsystems will also undergo orbital calibration and checkout during this initial 2-week period. All operations are assumed to be concurrent parallel activities.

The science instrument calibration and checkout period has been baselined to occur over a 2-week period immediately following major subsystem calibration and checkout activities. The FUV, PI, and HPI test operations will be conducted in parallel with moderate interaction between the principal investigators (at POCC's) and the spacecraft controllers (at the SOCC). One additional week may be required to perform an integrated operations checkout prior to committing to the normal operations phase of the mission (science data gathering).

The mission is expected to proceed until EOL at approximately 2 years after launch.

System Requirements

A system definition analysis provided a preliminary set of MI system functional and physical requirements for the flight and ground segments, and are provided in documents published by the System Requirements division at MSFC. The first document is the “MI System Functional Decomposition.” The decomposition began with the top-level mission and user needs, operational concepts, and known external interfaces, and broke them down one layer at a time until a complete set of agreed-to MI functional requirements were developed. Figure 79 contains a summary of the MI system external interfaces in a context diagram.

The second document is the “MI System Specification” which provides the top-level system requirements. This documents what the system is supposed to do in terms of salient system and performance requirements. A diagram of the overall MI system is shown in figure 80. Other products provided by this analysis are a preliminary WBS and an MI connectivity diagram. The connectivity diagram is the result of the allocation of space segment functional requirements to hardware and/or software. An example of the connectivity diagram for the C&DH subsystem is shown in figure 81. The physical elements in the WBS are identified through the tailoring of a standard WBS format, and the functional elements of the WBS were identified by team consensus.

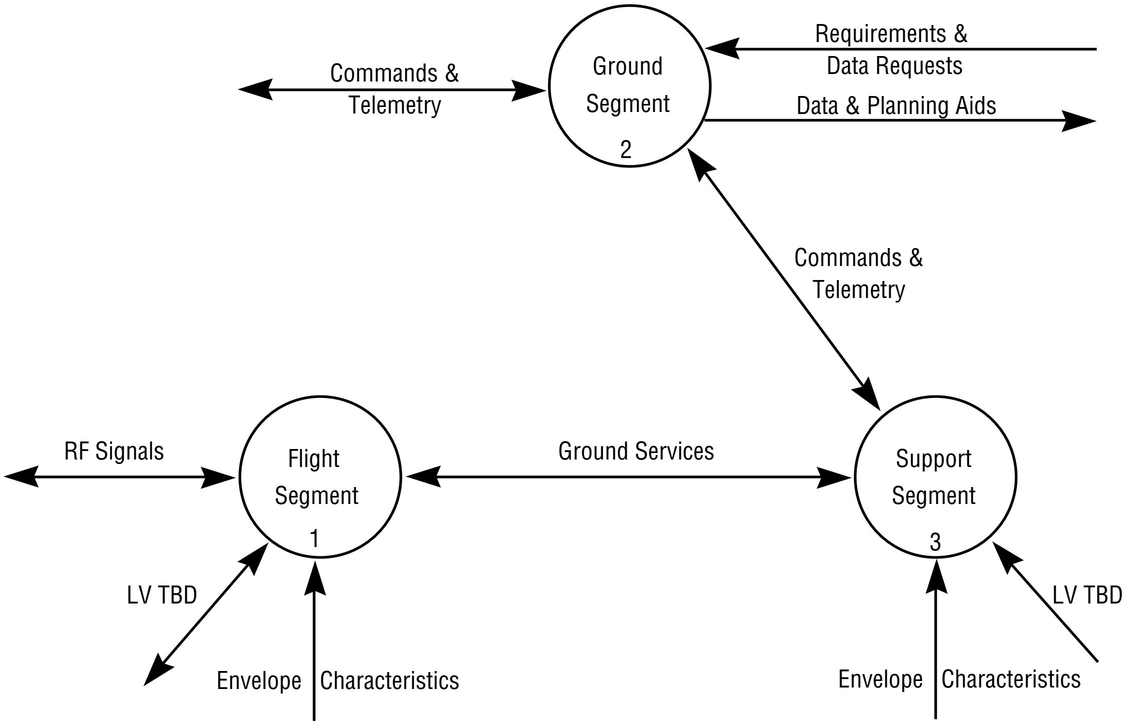
Commands &
Telemetry
Ground
Segment
2
Requirements &
Data Requests
Data & Planning Aids
Commands &
Telemetry
RF Signals
Flight
Segment
1
Ground Services
Support
Segment
3
LV TBD
Envelope
Characteristics
Envelope
Characteristics
LV TBD

FIGURE 79.—MI system external interfaces

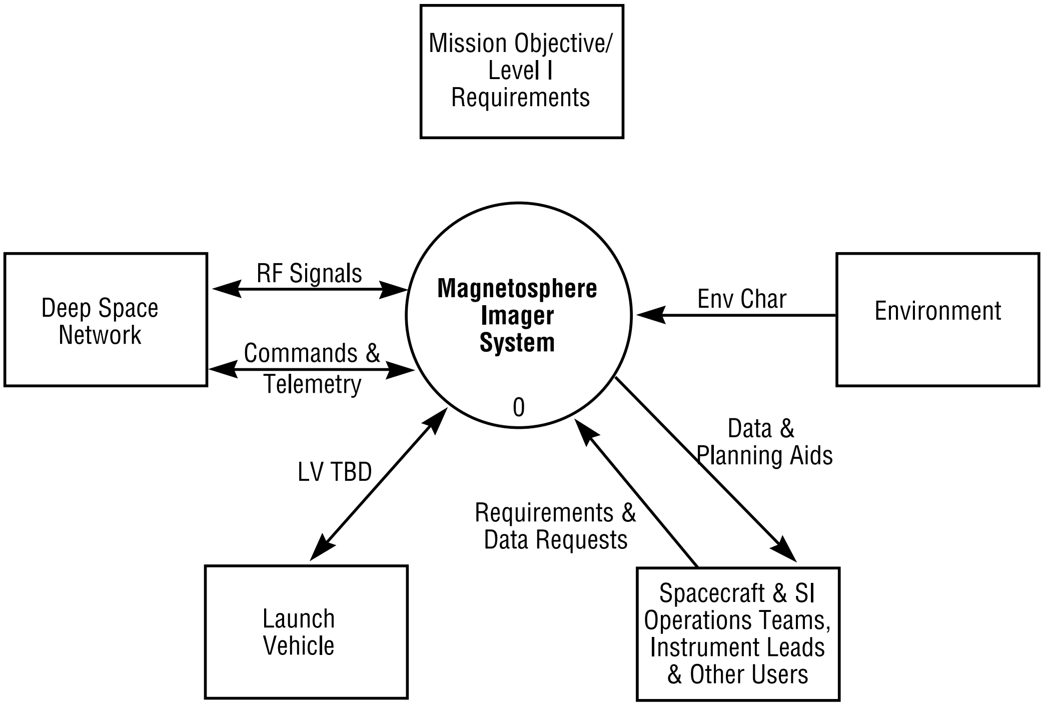
Mission Objective/
Level I
Requirements
Deep Space
Network
RF Signals
Commands &
Telemetry
Magnetosphere
Imager
System
0
Env Char
Environment
Data &
Planning Aids
LV TBD
Requirements &
Data Requests
Launch
Vehicle
Spacecraft & SI
Operations Teams,
Instrument Leads
& Other Users

FIGURE 80.—Overall MI system diagram.

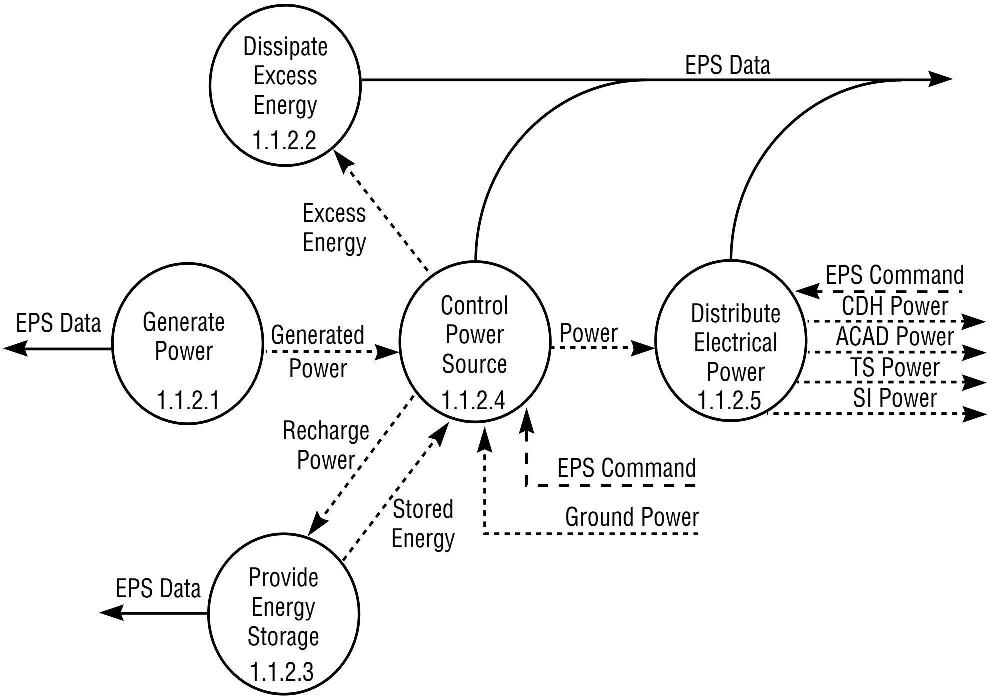
Dissipate
Excess
Energy
1.1.2.2
EPS Data
Excess
Energy
EPS Data
Generate
Power
1.1.2.1
Generated
Power
Control
Power
Source
1.1.2.4
Power
Distribute
Electrical
Power
1.1.2.5
EPS Command
CDH Power
ACAD Power
TS Power
SI Power
Recharge
Power
Stored
Energy
EPS Command
Ground Power
EPS Data
Provide
Energy
Storage
1.1.2.3

FIGURE 81.—C&DH connectivity diagram.

APPENDIX A

ACKNOWLEDGEMENTS

Membership of the MSFC Phase A Study Team

Since its inception in 1990, the (Inner) Magnetosphere Imager mission has undergone several conceptual changes and redefinitions. The following team list acknowledges the contributions to the study effort made by the MSFC engineers and scientists who have worked on the project in its many incarnations.

Reggie Alexander	Thermal Control
Brent Beabout	Flight Computer
Harold Blevins	Communications
Scott Bridge	Data Systems
Glenda Burruss	System Requirements
Tom Buzbee	Conceptual Art
Connie Carrington	Guidance and Control
Holly Chandler	Mass Analysis
Phillip Chu	Summer Faculty–Structures
Steve Chubb	Huntsville Operations Support Center Operations
Paul Cushman	System Requirements
Carmine De Sanctis	Director, Advanced Systems and Technology Office
Ted Edge	Electrical Power
Todd Freestone	Radio Frequency
Ray French	Schedules
Dennis Gallagher	Study Scientist
Greg Hajos	Configuration and Layout
Joel Herr	Environment
Melody Herrmann	Lead Engineer
Ken Hinkle	Communications and Data Handling
Bonnie James	Environment
Les Johnson	Study Manager

George Kearns	Propulsion
Ron Koczor	Program Development/Science and Engineering Chief Engineer
Larry Kos	Orbit Analysis
Dave Lanier	Operations
John Main	Summer Faculty–Avionics Requirements
Clovis Malmede	Requirements
Lou Maus	Power
Jim McCarter	Orbit Analysis
Mary Nehls	Materials
Jim Parker	Systems Requirements
Mike Polites	Attitude Control
Brian Price	Propulsion
Andy Prince	Cost Analysis
Larry Savage	Instrument Systems
Terri Schmitt	Launch Vehicles
Greg Schunk	Thermal Design
Wade Shrader	Flight Mechanics
Susan Spencer	Structures
John Watts	Radiation Environment
Philip West	Operations Development
Doug Willowby	Electrical Power
Fred Wills	Space Sciences Laboratory Support

Membership of the MI Science Definition Team

Thomas P. Armstrong (Chairman)	University of Kansas
A. Lyle Broadfoot	University of Arizona
Supryia Chakrabarti	Boston University
Louis A. Frank	University of Iowa
Dennis L. Gallagher (Study Scientist)	NASA Marshall Space Flight Center
James L. Green	NASA Goddard Space Flight Center
Ke Chaing Hsieh	University of Arizona
Barry H. Mauk	Johns Hopkins University Applied Physics Laboratory
David J. McComas	Los Alamos National Laboratory
Robert R. Meier	Naval Research Laboratory
Steven B. Mende	Lockheed Missiles and Space Corporation
Thomas E. Moore	NASA Marshall Space Flight Center
George K. Parks	University of Washington
Edmund C. Roelof	Johns Hopkins University Applied Physics Laboratory
Mark F. Smith	NASA Goddard Space Flight Center
Jan Sojka	Utah State University
Donald J. Williams	Johns Hopkins University Applied Physics Laboratory

Membership of the Radio Plasma Sounder Team

The Space Physics Division convened an ad hoc panel to evaluate the scientific feasibility and potential return from a radio plasma sounding (RPS) investigation of the magnetosphere. This possibility arose via suggestions that RPS might provide a valuable enhancement to MI science. This team met and provided its own report. However, highlights of their findings are included here under the category of potential scientific enhancements.

James L. Green (Chair)	NASA Goddard Space Flight Center
Robert F. Benson	NASA Goddard Space Flight Center
Wynne Calvert	University of Iowa
Donald Carpenter	Stanford University
Shing Fung	NASA Goddard Space Flight Center
Patricia Reiff	Rice University
Bodo Reinisch	University of Massachusetts, Lowell
William Taylor	Nichols Research Corporation

Liaisons

Dennis L. Gallagher	NASA Marshall Space Flight Center
Mark F. Smith	NASA Goddard Space Flight Center

NASA RESEARCH ANNOUNCEMENT (NRA)

Techniques and Technologies for Magnetospheric Imaging

In late 1993, MSFC released an NRA titled “Techniques and Technologies for Magnetospheric Imaging.” The NRA called for experimenters “to define scientific instruments, components of such instruments, and supporting techniques and technologies that might enhance the capability or performance of instruments suitable for imaging the Earth’s magnetosphere from space.” The full NRA text is included below. Approximately $500,000 was secured for the research efforts from the then-Code C, with additional funding from Code S.

NRA Solicitation

This NRA solicits proposals for the concept definition and research investigation of spacecraft-based instrument techniques and technologies that show promise for use in scientific investigations of the Earth’s magnetosphere.

The goal of this NRA is not to develop flight-qualified hardware, but rather to define scientific instruments, components of such instruments, and supporting techniques and technologies that will enhance the capability and/or performance of instruments suitable for imaging the Earth’s magnetosphere from space.

This NRA solicits proposals for research investigations that are distinctly separate from investigations selected for currently approved space flight missions. Therefore, proposals whose intent or purpose is to extend or directly supplement an investigation already selected for an approved space mission are not appropriate for this NRA. However, proposals for the definition of instrument concepts for long-duration space or suborbital flight through to the stage of laboratory (“brass board”) verification may be supported, provided the proposed activity is in the context of a clearly defined science investigation relevant to magnetospheric imaging. Funding of such instrument concepts does not guarantee a flight opportunity. New measurement concepts may be proposed, as well as methods to improve the performance of existing instruments. Instrument definition studies can take place at several stages, from feasibility studies, to conceptual design, to laboratory breadboarding of critical components and complete instruments. Proposers are encouraged to relate their study efforts as closely as possible to proposed, yet unapproved, future missions.

Thirty years of point-wise, in situ measurement has been inadequate to fully describe the complex, global behavior of the terrestrial magnetosphere. Further progress is dependent upon obtaining global perspectives of the magnetospheric system in addition to in situ measurement. A program to globally image important magnetospheric systems, when combined with existing and future in situ observations, will significantly enhance our understanding of global magnetospheric processes.

NASA’s Office of Space Science and Applications (OSSA) and MSFC are studying the feasibility of imaging component regions of the Earth’s inner magnetosphere from Earth orbit and from the Moon using the following general imaging techniques, hereafter referred to as Technical Areas (TA’s):

TA.1. The ring current and inner plasma sheet using energetic neutral atoms (ENA)

TA.2. The plasmasphere and outflowing ionosphere using extreme ultraviolet (UEUV)

TA.3. The electron and proton auroras using far ultraviolet (FUV) and x rays

TA.4. The geocorona using FUV

TA.5. Other unique imaging techniques.

Innovative techniques and technologies to enhance the capabilities of future magnetospheric imaging instruments or new analysis techniques that advance our ability to interpret images of optically thin plasmas are sought. The objective is to increase present magnetospheric imaging capabilities in the near term (three to five years or less) through the promotion of new techniques and technologies. Totally new concepts in these areas are welcome, however, they must be shown to have feasibility in the near term.

Proposals requiring restrictions on distribution of any aspect of the completed study and resulting technology must include a justification for the restriction and the time period for which the restriction would apply. Since it is important that the technology resulting from this NRA reside in the public domain, imposing restrictions on distribution of the subject technology could result in nonselection of the proposal. Proposers should therefore specify any restrictions to the open distribution of data used in or resulting from their proposed effort.

Proposals in response to this NRA should be formatted to include a simple Statement of Work (SOW) on any or all TA’s listed above. The scope of the overall study includes:

- Identification of the Technical Area (TA) their proposal supports.

- Description of how their proposal improves, enhances or demonstrates capability beyond the state-of-the-art in the specific TA.

- Description of the evolutionary path in which their proposal resides leading to a flight-quality magnetospheric imaging instrument.

- Recommendations for future work toward attaining this instrument goal.

Proposers should also highlight the offeror’s experience and capabilities in proposed areas and how the experience and capabilities would be employed in support of this study activity. It is anticipated that approximately four firm fixed price contracts may result from this NRA at an estimated funding level of between $50k–$75k per award, with a period of performance of up to 10 months each. Any award is subject to the availability of funds. This information is provided as a guide to the approximate level of activity MSFC has established will be required for the work to be accomplished.

Funded Research

Several innovative proposals were received and reviewed, with six contracts awarded. The research title, principal investigator, research summary, and approximate dollar value of the research are listed below. Copies of the final research reports are available for most of the projects and may be obtained by contacting Mr. Les Johnson, MSFC Magnetosphere Imager Study Manager, at 205–544–0614.

Surface Conversion Techniques for Low Energy Neutral Atom Imagers

Dr. Jack Quinn, Lockheed Palo Alto Research Laboratory, $72,843

The investigation focused on development of key technology elements for low energy neutral atom imaging. More specifically, the conversion of low energy neutral atoms to negatively charged ions upon reflection from specially prepared surfaces was investigated. This “surface conversion” technique appears to offer a unique capability of detecting, and thus imaging, neutral atoms at energies of 0.01–1 keV with high enough efficiencies to make practical its application to low energy neutral atom imaging in space. Such imaging offers the opportunity to obtain the first instantaneous global maps of Earth’s macroscopic plasma features and their temporal variation.

Through previous in situ plasma measurements, there exists a statistical picture of large scale morphology and local measurements of dynamic processes. However, with in situ techniques it is impossible to characterize or understand many of the global plasma transport and energization processes. A series of global plasma images would greatly advance our understanding of these processes and would provide the context for interpreting previous and future in situ measurements.

Fast neutral atoms, created from ions that are neutralized in collisions with exospheric neutrals, offer the means for remotely imaging plasma populations. Energy and mass analysis of these neutrals provides critical information about the source plasma distribution.

The flux of neutral atoms available for imaging depends upon a convolution of the ambient plasma distribution with the charge exchange cross section for the background neutral population. Some of the highest signals are at relatively low energies (well below 1 keV). This energy range also includes some of the most important plasma populations to be imaged, for example the base of the cleft ion fountain.

Neutral atom fluxes are typically many orders of magnitude lower than that of charged particles, thus a high efficiency detection technique is required. Conventional methods, such as electron beam or field ionization, do not have adequate efficiency for application to magnetospheric imaging. Carbon foil techniques are well established for space plasma instrumentation at energies above 1 keV. However, below 1 keV, the efficiency of carbon foil ionization falls off very rapidly. Integral techniques, using direct detection combined with UV rejection, offer reasonable efficiency but cannot identify the neutral atom’s mass or energy, and thus cannot address many of the key deconvolution and science issues.

In order to determine mass and energy of the imaged neutrals the incident atoms must be ionized for analysis. The use of surface conversion techniques to ionize incident neutrals offers the potential to fill the important energy gap below approximately 1 keV.

A neutral imaging instrument concept that uses the surface conversion technique was defined. Neutral and charged particles enter the instrument through an aperture and are collimated in energy and angle. Ions and electrons are deflected by an electrostatic deflector and broom magnet, allowing the remaining neutrals to impinge upon the conversion surface. The neutrals that undergo charge exchange at the surface (to become negative ions) are accelerated away and collected by a wide aperture, low aberration, lens which focuses the ions in the plane of a slit. Transmitted ions are imaged by a spherical analyzer and further accelerated onto a carbon foil entrance to a time-of-flight section.

Surface conversion of neutral atoms is well established in laboratory experiments where it was developed in conjunction with fusion research. However, its application to spaceflight instrumentation awaits resolution of important technological challenges. In particular, it is essential to: demonstrate the capability to manufacture conversion surfaces suitable for spaceflight, determine the efficiency of these surfaces, and investigate issues of surface stability. This research addresses these questions.

Measurement of Precipitation Induced FUV Emission and Geocoronal Lyman Alpha from the IMI Mission

Dr. Stephen Mende, Lockheed Palo Alto Research Laboratory, $105,600

One of the most promising techniques for remote sensing, imaging, and characterizing the magnetospheric particle population is measuring the directionality of the arriving fluxes or imaging the charged exchanged neutral particles. The flux of neutral particles is produced by the interaction of magnetospheric fast ions with the ambient neutral “population.” The goal of such imaging is to describe the distribution of the fast parent ions in magnetospheric regions. In order to derive the parent ion fluxes it is necessary to also measure the neutral densities which produce the charged exchanged neutrals. The measurement of the ambient neutral population can be accomplished in a remote sensing manner by measuring the solar Lyman alpha scattering by the neutrals. Knowing solar Lyman alpha fluxes would allow the computation of the density of the neutral hydrogen available for charge exchange.

Previously flown satellite imaging experiments have demonstrated the suitability of the vacuum ultraviolet region for remote sensing observations of auroral particle precipitation. In the wavelength region 120–145 nm, a downward viewing imager is uncontaminated by the Earth albedo and the intensity of the auroral emissions in most cases is competitive with the re-scattered light even during daylit conditions. These features permit the quantitative imaging of the auroral regions during day and night conditions. An instrument suitable for such observation should also have adequate wavelength resolution to separate key spectral features and simultaneously observe the Doppler profile of the auroral Lyman alpha line. The auroral Lyman alpha line provides a measure of the auroral ion precipitation which is a highly valued foot print generated by precipitating auroral protons.

In the evolution of the IMI program, it became clear that any near-term spacecraft program must utilize relatively modest size instruments. In order to economize in cost and instrument resource needs, it was suggested that a single multipurpose instrument be developed capable of: (1) measuring the scattered geocoronal Lyman alpha, (2) imaging the aurora day and night in the UV, and (3) observing proton precipitation. This research investigated approaches leading towards such a multipurpose single imaging instrument.

Simulation of Radio Sounding in the Plasmasphere

Professor Wynne Calvert, The University of Iowa, $75,000

The purpose of the research was to examine the density structure of the plasmasphere and determine the relevant mechanisms for producing radio echoes which can be detected by a radio sounder in the magnetosphere. As a part of the study we examined density irregularities, biteouts, and outliers of the plasmasphere; studied focusing, specular reflection, ducting, and scattering by the density structures expected to occur in the magnetosphere; and predicted the echoes which can be detected by a magnetospheric radio sounder.

The Structure of the Earth's Plasmasphere. International Sun-Earth Explorer and Combined Release and Radiation Effects Satellite wave data were analyzed for density structures which are relevant to radio sounding in the magnetosphere. The following features were identified and it was concluded that radio sounding is essential for understanding the plasmasphere:

- Irregularities at and beyond the plasmapause
- Biteouts inside the plasmasphere
- Outliers.

Echo Geometry and Focusing by the Magnetopause. The effects of a varying radius of curvature and ripples in the magnetopause were analyzed in order to determine the echo geometry and delectability of these features, including:

- Estimates for the strength of spread echoes from the magnetopause
- The geometry of multiple echoes from different directions
- Focusing at the center of curvature of the magnetopause.

The Feasibility of Radio Sounding in the Magnetosphere. An analysis of the feasibility of radio sounding in the magnetosphere was completed and submitted for publication. The new features of radio sounding determined by this study are as follows:

- Derivation of new formula for focusing by curved surfaces
- Predicted echo flux of the plasmapause as a function of latitude
- Analysis of transmitted power and receiver tuning
- Dependence of angular resolution on signal-to-noise ratio
- Optimum three-dimensional spatial resolution.

Ray-Tracing Studies. Ray-tracing studies were carried out in order to verify the predicted echoes from the plasmasphere and magnetopause:

- Calculation of plasmagrams showing echo delay as a function of frequency
- Confirmation of predicted echo power flux.

Wave Ducting. An analysis of wave ducting by magnetic-field-aligned density irregularities was completed, submitted, and accepted for publication. The new results of this study are as follows:

- Seven regions of ducting in the O, X, W, and X wave modes
- Calculations of the duct strength as a function of frequency and density.

UV Rejection for Low Energy Neutral Atom Imaging

Dr. Herbert Funsten, Los Alamos National Laboratory, $69,500

In space, plasma ions can be neutralized by charge exchange with cold neutral species or recombination with ambient electrons. The neutralized plasma ions, which follow ballistic trajectories and can be remotely detected, carry information about the source plasma region such as the velocity distribution, composition, and density. Therefore, imaging these neutral atoms provides an important method to characterize the global structure and dynamics of space plasmas.

A fundamental problem associated with detection of neutral atoms is separation from the ambient EUV to which detectors (e.g., microchannel plates) used in neutral atom detectors are sensitive. The EUV fluxes, predominantly hydrogen Lyman alpha, are >1011 cm^{-2}/second^{-1} from the Sun and can reach >10^{9} cm^{-2}/second^{-1} reflected from the terrestrial geocorona. Therefore, the crucial mechanism for neutral atom detection is separation of the neutral atoms from the EUV.

Different techniques for this separation are used for the energy regimes of neutral atoms listed in table 22. For neutral atom energies $\geq$ 30 keV/amu (ENA's), a thick carbon foil can be employed to directly block the EUV while the neutral atom passes through to the detector section of the instrument. For neutral atom energies $\leq$0.8 keV (VLENA's), oxygen and hydrogen are first negatively ionized by reflection from a low work function surface and are subsequently removed from the EUV by electrostatic deflection into a detector section. In the intermediate energy range between approximately 0.8 keV and 30 keV, the low energy neutral atoms (LENA's) are ionized by transit through an ultrathin foil and are subsequently electrostatically removed from the EUV and enter a detector section. An emerging technology uses free-standing transmission gratings that can block EUV but through which neutral atoms of any energy can pass. Typically, the detector section of each type of technique provides at a minimum a coincidence measurement due to the anticipated low neutral atom flux at the measurement point.

TABLE 22.—*Techniques used in energy regime separations of neutral atoms*.

Characteristic Energy Range	Method for Removal From EUV	Detector Type
$E \geq 30$ keV: ENA's	Thick EUV blocking foil	Microchannel plates (MCP's); possibly with solid state detector
0.8 keV $\leq E \leq$ 30 keV: LENA's	LENA ionization using ultrathin foil and subsequent electrostatic deflection from EUV	MCP's
$E \leq 0.8$ keV: VLENA's	LENA ionization via reflection from low work function surface and subsequent electrostatic deflection from EUV; high frequency shutter light trap	MCP's
$E \geq 0.2$ keV: all neutral atoms	Free-standing transmission gratings	MCP's

As a part of the research, laboratory results are presented on beam-foil interaction properties that are used to define LENA instrument operation specification. Second, laboratory results describing transmission of atomic projectiles and EUV through free-standing transmission gratings are presented.

Development and Evaluation of Multilayer Coatings for the O^+834 Imagers for IMI

Professor Supriya Chakrabarti, Boston University, $70,645

One of the goals of the MI mission is to image the plasmasphere and upflowing O^+ ions using O^+834A emissions. Unfortunately, although this is a highly desirable measurement, technical challenges in developing suitable optical coatings have prohibited the adoption of such an imager in the core instrument category for the mission. There have been three reports of theoretical designs of filters suitable for MI applications, of which only two groups have reported the fabrication of prototype filters. During the research, a family of filter coatings to selectively reflect 834A with high efficiency while suppressing reflectance at 1216A, 1026A, and other specific FUV/EUV wavelengths was developed.

The spectral characteristics of coatings presently available severely limit the performance of a class of magnetospheric imagers that operate at the 834A wavelength. The intensity of the 1216A line is several orders of magnitude brighter than the 834A line, placing extreme demands on the filter coating performance. The earlier filter fabrications were conducted under less than ideal manufacturing conditions required for the chosen materials. The filters for this research were developed by Barr Associates, a leading manufacturer of optical filters used in ground and space based applications. Barr was responsible for filter fabrication, while the Center for Space Physics of Boston University evaluated their optical performance.

The most promising approaches to isolate the 834A line in imaging instruments are wavelength selective reflecting filters, transmissive bandpass filters, and wavelength-selective photo cathodes.

There are several challenges to the development of an 834A reflecting filter. First, there are several bright emission features in the terrestrial nightglow (e.g., H I 1216A, 1026A, He I 584A, He II 304A), which must be suppressed while allowing high reflectivity at 834A. Secondly, since these filters are very sensitive to the angle of incidence on the filter, the optical design must be such that it provides a high angle of acceptance for the instrument while maintaining a small range of incidence angles on the mirror and filter.

Several instrument designs have been proposed and built. The simplest consists of a single focusing mirror, a broad band transmission filter for visible light rejection, and a microchannel plate detector. The mirror, in this design, provides a substrate for a selective reflecting filter. With only one reflection, most of the wavelength selectivity must be achieved with one coating.

This means that the night-glow contamination (especially 1216A) must be rejected, by a factor of 1,000 by the reflective coating. A thin metal film visible and Lyman alpha rejecting transmission filter can also be used.

Another approach utilizes two or more mirror surfaces. In this case, very high 834A reflectively must be achieved while the 1216A suppression requirements of any single reflection system may be relaxed. For this type of system the visible blocking transmissive filter can probably be eliminated.

Examples of each type filter were investigated. During the effort, Barr built on previously reported design concepts. A1/MgF$_2$/Si due to Chakrabarti et al.; and A1/MgF$_2$/Ge due to Zukic et al.

Instrument Definition of a Radio Sounder for Global Magnetospheric Imaging

Professor Bodo Reinisch, The University of Massachusetts at Lowell, $120,953

Magnetospheric radio sounding from space will provide remote density measurements of unprecedented precision and coverage in the plasmasphere, inner magnetosphere and magnetopause, from which the structure, inter-relationship, and variations of different plasma regions can be determined. It has been suggested that a space-borne Radio Plasma Imager (RPI) could provide a unique global view of the magnetosphere from these measurements. These measurements would also yield important physical parameters that reveal the underlying structure of remote plasma regions, thereby providing a framework for the interpretation of images obtained by other techniques. The incorporation of an RPI on the proposed IMI has been suggested.

The objectives of the research were to develop techniques for very low frequency sounding which would be necessary for determining the densities of remote tenuous magnetospheric plasmas.

Research was conducted into extending the lower frequency limit of the highly successful University of Massachusetts Lowell Digisonde Portable Sounder from 1 MHz down to 100 kHz as a first step in achieving the goal of reducing the frequency to 3 kHz as required for magnetospheric sounding from space. Breadboard components were developed and field tested in order to verify that the power generated from such a system follows the current theoretical calculations. These field tests included antenna impedance measurements on a dipole antenna of the size (0.5 km) considered for spaceflight. In addition, the feasibility of achieving a very high digital signal processing gain (so as to be able to operate at very low power) was investigated.

Radio sounding is a proven technique in the ionosphere which now promises to provide remote density measurements of remarkable precision and spatial resolution in the magnetosphere. These measurements will be pertinent to future studies directed toward understanding the basic physical processes that determine magnetospheric structures and drive magnetospheric dynamics.

APPENDIX C

SOLAR ARRAY RADIATION ANALYSIS FOR THE MAGNETOSPHERE IMAGER

Sverdurp Corp.

George C. Marshall Space Flight Center
Science and Engineering
Contract NAS8-37814

Solar Array Radiation Analysis for the Magnetosphere Imager

Report No.: 212-010-94-011

Prepared By:

Joel L. Herr

August 1994

Sverdrup Technology, Inc.
MSFC Group
620 Discovery Drive
Huntsville, AL 35806

TABLE OF CONTENTS

Page

Table of Contents ---------- i
List of Figures ---------- ii
List of Tables ---------- iii

1.0 Introduction ---------- 1
1.1 Overview ---------- 1
1.2 Background ---------- 1

2.0 Radiation Analysis for MI Solar Array ---------- 3
2.1 Radiation Environment ---------- 3
2.1.1 Trapped Radiation Environment Models ---------- 3
2.1.2 Solar Flare Proton Environment Model ---------- 3
2.2 Equivalent Fluence Procedure ---------- 4
2.2.1 Trapped Electrons and Protons Equivalent Fluence Example ---------- 4
2.2.2 Solar Flare Protons Equivalent Example ---------- 5
2.3 MI Equivalent Fluence Results ---------- 6

3.0 Conclusion ---------- 9

References ---------- 10

Appendix – Radiation Environment Description

LIST OF FIGURES

Page

Figure 1. Solar Flare Proton Differential Flux Data and Straight Line Fit, 4800 km Perigee. ---------- 14

Figure 2. Trapped Electron Radiation Environment 1 MeV Electron Equivalent Fluence as a Function of Orbit Perigee. ---------- 15

Figure 3. Trapped Proton Radiation Environment 1 MeV Electron Equivalent Fluence as a Function of Orbit Perigee. ---------- 16

Figure 4. Solar Flare Proton Radiation Environment 1 MeV Electron Equivalent Fluence as a Function of Orbit Perigee. ---------- 17

Figure 5. 1500 km Perigee Radiation Environment 1 MeV Electron Equivalences. ---------- 18

Figure 6. 3800 km Perigee Radiation Environment 1 MeV Electron Equivalences. ---------- 19

Figure 7. 4800 km Perigee Radiation Environment 1 MeV Electron Equivalences. ---------- 20

Figure 8. 1 Re Perigee Radiation Environment 1 MeV Electron Equivalences. ---------- 21

Figure 9. Combined 1 MeV Electron Equivalent Fluence as a Function of Orbit Perigee. ---------- 22

LIST OF TABLES

Page

Table 1. Equivalent 1 MeV Electron Fluence for the Trapped Electron Environment, 4800 km Perigee, GaAs/Ge Solar Cells, 6 mil Coverslide Thickness. -- 11

Table 2. Equivalent 1 MeV Electron Fluence for the Trapped Proton Environment, 4800 km Perigee, GaAs/Ge Solar Cells, Isc Relative Damage Coefficients, 6 mil Coverslide Thickness. ------------------------------------- 12

Table 3. Equivalent 1 MeV Electron Fluence Summary for MI GaAs/Ge Solar Cells. --- 13

1.0 INTRODUCTION

1.1 OVERVIEW

The following report presents the results of an ionizing radiation analysis conducted by EL54 for the Magnetosphere Imager (MI) mission. A description of the radiation environment that MI is expected to experience during its two year mission was provided to the MI phase A team by the Space Science Lab, ES62. The description was obtained using standard ionizing radiation computer programs and was duplicated by EL54 to ensure EL54's proper use of the programs. The radiation environment was determined for four different orbits assuming solar maximum conditions, and then related to 1 MeV electron fluences to aid the MI phase A team in estimating solar array degradation.

1.2 BACKGROUND

The particles associated with ionizing radiation are categorized into three main groups: trapped radiation belt particles, cosmic rays, and solar flare particles. The high energy particles comprising the radiation environment can travel through spacecraft materials and deposit energy. This process causes atomic displacement or leaves a stream of charged atoms in the incident particle's wake. Spacecraft damage includes decreased power production by solar arrays, failure of sensitive electronics, and increased background noise in sensors. Modern electronics are becoming increasingly sensitive to ionizing radiation.[1]

In the case of solar arrays, ionizing radiation can degrade solar cell electrical performance. As radiation interacts with the solar cells, atomic displacements are created. As a result, the mean free path for the electronics decreases and fewer electrons can make it from the interior of the cell to the space charge region. Consequently, the current and the power that is produced by the cell decreases.

The amount of damage to solar cells depends on the type of solar cells being used, the type and thickness of the coverslide, and on the energy of the radiation particles impinging on the cells. The amount of damage is quantified by specifying the percent decrease in solar cell engineering output parameters (i.e., cell short circuit current, open circuit voltage and maximum power) after being exposed to radiation. The analysis is complicated by the fact that no precise theoretical treatment is available to determine the amount of damage caused by irradiation as a function of particle energy, species and solar cell characteristics. Therefore, the approach has been to experimentally determine the damage caused by various types of irradiation in the laboratory. The experimental approach is complicated, however, because the species of particles present in space have a wide range of energies. A comprehensive experimental treatment would therefore involve determining the damage caused by many different species of particles at all practical energies occurring in the space environment.

The problem necessitated a method of describing the damage caused by the different types of radiation occurring in space in terms of a radiation environment that can be produced in the laboratory. This concept, known as the ‘damage equivalent fluence scheme,’ involves two steps. The first step is to adequately describe the degradation of a solar cell exposed to a chosen type of radiation under laboratory conditions. The second step is to relate the damage caused by the different types of space radiation to a damage equivalent fluence of the chosen laboratory radiation.

1 MeV unidirectional (i.e., impinging normal to the solar cell surface) electrons have been used as a basis of the damage equivalent fluence scheme for electrons because they form a significant component of space radiation and they can be produced relatively easily in the laboratory. 10 MeV protons have been used as a basis for the proton radiation environment.[2]

Relating the damage caused by the different types of space radiation to 1 MeV electron or 10 MeV proton fluences requires the use of relative damage coefficients which are determined from experimental results, and by accounting for the omnidirectional nature of the space radiation and the thickness and properties of solar cell coverslides. The omnidirectional fluence of electrons or protons at a given energy impinging on a solar cell covered by a coverslide of certain thickness is multiplied by the relative damage coefficient for electrons or protons at that energy and coverslide thickness to reduce the fluence to unidirectional 1 MeV electrons or 10 MeV protons. The equivalent fluences for all particle energies are summed and the result compared with experimental studies relating the amount of solar cell degradation to the total fluence of 1 MeV electrons or 10 MeV protons. The amount of damage is quantified by specifying the percent decrease in solar cell engineering output parameters, i.e., cell short circuit current, open circuit voltage and maximum power.

Experimental studies further indicate that the damage of silicon solar cells caused by a fluence of normally incident 10 MeV protons is approximately the same as the damage caused by the fluence of 1 MeV electrons that is 3000 times that of the 10 MeV proton fluence. [2] For gallium arsenate on germanium (GaAs/Ge) solar cells, a 1 MeV electrons fluence that is 1000 times that of a 10 MeV proton fluence causes approximately the same amount of damage.[3] Therefore, it is possible to reduce the proton and electron space radiation environment to an equivalent 1 MeV electron fluence for the purposes of solar cell degradation analysis.

2.0 RADIATION ANALYSIS FOR MI SOLAR ARRAY

2.1 RADIATION ENVIRONMENT

Trapped electrons, trapped protons and solar flare protons will cause the most damage to the MI solar arrays. Cosmic rays are important in calculating single upset event phenomena in electronics, but do not contribute greatly to solar array degradation. The MI orbit will pass through the outer electron radiation belt during every orbit and the amount of time spent in the proton radiation belt will depend on the perigee and possible orbital perturbations during the mission. The high apogee and high inclination of the orbit makes solar flare protons an important component of the radiation environment because the attenuation of the solar flare protons by the Earth's geomagnetic field is less during the apogee portion of the MI orbit.

2.1.1 Trapped Radiation Environment Models

A description of the trapped electron and proton radiation environment that MI is expected to experience during its two year mission was provided to the MI phase A team by the Space Science Lab, ES62. The data was obtained by running standard ionizing radiation computer tools, ORBIT and VETTE ORP. ORBIT is a uniform time-step orbital program that passes orbital parameters on to VETTE ORP. VETTE ORP contains the AE8MAX and AE8MIN electron environment and the AP8MAX and AP8MIN proton environment models that describe the geomagnetically trapped particle environment. In order to determine solar cell degradation, the radiation environments need to be described in terms of an integrated flux which is defined as the number of particles above each energy level, per unit area, per unit time, that impinge on the solar cells. The Appendix shows the integrated flux tables provided by ES62 and duplicated by EL54 to ensure EL54's proper use of the programs.

2.1.2 Solar Flare Proton Environment Model

A description of the solar flare proton radiation environment that MI is expected to experience during its two year mission was provided to the MI phase A team by the Space Science Lab, ES62. A feynman flare 90% flare flux was assumed with a power law spectrum beyond 60 MeV. The differential flare proton fluence as a function of proton energy for a two year mission is given by

$$\phi(E) = 2.02 \times 10^{13}\ E^{-3}\ (\text{protons/cm}^2/\text{MeV})(1)$$

Equation 1 gives the flare proton fluence that impinges on the outside of the Earth's magnetosphere as a function of proton energy, and must be adjusted to account for the attenuation of the protons by the Earth's geomagnetic field. The attenuation depends on the spacecraft orbit and on the energy of the solar protons such that higher energy protons are able to penetrate farther into the Earth’s atmosphere. The fraction of protons that are able to penetrate to a particular spacecraft orbit is determined by multiplying the fluence by a geomagnetic transmission fraction which is a function of proton energy and the orbit of the spacecraft. The geomagnetic transmission fractions have values increasing from zero to one with increasing proton energy and are obtained by running the GEOMAG2 computer program which is an auxiliary program associated with the CREME computer programs.[4]

Output from the GEOMAG2 program given to EL54 by SSL ES62 was duplicated to ensure EL54’s proper use of the program. The adjusted differential fluence provided by ES62 are shown in the Appendix. These values are used to determine the equivalent 1 MeV electron fluence of the solar flare protons. This procedure is described in Section 2.2.2 of this document.

2.2 EQUIVALENT FLUENCE PROCEDURE

To determine the equivalent fluence of 1 MeV electrons or 10 MeV protons, the different components of the radiation environment need to be described in terms of an averaged integrated flux at a range of energies. An integrated flux is defined as the number of particles above each energy level, per unit area, per unit time, that impinge on the solar cells. The difference between the averaged integrated flux, or delta flux, between each consecutive energy level is multiplied by a relative damage coefficient to convert the flux into an equivalent 1 MeV electron fluence for electrons and an equivalent 10 MeV proton fluence for protons. The relative damage coefficients are a function of the coverslide thickness, the energy of the radiation, and the radiation particle species. The coefficients can be found in graphical and tabular form, and interpolation may be necessary if the energies associated with the coefficients do not match those associated with the integrated fluxes. The equivalent fluences for all particle energies are summed to give a total equivalent fluence.

2.2.1 Trapped Electrons and Protons Equivalent Fluence Example

As an example, the steps involved in determining the equivalent 1 MeV electron fluence of the trapped electron and proton radiation environments during solar maximum conditions for the MI orbit are described. The parameters describing the MI orbit, assuming a perigee of 4800 km, are as follows:

apogee: 7 Earth radii
perigee: 4800 km
inclination: 90 degrees
semi-major axis: 31101 km
eccentricity: .64059

The ORBIT program was run using the above orbital description, and the results were passed onto VETTE ORP from which the trapped electron and proton environment description was obtained using the AE8MAX electron and AP8MAX proton environment models. Output from VETTE ORP was chosen to be in the form of integrated flux tables for the electrons and protons. This description shown in the Appendix was provided to the MI phase A team by the Space Science Lab, ES62. However, the energies levels associated with the integrated flux tables did not match the energies associated with the relative damage coefficients obtained from ASEC for GaAs/Ge solar cells. The integrated flux tables therefore had to be interpolated which introduced some error. To remove the error due to interpolation, VETTE ORP was run again using the identical orbital description used by ES62 but with different output energy ranges for the integrated flux tables to match the damage coefficient energy levels.

Tables 1 and 2 demonstrate the equivalence fluence procedure for the electrons and protons respectively. The second column of Tables 1 and 2 is the averaged integrated flux at each energy level 'E1', and the third column gives the difference in the averaged integrated flux, or delta flux, values between each consecutive energy level obtained from VETTE ORP. The fourth column gives the relative damage coefficients for a coverslide thickness of 6 mil. A 6 mil coverslide prevents electrons with an energy less than 0.24 MeV and protons with an energy less than 4.0 MeV from reaching the solar cell. Therefore, the damage coefficients are zero for particle energies less than these values.

The delta flux values in the third column are multiplied by the relative damage coefficients to give equivalent fluences shown in the fifth column. The values in the fifth column of Tables 1 and 2 are summed to give the total 1 MeV electron and 10 MeV proton equivalent fluences respectively. Since one 10 MeV proton does approximately the same amount of damage as 1000 1 MeV electrons in a GaAs/Ge solar cell, the total equivalent 10 MeV proton fluence is multiplied by 1000 to convert to a total of 1 MeV electron fluence. The two equivalent fluences are added for a combined trapped radiation 1 MeV electron fluence value of 1.74 E15 electrons per centimeter squared for a two year mission.

2.2.2 Solar Flare Protons Equivalent Fluence Example

The steps involved in determining the equivalent 1 MeV electron fluence of the solar flare protons are essentially the same as those applied to the trapped radiation environment. The only difference, however, is that the solar flare proton environment given to the MI phase A team by ES62 and shown in the Appendix was in the form of a differential fluence at a range of energies. A differential fluence is defined as the number of particles per unit area, per MeV, that impinge on the solar cells during the mission. The integrated fluence above a certain energy is obtained by integrating the differential fluence function over energy between the limits of the chosen energy level and infinity. The differential fluence function is obtained by fitting a curve to the differential fluence data points. Plotting the differential fluence versus energy in MeV on a log-log plot, the data points are nearly a straight line implying a power law relation, i.e., the differential fluence equals the energy in MeV to some power times a constant. The constant and the exponent can be determined by fitting a straight line to the log-log plot and determining the slope (the exponent) and the y-intercept (the constant).

Figure 1 shows the solar flare proton differential fluence versus energy and the straight line fit to the data for solar maximum condition assuming a perigee of 4800 km. The equation for the straight line was found to be

$$1n(\phi_{diff}) = m\ 1n(E) + 1n(b)(2a)$$

or,

$$\phi_{diff} - b\ E^{m} = 1.11098 \times 10^{13}\ E^{-2.924}(2b)$$

where m is the slope and b is the y-intercept of the fitted straight line. The values for m and b for the case of a 4800 km perigee are given in equation (2b).

Integrating equation (2b) over energy between the limits of an energy 'E' and infinity, and noting that the result is zero at infinity, the integrated fluence for a 4800 km perigee is given by the equation

$$\phi_{int\,eg} = \int_{E}^{\infty} \phi_{diff} dE = b\,E^{(m+1)} / |m+1| = 5.774 \times 10^{12}\ E^{-1.924}(3)$$

which can be evaluated at the energies associated with the relative damage coefficients.
The same relative damage coefficients for the 6 mil coverslide thickness used for the trapped protons are applied to the solar flare proton delta fluences resulting in an equivalent 1 MeV electron fluence of 3.88×10^{15} for the combined trapped and solar flare radiation environment.

2.3 MI EQUIVALENT FLUENCE RESULTS

The equivalent 1 MeV electron fluence was determined for four different MI orbits (the three orbits evaluated by ES62 and an orbit with a 3800 km perigee all having a seven Earth radii apogee) assuming solar maximum conditions and a two year mission. The 38900 km perigee orbit corresponds to a possible drop in perigee from 4800 km to 3800 km due to gravitational perturbations by the moon. The solar cells were assumed to be GaAs/Ge, and five coverslide thicknesses were evaluated. Table 3 shows the 2 year, 1 MeV electron equivalent fluences as a function of perigee and coverslide thickness. These values can be compared with experimental studies relating the amount of solar cell degradation to the total fluence of 1 MeV electrons to estimate the percent decrease in output from the MI solar cells. Figures 2–9 demonstrate the trends shown in Table 3.

The trapped electron 1 MeV equivalences increase while the trapped and solar proton 1 MeV equivalences decrease with increasing perigee. The decrease in the trapped and solar proton 1 MeV equivalences is large enough to result in an overall decrease in the total 1 MeV equivalences as perigee increases.

The 1 MeV equivalences of all the components of the radiation environment decrease with an increase in the solar cell coverslide thickness. A thicker coverslide prevents more of the lower energy radiation particles from reaching the solar cell. Since the spectrum of the trapped and solar flare radiation environments are peaked at the lower energies, an increase in coverslide thickness reduces the damage to the solar cell.

3.0 CONCLUSION

The radiation environment that MI is expected to experience during its two year mission has been reduced to an equivalent 1 MeV electron fluence to aid the MI phase A team in estimating solar array degradation. The values obtained can be compared with experimental studies (relating the amount of solar cell degradation to the total fluence of 1 MeV electrons) to estimate the percent decrease in output from the MI solar array as a function of coverslide thickness and orbit perigee. The results show that increasing the coverslide thickness and/or increasing the orbit perigee will decrease the solar array degradation.

The results contained in this report should be expanded to account for possible orbital perturbations during the two year mission. For example, gravitational perturbations by the moon could lower or even raise the perigee of the orbit. These changes should be accounted for by calculating the average equivalent 1 MeV electron fluence based on the amount of time spent in the different perigee orbits.

REFERENCES

1. ‘The Natural Space Environment: Effects on Spacecraft,’ Electromagnetics and Environments Branch, NASA MSFC, March 1994.

2. Tada, H.Y., et al., ‘Solar Cell Radiation Handbook, Third Edition,’ JPL Publication 82–69, Nov. 1982.

3. Private Communication, Douglas Willowby.

4. Adams, H.J. Jr., ‘Cosmic Ray Effects on Microelectronics, Part IV,’ NRL report 5901, December 1986.

Table 1. Equivalent 1 MeV Electron Fluence for the Trapped Electron Environment, 4800 km Perigee, GaAs/Ge solar cells, 6 mil coverslide thickness.

ELECTRON ENERGY E1 (MeV)	AVERAGED FLUX ABOVE E1 (PER DAY)	AVERAGED INTEGRAL FLUX IN ENERGY BAND	RELATIVE DAMAGE COEFF	EQUIV 1 MeV ELECTRONS
0.24	2.64 E11	2.89 E10	6.8 E–07	1.97 E04
0.26	2.35 E11	2.00 E10	5.55 E–06	1.11 E05
0.28	2.15 E11	1.80 E10	2.77 E–05	4.99 E05
0.3	1.97 E11	1.63 E10	8.54 E–05	1.39 E06
0.32	1.80 E11	2.82 E10	0.000342	9.64 E06
0.4	1.29 E11	2.37 E10	0.005163	1.20 E08
0.45	1.05 E11	1.90 E10	0.03643	6.92 E08
0.5	8.61 E10	2.24 E10	0.06232	1.40 E09
0.6	6.37 E10	1.59 E10	0.1215	1.93 E09
0.7	4.78 E10	1.03 E10	0.1835	1.89 E09
0.8	3.75 E10	6.95 E09	0.2467	1.72 E09
0.9	3.05 E10	5.57 E09	0.3083	1.72 E09
1.0	2.49 E10	7.41 E09	0.3704	2.75 E09
1.2	1.75 E10	5.13 E09	0.4947	2.54 E09
1.4	1.24 E10	3.62 E09	0.6146	2.23 E09
1.6	8.78 E09	2.57 E09	0.7334	1.89 E09
1.8	6.21 E09	1.81 E09	0.8516	1.54 E09
2.0	4.41 E09	1.51 E09	0.9643	1.46 E09
2.25	2.90 E09	9.83 E08	1.103	1.08 E09
2.5	1.91 E09	7.06 E08	1.203	8.49 E08
2.75	1.21 E09	4.43 E08	1.341	5.94 E08
3.0	7.64 E08	2.88 E08	1.501	4.32 E08
3.25	4.75 E08	1.79 E08	1.637	2.93 E08
3.5	2.97 E08	1.23 E08	1.76	2.17 E08
3.75	1.74 E08	7.13 E07	1.885	1.34 E08
4.0	1.02 E08	7.06 E07	2.03	1.43 E08
4.5	3.17 E07	2.23 E07	2.291	5.11 E07
5.0	9.37 E006	6.91 E06	2.54	1.76 E07
5.5	2.46 E006	1.89 E06	2.755	5.21 E06
6.0	5.76 E06	5.63 E05	2.987	1.68 E06
7.0	1.30 E04	1.03 E04	3.44	4.47 E04
8.0	0.0	0.0	3.884	0.0
9.0	0.0	0.0	4.328	0.0
10.0	0.0	0.0	4.733	0.0
15.0	0.0	0.0	6.709	0.0
20.0	0.0	0.0	8.45	0.0
25.0	0.0	0.0	10.04	0.0
30.0	0.0	0.0	11.61	0.0
40.0	0.0		14.49	0.0
		TOTAL 1 MeV		2.61 E10 (PER DAY)
		ELECTRON FLUENCE:		1.90 E13 (2 YEARS)

Table 2. Equivalent 1 MeV Electron Fluence for the Trapped Proton Environment, 4800 km Perigee, GaAs/Ge solar cells, Isc Relative Damage Coefficients, 6 mil coverslide thickness.

PROTON ENERGY E1 (MeV)	AVERAGED FLUX ABOVE E1 (PER DAY)	AVERAGED INTEGRAL FLUX IN ENERGY BAND	RELATIVE DAMAGE COEFF	EQUIV 10 MeV PROTONS
4.0	2.17 E09	3.14 E08	0.8588	2.69 E08
4.2	1.85 E09	2.68 E08	1.134	3.04 E08
4.4	1.59 E09	2.28 E08	1.16	2.65 E08
4.6	1.36 E09	1.95 E08	1.153	2.25 E08
4.8	1.16 E09	3.08 E08	1.175	3.62 E08
5.2	8.55 E08	2.25 E08	1.298	2.92 E08
5.6	6.30 E08	1.65 E08	1.23	2.03 E08
6.0	4.65 E08	9.35 E07	1.158	1.08 E08
6.4	3.72 E08	7.45 E07	1.086	8.09 E07
6.8	2.97 E08	5.94 E07	1.017	6.04 E07
7.2	2.38 E08	4.74 E07	0.9575	4.54 E07
7.6	1.90 E08	3.78 E07	0.8971	3.39 E07
8.0	1.50 E08	5.06 E07	0.8465	4.28 E07
9.0	1.02 E08	3.37 E07	0.7347	2.48 E07
10.0	6.82 E07	1.87 E07	0.68	1.27 E07
11.0	4.95 E07	1.35 E07	0.5909	7.98 E06
12.0	3.59 E07	9.80 E06	0.5055	4.95 E06
13.0	2.61 E07	7.11 E06	0.4642	3.30 E06
14.0	1.90 E07	5.16 E06	0.4295	2.22 E06
15.0	1.38 E07	2.78 E06	0.4067	1.13 E06
16.0	1.11 E07	3.99 E06	0.3722	1.49 E06
18.0	7.08 E06	2.54 E06	0.3263	8.29 E05
20.0	4.54 E06	1.28 E06	0.2913	3.73 E05
22.0	3.25 E06	9.19 E05	0.2715	2.50 E05
24.0	2.33 E06	6.58 E05	0.2439	1.60 E05
26.0	1.68 E06	4.71 E05	0.2301	7.21 E04
28.0	1.20 E06	3.38 E05	0.2133	7.21 E04
30.0	8.67 E05	2.86 E05	0.2016	5.77 E04
34.0	5.80 E05	1.91 E05	0.1882	3.59 E04
38.0	3.90 E05	1.27 E05	0.1683	2.14 E04
42.0	2.62 E05	8.52 E04	0.1535	1.31 E04
46.0	1.77 E05	5.74 E04	0.1462	8.39 E03
50.0	1.20 E05	3.25 E04	0.1369	4.45 E03
55.0	8.74 E04	2.33 E04	0.1264	2.95 E03
60.0	6.41 E04	1.46 E04	0.1196	1.75 E03
65.0	4.95 E04	1.12 E04	0.1124	1.26 E03
70.0	3.83 E04	1.50 E04	0.1082	1.62 E03
80.0	2.33 E04	8.29 E03	0.09926	8.23 E02
90.0	1.50 E04	5.11 E03	0.09259	4.73 E02
100.0	9.92 E03	7.53 E03	0.08796	6.62 E02
130.0	2.39 E03	1.98 E03	0.07795	1.54 E02
160.0	4.18 E02	2.97 E02	0.07099	2.11 E01
200.0	1.21 E02			

TOTAL 10 MeV PROTON FLUENCE:	2.35 E09 (PER DAY) 1.72 E12 (2 YEARS)
	× 1000
TOTAL 1 MeV ELECTRON FLUENCE:	1.72 E15 (2 YEARS)

Table 3. Equivalent 1 MeV Electron Fluence Summary for GaAs/Ge solar cells.

		Coverslide Thickness				
PERIGEE		6 mil	12 mil	20 mil	30 mil	60 mil
1500 km	Trpd Elec	1.22 E13	8.42 E12	5.88 E12	4.16 E12	1.85 E12
	Trpd Prot	4.39 E15	1.16 E15	3.85 E14	1.27 E14	2.59 E13
	Flare Prot	4.35 E14	1.32 E14	5.44 E13	2.33 E13	8.07 E12
	Total	4.84 E15	1.30 E15	4.46 E14	1.54 E14	3.59 E13
3800 km	Trpd Elec	1.63 E13	1.20 E13	8.78 E12	6.36 E12	2.88 E12
	Trpd Prot	2.71 E15	4.61 E14	1.20 E14	3.47 E13	6.14 E12
	Flare Prot	3.95 E14	1.20 E14	5.01 E13	2.16 E13	7.51 E12
	Total	3.12 E15	5.93 E14	1.79 E14	6.26 E13	1.65 E14
4800 km	Trpd Elec	1.90 E13	1.42 E13	1.05 E13	7.66 E12	3.50 E12
	Trpd Prot	1.72 E15	2.41 E14	5.56 E13	1.52 E13	2.47 E12
	Flare Prot	3.88 E14	1.18 E14	4.93 E13	2.13 E13	7.42 E12
	Total	2.12 E15	3.73 E14	1.15 E14	4.41 E13	1.34 E13
1 Re	Trpd Elec	2.41 E13	1.83 E13	1.37 E13	1.01 E13	4.65 E12
	Trpd Prot	6.48 E14	6.78 E13	1.31 E13	3.03 E12	3.96 E11
	Flare Prot	3.82 E14	1.17 E14	4.87 E13	2.10 E13	7.33 E12
	Total	1.05 E15	2.03 E14	7.54 E13	3.41 E13	1.24 E13

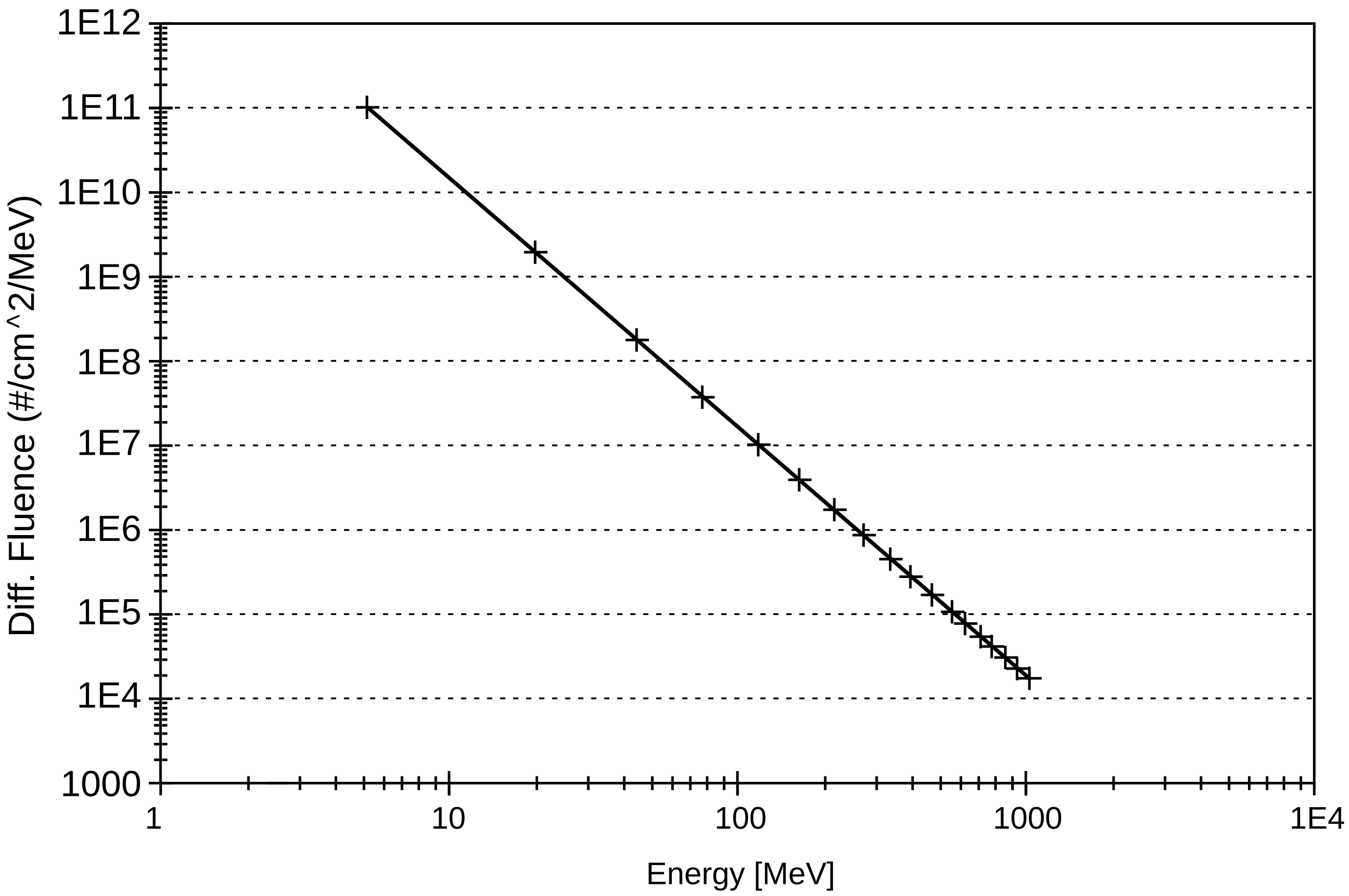

Figure 1. Solar Flare Proton Differential Fluence Data and Straight Line Fit, 4800 km Perigee, 2 Year Mission.

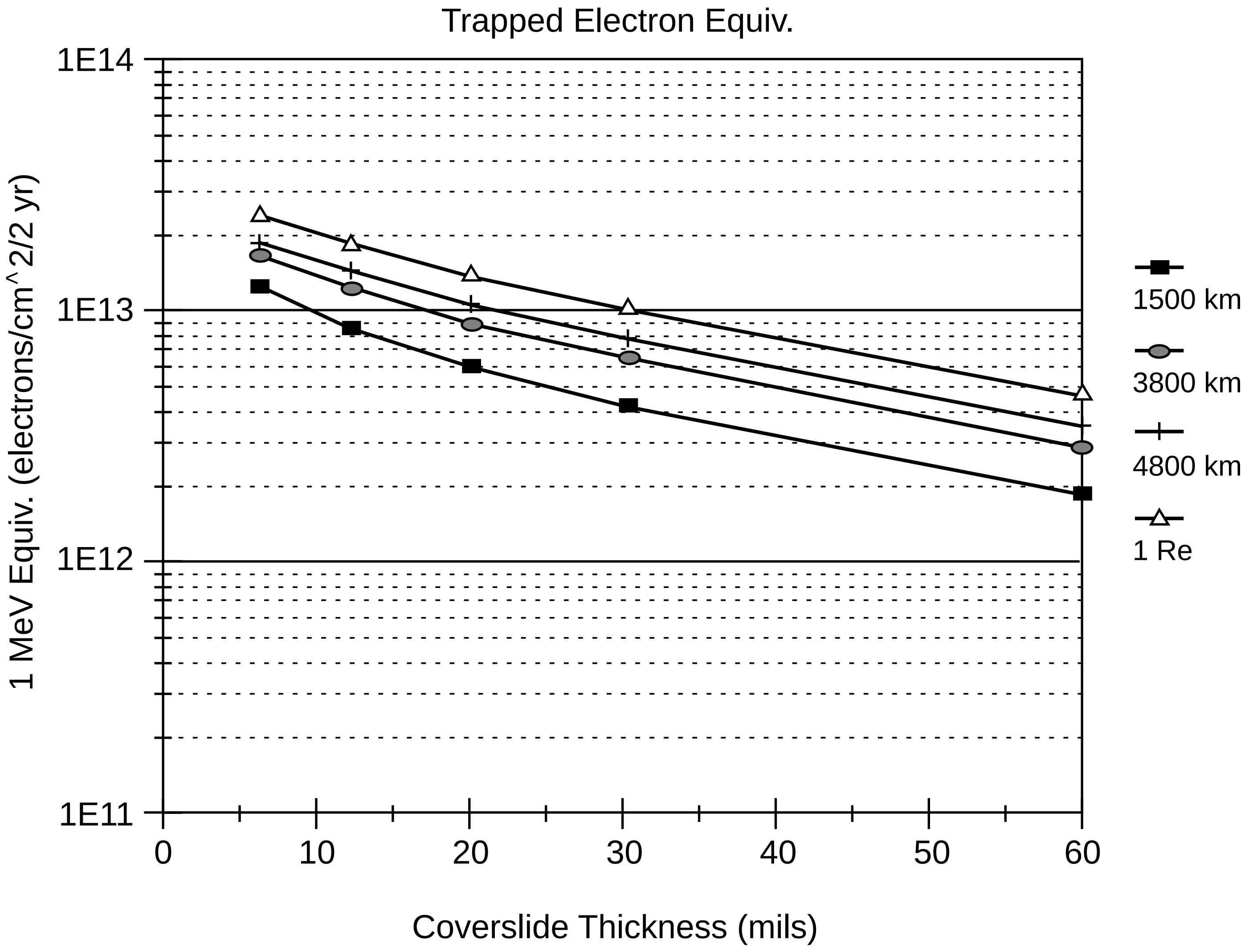

Figure 2. Trapped Electron Radiation Environment 1 MeV Electron Equivalent Fluence as a Function of Orbit Perigee.

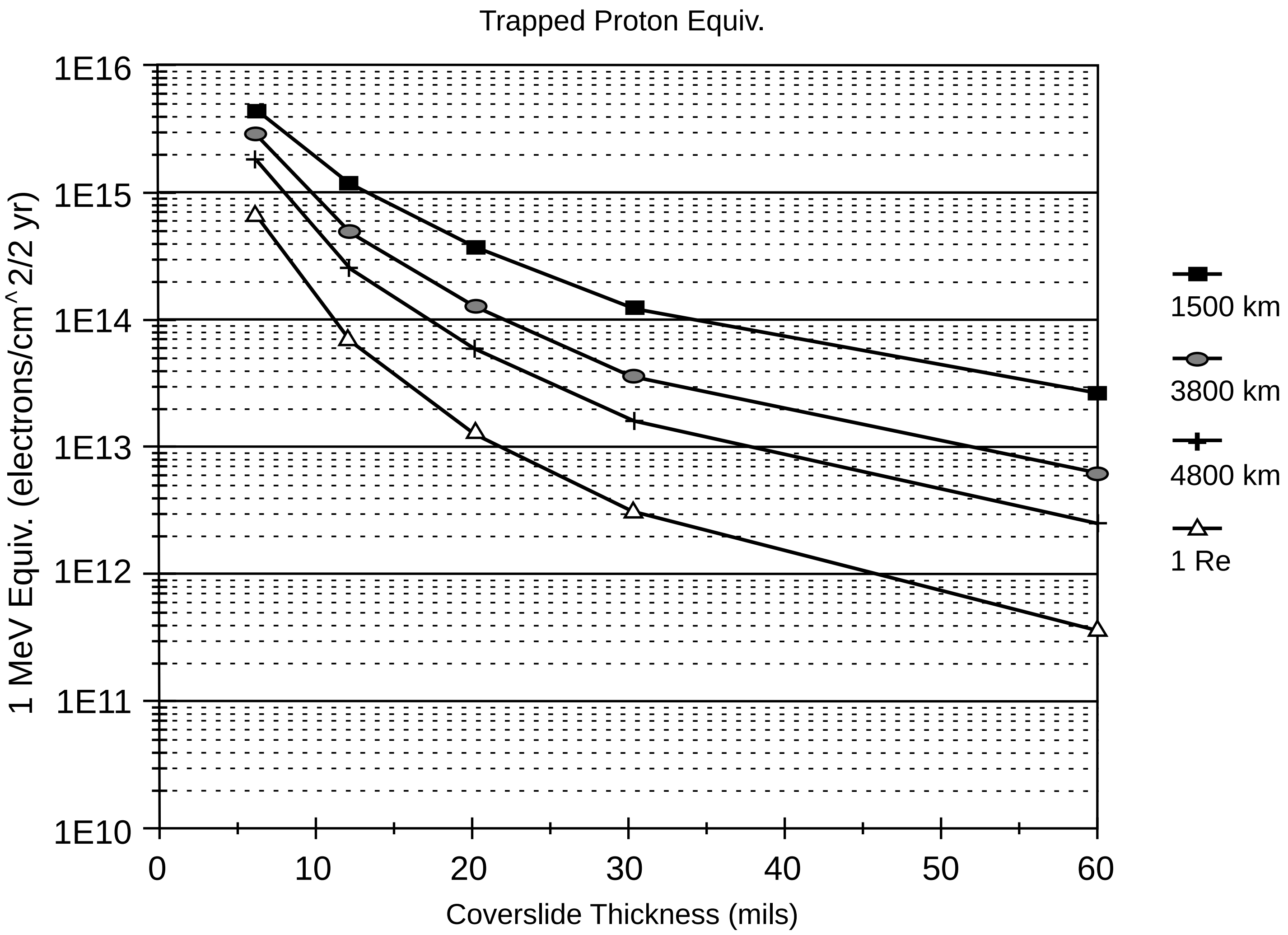

Figure 3. Trapped Proton Radiation Environment 1 MeV Electron Equivalent Fluence as a Function of Orbit Perigee.

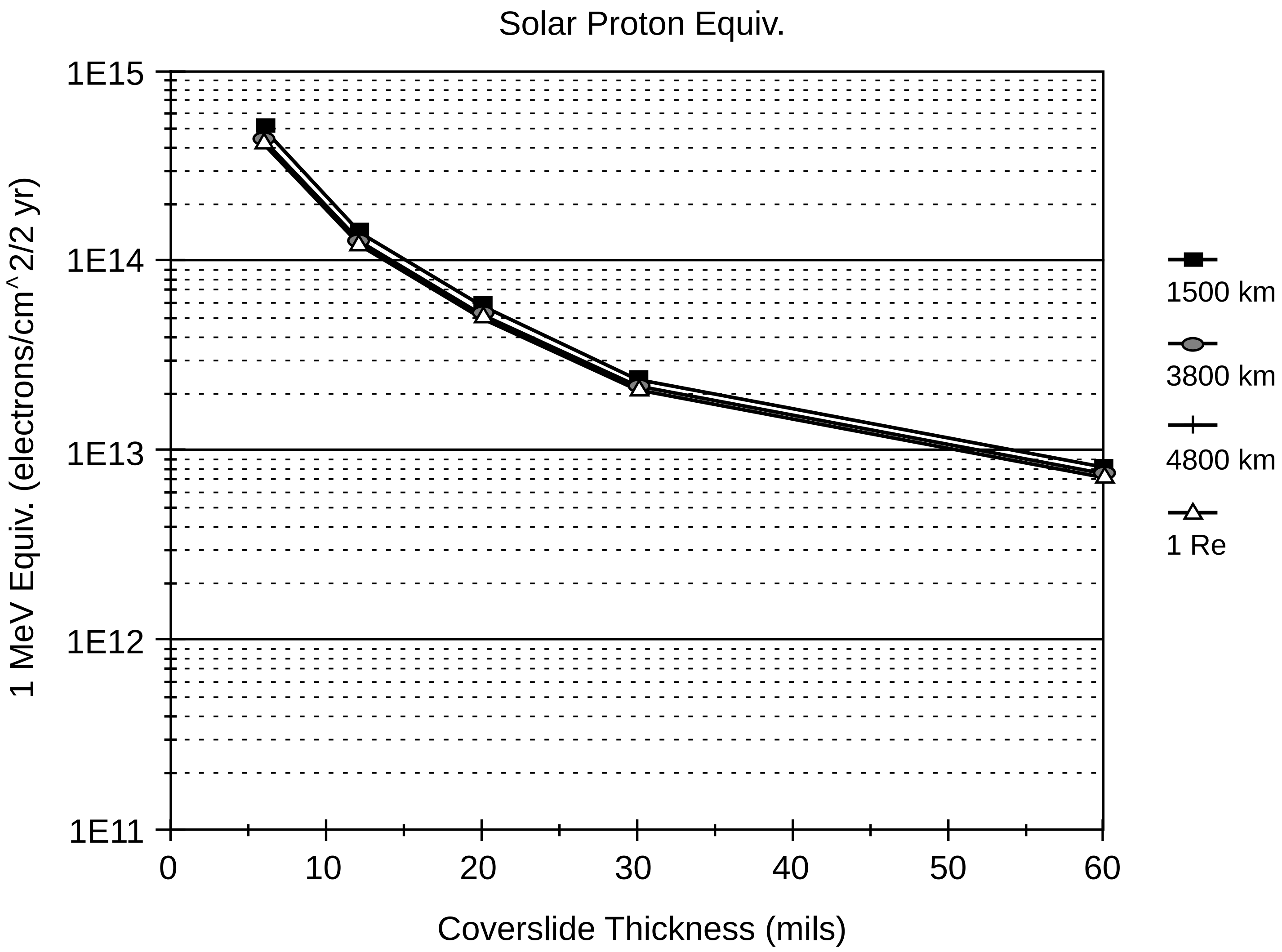

Figure 4. Solar Flare Proton Radiation Environment 1 MeV Electron Equivalent Fluence as a Function of Orbit Perigee.

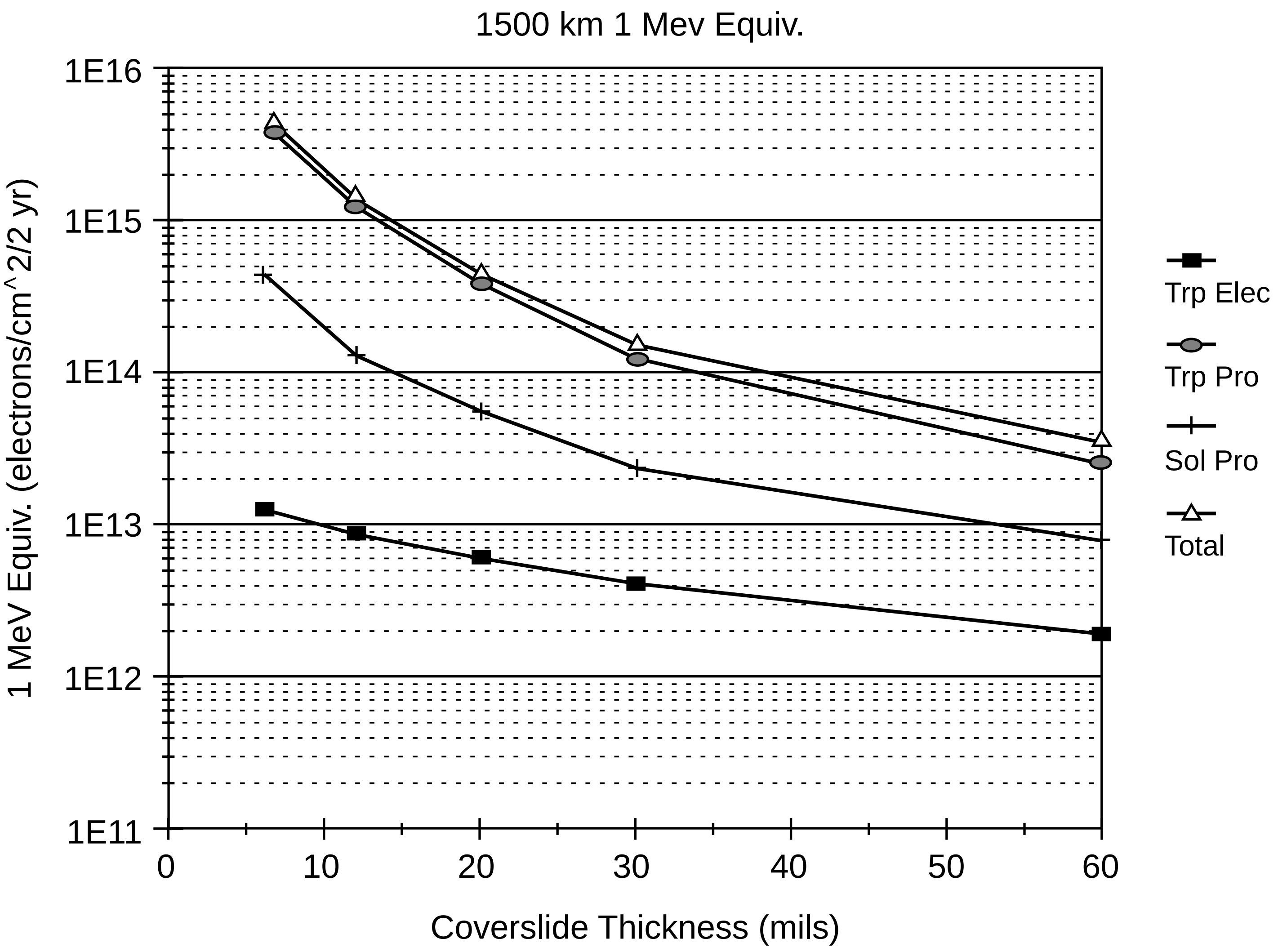

Figure 5. 1500 km Perigee Radiation Environment 1 MeV Electron Equivalences.

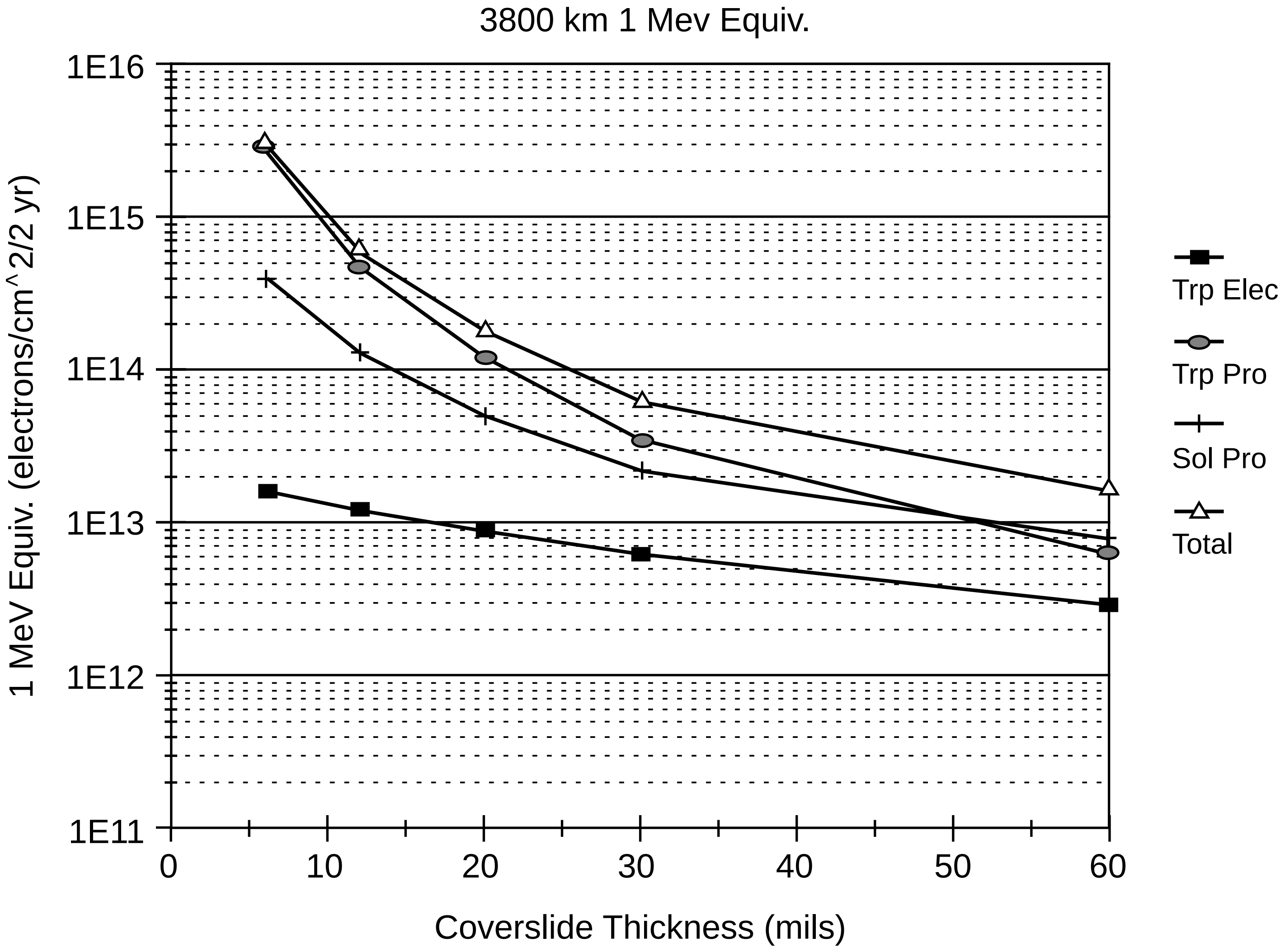

Figure 6. 3800 km Perigee Radiation Environment 1 MeV Electron Equivalences.

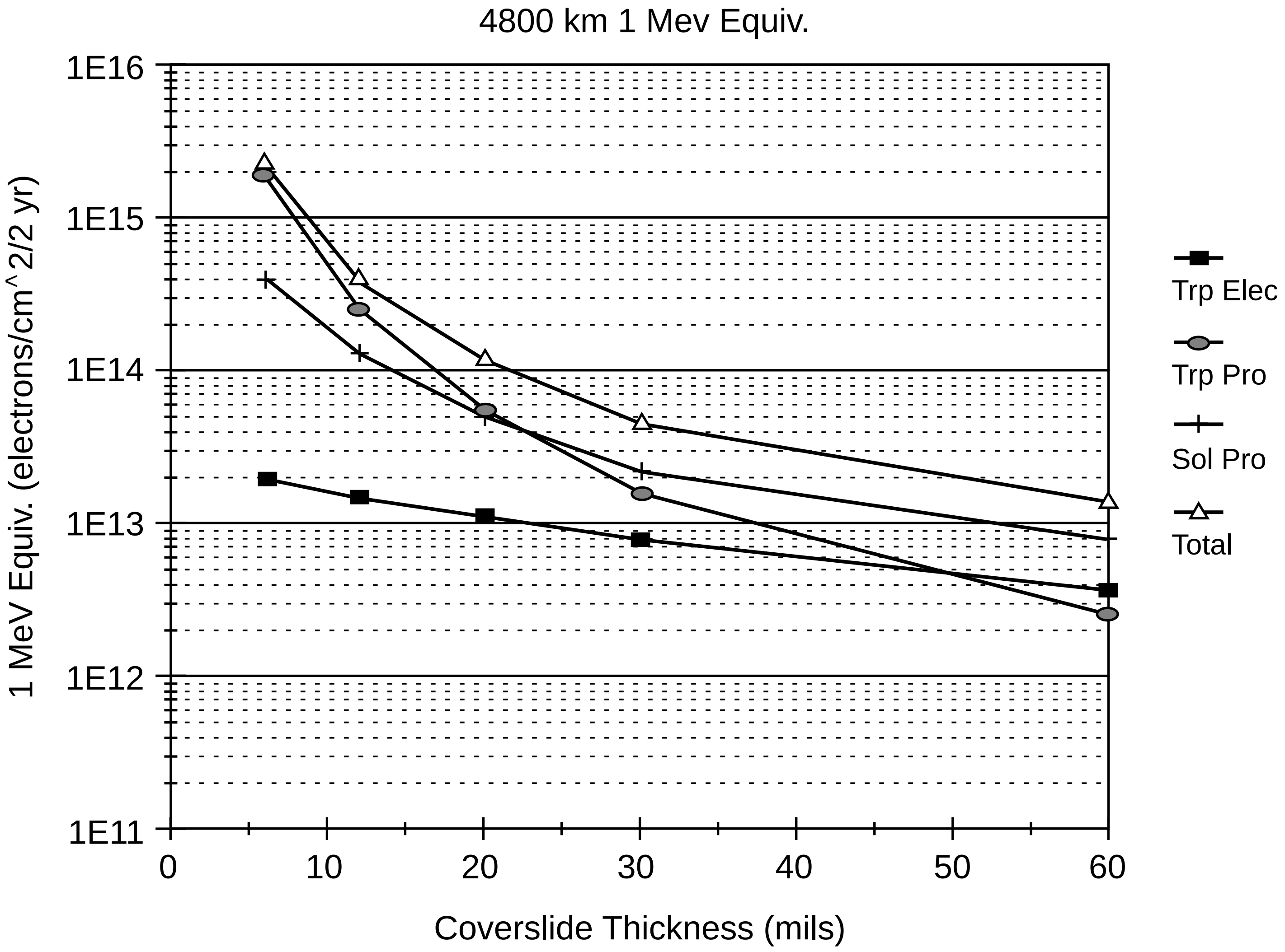

Figure 7. 4800 km Perigee Radiation Environment 1 MeV Electron Equivalences.

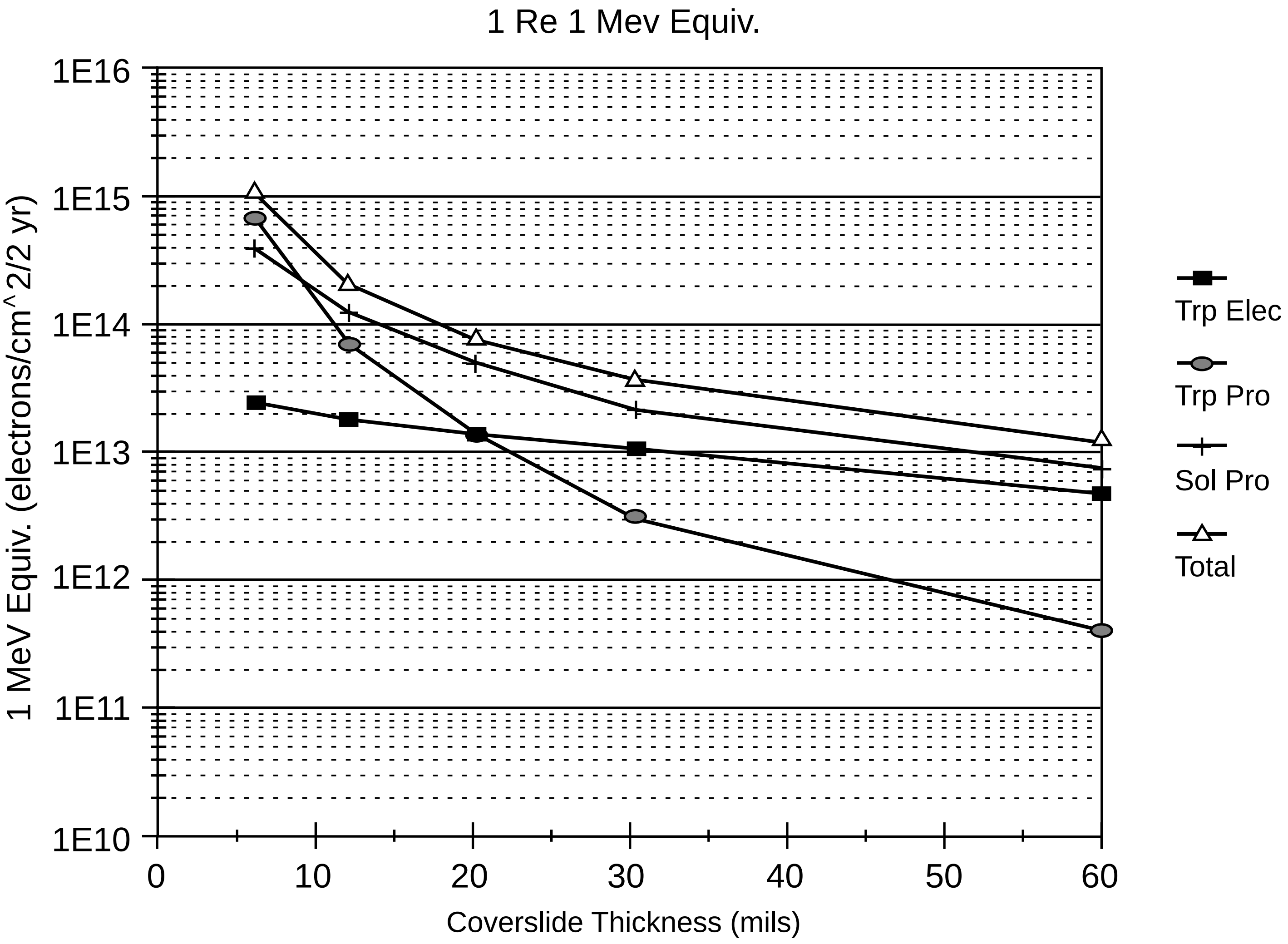

Figure 8. 1 Re Perigee Radiation Environment 1 MeV Electron Equivalences.

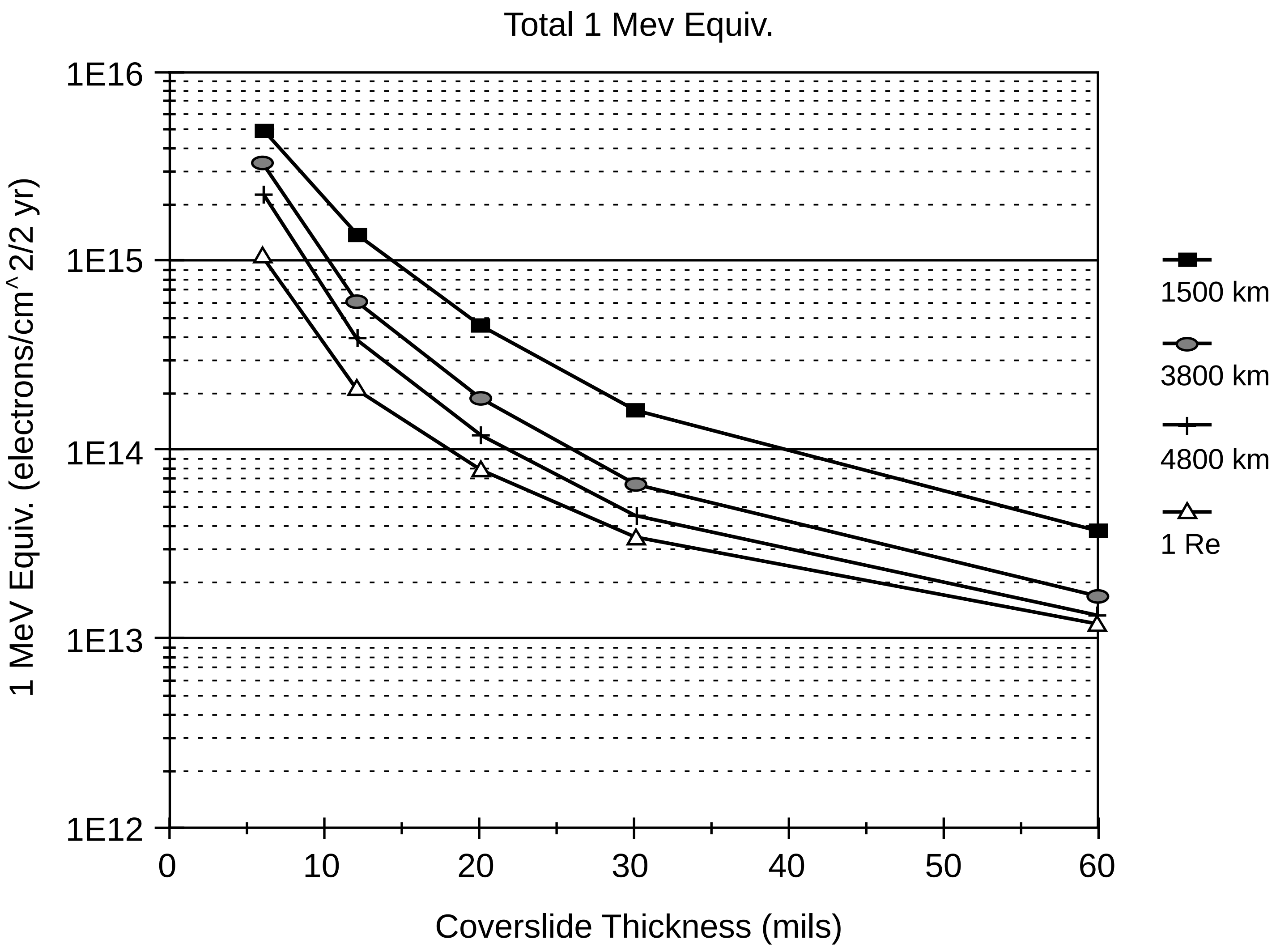

Figure 9. Combined 1 MeV Electron Equivalent Fluence as a Function of Orbit Perigee.

Appendix

Radiation Environment Description

The following tables describe the radiation environment that MI is expected to experience during its two year mission. This data was provided to the MI phase A team by the Space Science Lab, ES62, and was also generated by EL54 to ensure EL54's proper use of the radiation environment models. Tables A-1 through A-6 describe the trapped electron and trapped proton radiation environments. The second column of these tables give the averaged integral flux above each energy level in particles per square centimeter per day, the third column gives the averaged integral flux between energy levels, the fourth column gives the percent of total energy that each averaged integral flux value represents, and the fifth column gives the differential flux in particles per square centimeter per MeV per day at each energy level. Tables A-7 through A-9 describe solar flare proton radiation environment. The second column of these tables give the adjusted solar flare differential fluence for the two year mission in protons per square centimeter per MeV.

Table A-1 1500 km Perigee Trapped Electron Integrated Flux

INTEGRATED FLUX TABLE
1500 × 7 Re 90.0 degree solar maximum 1970
MODELS USED = AE8MAX
TOTAL TIME = 23.29 DAYS. TIME INTERVAL = 0.98 MIN.

ENERGY RANGES (MEV) E1–E2	AVERAGED FLUX ABOVE E1 (PER DAY	AVERAGED INTEGRAL FLUX IN ENERGY BAND E1–E2 (PER DAY)	PER CENT OF TOTAL ENERGY	DIFF. FLUX (PER DAY)
.05– .25	1.62E+12	1.29E+12	79.47	1.28E+13
.25– .50	3.32E+11	2.66E+11	16.45	2.38E+12
.50– 1.00	6.61E+10	5.25E+10	3.24	2.99E+11
1.00– 1.50	1.35E+10	8.02E+09	.50	3.23E+10
1.50– 2.00	5.52E+09	3.23E+09	.20	9.81E+09
2.00– 2.50	2.29E+09	1.31E+09	.08	3.95E+09
2.50– 3.00	9.88E+08	6.00E+08	.04	1.75E+09
3.00– 3.75	3.88E+08	3.02E+08	.02	7.53E+08
3.75– 4.50	8.59E+07	7.09E+07	.00	1.86E+08
4.50	1.50E+07		.00	3.49E+07

Table A-2 4800 km Perigee Trapped Electron Integrated Flux

INTEGRATED FLUX TABLE
4800 × 7 Re 90.0 degree solar maximum 1970
MODELS USED = AE8MAX
TOTAL TIME = 23.29 DAYS. TIME INTERVAL = 0.98 MIN.

ENERGY RANGES (MEV) E1–E2	AVERAGED FLUX ABOVE E1 (PER DAY	AVERAGED INTEGRAL FLUX IN ENERGY BAND E1–E2 (PER DAY)	PER CENT OF TOTAL ENERGY	DIFF. FLUX (PER DAY)
.05– .25	1.15E+12	9.03E+11	78.63	8.86E+12
.25– .50	2.46E+11	1.59E+11	13.87	1.40E+12
.50– 1.00	8.61E+10	6.12E+10	5.33	2.78E+11
1.00– 1.50	2.49E+10	1.45E+10	1.26	5.18E+10
1.50– 2.00	1.05E+10	6.05E+09	.53	1.81E+10
2.00– 2.50	4.41E+09	2.49E+09	.22	7.48E+09
2.50– 3.00	1.91E+09	1.15E+09	.10	3.35E+09
3.00– 3.75	7.64E+08	5.90E+08	.05	1.45E+09
3.75– 4.50	1.74E+08	5.90E+08	.01	3.67E+08
4.50	3.17E+07		.00	7.18E+07

Table A-3 1 Re Perigee Trapped Electron Integrated Flux

INTEGRATED FLUX TABLE
1 Re × 7 Re 90.0 degree solar maximum 1970
MODELS USED = AE8MAX
TOTAL TIME = 23.29 DAYS. TIME INTERVAL = 0.98 MIN.

ENERGY RANGES (MEV) E1–E2	AVERAGED FLUX ABOVE E1 (PER DAY	AVERAGED INTEGRAL FLUX IN ENERGY BAND E1–E2 (PER DAY)	PER CENT OF TOTAL ENERGY	DIFF. FLUX (PER DAY)
.05– .25	1.02E+12	7.59E+11	74.64	6.97E+12
.25– .50	2.58E+11	1.54E+11	15.17	1.29E+12
.50– 1.00	1.04E+11	710E+10	6.99	3.01E+11
1.00– 1.50	3.26E+10	1.88E+10	1.85	6.49E+10
1.50– 2.00	1.38E+10	7.92E+09	.78	2.36E+10
2.00– 2.50	5.90E+09	3.29E+09	.32	9.84E+09
2.50– 3.00	2.60E+09	1.56E+09	.15	4.50E+09
3.00– 3.75	1.05E+09	8.06E+08	.08	1.98E+09
3.75– 4.50	2.40E+08	8.06E+08	.02	5.08E+08
4.50	4.33E+07		.00	9.89E+07

Table A-4 1500 km Perigee Trapped Proton Integrated Flux

INTEGRATED FLUX TABLE
1500 × 7 Re 90.0 degree solar maximum 1970
MODELS USED = AP8MAX
TOTAL TIME = 23.29 DAYS. TIME INTERVAL = 0.98 MIN.

ENERGY RANGES (MEV) E1–E2	AVERAGED FLUX ABOVE E1 (PER DAY	AVERAGED INTEGRAL FLUX IN ENERGY BAND E1–E2 (PER DAY)	PER CENT OF TOTAL ENERGY	DIFF. FLUX (PER DAY)
.05– .25	9.97E+11	5.21E+11	52.25	3.68E+12
.25– .50	4.76E+11	2.34E+11	23.44	1.50E+12
.50– 1.00	2.42E+11	1.51E+11	15.19	5.57E+11
1.00– 1.50	9.09E+10	4.74E+10	4.76	1.55E+11
1.50– 2.00	4.35E+10	2.01E+10	2.02	5.89E+10
2.00– 2.50	2.34E+10	7.59E+09	.76	2.31E+10
2.50– 3.00	1.58E+10	4.77E+09	.48	1.19E+10
3.00– 3.75	1.10E+10	4.24E+09	.43	7.53E+09
3.75– 4.50	6.78E+09	2.22E+09	.22	3.96E+09
4.50– 6.00	4.56E+09	2.29E+09	.23	2.26E+09
6.00–10.00	2.27E+09	1.72E+09	.17	9.21E+08
10.00–15.00	5.53E+08	4.04E+08	.04	1.68E+08
15.00–30.00	1.49E+08	1.27E+08	.01	2.74E+07
30.00–50.00	2.14E+07	1.31E+07	.00	1.67E+06
50.00–100.00	8.26E+06	5.60E+06	.00	2.71E+05
100.00–200.00	2.66E+06	2.16E+06	.00	5.18E+04
200.00–300.00	5.01E+05	3.66E+05	.00	7.41E+03
300.00–400.00	1.35E+05	9.79E+04	.00	1.76E+03
400.00–600.00	3.76E+04	3.49E+04	.00	4.90E+02
600.00	2.64E+03		.00	3.50E+01

Table A-5 4800 km Perigee Trapped Proton Integrated Flux

INTEGRATED FLUX TABLE
4800 × 7 Re 90.0 degree solar maximum 1970
MODELS USED = AP8MAX
TOTAL TIME = 23.29 DAYS. TIME INTERVAL = 0.98 MIN.

ENERGY RANGES (MEV) E1–E2	AVERAGED FLUX ABOVE E1 (PER DAY	AVERAGED INTEGRAL FLUX IN ENERGY BAND E1–E2 (PER DAY)	PER CENT OF TOTAL ENERGY	DIFF. FLUX (PER DAY)
.05– .25	2.37E+12	1.21E+12	51.22	8.49E+12
.25– .50	1.15E+12	5.97E+11	25.26	3.73E+12
.50– 1.00	5.56E+11	3.86E+11	16.33	1.46E+12
1.00– 1.50	1.70E+11	1.09E+11	4.59	3.74E+11
1.50– 2.00	6.15E+10	3.77E+10	1.60	1.21E+11
2.00– 2.50	2.37E+10	1.11E+10	.47	3.68E+10
2.50– 3.00	1.26E+10	5.75E+09	.24	1.56E+10
3.00– 3.75	6.89E+09	4.01E+09	.17	8.19E+09
3.75– 4.50	2.88E+09	1.41E+09	.06	2.94E+09
4.50– 6.00	1.47E+09	1.00E+09	.04	1.22E+09
6.00–10.00	4.65E+08	3.97E+08	.02	2.82E+08
10.00–15.00	6.82E+07	5.43E+07	.00	2.67E+07
15.00–30.00	1.38E+07	1.30E+07	.00	3.36E+06
30.00–50.00	8.67E+05	7.47E+05	.00	1.17E+05
50.00–100.00	1.20E+05	1.10E+05	.00	8.42E+03
100.00–200.00	9.92E+03	9.80E+03	.00	4.65E+02
200.00–300.00	1.21E+02	1.21E+02	.00	5.35E+00
300.00–400.00	0.00E+00	0.00E+00	.00	1.00E–37
400.00–600.00	0.00E+00	0.00E+00	.00	1.00E–37
600.00	0.00E+00		.00	1.00E–37

Table A-6 1 Re Perigee Trapped Proton Integrated Flux

INTEGRATED FLUX TABLE
1 Re × 7 Re 90.0 degree solar maximum 1970
MODELS USED = AP8MAX
TOTAL TIME = 23.29 DAYS. TIME INTERVAL = 0.98 MIN.

ENERGY RANGES (MEV) E1–E2	AVERAGED FLUX ABOVE E1 (PER DAY	AVERAGED INTEGRAL FLUX IN ENERGY BAND E1–E2 (PER DAY)	PER CENT OF TOTAL ENERGY	DIFF. FLUX (PER DAY)
.05– .25	2.81E+12	1.51E+12	53.81	1.09E+13
.25– .50	1.30E+12	7.16E+11	25.45	4.57E+12
.50– 1.00	5.84E+11	4.31E+11	15.32	1.71E+12
1.00– 1.50	1.53E+11	1.06E+11	3.75	3.84E+11
1.50– 2.00	4.70E+10	3.17E+10	1.13	1.08E+11
2.00– 2.50	1.53E+10	8.12E+09	.29	2.82E+10
2.50– 3.00	7.19E+09	3.76E+09	.13	1.08E+10
3.00– 3.75	3.43E+09	2.27E+09	.08	5.02E+09
3.75– 4.50	1.16E+09	6.48E+08	.02	1.46E+09
4.50– 6.00	5.11E+08	3.81E+08	. 01	5.10E+08
6.00–10.00	1.30E+08	1.16E+08	.00	9.25E+07
10.00–15.00	1.42E+07	1.19E+07	.00	6.40E+06
15.00–30.00	2.27E+06	2.17E+06	.00	6.33E+05
30.00–50.00	9.35E+04	8.51E+04	.00	1.50E+04
50.00–100.00	8.42E+03	8.36E+03	.00	9.30E+02
100.00–200.00	5.29E+01	5.29E+01	.00	5.37E+00
200.00–300.00	0.00E+00	0.00E+00	.00	1.00E–37
300.00–400.00	0.00E+00	0.00E+00	.00	1.00E–37
400.00–600.00	0.00E+00	000E+00	.00	1.00E–37
600.00	0.00E+00		.00	1.00E–37

Table A-7 1500 km Perigee Adjusted Solar Flare Differential Fluence Values

ENERGY LEVEL (MEV)	ADJUSTED DIFF. FLUENCE (2 YEARS)
4.987	1.139E+11
19.79	1.988E+09
43.97	1.896E+08
76.85	3.635E+07
117.6	1.036E+07
165.4	3.782E+06
219.4	1.647E+06
278.6	8.104E+05
342.5	4.407E+05
410.3	2.589E+05
481.4	1.605E+05
555.5	1.052E+05
632.1	7.198E+04
710.7	5.078E+04
791.3	3.698E+04
873.4	2.776E+04
956.9	2.114E+04
1042.0	1.650E+04

Table A-8 4800 km Perigee Adjusted Solar Flare Differential Fluence Values

ENERGY LEVEL (MEV)	ADJUSTED DIFF. FLUENCE (2 YEARS)
4.987	1.012E+11
19.79	1.829E+09
43.97	1.762E+08
76.85	3.454E+07
117.6	9.906E+06
165.4	3.653E+06
219.4	1.588E+06
278.6	7.881E+05
342.5	4.315E+05
410.3	2.537E+05
481.4	1.590E+05
555.5	1.052E+05
632.1	7.205E+04
710.7	5.103E+04
791.3	3.737E+04
873.4	2.807E+04
956.9	2.160E+04
1042.0	1.689E+04

Table A-9 1 Re Perigee Adjusted Solar Flare Differential Fluence Values

ENERGY LEVEL (MEV)	ADJUSTED DIFF. FLUENCE (2 YEARS)
4.987	9.960E+10
19.79	1.803E+09
43.97	1.741E+08
76.85	3.400E+07
117.6	9.747E+06
165.4	3.600E+06
219.4	1.572E+06
278.6	7.824E+05
342.5	4.295E+05
410.3	2.546E+05
481.4	1.602E+05
555.5	1.055E+05
632.1	7.279E+04
710.7	5.193E+04
873.4	2.878E+04
956.9	2.215E+04
1042.0	1.726E+04

APPENDIX D

PRELIMINARY SPACECRAFT CHARGING ANALYSIS FOR THE MAGNETOSPHERE IMAGER

Sverdrup Corp.

George C. Marshall Space Flight Center
Science and Engineering
Contract NAS8-37814

Preliminary Spacecraft Charging Analysis for the Magnetosphere Imager

Report No.: 212-010-94-009

Prepared By:

Joel L. Herr

June 1994

Sverdrup
CORPORATION

Sverdrup Technology, Inc.
MSFC Group
620 Discovery Drive
Huntsville, AL 35806

TABLE OF CONTENTS

Page

Table of Contents i
List of Figures ii
List of Tables ii

1.0 Introduction 1

2.0 Spacecraft Charging Overview 3
2.1 Natural Space Plasma Environment 3
2.2 Cause of Spacecraft Charging 3
2.3 Sources of Electric Current to Spacecraft Surfaces 4
2.3.1 Magnitudes of the Different Sources of Electric Current 4
2.4 Differential Charging
2.5 Effects Attributed to Spacecraft Charging 5
2.6 Design Factors Influencing Charging at High Altitudes 5
2.6.1 Dielectric Surface Materials 6
2.6.2 Sun/Shade Effects 6
2.7 Arc-Discharge Mechanisms 6

3.0 General Design Guidelines 7
3.1 Bonding 7
3.2 Wiring and Cabling 7
3.3 Signal and Power Grounding 7
3.4 External Surfaces and Coatings 8
3.5 Subsystem Design Guidelines 8
3.5.1 Electronics 8
3.5.2 Thermal Control System 8
3.5.3 Structural and Mechanical 9

4.0 MI Charging Analysis 11
4.1 NASCAP Computer Code Description 11
4.2 Simulation Overview 11
4.2.1 Plasma Environment 11
4.2.2 MI Solar Environment Related to Spacecraft Charging 11
4.2.3 NASCAP MI Geometric Model 12
4.2.4 Modeling Summary 12
4.3 MI Charging Analysis Results 13
4.3.1 Ninety Degree Sun Angle Charging Results 13
4.3.2 Forty-Five Degree Sun Angle Charging Results 13
4.4 MI Charging Summary 14

References 16

LIST OF FIGURES

Page
Figure 1. Cause of Spacecraft Charging. 18

Figure 2. Negative Charging of Spacecraft Surfaces at High Altitudes. 18

Figure 3. Positive Charging of Spacecraft Surfaces at High Altitudes. 19

Figure 4. NASCAP MI Spacecraft Model. 21

Figure 5. Differential Potentials Between MI Dielectric Surface Materials and the Underlying Metallic Structure. (Sun angle 90 degrees relate to rotation axis, 205 second simulation) 23

Figure 6. NASCAP Predicted Surface Material Electric Potentials After Being Exposed for 205 Seconds to a Worst-Case Geomagnetic Substorm (Sun angle 90 degrees relative to rotation axis) 23

Figure 7. Differential Potentials Between MI Dielectric Surface Materials and the Underlying Metallic Structure. (Sun angle 45 degrees relative to rotation axis, 201 second simulation) 25

Figure 8. NASCAP Predicted Surface Material Electric Potentials After Being Exposed for 201 Seconds to a Worst-Case Geomagnetic Substorm. (Sun angle 45 degrees relative to rotation axis) 25

Figure 9. Differential Potentials Between MI Dielectric Surface Materials and the Underlying Metallic Structure. (Sun angle 45 degrees relative to rotation axis, 20 minute simulation) 27

LIST OF TABLES

Page
Table 1. Materials and Surface Coatings to Avoid at High Altitudes 17

Table 2. 90th Percentile Worst-Case Substorm Plasma Environment 17

1.0 INTRODUCTION

Plasma is one of the many natural environments to which an Earth orbiting spacecraft is exposed. All orbiting spacecraft accumulate electric charge on external surfaces from the space plasma, a process called spacecraft charging. An understanding of spacecraft charging is needed because the effects attributed to spacecraft charging have proven to be of serious engineering concern. These effects include:

- Operational anomalies (i.e., telemetry glitches, logic upsets, component failure) caused by the coupling of arc-discharge induced transients into spacecraft electronics.
- Physical surface damage as a result of arc-discharging
- Degradation of spacecraft surface material thermal and electrical properties due to increased surface contamination and sputtering.

Arc-discharging, the rapid release of large amounts of charge from one area of a spacecraft to another, has received the most attention in recent years because it is the primary mechanism by which spacecraft charging disturbs mission activities. The resulting electrical transients can couple with spacecraft electronics and cause anomalies. As of 1990, the National Geophysical Data Center at Boulder, Colorado, had assembled a database of over 2000 entries of spacecraft charging operational anomalies. These entries range from “minor-irritations” (i.e., telemetry glitches, logic upsets, etc.) to the fatally catastrophic [1]. Just recently, for example, the electronics controlling the gyroscopic stabilizing wheels on Telesat’s Anik E-2 telecommunications satellite were permanently damaged by effects believed to be due to spacecraft charging [2].

Computer modeling is used to identify areas on a spacecraft where arc-discharging is most likely to occur. The charging levels of a spacecraft are estimated as a function of the characteristics of the ambient space plasma and the design of the spacecraft. Areas on the spacecraft where large electric fields develop due to different surfaces charging to different levels are identified as possible discharge sites. Modeling is then used to investigate the effect of alternative spacecraft designs on the charging levels. On the basis of the analysis, design guidelines and recommendations are developed with the purpose of reducing or eliminating the detrimental effects of spacecraft charging.

The following report presents the results of a preliminary charging analysis conducted on the Magnetosphere Imager (MI) which will be flown in a high altitude polar elliptical orbit. Section 2 provides a general description of spacecraft charging and its effects, and the design factors influencing charging at high altitudes. Design guidelines applicable to all spacecraft are summarized in Section 3 with reference to other more complete documents. The results of the preliminary charging analysis conducted on MI are summarized in Section 4.

2.0 SPACECRAFT CHARGING OVERVIEW

2.1 NATURAL SPACE PLASMA ENVIRONMENT

Above an altitude of 90 km, a portion of the molecules comprising the Earth's atmosphere is ionized by solar radiation producing positively charged ions and free electrons. This collection of electrically charged particles, known as the natural space plasma, exists in all spacecraft orbits.

Definition of the natural space plasma depends on several factors. The most dramatic variations in its properties are due to changes in altitude and latitude. The properties of the natural space plasma are described by specifying particle density and particle energy. The particle density and energy are approximately the same for the electrons and positively charged ions in the different spacecraft orbits. Low inclination, low altitude Earth orbit (LEO) plasma is relatively dense, as compared with other plasma around the Earth, and has low energy. At high inclination, low altitude Earth orbit (polar), high energy electrons are precipitated during auroral events. These high energy electrons are best known for the aurora they produce. At geosynchronous altitudes (GEO), spacecraft frequently encounter high energy, low density plasma associated with geomagnetic substorms.

The energy of the charged particles comprising the natural space plasma causes them to continuously move. The particles are said to have a "thermal velocity." Moving charged particles create an electric current. When a spacecraft orbits the Earth, some of the electric current will flow to the spacecraft resulting in charge accumulating on its exposed surfaces. This phenomenon is known as spacecraft charging.

2.2 CAUSE OF SPACECRAFT CHARGING

Spacecraft charging is the accumulation of charge on the exposed surfaces of a spacecraft and is caused by unequal negative and positive currents to spacecraft surfaces (see Figure 1). As one type of charge (positive or negative) accumulates, it generates an electric force field that decelerates like-charged particles, decreasing their current (positive or negative), and accelerates oppositely-charged particles, increasing their current (negative or positive). The charging process continues until the accelerated particles can be collected rapidly enough to balance the currents. At this point the spacecraft has reached its equilibrium charging level or "floating potential," and no more charge accumulates. Spacecraft charging is the process by which a spacecraft reaches an equilibrium with the natural space plasma environment. The level of charging required for equilibrium to be established is influenced by the characteristics of the ambient plasma environment and by the design of the spacecraft.

2.3 SOURCES OF ELECTRIC CURRENT TO SPACECRAFT SURFACES

The main sources of current to a spacecraft surface are the plasma electrons, plasma ions, and material dependent contributions from photoelectron and secondary electron currents. The charging level of spacecraft depends on the relative magnitudes of the positive (i.e., plasma ions, secondary electrons and photoelectrons) and negative (i.e., plasma electrons) currents.

It is important to realize that the satellite as a whole comes to an equilibrium with the space plasma, and that the charging of one area on a satellite can affect the charging of another. This is particularly true for the spacecraft structure which is typically metallic and acts as the electrical ground. Because charge flows freely within a metal, the structure will all be at a single potential determined by the current to its entire area. This current includes current to exposed metallic surfaces electrically connected to the structure as well as current through ‘leaky’ dielectric surface materials. Dielectric surfaces, on the other hand, are less efficient at redistributing the charge deposited on them, and will charge according to the magnitudes of the current incident on them. In general, different surfaces will charge to different levels relative to each other and relative to the underlying structure.

2.3.1 Magnitudes of the Different Sources of Electric Current

Plasma ions are much more massive than the electrons. Therefore, the inverse relationship between mass and thermal velocity typically results in the plasma electron current to the surface being greater than the ion current. As a result, surfaces tend to accumulate a negative charge (see Figure 2). In some situations, however, the photoelectron current exceeds the plasma electron current resulting in a slightly positive potential on the spacecraft (see Figure 3). In still other instances, the negative charging of shaded surfaces can influence the charging of nearby sunlit surfaces by forming what is called a “potential barrier” in front of the sunlit surface. The potential barrier creates a retarding electric field that prevents low energy photoelectrons from leaving the sunlit surface. A lack of photoelectron emission causes the sunlit surface to charge negative.

2.4 DIFFERENTIAL CHARGING

Spacecraft charging is caused by unequal positive and negative electric current to spacecraft surfaces. Equilibrium is reached when the sum of the current to and from spacecraft surfaces is zero. If the spacecraft is all metal (i.e., conductive), the entire spacecraft will be charged to the same potential. However, if dielectric surface materials are used on a spacecraft, and the current from surface to surface varies, surfaces may charge to different floating potentials, a process called differential charging.

Dielectric (e.g., Kapton and Teflon) are poor distributors of accumulated charge, maintaining a portion of the charge deposited on them. A variation in the charged particle flux causes surfaces to reach different floating potentials. The largest levels of differential charging will typically develop between sunlit and shaded surface because the photoelectron current (which in some cases can be the largest source of positive current to a surface) maintains the floating potential of sunlit surfaces positive relative to shaded surfaces. A difference in floating potentials causes an electric force field to develop between two surfaces. Electric force fields can produce stress in spacecraft surface materials and can lead to some of the effects discussed in the next section.

2.5 EFFECTS ATTRIBUTED TO SPACECRAFT CHARGING

The primary mechanism by which spacecraft charging disturbs mission activities is through arc-discharging. Arc-discharging occurs electric fields generated by differential charging exceed breakdown thresholds. The arc-discharge process rapidly releases large amounts of electric charge which give rise to currents flowing in the spacecraft structural elements. The arcing produces a broad band electromagnetic field which can couple into spacecraft electronics and cause operational anomalies ranging from minor irritations to the fatally catastrophic.

Besides generating electromagnetic interference that can couple with spacecraft electronics, arc-discharging leads to physical damage of affected surfaces. Arc-discharging produces localized heating and ejection of surface material from the arc-discharge site. The loss of material degrades spacecraft structural integrity and alters the properties of spacecraft surface materials. The ejected material is also a source of contamination for other spacecraft surfaces.

Other spacecraft-charging-related effects of concern include degradation of spacecraft surface material properties due to increased surface contamination and ion sputtering. In the case of sputtering, large negative floating potentials of spacecraft surfaces accelerate positively charged ions to high energies leading to the physical removal of surface atoms (i.e., sputtering) by the impacting ions.

Organic molecules outgassed from spacecraft surfaces can be ionized while still near the spacecraft by solar radiation and can be attracted to negatively charged surfaces. The more negative the floating potential of a surface is, the greater the probability of its contamination.

2.6 DESIGN FACORS INFLUENCING CHARGING AT HIGH ALTITUDES

Most of the adverse effects caused by spacecraft charging at high altitudes depend on the level of differential charging that occurs. Several spacecraft design factors influence the level of differential charging that occurs for given plasma characteristics. Most depend on the electrical properties of the spacecraft outer surface materials. These include the amount of dielectric material that comprises the spacecraft outer surface area, the sun/shade effects. Presently the only sure way to eliminate differential charging is to make the entire spacecraft outer surface conductive and tie all elements to spacecraft ground.

2.6.1 Dielectric Surface Material

Whenever dielectric surfaces are present differential charging will occur. Dielectric surfaces are inefficient at distributing accumulated charge, and will develop a differential potential relative to the underlying structure and to other nearby surfaces.

2.6.2 Sun/Shade Effects

Because of the low plasma density at high altitudes, ambient plasma current fluxes are on the order of micro amps per square meter square. Photoelectron emission from surfaces, which is on the order of tens of micro amps per square meter, can therefore play an important role in balancing currents to the spacecraft. Typically, photoelectron emission dominates the ambient currents preventing sunlit surfaces from charging highly negative. However, regions of the spacecraft that are shaded lack the photoelectron contributions. If these surfaces are conductive and connected to spacecraft ground, the photoemission from sunlit surfaces will prevent them from charging highly negative. If however they are dielectric, the surfaces will charge negatively resulting in a differential potential. The largest differential potentials will generally be between shaded surfaces and surfaces or structure whose potential is dominated by photoemission.

2.7 ARC-DISCHARGE MECHANISMS

Differential charging can result in arc-discharging if the generated electric fields exceed breakdown thresholds. The conditions necessary for a discharge to occur are not completely understood. However, mechanisms have been identified and breakdown criteria has been established by conducting computer modeling [3] [4] [5]. A discharge between neighboring surfaces, termed “flashover”, [6] occurs when neighboring surfaces charge to different potentials resulting in an electric field strength greater than 2×10^6 V m^{-1}. This type of discharge occurs along edges between dielectric surfaces, at cracks or holes in dielectric exposing the metallic structure beneath or at exposed solar array interconnect-coverglass interfaces.

Any area of dielectric material is a possible site for a “punch-through” [6] discharge that occurs when a surface material charges differentially relative to the underlying structure. Electric field strengths of 2×10^7 Vm^{-1} or greater are typically required to cause punch-through discharges.

3.0 GENERAL DESIGN GUIDELINES

General design guidelines based on known charging control techniques serve to limit the detrimental effects of spacecraft charging. If implemented, these guidelines accomplish two things: provide a design that limits the factors thought to cause arc-discharging, and provide a design that is immune to arc-discharges. Some general "good-practice" guidelines are given below. Refer to "Design Guidelines for Assessing and Controlling Spacecraft Charging Effects," NASA TP-2361 [3] for a more in-depth overview of design techniques that control spacecraft charging.

3.1 BONDING

All conducting elements (internal and external) should be tied to the spacecraft ground. All enclosures should be designed to form a "Faraday Cage". Bonding of all metallic structural elements should have a dc resistance of less than 2.5 milli-ohms across the bond. Ground straps should have less than a 5:1 length-to-width ratio. At least two slip rings should be dedicated to ground structures across rotating joints and the slip rings should be grounded to structure at a distance no greater than 15 cm away from the slip ring.

3.2 WIRING AND CABLING

All wiring and cabling should be shielded and the shielding should have 360 degree termination at the backshell. The connector backshell should be terminated 360 degrees to the box. The shield should not be carried into the box on a pin and grounded internal to the box. This is to protect the shielding integrity of the Faraday cage [7]. Pigtail termination of shields should be avoided if at all possible. Floating one end of the shield should also be avoided if possible. Proper shield termination at both ends of the cable or wire protects the integrity of the Faraday cage.

3.3 SIGNAL AND POWER GROUNDING

All signal and power grounds should be properly grounded to structure. For circuitry that must be isolated from structure for the purpose of avoiding ground loops, a large (5-100 mega-ohm) resistor may be used to reference circuitry to ground. This application should be analyzed to assure that it is acceptable from an electromagnetic compatibility and electrical design standpoint.

3.4 EXTERNAL SURFACES AND COATINGS

All exterior surfaces should be somewhat conductive and referenced to spacecraft ground. Highly conductive materials such as metal should be bonded to structure with the smallest resistance possible. A rule of thumb is that the bonding resistance should be smaller than the product of 10^9 times the inverse of the area measured in square centimeters [3]. Surfaces such as paints or thermal coatings over conductive substrates should have a bulk resistivity of less than 10^{11} ohm-cm. It should be stressed that all grounding methods should be demonstrated to survive thermal and vacuum exposure, discharge events, etc., for the lifetime of the spacecraft. Materials and surface coatings to avoid on external surfaces are shown in Table 1 [3]. It should be noted that while glass and quartz do not have acceptable substitutes, these materials are highly nonconductive. Indium-tin oxide (ITO) has been used to provide a thin conductive coating on surfaces, but grounding of such coatings is costly and of questionable reliability [3]. Paints should be applied only to grounded conductive substrates, and conductive adhesives should be tested for suitability to the space environment.

3.5 SUBSYSTEM DESIGN GUIDELINES

3.5.1 Electronics

Electrical inputs to boxes should be immune to possible discharges by use of filtering, clamping diodes, etc. All electronic component enclosures should form a Faraday cage. Circuit boards and wire insulation materials (other than Teflon) do not seem to be a problem. However, for wires and cables external to the equipment chassis, a conductive overbraid is recommended. This is to help prevent discharges in cabling due to high energy particles charging the interior of the cable. The cable overbraid should be grounded in the same manner as described in Section 5.3. All circuit trace areas greater than 3 cm squared should be referenced to ground [7]. All wiring should be referenced to ground. A large (5-100 mega-ohm) resistor may be used to reference wiring, circuit traces, and capacitor and relay cans to ground. The resistor should be sized to avoid circuit performance degradation.

3.5.2 Thermal Control System

Thermal blanket using beta cloth, beta cloth with steel threading, and silvered Teflon outer covers should be avoided as these materials prevent charge bleedoff [8]. All metalized layers of multilayer insulation (MLI) should be electrically tied to structure. Blanket to structure bond resistance should be 10 ohm or less. At least two ground tabs should be provided per MLI blanket and additional ground tabs should be added so that no point on the MLI blanket is more than one meter from a ground tab. NS43G [9] and zinc orthotitanate paint (white) [3] are two acceptable thermal coatings. Outer covers of thermal blankets may be coated with ITO to provide a conductive surface, but this requires special procedures for the handling of the blanket [10].

3.5.3 Structural and Mechanical

Aluminum honeycomb substructures require special attention and consideration. Techniques for grounding honeycombs and facesheets include using rivets, metal inserts, and copper wire. The copper wire, for example, is actually sewn into the facesheet and through the honeycomb structure, making contact with as many cell walls as possible. The copper wire method should be employed at intervals of 30 cm or less, measured across the facesheet [3]. No unreferenced or ungrounded structures should be allowed.

4.0 MI CHARGING ANALYSIS

This section describes the computer code and the approach used for the analysis, and summarizes the results of the charging analysis conducted.

4.1 NASCAP COMPUTER CODE DESCRIPTION

The NASA Charging Analyzer Program [6] for geosynchronous spacecraft (NASCAP) is a 3-dimensional computer code designed to analyze spacecraft charging at geosynchronous altitudes. NASCAP provides a spacecraft designer with an understanding of how a spacecraft will interact with a geomagnetic substorm as a function of time, spacecraft design, and substorm characteristics. NASCAP considers the important charging currents and geometric electric field effects on and around a spacecraft.

A NASCAP model of a spacecraft is formed by combining various geometric shapes in a limited-sized three-dimensional grid. Surface materials are assigned to the outer surface of the model and can be dielectrics or conductors. The characteristics of the geomagnetic substorm plasma must be specified. Surface voltage levels attained by the model of the spacecraft and provided as standard output assist in evaluating the possibility and location of arc-discharges on the spacecraft.

4.2 SIMULATION OVERVIEW

4.2.1 Plasma Environment

The high altitude polar plasma environment (i.e., 1500 km to 7 Earth radii altitude) has not been well defined in the literature. It is expected in the worst case, however, that the MI will encounter plasmas with characteristics much like those associated with geomagnetic substorms experienced by geosynchronous spacecraft. Table 2 gives a 90th percentile representation of a worst-case environment [3] used in this analysis. The environment is based on measurements by the Applied Technology Satellites 5 and 6 (ATS-5 and ATS-6), and on measurements by the P78-2 satellite as part of the Satellite Charging at High Altitudes (SCATHA) program [11]. The MI plasma environment can be refined during the next phase of a charging analysis.

4.2.2. MI Solar Environment Related to Spacecraft Charging

The MI is spin stabilized at 10 rpm. In orbit, portions of the spacecraft body will move in and out of sunlight as the satellite rotates. This will cause the charging level of those areas to oscillate more and less negative due to changes in the photoelectron contribution to the total current. Other areas of the spacecraft body will be continually shaded and completely lack the photoelectron current. In conducting a charging analysis, the distribution of sunlight is important because photoelectrons are a major source of current to a spacecraft. The distribution of sunlight will also change on a longer timescale as the angle between the rotation axis and the sun changes due to seasonal variation of the sun angle relative to the orbit plane and due to orbit precession.

In the present analysis, two sun angels are simulated. In the first case, the sun is perpendicular to the sides of the MI cylindrical body (i.e., 90 degrees relative to the rotation axis). The top and bottom ends of the body are completely shaded while the rest of the body rotates in the sunlight. In the second case, the sun is at a 45 degree angle so that the top end of the MI is continually in sunlight while the sides rotate in the sunlight. The bottom end is continually shaded in this case.

4.2.3 NASCAP MI Geometric Model

The NASCAP geometric model of the MI is made to resemble the actual design of the satellite to within the restrictions of the computer program. These restrictions stem mainly from a limited sized three-dimensional computational grid. The grid size is chosen to approximate the overall dimensions of the satellite which sacrifices the detail of individual components.

Figure 4 shows the NASCAP model of the MI spacecraft. The radiator band is coated with non-conducting paint, ‘npai’ that is assumed to be 2 miles thick. The rest of the MI cylindrical body is solar cells that are covered with coverglass and have exposed metallic interconnects. This combination of materials on the solar arrays (i.e., coverglass and interconnects) is represented by a single material in NASCAP called ‘solar.’

4.2.4 Modeling Summary

The present analysis is conducted to obtain a first order estimate of the charging levels of the MI exterior surfaces and the underlying metallic structure that acts as the electrical ground. IT is assumed that the MI encounters plasma characteristic of a geomagnetic substorm environment at a point in time referenced as time zero. The NASCAP computer code is used to simulate the charging behavior of the MI exterior surface materials and the underlying structure as a function of time after the encounter with the plasma environment for two sun angles. Two simulations are run for approximately 200 seconds while a third is run for 20 minutes. The important results are the levels of differential charging that develop at the end of the simulations. The figures to follow show the differential potentials between the surface materials and the underlying structure as a function of time, and also the surface material charging levels that occur at the end of the simulations in the form of surface electric potential contours. The differential potentials that develop are used to identify areas on the satellite where arc-discharges could occur.

4.3 MI CHARGING ANALYSIS RESULTS

4.3.1 Ninety Degree Sun Angle Charging Results

Figure 5 shows the differential potentials that develop between the dielectric surface materials and the underlying metallic structure as a function of time with the sun at ninety degrees relative to the rotation axis. The top and bottom ends of the MI body are completely shaded while the rest of the body rotates in the sunlight. The solar cells on the ends of the spacecraft body lack photoelectron current and therefore charge more negative than the rest of the satellite resulting in a larger negative differential potential relative to the structure. The charging levels of the radiator band and the solar cells on the sides of the body oscillate as the surfaces rotate from the shaded to the sunlit side of the spacecraft. However, because of the fast spin rate, the oscillation is small and the radiator band and the solar cells maintain positive potentials relative to the structure.

Figure 6 shows the surface material electric potentials occurring at 205 seconds into the charging simulation. Differential charging levels are below punch-through arc-discharge threshold levels which are at 1000 V for the non-conducting paint on the radiator. The flashover arc-discharge criteria is less than the punch-through criteria so it is assumed that the solar cells would discharge by flashover before generating the potentials necessary to exceed the punch-through criteria. Depending on the distance between the interconnects and coverglass, flashover discharges could occur on the solar arrays.

4.3.2 Forty-Five Degree Sun Angle Charging Results

Figure 7 shows the differential potentials that develop between the dielectric surface materials and the underlying metallic structure as a function of time with the sun at forty-five degrees relative to the rotation axis. The solar cells on the top the MI are continually in sunlight and charge less negative than the rest of the spacecraft. The solar cells on the bottom end of the MI body are continually shaded in this case and charge more negatively resulting in a larger negative differential potential relative to the structure. The differential charging levels are about the same as in the previous case except that more of the solar cells on the sides of the spacecraft body charge negative relative to the structure than in the previous sun angle case. With more of the satellite body in sunlight, the structure charges less negative than the solar cells in this case. Again the charging levels of the radiator band and the solar cells on the sides of the body oscillate as the surfaces rotate from the shaded to the sunlit side of the spacecraft.

Figure 8 shows the surface material electric potential occurring at 201 seconds into the charging simulation. Differential charging levels are below punch-through arc-discharge threshold levels while the possibility of flashover discharges again depends on the distance between the interconnects and coverglass on the solar arrays.

In the previous two simulations, time steps were taken small enough to resolve the oscillation in the charging levels of the surface materials on the sides of the spacecraft. However, geosynchronous spacecraft may be exposed to a geomagnetic substorm plasma environment for on the order of hours. To account for charging on a longer time scale, a third simulation is run that determines the average potential of the surface materials as they rotate in and out of the sunlight. Longer timesteps can then be used during the simulation. Figure 9 shows the differential charging levels that develop for the sun at forty-five degrees relative to the rotation axis and for a period of twenty minutes. Even after twenty minutes, the differential potential on the radiator non-conducting paint is still below the punch-through arc-discharge threshold. On the other hand, the shaded solar cells and the continually sunlit solar cells have differential potentials that could result in flashover arc-discharges on the solar arrays.

4.4 MI CHARGING ANALYSIS SUMMARY

The NASCAP computer code was used to simulate the spacecraft charging behavior of the Magnetosphere Imager (MI) when exposed to a worst-case geomagnetic substorm plasma environment. The important results are the levels of differential charging that developed at the end of the simulations. Differential charging can result in arc-discharging when generated electric fields exceed breakdown thresholds. The main results of the charging analysis conducted are summarized as follows:

- Possibility of punch-through arc-discharges occurring on the radiator band:

    - Differential charging levels that developed between the radiator band and the underlying metallic structure were below punch-through arc-discharge thresh olds. The charging behavior of the coating on the radiator band will mostly depends on its thickness and electrical resistivity. A possible candidate for the coating is Z93 which may have a low electrical resistivity [12]. The lower the resistivity, the lower the level of differential charging that will occur relative to the structure. However, this in turn may increase the differential potential between the radiator band and the nearby solar cells, increasing the possibility of a flashover arc-discharge between those two areas.

- Possibility of flashover arc-discharges occurring on the solar arrays:

    - Differential charging levels that developed between the interconnects (which are assumed to be at or near the potential of the structure) and the coverglass on the solar arrays may be large enough in some areas to satisfy the flashover arc-discharge criteria. This depends on the distance between the interconnects and coverglass, and on the construction of the solar cells (i.e., are there exposed interconnects). There are questions as to the severity of flashover discharges occurring on solar arrays (i.e., how much charge is involved and what kind of current pulse results). No clear consensus exists at this time.

These results are preliminary and are very dependent on the plasma environment and on the model of the MI spacecraft used for the simulations. The high altitude polar plasma environment (i.e., 1500 km to 7 Earth radii altitude) has not been well defined in the literature. It is expected in the worst case, however that the MI will encounter plasmas with characteristics much like those associated with geomagnetic substorms. A simplified model of the MI spacecraft was used in the present analysis. As the spacecraft design evolves, further spacecraft charging analysis should be conducted. Taking these issues into consideration, the preliminary results do not show a charging behavior that warrants critical design changes at this time.

At this point in the development of the MI mission and spacecraft, the best approach is to design the spacecraft based on known charging control techniques that will serve to limit the detrimental effects of spacecraft charging. The only sure way to eliminate differential charging is to make the entire outer surface of the spacecraft conductive and tie all elements to spacecraft ground. However, this often involves added cost and weight. Based on the results of the preliminary analysis, it may be sufficient at this point to incorporate into the design immunity to the effects of arc-discharges. This is accomplished by electrically shielding electronics and incorporating electric filters to protect circuits from arc-discharge induced currents.

General design guidelines that should be considered are summarized as follows:

- Electrical Grounding:
  - All conductive elements should be tied to a common electrical ground.

- Surface Materials:
  - All exterior surfaces should be at least partially conductive.

- Shielding:
  - Electronics and wiring should be physically and electrically shielded.

- Electrical Filtering:
  - Electrical filtering should be used to protect circuits from arc-discharge induced currents.

- Procedures
  - Proper handling, assembly, inspection and test to ensure electrical conductivity.

REFERENCES

1. Wrenn, Gordon L., Spacecraft Charging Effects, 1990.

2. Knapp, Bill, ‘Telesat Ponders Using Thrusters to Salvage Anik,’ Space News, Jan. 31 - Feb. 6, 1994.

3. Purvis, C.K., et al., ‘Design Guidelines for Assessing and Controlling Spacecraft Charging Effects,’ NASA TP-2361, 1984.

4. Stevens, N.J., ‘Modeling of Environmentally Induced Discharges in Geosynchronous Satellites,’ NASA TM-81598, 1980.

5. Davis, V.A., Duncan, L.W., ‘Spacecraft Surface Charging Handbook,’ Maxwell Lab., Inc., S-Cubed Div., PL-TR-92-2232, Nov. 1992.

6. Mandell, M.J., Stannard, P.R., Katz, I., ‘NASCAP Programmer’s Reference Manual,’ Maxwell Lab., Inc., S-Cubed Div., NASA Contract NAS3-22536, 1984.

7. Whittlesey, A., et al., ‘The Satellite Space Charging Phenomenon, and Design and Test Considerations,’ 1992.

8. Bever, R., Kauder, L., ‘Spacecraft Charging Tests of COBE Outer Surface Materials,’ Goddard Space Flight Center.

9. Leung, P., Private Communication.

10. Whittlesey, A.C., Private Communication.

11. Gussenhoven, M.S., Mullen, E.G., ‘A “Worst Case” Spacecraft Charging Environment as Observed by SCATHA on 24 April 1979,’ AIAA Paper 82-0271, Jan. 1982.

12. Mell, Richard, AZ Technologies, Private Communication.

Table 1. Materials and Surface Coatings to Avoid at High Altitudes

MATERIAL	RATIONALE
Anodized coating	High resistivity prevents charge bleedoff
Fiberglass material	High resistivity prevents charge bleedoff
Uncoated mylar	High resistivity prevents charge bleedoff
Teflon	Has long term charge storage ability and causes catastrophic discharges
Kapton	High resistivity prevents charge bleedoff

Table 2. 90th Percentile Worst-Case Substorm Plasma Environment

Electron number density:	1.12 cm^{-3}
Electron temperature:	12000 eV
Ion number density:	.236 cm^{-3}
Ion temperature:	29500 eV

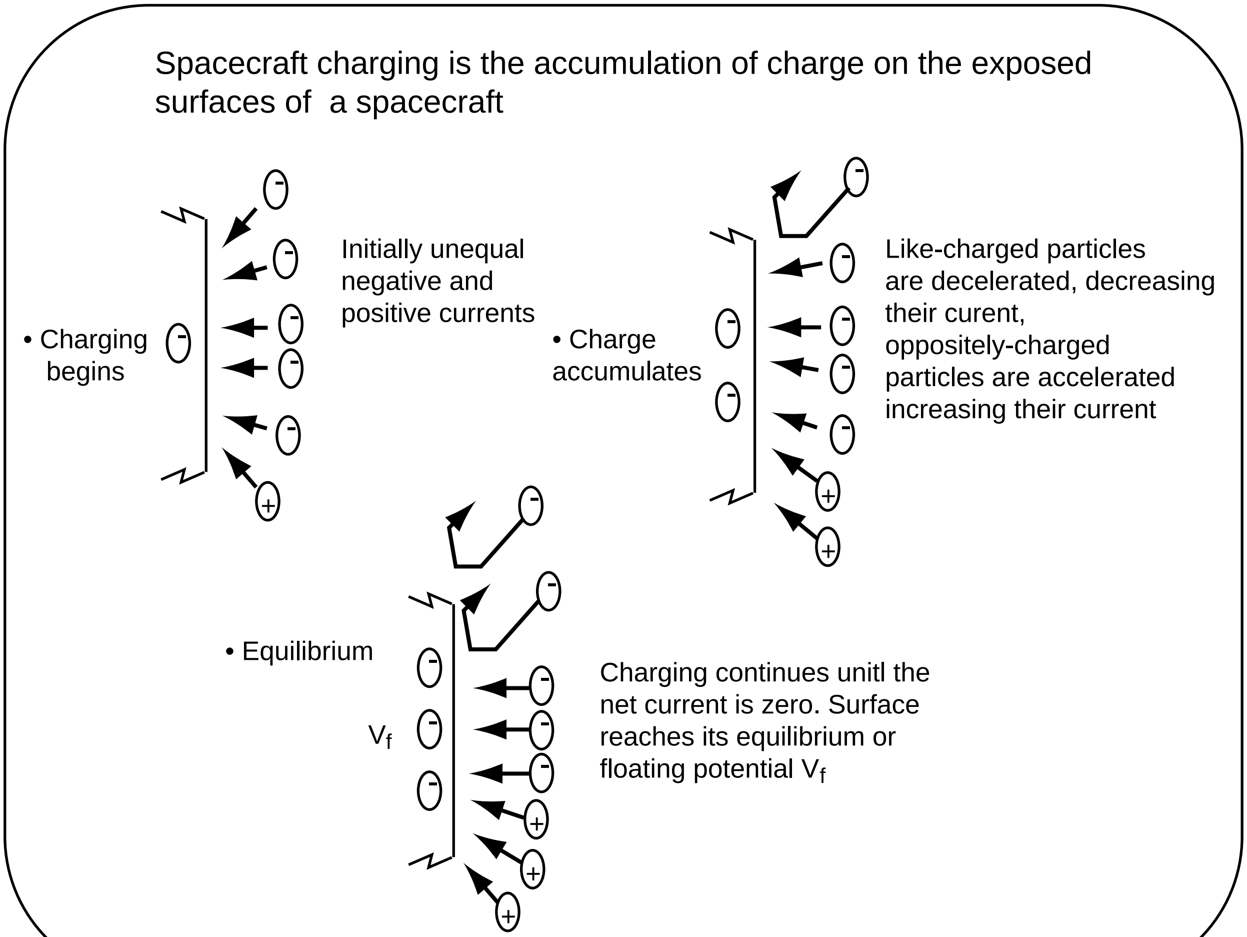
Spacecraft charging is the accumulation of charge on the exposed surfaces of a spacecraft
• Charging begins
Initially unequal negative and positive currents
• Charge accumulates
Like-charged particles are deceleraled, decreasing their curent, oppositely-charged particles are accelerated increasing their current
• Equilibrium
V_f
Charging continues unitl the net current is zero. Surface reaches its equilibrium or floating potential V_f
-
+

Figure 1. Cause of Spacecraft Charging

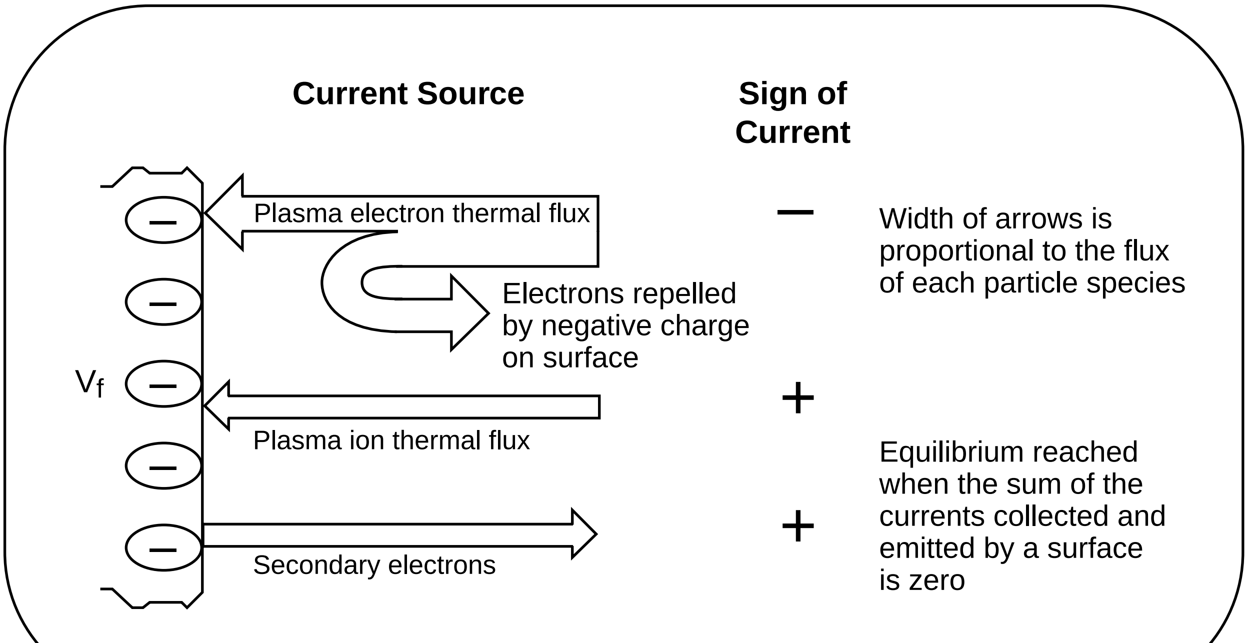
Current Source
Sign of Current
Plasma electron thermal flux
–
Width of arrows is proportional to the flux of each particle species
Electrons repelled by negative charge on surface
V_f
Plasma ion thermal flux
+
Equilibrium reached when the sum of the currents collected and emitted by a surface is zero
Secondary electrons
+
–

Figure 2. Negative Charging of Spacecraft Surfaces at High Altitudes

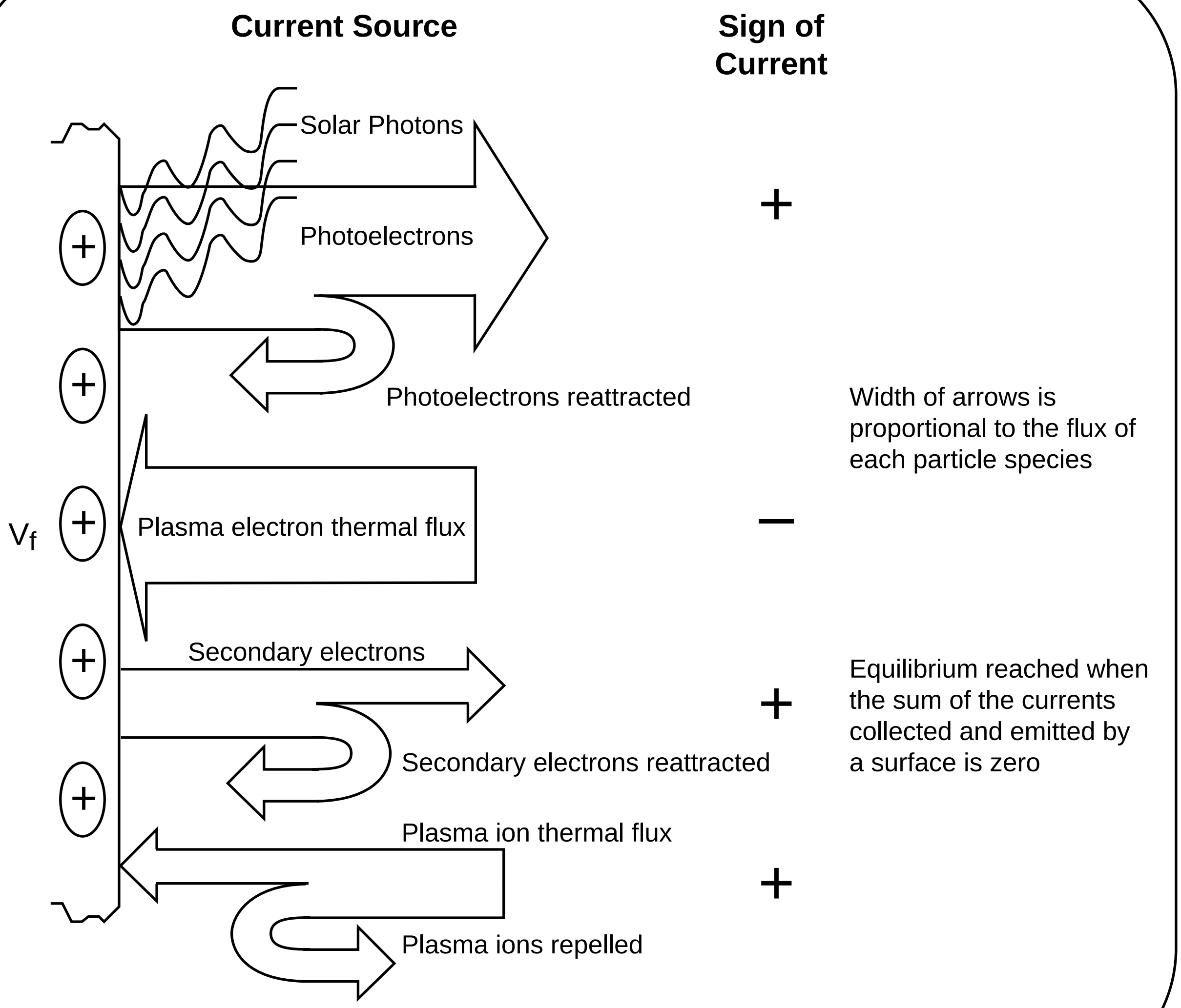
Current Source
Sign of Current
Solar Photons
Photoelectrons
+
Photoelectrons reattracted
Width of arrows is proportional to the flux of each particle species
V_f
Plasma electron thermal flux
–
Secondary electrons
+
Equilibrium reached when the sum of the currents collected and emitted by a surface is zero
Secondary electrons reattracted
Plasma ion thermal flux
+
Plasma ions repelled

Figure 3. Positive Charging of Spacecraft Surfaces at High Altitudes

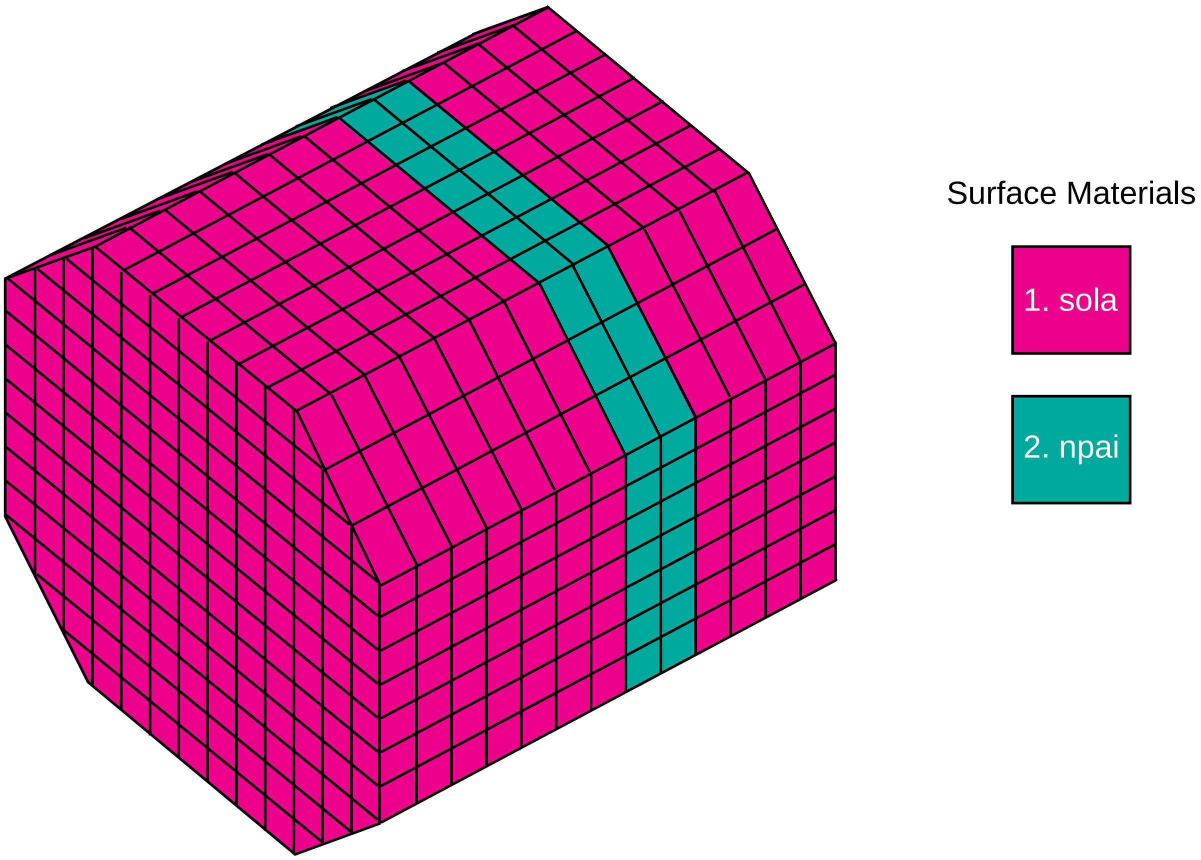
Surface Materials
1. sola
2. npai

Figure 4. NASCAP MI Spacecraft Model.

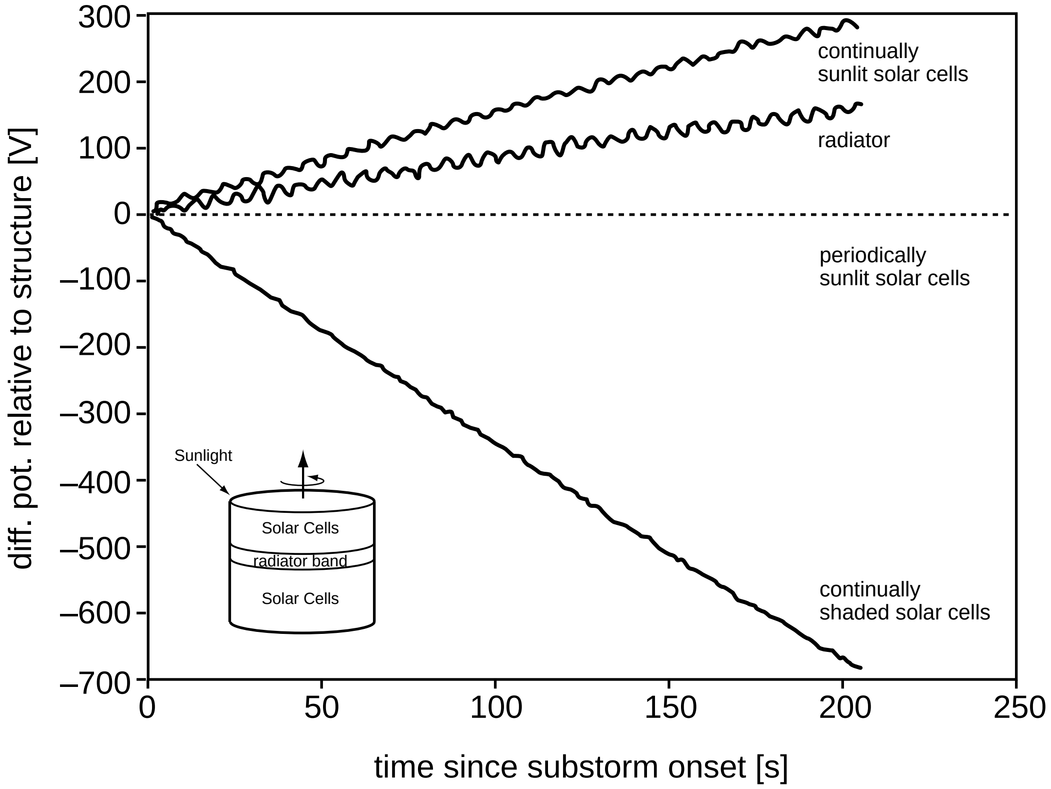

Figure 5. Differential Potentials Between MI Dielectric Surface Materials and the Underlying Metallic Structure. (Sun angle 90 degrees relative to rotation axis, 205 second simulation)

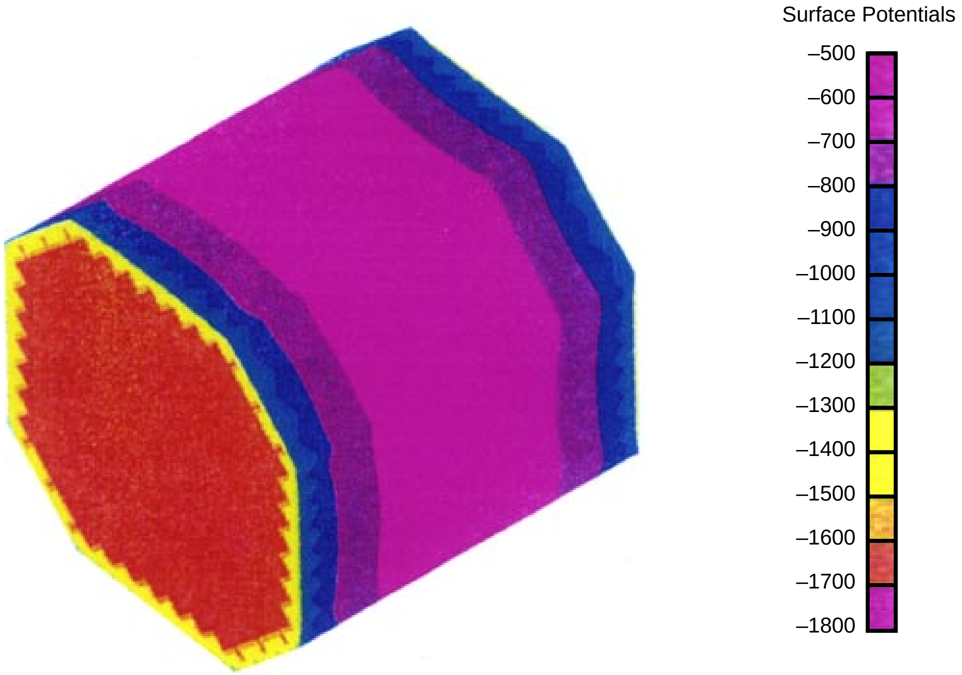
Surface Potentials
–500
–600
–700
–800
–900
–1000
–1100
–1200
–1300
–1400
–1500
–1600
–1700
–1800

Figure 6. NASCAP Predicted Surface Material Electric Potentials After Being Exposed for 205 Seconds to a Worst-Case Geomagnetic Substorm. (Sun angle 90 degrees relative to rotation axis)

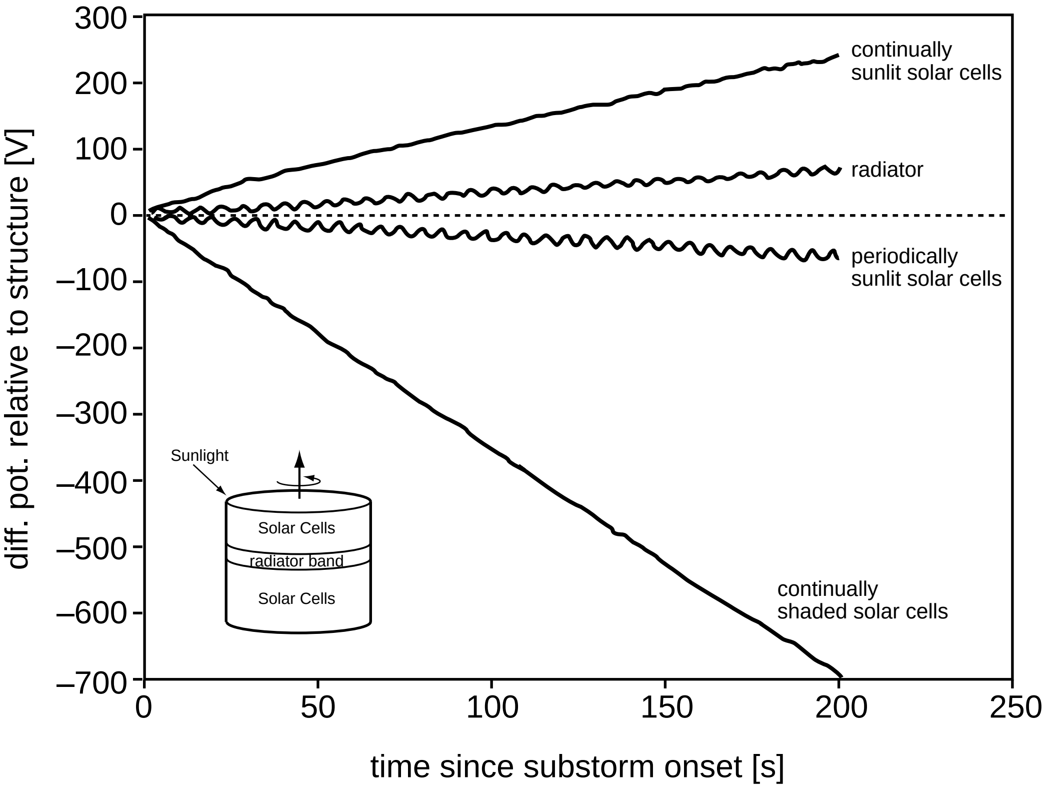

Figure 7. Differential Potentials Between MI Dielectric Surface Materials and the Underlying Metallic Structure. (Sun angle 45 degrees relative to rotation axis, 201 second simulation)

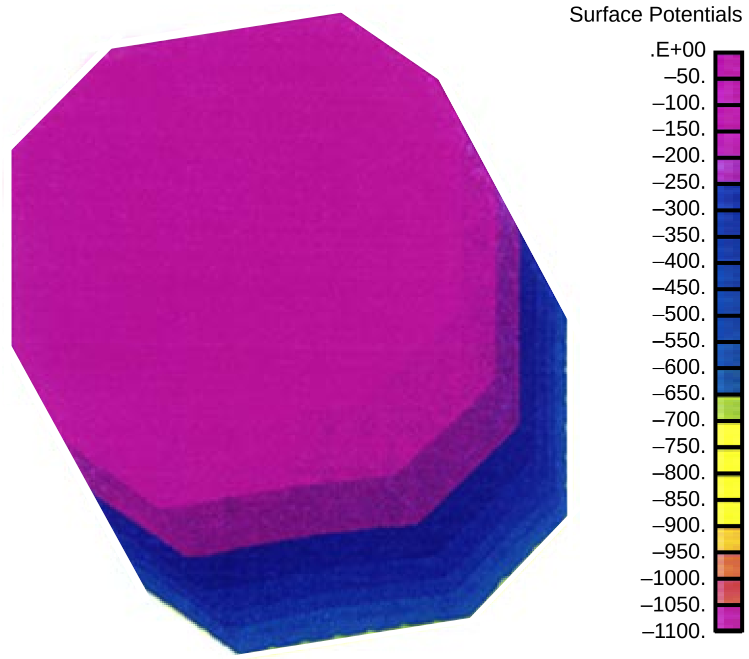
Surface Potentials
.E+00
–50.
–100.
–150.
–200.
–250.
–300.
–350.
–400.
–450.
–500.
–550.
–600.
–650.
–700.
–750.
–800.
–850.
–900.
–950.
–1000.
–1050.
–1100.

Figure 8. NASCAP Predicted Surface Material Electric Potentials After Being Exposed for 201 Seconds to a Worst-Case Geomagnetic Substorm. (Sun angle 45 degrees relative to rotation axis)

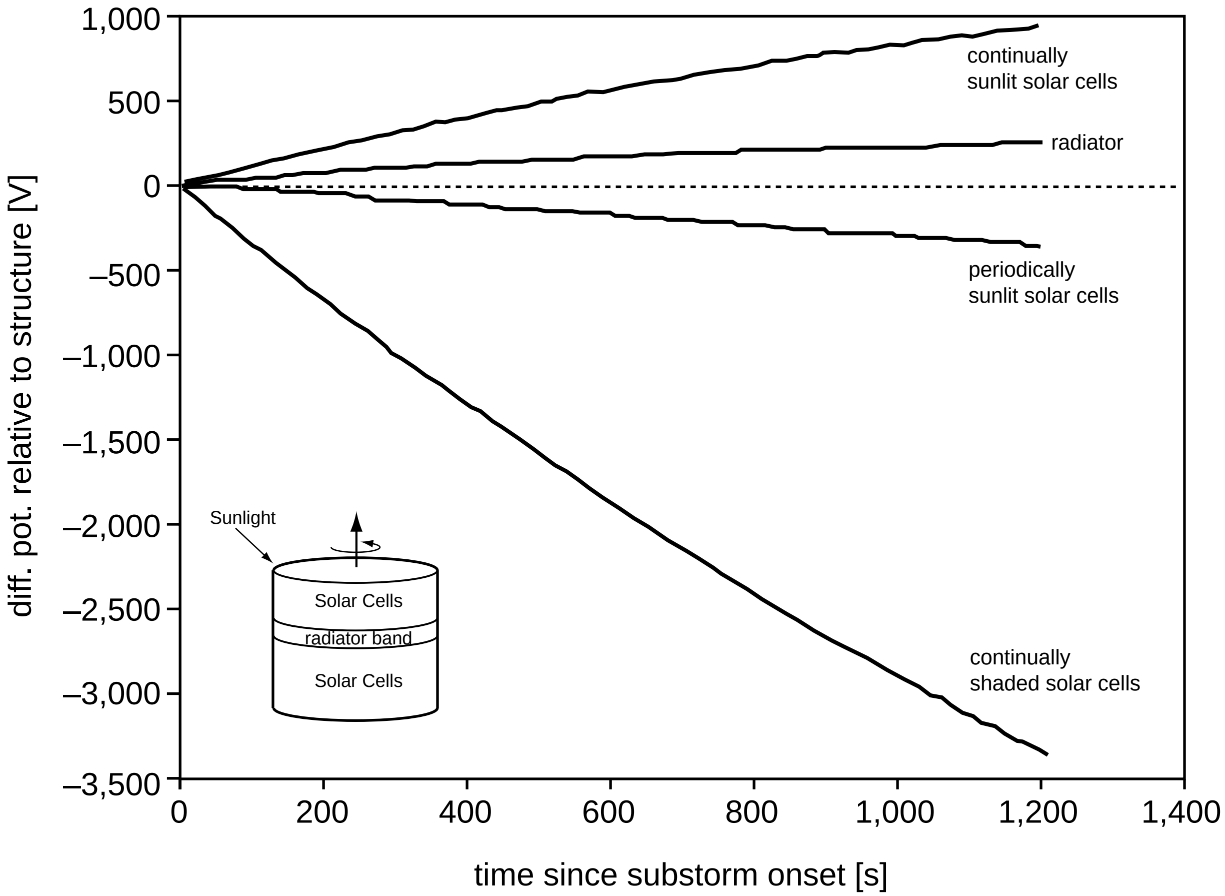

Figure 9. Differential Potentials Between MI Dielectric Surface Materials and the Underlying Metallic Structure. (Sun angle 45 degrees relative to rotation axis, 20 minute simulation)

REPORT DOCUMENTATION PAGE

Form Approved
OMB No. 0704-0188

Public reporting burden for this collection of information is estimated to average 1 hour per response, including the time for reviewing instructions, searching existing data sources, gathering and maintaining the data needed, and completing and reviewing the collection of information. Send comments regarding this burden estimate or any other aspect of this collection of information, including suggestions for reducing this burden, to Washington Headquarters Services, Directorate for Information Operation and Reports, 1215 Jefferson Davis Highway, Suite 1204, Arlington, VA 22202-4302, and to the Office of Management and Budget, Paperwork Reduction Project (0704-0188), Washington, DC 20503

1. AGENCY USE ONLY *(Leave Blank)*	**2. REPORT DATE** April 1997	**3. REPORT TYPE AND DATES COVERED** Reference Publication

4. TITLE AND SUBTITLE

The Magnetosphere Imager Mission Concept
Definition Study Final Report

5. FUNDING NUMBERS

6. AUTHORS

L. Johnson, M. Herrmann, and the MSFC MI Study Team

7. PERFORMING ORGANIZATION NAMES(S) AND ADDRESS(ES)

George C. Marshall Space Flight Center
Marshall Space Flight Center, Alabama 35812

8. PERFORMING ORGANIZATION REPORT NUMBER

M–832

9. SPONSORING/MONITORING AGENCY NAME(S) AND ADDRESS(ES)

National Aeronautics and Space Administration
Washington, DC 20546–0001

10. SPONSORING/MONITORING AGENCY REPORT NUMBER

NASA RP–1401

11. SUPPLEMENTARY NOTES

Prepared by Advanced Systems and Technology Office, Program Development Directorate

12a. DISTRIBUTION/AVAILABILITY STATEMENT

Unclassified–Unlimited
Subject Category 18

12b. DISTRIBUTION CODE

13. ABSTRACT *(Maximum 200 words)*

For three decades, magnetospheric field and plasma measurements have been made by diverse instruments flown on spacecraft in many different orbits, widely separated in space and time, and under various solar and magnetospheric conditions. Scientists have used this information to piece together an intricate, yet incomplete view of the magnetosphere. A simultaneous global view, using various light wavelengths and energetic neutral atoms, could reveal exciting new data and help explain complex magnetospheric processes, thus providing us with a clear picture of this region of space.

The George C. Marshall Space Flight Center (MSFC) is responsible for defining the Magnetosphere Imager mission which will study this region of space. A core instrument complement of three imagers (with the potential addition of one or more mission enhancing instrument) will fly in an elliptical polar Earth orbit with an apogee of 44,600 kilometers and a perigee of 4,800 km. This report will address the mission objectives, spacecraft design concepts, and the results of the MSFC concept definition study.

14. SUBJECT TERMS

natural space environment, spacecraft environment, environmental effects and impacts, solar activity influences, effects, and prediction

15. NUMBER OF PAGES 191

16. PRICE CODE A09

17. SECURITY CLASSIFICATION OF REPORT Unclassified	**18. SECURITY CLASSIFICATION OF THIS PAGE** Unclassified	**19. SECURITY CLASSIFICATION OF ABSTRACT** Unclassified	**20. LIMITATION OF ABSTRACT** Unclassified